ENEA Ricerca Sistema Elettrico	Sigla di identificazione	Distrib.	Pag.	di
	ADPFISS – LP2 – 055	L	1	137

Titolo

Development and validation of an approach and numerical models for safety analysis of FBR

Descrittori

Tipologia del documento:	Rapporto Tecnico
Collocazione contrattuale:	Accordo di programma ENEA-MSE su sicurezza nucleare e Reattori di IV generazione
Argomenti trattati:	Reattori Nucleari Veloci, Termoidraulica dei reattori nucleari Sicurezza nucleare, Analisi incidentale

Sommario

Il report rappresenta un contributo all'analisi numerica di scenari operativi e incidentali e consiste nella messa a punto, nell'applicazione e nella validazione di un approccio e di modelli per analisi di sicurezza di reattori veloci di IV generazione. L'attività è svolta in sinergia con International Coordinated Research Project (CRP) on EBR-II Shutdown Heat Removal Tests promosso dall'IAEA. L'attività, di lungo respiro, è multi-physics e multi-scale e trarrà beneficio dalla disponibilità di dati sperimentali misurati in reattore durante l'esecuzione di test sperimentali: protected (SHRT-17) ed unprotected (SHRT-45r) loss of flow nel reattore americano di ricerca EBR-II. L'attività nel suo complesso richiede uno sforzo sinergico di differenti competenze tecniche, dalla fisica del reattore, alla termoidraulica di sistema, alla fluidodinamica computazionale, alla termomeccanica del fuel.

Il documento presenta l'impianto EBR-II, oggetto delle simulazioni numeriche, e descrive il test sperimentale SHRT-17. Successivamente, riporta il modello termoidraulico realizzato per il codice di sistema RELAP5-3D©, la qualifica della nodalizzazione, il raggiungimento dello stato stazionario e la simulazione *blind* dell'esperimento. I risultati ottenuti sono stati poi confrontati con i dati sperimentali rilasciati nell'ambito del benchmark: il documento presenta un'analisi dettagliata finalizzata alla preparazione dell'analisi di posttest. Visto il livello di dettaglio della strumentazione negli assemblies sperimentali XX09 e XX10, installati nel driver del reattore, è stato realizzato un modello CFD attraverso il codice ANSYS CFX per fornire informazioni dettagliate sulla distribuzione di temperature nell'assembly, partendo dalle condizioni al contorno fornite dalla termoidraulica e dalla neutronica. Il modello include in principio la conduzione nelle guaine e nel filo, la convezione nel refrigerante, la conduzione nella scatola esagonale ed il bypass flow. Infine, si descrivono le attività di neutronica previste nell'ambito dell'attività, finalizzate prevalentemente alla valutazione dei coefficienti di reattività dei due test sperimentali (codici ERANOS e MONTECARLO) e alla simulazione del transitorio SHRT-45r con la cinetica neutronica tridimensionale (codice PHYSICS).

Note:

Autori:

A. Del Nevo, I. Di Piazza, C. Parisi, P. Console Camprini (ENEA)

E. Martelli, P. Balestra, F. Giannetti, A. Naviglio (CIRTEN-UNIROMA1)

REV.	DESCRIZIONE	DATA		REDAZIONE	CONVALIDA	APPROVAZIONE
1			NOME			
			FIRMA			
0	EMISSIONE	25/09/14	NOME	A. Del Nevo	M. Tarantino	M. Tarantino
			FIRMA			

(Page intentionally left blank)

SUMMARY

The present report is a contribution to the "Numerical analysis of operational scenarios and incidental" activity, that consists in the development, application and validation of approach and models for safety analysis of liquid metal Gen. IV reactors. The activity, developed in the framework of the International Coordinated Research Project (CRP) on EBR-II Shutdown Heat Removal tests promoted by IAEA, is multi-physics and multi-scale and will require the synergistic effort of different technical skills. The report, that summarize the main parts of the activity, is divided into two parts.

The former presents first the EBR-II plant and SHRT-17 description, correlated with the experimental data available. Then, the 3D thermalhydraulic model realized with RELAP5-3D© system code is presented. On the basis of the available data and initial conditions the steady state conditions are verified and the blind simulation of SHRT-17 is performed. The comparison between results obtained and the experimental data is executed and presented in the report.

The second part describes the CFD model, realized with ANSYS CFX code to provide detailed information about temperature distribution in the assembly, on the basis of information provided for XX09 and XX10 assemblies instrumentation. The model developed includes the entire pin bundle length with the preceding and follower unheated regions and the heated one. The cladding and wire conduction, the coolant convection, the hexagonal box and the bypass flow conduction are also included in the model.

The last two sections present the neutronic model that will be implemented with the deterministic code ERANOS and with MCP code, respectively.

LIST OF CONTENTS

LIST OF FIGURES

LIST OF TABLES

LIST OF ABBREVIATIONS

3D	Three Dimensional
ANL	Argonne National Laboratory
ATC	Annulus Thimble Thermocouple
BAF	Bottom of Active Fuel
BOP	Balance of Plant
CEA	Commissariat à l'énergie atomique et aux énergies alternatives
CFD	Computational Fluid Dynamics
CIAE	China Institute of Atomic Energy
CRP	Coordinated Research Project
DAS	Data Acquisition System
EBR-II	Experimental Breeder Reactor II
EC	European Commission
EU	European Union
FA	Fuel Assembly
FR	Fast Reactor
GEN IV	Generation IV
GFR	Gas-Cooled Fast Reactor
GIF	Generation IV International Forum
gpm	United Sates gallon per minute
HFD	High-Flow Driver
HWCR	High Worth Control Rod
IAEA	International Atomic Energy Agency
IB	Inner Blanket
IFR	Integral Fast Reactor
IHX	Intermediate Heat Exchanger
INCOT	In-Core Instrument Test facility
INL	Idaho National Laboratory
INSAT	Instrumented Subassembly
IPPE	Institute of Physics and Power Engineering
JAEA	Japan Atomic Energy Agency
KAERI	Korea Atomic Energy Research Institute
KINS	Korean Institute for Nuclear Safety
LFR	Lead-Cooled Fast Reactor
LWR	Light Water Reactor
LMR	Liquid Metal Reactor
MCP	Main Coolant Pump
M-G	Motor-Generator set
MSR	Molten Salt Reactor

NK	Neutron Kinetics
OB	Outer Blanket
ORNL	Oak Ridge national Laboratory
OTC	Outlet-Coolant Thermocouple
PPS	Plant Protection System
PS	Primary Side
R&D	Research and Development
SCWR	Supercritical Water Reactor
SDC	Safety Design Criteria
SFR	Sodium Fast Reactor
SHRT	Shutdown Heat Removal Test
SS	Secondary Side
SSC	Structures, Systems and Components
TAF	Top of Active Fuel
TH	Thermal-Hydraulic
SYS	System
TTC	Top-of-core Thermocouple
ULOF	Unprotected Loss-of-Flow
VHTR	Very High Temperature Reactor

1 INTRODUCTORY REMARKS

1.1 Framework

The activity is developed and set-up in synergy of IAEA Coordinated Research Project (CRP) on EBR-II Shutdown Heat Removal Tests (SHRT) [1].

The CRP aims at improving design and simulation capabilities in fast reactor neutronics, thermal hydraulics, plant dynamics and safety analyses through benchmark analyses of a protected and an unprotected loss-of flow test from the EBR-II SHRT program. Activities include core physics and thermal-hydraulics/safety assessments. Investigations of thermal hydraulics characteristics and plant behavior focus on predicting natural convection cooling accurately by evaluating the reactor core flow and temperatures in comparison to experimental data.

The activity has been established to support validation of simulation tools and models for the safety analysis of liquid metal fast reactors. Validated tools and models are needed both to evaluate liquid metal fast reactors passive safety phenomena and to assess reactor designs incorporating passive features into the system response to accident initiators.

Passive safety response in liquid metal fast reactors is the result of reactor design features that shut down the reactor, remove residual heat, and keep the core cooled during accidents. In addition to the Doppler effect, negative reactivity feedback mechanisms can be used to passively shut down the fission process. Negative reactivity feedback mechanisms are based on thermal expansion and contraction of structural materials, which affects neutron leakage in the fast spectrum core. Radial and axial core expansion, subassembly bowing, and control rod driveline expansion are examples of these passive reactivity feedbacks. Coolant density changes in sodium are utilized in the design to produce natural circulation flow, thus to keep the core cooled when forced circulation is lost. Passive heat removal is accomplished through use of natural convection, conduction and vessel wall radiation.

The potential for a liquid metal cooled fast reactor to survive severe accident initiators with no core damage has been extensively demonstrated during landmark shutdown heat removal tests in Experimental Breeder Reactor-II (EBR-II). Two of these test, identified as SHRT-17 and SHRT-45R tests, have been chosen because of the availability of extensive thermocouple and flow rate data at various elevations in two instrumented subassemblies, placed in row 5 of the core (one representing a fuel subassembly and the other a blanket subassembly), plus the range of conditions encountered in both tests. They simulated a loss of pumping power (normal and emergency) to the plant operating at full power and flow.

The objectives are to validate state-of-the-art computer software, to improve participants' analytical and numerical capabilities in fast reactor design and analysis through comparison of numerical predictions with test data from the EBR-II SHRT-17 protected loss of flow and SHRT-45R unprotected loss of flow tests.
The activity will specifically contribute toward extending the validation and verification base of sodium-cooled fast reactor safety analysis codes to accurately simulate the primary coolant system behavior during loss of flow transient. Particular focus will be on predicting the natural convective cooling.

- To improve the understanding of FR neutronics, thermal-hydraulics, and system analysis.

- To improve understanding of the methodology employed to simulate fast reactor transient behavior.
- To improve verification, validation and qualification status of this methodology.
- To reduce uncertainty in liquid metal fast reactor safety codes, contributing also to the long-term goal of reducing the costs of building metal-cooled fast reactor.
- To enhance reliability of the safety behavior predictions for new advanced reactor.

1.2 Objective of the activity

The ENEA activity addresses to the following objectives:

- To compare best-estimate thermal-hydraulic system code calculations to experimental data, thus to validate RELAP5-3D© system code in simulating sodium fast reactors designs.
- To identify and, as far as possible, to quantify the RELAP5-3D© code limitations and the source of uncertainties in simulating postulated accidents occurring in liquid metal FR designs.
- To improve the understanding of the thermal-hydraulics processes and phenomena observed in EBR-II test.
- To compare the performances of TH system codes in the domain of interest.
- To develop reliable approaches for the application of TH-SYS codes in safety analysis of new generation FR systems (i.e. LFR), including the coupling with CFD and NK.

2 DESCRIPTION OF EBR-II PLANT

2.1 Introduction

EBR-II [3][5] was operated initially to demonstrate the feasibility of a closed fuel cycle that required the addition only of uranium-238 to the fuel breeding process allowing for sustained operation. To achieve the intended fuel utilization, the initial EBR-II operating period was closely tied to research into pyrometallurgical reprocessing for irradiated nuclear fuel. This period lasted five years. Following the fuel cycle demonstration phase, the focus of EBR-II shifted for much of the next ten years towards irradiation experiments of advanced binary and ternary metal fuels and also advanced oxide fuels. From 1983 and 1994, EBR-II was used for experiments designed to demonstrate the importance of passive safety in liquid metal reactors (LMR).

The Shutdown Heat Removal Test (SHRT) program [3][4] was carried out in EBR-II between 1984 and 1986. The objectives of this program were to support U.S. LMR plant design, provide test data for validation of computer codes for design, licensing and operation of LMRs, and demonstrate passive reactor shutdown and decay heat removal in response to protected and unprotected transients. The protected and unprotected transients tested included loss of flow in the primary and/or intermediate sodium loops as well as a loss of heat sink from balance of plant. Additional tests were performed to examine the response of the system to balance of plant changes and others were performed to characterize reactivity feedbacks.

Passive safety response in sodium fast reactors is the result of reactor design futures that will shut down the reactor, remove residual heat, and keep the core cooled during accidents. In addition to Doppler effect, negative reactivity feedback mechanisms based on thermal expansion and contraction of structural materials, which affect neutron leakage in the fast spectrum core, can be used to passively shut down the fission process. Radial and axial core expansion, subassembly bending, and control rod driveline expansion are examples of these passive reactivity feedbacks. To keep the core cooled when forced circulation is lost, coolant density changes in sodium can be utilized in the design to produce natural circulation flow. Passive heat removal can be accomplished through use of natural convection, conduction and vessel wall radiation.

On June 20, 1984, the SHRT-17 loss of flow test [1][4], was conducted where a loss of electrical power to all the plant sodium coolant pumps was used to demonstrate the effectiveness of natural circulation cooling characteristics. Starting from full power and flow, both the primary and intermediate-loop coolant pumps were simultaneously tripped and the reactor was scrammed to simulate a protected loss-of-flow accident. In addition, the primary system auxiliary coolant pump that normally had an emergency battery power supply was turned off. Temperatures in the reactor quickly rose to high, but acceptable levels as the natural circulation characteristics cooled the reactor down safely at decay heat levels. SHRT-17 demonstrated that natural phenomena such as thermal expansion of the sodium coolant and thermal inertia of the primary pool sodium, as opposed to electromechanical systems such as electrically driven pump, can be effective in protecting the reactor against potentially adverse consequences from protected loss-of-flow and loss-of heat-sink accidents.

2.2 EBR-II plant overview

The EBR-II plant is a sodium cooled reactor located in Idaho, it was designed and operated by Argonne National Laboratory for the US Department of Energy [5]. Operation began in 1964 and

continued until 1994. EBR-II was rated for a thermal power of 62.5 MW_t with an electric output of approximately 20MW_e [3][4]. Mass flow rates in three cooling loops were rated as [2][3]:

- *Primary sodium: 485 kg/s*
- *Intermediate sodium: 315 kg/s*
- *Secondary steam: 32 kg/s*

All primary system components were submerged in the primary tank, which contained approximately 340 m^3 of liquid sodium at 371°C. An argon cover gas was maintained over the surface of the sodium in the primary vessel to minimize the opportunity for air to contact the sodium. Fig. 1 shows the primary tank and the other components The primary cooling system consisted of two mechanical centrifugal pumps operated in parallel and pumping a total of 485 kg/s of sodium. The two pumps drew sodium from this pool and provided sodium to the two inlet plena for the core. Subassemblies in the inner core and the extended core regions received sodium from the high-pressure inlet plenum, accounting for approximately 85% of the total primary flow. The blanket and the reflector subassemblies in the outer blanket region received sodium from the low-pressure inlet plenum.

Hot sodium left the subassemblies into a common upper plenum where it mixed before passing through the outlet pipe into the intermediate heat exchanger (IHX). The pipe feeding sodium to the IHX is referred to as “Z-pipe” and will be described in greater detail in 0. Sodium then exited the IHX back into the primary sodium tank before entering the primary sodium pumps again.

Sodium in the intermediate loop traveled from the IHX to the steam generator where its heat was transferred to the balance-of plant (BOP). The colder sodium intermediate loop then traveled through a similar length of piping back to the IHX. The steam generator consisted of two parallel superheaters and seven parallel evaporators. Fig. 2 shows a simple schematic of the primary, intermediate and steam systems. Note that power, flow and temperature conditions described earlier are for typical EBR-II operation. These conditions differ slightly from initial conditions for the SHRT-17 test which is discussed in Section 3.

The reactor-vessel grid-plenum assembly accommodated 637 hexagonal subassemblies. The subassemblies were segregated into three regions: core, inner blanket (IB) and outer blanket (OB). The central core comprised 61 subassemblies in the first five rows. The inner blanket region was composed of Rows 6 and 7. Originally these rows were loaded with blanket subassemblies. However, during SHRT-17 no blanket subassemblies were loaded in this region. Instead, Row 6 contained the driver-fuel and irradiation subassemblies of the expanded core and Row 7 contained reflector and subassemblies. The outer blanket region comprised the 510 subassemblies in Rows 8-16, which were either blanket or reflector subassemblies.

EBR-II was heavily instrumented to measure mass flow rates, temperatures and pressures throughout the system [2][3].

2.3 Reactor Core

The EBR-II reactor core [1][3][26] vessel grid-plenum assembly accommodated 637 hexagonal subassemblies, which were installed in one of three regions: central core, inner blanket (IB) or outer blanket (OB). Each subassembly position was identified by a unique combination of three parameters: row, sector and position within the sector.

Fig. 3 illustrates the subassemblies arrangement of the reactor and the subassembly identification convention. Subassembly row identification begins at Row 1 for the subassembly in the core-center and moves outward to Row 16. Row 1 has one subassembly, Row 2 has six subassemblies. From Row 2 outward to Row 14, each row has 6 additional subassemblies than the last. Rows 15 and 16 are not complete rows and have 66 and 24 subassemblies, respectively. Each row is broken up into six sectors A through F. As each row approximates an hexagon, each side of the row is assigned to one of the six sectors. The final parameter needed to identify a subassembly location is the position within the sector. The line of subassemblies dividing sectors A and F are defined as the subassemblies in position 1 of their respective rows within the sector A. The line of subassemblies that divide sector A and B are therefore defined as the subassemblies in position 1 of their respective rows within sector B. This pattern continues for the remaining four sides of the core layout. As an example, the subassembly XX09 is positioned in subassembly location 5D3, where 5 is the row, D is the sector and 3 is the position within the sector.

The central core comprised the 61 subassemblies in the first 5 rows. Two of these positions contained safety-rod subassemblies and eight positions contained control-rod subassemblies. These subassemblies are identified by the letter S and C, respectively, in Fig. 4. Two positions in Row 5 contained the in-core instrument subassemblies (INSAT) XX09 and XX10, and one position in Row 5 contained the in-core instrument test facility (INCOT) XY16. The remaining central core subassemblies were either driver-fuel or experimental-irradiation subassemblies of varying types. For SHRT-17 test only the MARK-II A I type driver subassembly was used.
In Fig. 4, driver subassemblies are denoted by the letter D, instead the letter P indicates a partial driver, which are driver subassemblies where approximately half of the fuel elements are replaced by steel elements. HFD in Fig. 4 refers to a high-flow driver, all of which were located in Row 6. An high flow driver subassembly was the basic driver subassembly with extra inlet flow holed drilled into the subassembly inlet nozzle region to allow higher subassembly coolant flow.

The expanded core region was composed of Rows 6 and 7. This region is also named inner blanket region because originally housed blanket subassemblies. But for SHRT-17 test no blanket subassemblies were loaded in this region. Instead, Row 6 contained the driver-fuel and irradiation subassemblies and Row 7 contained reflector subassemblies. The outer blanket region comprised the 545 subassemblies in Rows 8-16, which were either blanket or reflector subassemblies. In Fig. 4 reflector subassemblies are identified with the letter R.

In Fig. 4, those subassemblies whose label begins with letter K were steel subassemblies. The remaining subassemblies were experimental or driver-irradiation type subassemblies. Fig. 3 illustrates the rest of the core. Each type of subassembly is discussed in Ref. [3].

Subassembly geometries
The outer configuration of all subassemblies [3][26] was very similar. The upper adapter was formed to fit the top of the hexagonal outer tube of the central region and the top part of the upper adapter was slotted to adjust the orientation of the subassembly within the reactor grid. The lower surface of the mushroom-shape head on the upper adapter provided a solid surface for grasping during fuel handling with gripper devices.

The center region of each subassembly was surrounded by a hex tube, which created an independent flow channel for each subassembly. Each face of the hexagonal tube contained a spacer button, formed by dimpling the tube wall outward. The buttons served to prevent the subassemblies from touching in case of bowing induced by accident. .

The lower adapter positioned the subassembly within the reactor grid and determined the amount of coolant flow through the subassembly. Subassemblies positioned in Rows 1 through 5 had core-type lower adapters. The core-type adapter was a stainless steel, machined cylindrical nozzle. The upper portion had a rounded shoulder, which sat in the hole of the upper grid plate in the core region. The core region lower adapters had four sets of coolant flow holes. Depending on the row in which the subassembly was positioned, a different number of flow holes were covered by the various step sizes of the lower grid plate.

The expanded core-type lower adapter was used for driver fuel in Row 6 and irradiation subassemblies located in Rows 6 or 7 of the reactor. The inner blanket lower adapter with two sets of flow holes was used for the subassemblies, other than driver fuel type, located in Rows 6 or 7. The outer blanket lower adapter was used for subassemblies in Rows 8-16. These adapters fit into stainless steel tubes that interconnected the upper and lower grid of the reactor grid assembly to provide a flow path from the low-pressure plenum. Yet another type of lower adapter was used for the control rod and safety rod subassemblies.

The inner configuration of the center section of subassembly varied depending upon the specific subassembly type. For those subassemblies types that included fuel elements, Tab. 1 presents selected nominal design parameters of the fuel element by type. Tab. 2 presents selected nominal design parameters for the subassembly hexagonal duct wall. Full set of data is available in in Ref. [3].

Fig. 5 shows an isometric view of the inner configuration of a MARK-II AI subassembly. The center section of the MARK-II AI subassembly consisted of an upper shield, a core bundle of fuel elements and a lower shield. The MARK-II AI and MARK-II A fuel elements were part of the central core driver and expanded core driver subassembly designs. The MARK-II S element was used in the high worth control rod design.

Each fuel element clad tube contained a single metal fuel slug U-5Fs is the fission alloy uniquely developed and fabricated for the Argonne EBR-II reactor [6]. The fuel element were sodium bonded. Above the sodium bond level was a fission gas plenum that was initially filled with an inert gas until fission gas was produced. The inert gas used was Helium with Xenon tracer isotope added for tagging a leaking fuel element.

The linear thermal expansion of the U-5 wt % Fs fuel pins pre-irradiated in EBR-II [3][6] was given as:

$$\frac{\Delta L(T)}{L_2} = \begin{cases} 1.62 \times 10^{-5}(T - 273) & T < 823\ K \\ 0.0089 + 5.7 \times 10^{-5}(T - 823)\ 823 < T < 913\ K \\ 0.014 + 2.1 \times 10^{-5}(T - 913) & T > 913\ K \end{cases}$$

Where $\frac{\Delta L(T)}{L_2}$: linear thermal expansion from a fixed temperature 273 K to any temperature T, expressed as a fraction of length L_2 at the temperature 273 K. This correlation is independent of the fission content of the alloy. It was implemented in and tested with the SAS4A code for analysis of EBR-II transient tests. The reference density which was used for the U-Fs fuel is $18.2 \times 10^3\ kg/m^3$ at 300 K. The heat capacity for U-5Fs fuel based on Argonne fuel properties work in Ref. [3]. Thermal conductivity data are reported in Ref. [3].

2.4 Coolant System

The EBR-II coolant systems model [2][3][4] for the SHRT-17 test included the major components in the primary sodium circuit and the intermediate side of the intermediate heat exchanger. Starting from the outlet of the reactor core, the primary sodium circuit included the upper plenum, reactor outlet piping, auxiliary EM sodium pumps, reactor inlet piping and high- and low-pressure inlet plena.

Fig. 6 illustrates the major components of the EBR-II primary sodium circuit. The two primary sodium pumps took suction from the primary sodium tank and provided sodium to the reactor inlet piping. Both sets of inlet piping provided sodium to the high-pressure and low-pressure inlet plena. The high pressure inlet plenum provided sodium to the subassemblies in the first 7 rows; while the low-pressure inlet plenum provided sodium to Rows 8-16. Sodium discharged from the right side of the reactor vessel into the reactor outlet piping, known as the 'Z-Pipe'. The shape of this pipe accommodated thermal expansion. The top of the Z-Pipe contained the auxiliary EM pump, which rated to provide up the 0.5% of the nominal pump head. Sodium exited the Z-Pipe and entered the shell side of the intermediate heat exchanger. Cold sodium was finally discharged into the primary sodium tank. Fig. 6 shows the two primary sodium pumps and their inlet piping.

Simplified geometry was given for the major components of the primary sodium circuit in the benchmark model [3].
The primary tank was the outer boundary of the primary sodium circuit and was modeled as a vertically cylinder. It encompassed all of the major primary sodium components. The reactor vessel, intermediate exchanger and two primary sodium pumps were modeled as vertically oriented cylinders. Sodium piping was modeled as a series of straight pipes connected by pipe bends that, unless otherwise stated, had a bend radius equal to the pipe radius. The reactor vessel, IHX, pumps and sodium piping were assumed to be the only components that displaced sodium in the primary tank. The main characteristics of the all components are given in the following sections.

Primary Sodium Tank
The cylindrical primary sodium tank, illustrated in Fig. 7, contained two vessel walls with the space between the inner and outer vessel walls filled with argon. Outside of the inner vessel wall was the argon layer; outside of the argon layer was the outer vessel wall. Both vessel walls were composed of Type 304 stainless steel.

The total volume of sodium in the primary system was approximately 340.69 m^3 at an average nominal temperatures of 644.26 K. This volumes of sodium included all sodium in the major components, piping, reactor subassemblies and primary tank sodium. The core support structure below the reactor vessel was assumed to displace a negligible amount of the sodium.

Reactor Vessel
The EBR-II reactor vessel and its internal components are illustrated in Fig. 8. Sodium discharged from the primary sodium pumps entered the low-pressure inlet plenum from the two inlet pipes or the high-pressure inlet plenum. Sodium from these two inlet plena was provided to the reactor subassemblies and then discharged into the common upper plenum. Sodium exited the upper plenum through the Z-Pipe.

The neutron shielding surrounded the reactor, upper plenum and lower plena with sections removed from the inlet and outlet piping. Other than the grid plates that separateed the lower plena, there

wass no significant shielding below the reactor. Above the upper plenum sat the reactors cover, through which control rod drive shafts and instrumentation led enter the reactor vessel.

Inlet Plena

Fig. 9 illustrates the EBR-II high- and low-pressure inlet plena. The lower plenum received coolant from the two low-pressure inlet pipes. Sodium passed through a vertically oriented baffle plate with 50 baffle flow holes and then through an horizontally oriented baffle plate with 592 baffle holes. Then, sodium entered one of the 510 outer blanket stainless steel tubes that fed the outer blanket region subassemblies (Rows 8-16), which are identified in Fig. 9. All structure in the inlet plena was composed of Type 304 stainless steel.

The upper inlet plenum received sodium from the two high-pressure inlet pipes. Sodium then passed through a vertical baffle plate, around the stainless steel tubes connecting the low-pressure plenum with the core, and into the high-pressure inlet plenum. In the high-pressure inlet plenum, sodium was distributed to the subassemblies in Rows 1-7.

The central core region of the high-pressure inlet plenum contained a series of seven concentric hexagonal steps. Each step had an aperture for each subassembly in the row in which the bottom of each subassembly was inserted. These steps had varying heights to block off certain holes depending on the desired amount of sodium flow through the subassembly (as the lower adapter of each subassembly in Rows 1-7 had a series of sodium inlet flow holes).

Upper plenum

The EBR-II upper plenum contained a baffle plate to mix the outlet sodium flow. Since not enough details were available, it was assumed that the sodium leaving the upper plenum was fully mixed when it entered the reactor outlet pipe.

The upper plenum consisted of two regions: a cylindrical region directly above the reactor subassemblies and an annular region surrounding the cylindrical region. Sodium left the upper plenum through the reactor outlet pipe and entered into the Z-Pipe.

Pumps

The primary sodium circuit had three pumps: two main and one electromagnetic pump. The two main primary pumps laid opposite each other at a radius of 3.251 meters from the center of the core. Primary sodium pump #1 was located 120° counter-clockwise from the IHX, while the primary sodium pump #2 was located 60° clockwise from the IHX. The electromagnetic pump was located around part of the Z-Pipe. It was assumed that both types of pumps were fabricated with Type 304 stainless steel.

Piping

Two sets of sodium piping were installed in the primary sodium circuit: the reactor outlet and the reactor inlet piping. The reactor outlet pipe, or Z-Pipe, began at the reactor outlet plenum and ended at the intermediate exchanger. It was constructed in a Z-shape to account for thermal expansion during periods of elevated outlet and cold pool sodium temperatures. The reactor inlet piping consisted of two identical sets of piping, from both the primary sodium to the inlet plena. Both sets of piping were made of Type 304 stainless steel. In the following piping descriptions, the x-axis was assumed to be on the line between the axial centerlines of the reactor core and IHX.

Since the sodium in the reactor outlet pipe experienced higher temperature than the bulk sodium surrounding it, the Z-Pipe was a double-walled structure. The annular region between the two pipe walls was filled with static sodium. In the upper section of the Z-Pipe was located the auxiliary EM pump.

Intermediate Heat Exchanger

The intermediate heat exchanger transferred (Fig. 10) heat from the radioactive primary system to the intermediate system and isolated the primary system from the water inventory in the steam plant. The heat exchanger was a tube-and shell design with single-wall straight tubes and was operated in the counter flow mode.

The heat exchanger consisted of three modules or components, all composed of Type 304 stainless steel. The well casing was a cylindrical annulus with its major axis oriented vertically and it hangs from the primary tank cover from a lip at the upper end of the well casing and continues downward to an elevation of 1.559 meters above the bottom of the active core. It consisted of four concentric steel cylinders with stagnant sodium between each layer. The lower end of the casing was terminated by a hemispherical head. Welded to the top of the tube bundle was the shield plug. Once the tube bundle and shield plug were lowered as a unit into the well casing, a cover was placed over the open end of the well casing and welded shut.

Heat transfer from primary to intermediate sodium took place in the lower half of the intermediate exchanger where the tube bundle was located. The primary coolant was admitted on the shell side through a horizontal inlet pipe (i.e. the outlet of the Z-Pipe) that penetrates the well casing wall 4.939 meters above the bottom of the active core. The fluid exited the inlet pipe and entered the upper region of the tube bundle, where it was distributed horizontally by baffles. The upper end of the tube bundle (above the inlet pipe) was terminated by the upper tube sheet, resulting in the primary sodium being directed downward parallel to the tubes. The primary sodium traveled down the length of the tubes and exited the well casing horizontally just above the lower tube sheet through an annular opening in the well casing.

The intermediate sodium entered the intermediate heat exchanger through a vertical pipe that penetrated the well casing cover. This pipe extended down the length of the well casing to the hemispherical region defined by the lower tube sheet and the well casing lower hand. A set of hemispherical baffles redirected the fluid 180° so that it flowed upward. The fluid then entered the bottom of the tubes at the lower tube sheet. The fluid flowed up the length of the tubes and then exited the tubes into another hemispherical-shaped region defined on its bottom by the upper tube sheet and on its upper side by a hemispherical-shaped spun from metal. An exit pipe was welded to the hemispherical cap. The exit pipe traveled the length of the upper-half of the well casing up to the well casing cover, where it exited the intermediate heat exchanger through a penetration the well casing cover.
The collection of internals in the upper half of the well casing was known as the shield plug. The shield plug contained the inlet and the outlet intermediate side pipes, while the remaining space was occupied by various thermal and radiation shields. The shield plug represented a large thermal connections to both the primary and intermediate flow paths were rather weak, with time scales on the order of seconds or minutes. The areas available for heat transfer and the radius of the shield plug were such that the heat transfer rates were small compared to the energy storage capability of the shield material.

PIN GEOMETRY	MARK-II AI	MARK-II A	MARK-IIS	XX09	XX10	OUTER BLANKET
Number of pins	91	91	61	59	18	19
Number of elements	--	--	--	61	--	--
Fuel alloy	U-5Fs	U-5Fs	U-5Fs	U-5Fs	Stainless Steel	Depleted U
Fuel -slug lenght [m]	0.3429	0.34290	0.3429	0.3429	N/A	1.397
Element lenght [m]	0.6108	0.6362	0.5334	0.6108	0.6108	1.575
Restrainer height above fuel [m]	0.0127	0.0127	0.0127	--	None	N/A
Sodium level above fuel [m]	0.03175	0.00635	0.00635	0.03175	N/A	0.03048
Plenum gas	Inert gas	Inert gas	Inert gas	Inert gas	N/A	Inert gas
Cladding Material	316	316	316	316	316	304
Spacer-wire diameter [m]	0.00124	0.00124	0.00124	0.00124	0.00124	None
Spacer-wire material	316	316	316	316	316	N/A
Spacer-wire pitch [m]	0.15240	0.15240	0.15240	0.15240	0.15240	None

Tab. 1 – EBR-II subassembly fuel elements design parameters (nominal).

	MARK-II AI MARK-II A	XX09 XX10	SAFETY HWCR	REFLECTOR URANIUM BLANKET
OUTER HEX TUBE				
Flat to flat outside [m]	0.05817	0.05817	0.05817	0.05817
Flat to flat inside[m]	0.0561	0.0561	0.0561	0.0561
Material	316SS	304SS	304SS	304SS
INNER HEX TUBE				
Flat to flat outside [m]		0.0484	0.0484	
Flta to flat inside [m]		0.0464	0.0464	
Material		304SS	304SS	
Upper Adapter/Fixture	304SS		304SS	304SS
Upper Axial Shield	304SS		304SS	
Lower Axial Shield	304SS		304SS	
Lower Adapter	304SS		304SS	304SS

Tab. 2 – EBR-II subassembly structure design parameters (nominal).

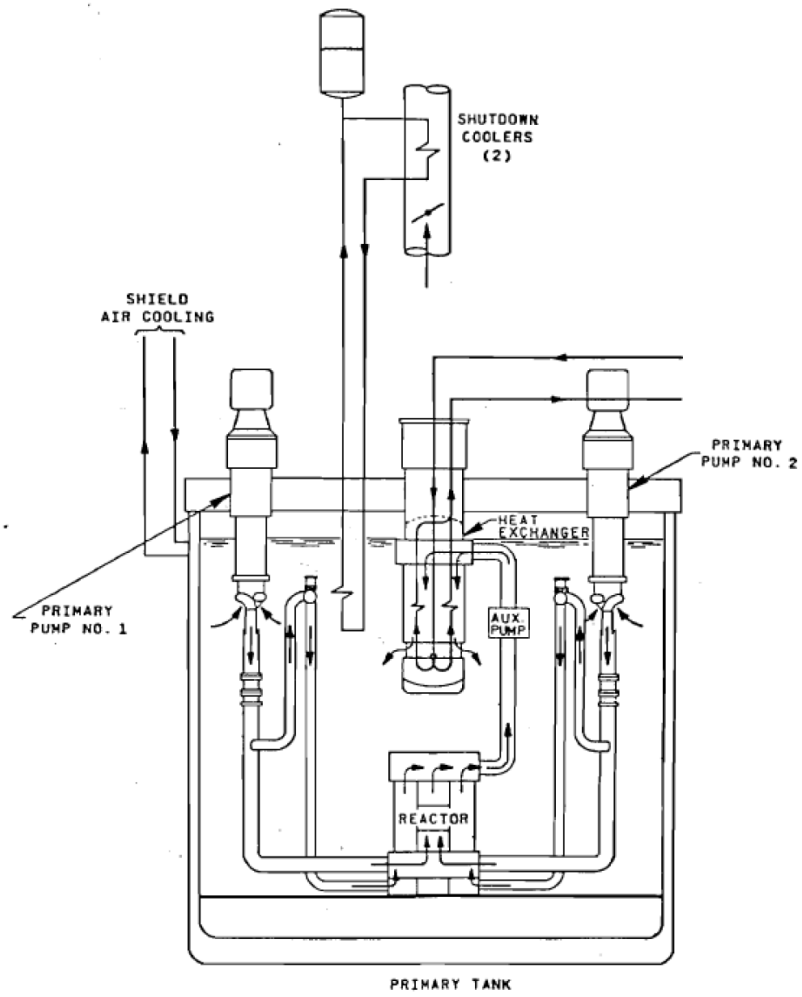

Fig. 1 – EBR-II Primary Tank Sodium Flow Paths.

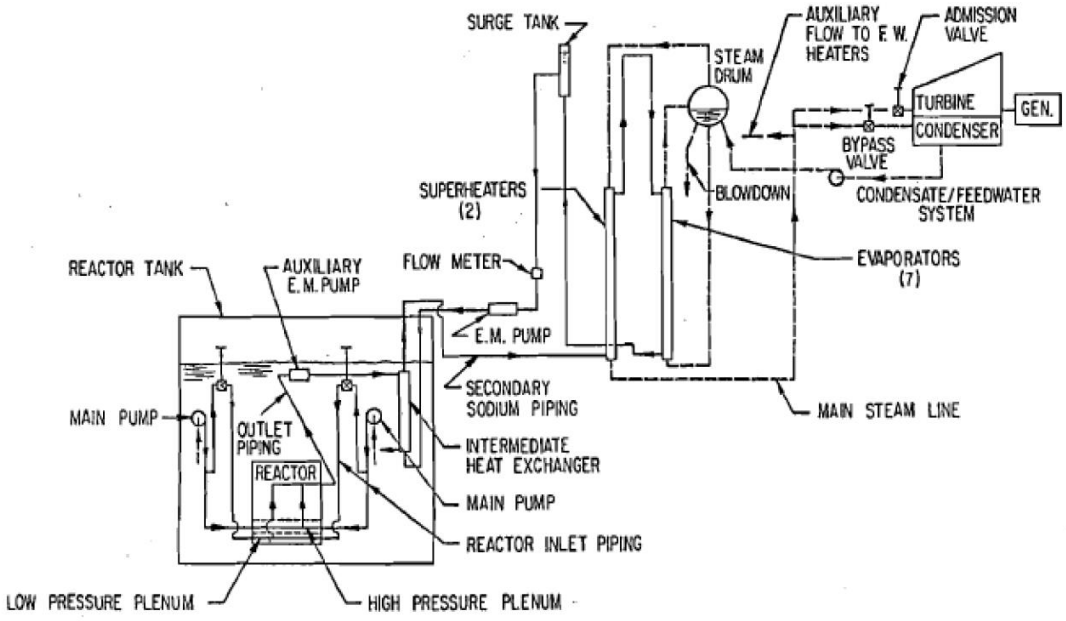

Fig. 2 – EBR-II Plant Schematic.

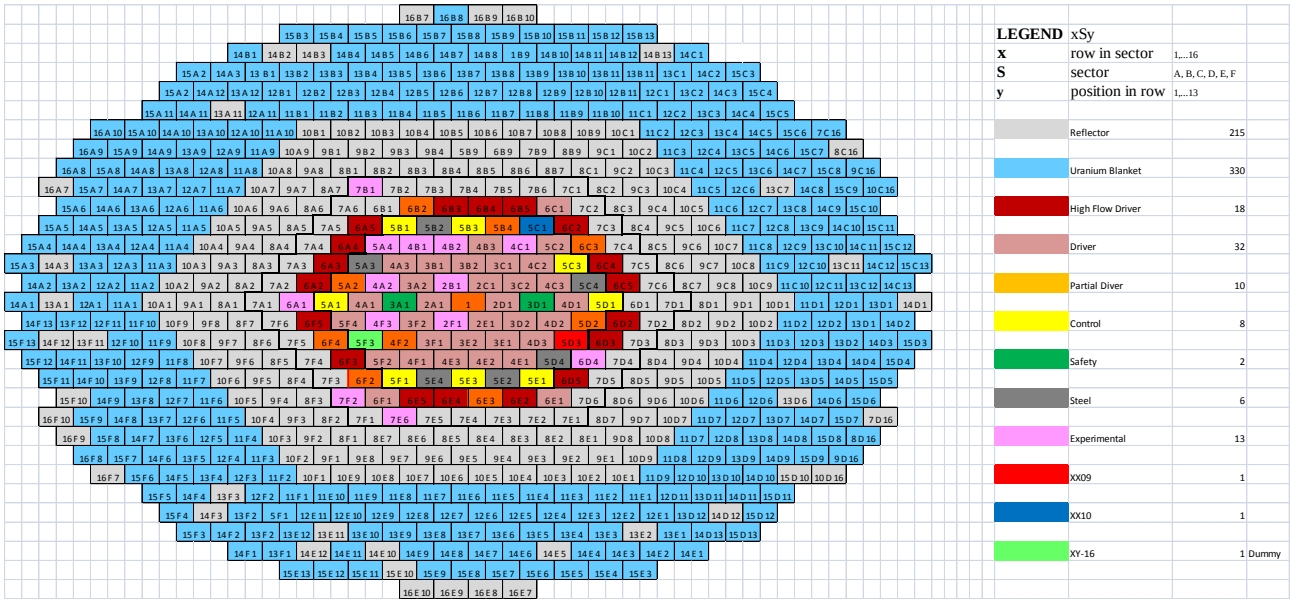

Fig. 3 – EBR-II Core Layout.

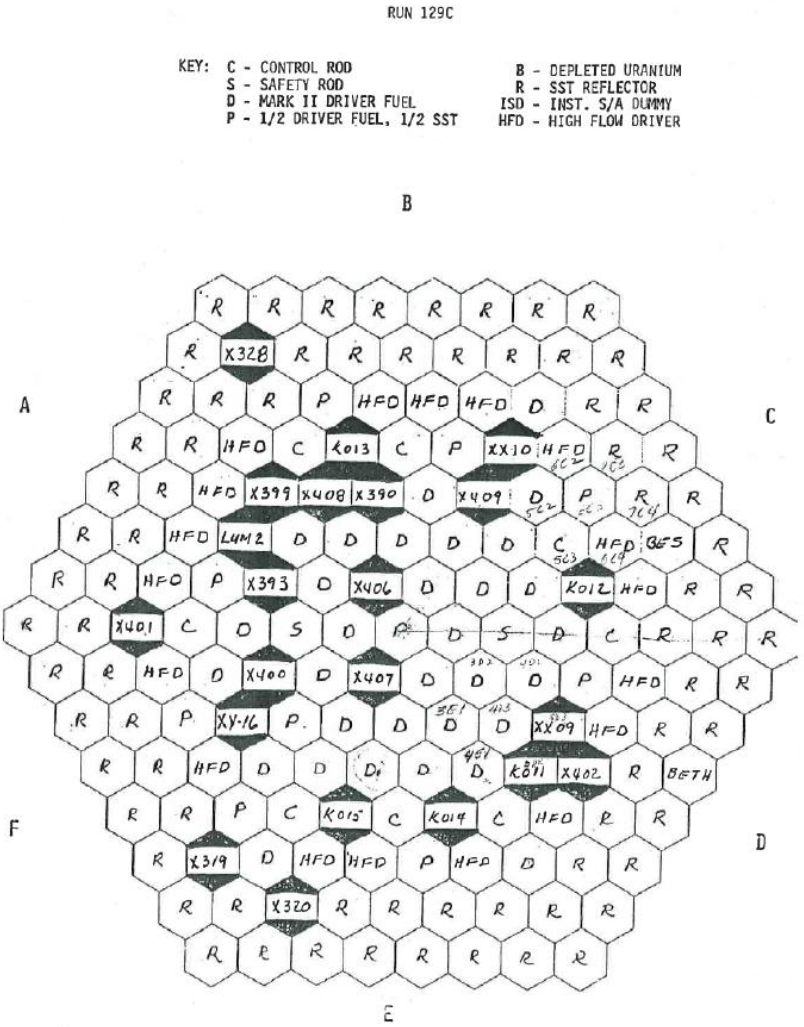

Fig. 4 – EBR-II, SHRT-17 Core Loading Pattern (First 8 Rows).

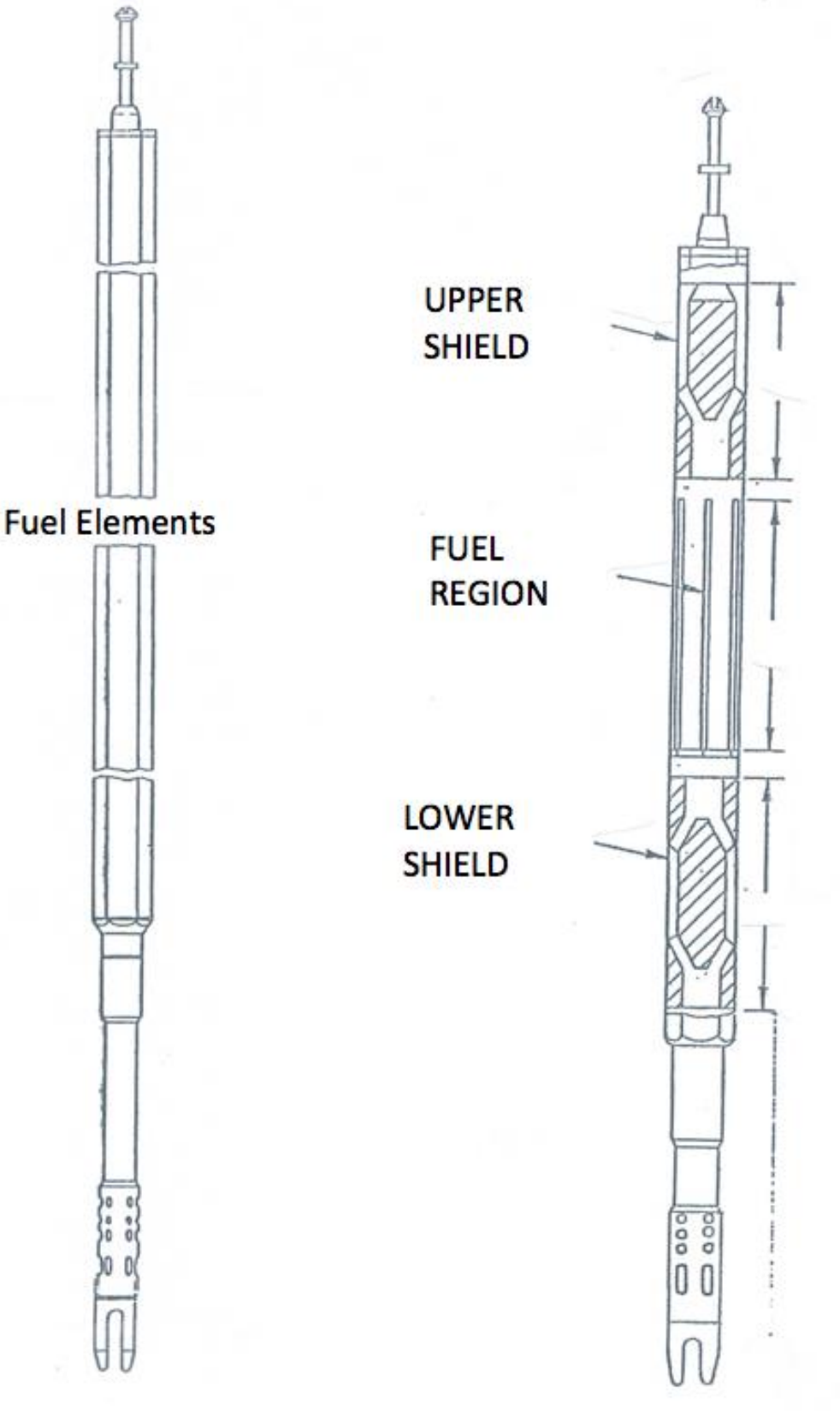

Fig. 5 – EBR-II, MARK-II AI Subassembly Configuration.

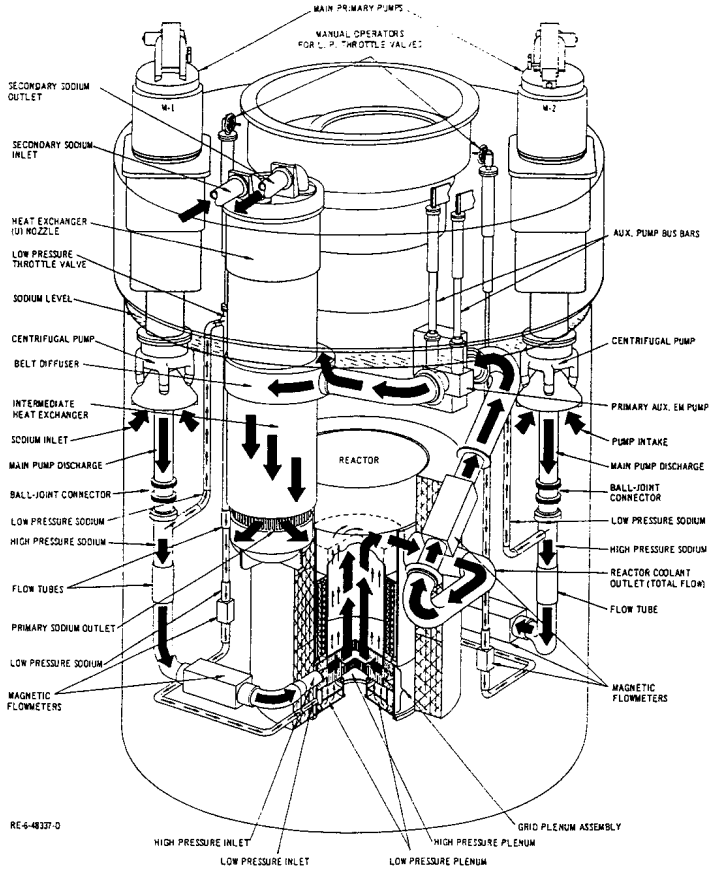

Fig. 6 – EBR-II Primary Tank Layout.

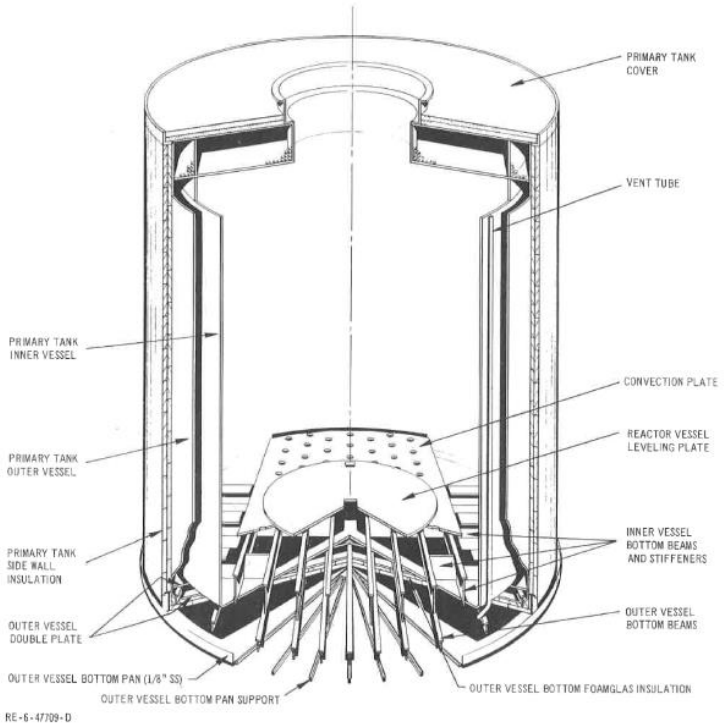

Fig. 7 – EBR-II Primary Tank Vessel.

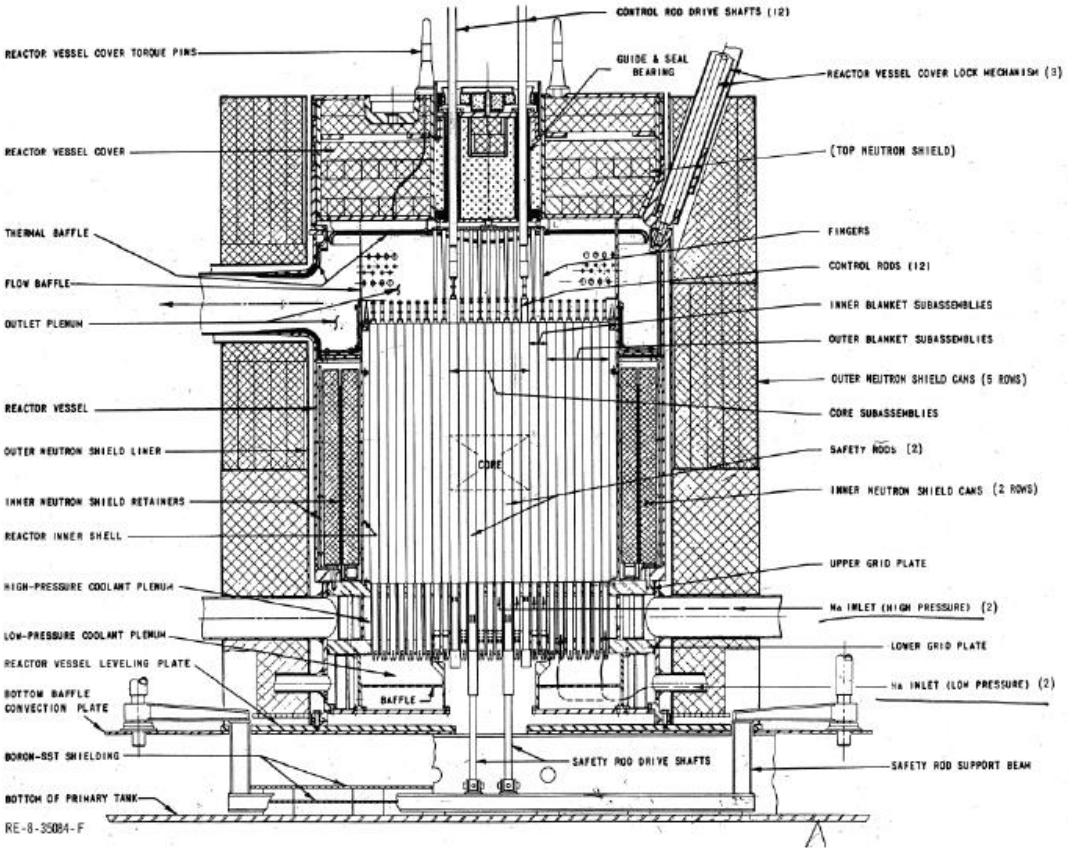

Fig. 8 – EBR-II Reactor Vessel.

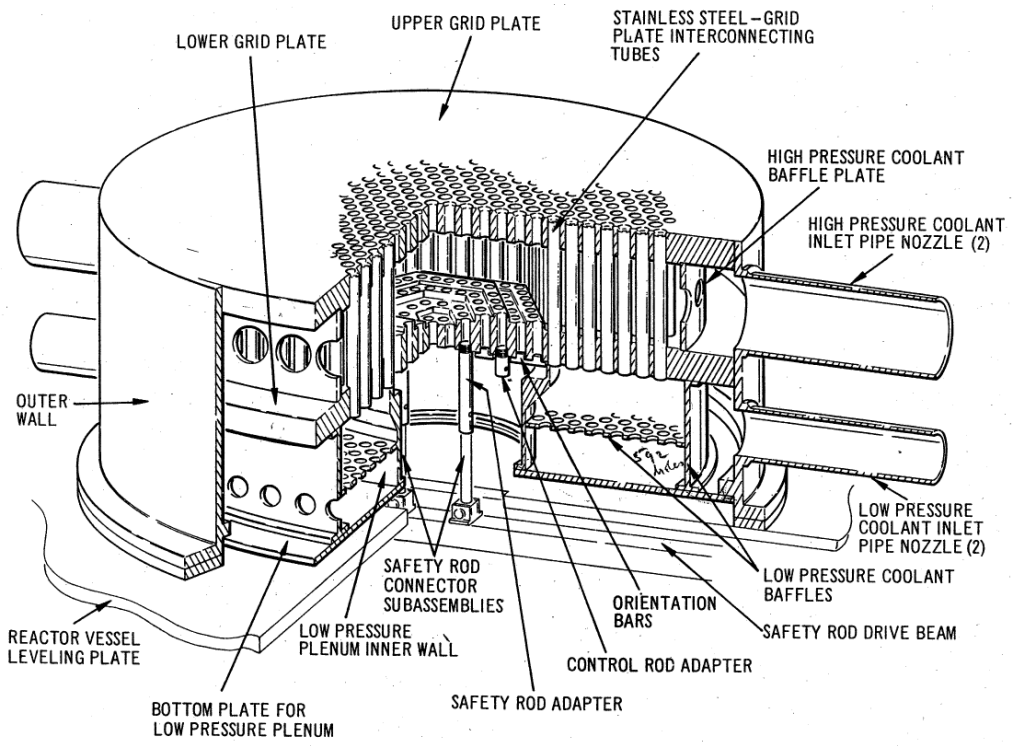

Fig. 9 – EBR-II High - and Low - Pressure Inlet Plena.

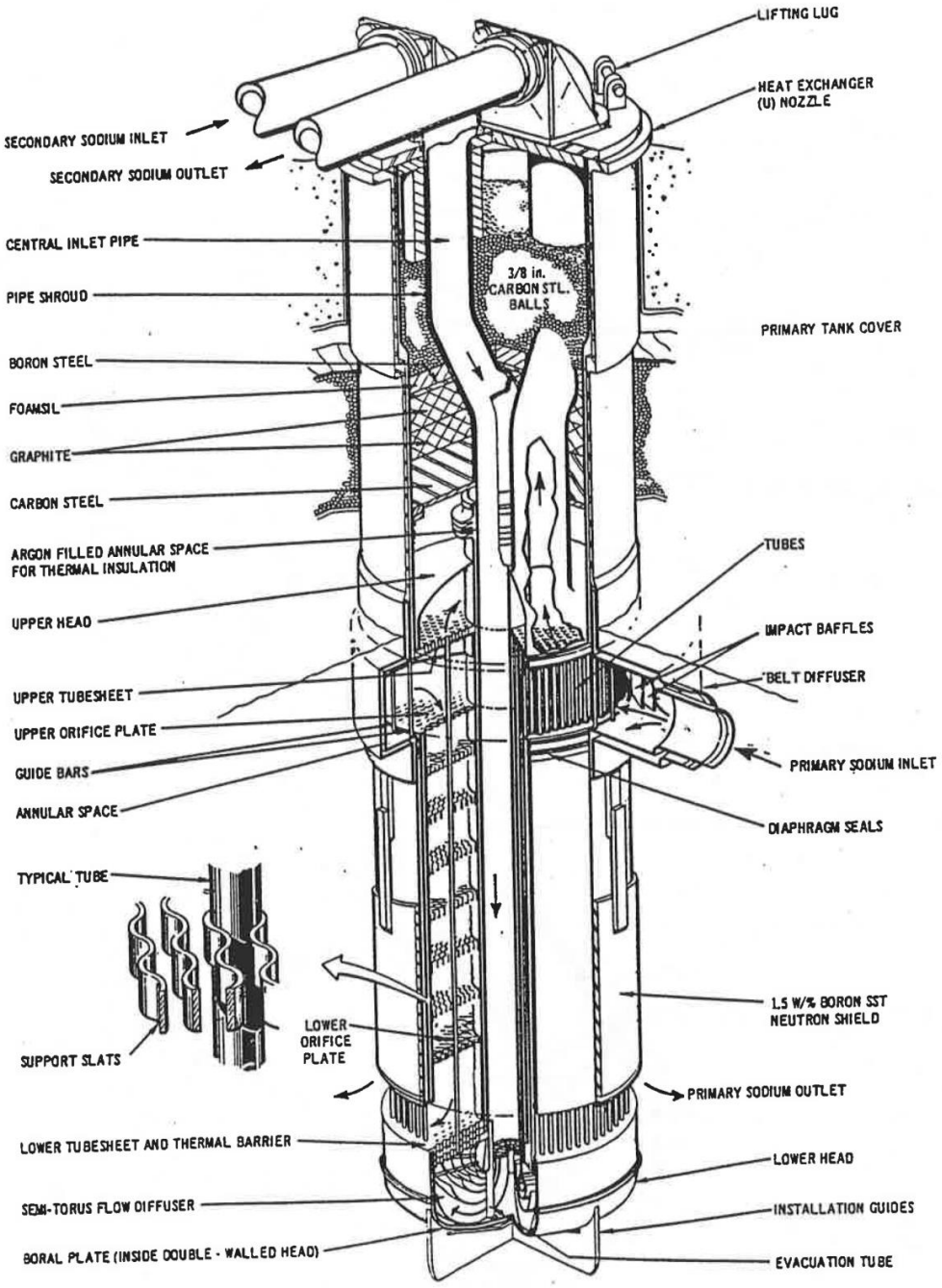

Fig. 10 – EBR-II Intermediate Heat Exchanger.

3 DESCRIPTION OF THE SHRT-17 EXPERIMENT

3.1 Objectives of SHRT-17

The main objectives of SHRT-17 [1][3][4] are:

- To support U.S. LMR plant design and to provide test data for validation of computer codes for design, licensing and operation of LMRs.
- To demonstrate effectiveness of natural circulation and natural phenomena (thermal expansion of the sodium coolant and thermal inertia of the primary pool sodium) in protecting the reactor against potentially adverse consequences from protected loss-of-flow and loss-of-heat-sink accidents.

3.2 Configuration of the facility, boundary and initial conditions of SHRT-17

To initiate the SHRT-17 test, both primary coolant pumps and the intermediate-loop pump were tripped to simulate a protected loss-of-flow accident beginning from full power and flow conditions. In addition, the primary system auxiliary coolant pump that normally had an emergency battery power supply was turned off. The reduction in coolant flow rate caused reactor temperatures to rise temporarily to high, but acceptable levels as the reactor safely cooled itself down at decay heat levels by natural circulation.

Pre-Transient History
Prior to the start of SHRT-17, EBR-II was operated at full power and full flow for long enough that temperatures throughout the system had reached an equilibrium state. The full power operation was less than two hours in order to allow control rod insertion at the start of the transient period.

SHRT-17 occurred during EBR-II Run 129-C. At 12:20 AM, the SHRT-26 test was concluded and the reactor was shutdown. The reactor remained shutdown until 5:45 AM. Between 5:45 and 8:14 AM the reactor was slowly brought back up to power. Between 8:14 and 10:00 AM, EBR-II remains at full power and flow to ensure that temperatures throughout the system had reached equilibrium.

Initial Conditions
Fig. 11 and Fig. 12 show the pre-test calculated powers and flows by core subassembly for the SHRT-17 test. The flow values were obtained as part of the test planning and are the results of calculations from the EBRFLOW code. EBRFLOW was a steady-state thermal-hydraulic design code developed and used by EBR-II project staff to predict flow and outlet mixed mean temperature per subassembly in the reactor. It was based on both EBR-II plant instrument data and data from a separate effects hydraulic rig that was dedicated to obtaining full-scale subassembly pressure drop data for various EBR-II subassembly designs. The ORNL two-dimensional discrete ordinates transport code DOT-III was used to determine individual subassembly power distributions for EBR-II tests. DOT-II calculated both neutron and gamma flux distributions within each subassembly.

Primary sodium heat balance calculations are not available for the SHRT-17 test. According to post run-reports for Run 129-C (ANL-EBR-132), the initial power for the SHRT-17 test was 57.3 MW. Fig. 11 and Fig. 12 are for RUN 129C, not SHRT-17 specifically, and should be renormalized to the appropriate initial power and flow for SHRT-17.

Fig. 12 illustrates the subassembly flow distribution based on the proposed core loading pattern as calculated with EBRFLOW. Four different measurements taken of the inlet plena temperatures show that the average core inlet temperature at the start of the SHRT-17 test was ~624.7 K.

Pressure measurements taken in EBR-II were calibrated to no include gravity head so that during zero flow conditions, they all read zero. The initial pressure at the discharge of primary sodium pump #1 was ~295785 Pa. The initial pressure at the discharge of primary sodium pump #2 was ~288890 Pa. At the outlet of the core, the initial upper plenum pressure was ~43850 Pa.

The intermediate sodium loop had an initial mass flow rate of ~307.5 kg/s. Intermediate sodium flow rates were calibrated at ~578.7 K. The temperature at the inlet to the IHX in the intermediate loop was initially ~574.1 K.

Tab. 3 and Tab. 4 summarize the initial conditions and transient initiators for the SHRT-17 test.

Transient Boundary Conditions

The pump speeds of the two primary sodium pumps are treated as boundary conditions in the primary sodium circuit. In the intermediate sodium loop, the boundary conditions are the flow rate and temperature of the sodium at the inlet of the IHX. Data is provided for each of the boundary conditions for the 15-minute duration of the test.

Primary sodium pump speeds are illustrated in Fig. 13. The EBR-II pump model was developed specifically for EBR-II and was implemented in the NATDEMO system simulation code. The pump characteristics in this model are based upon EBR-II experience and can be used together with the pump speed histories above to provide the pump heads during SHRT-17. The pump model is mainly applicable to the first quadrant (positive flow, positive pump speed) and can be used for negative flow. When the users specifies the pump speed as a function of time, the pump head is calculated from the following set of equations.

$$\overline{H} = b_1\overline{s}^2 + b_2\overline{s}\,\overline{w} + b_3\frac{\overline{w}}{|w|}|\overline{w}|^{b_4}$$

Where

$\overline{H} = {}^{H}/_{H_r}$

$\overline{s} = {}^{s}/_{s_r}$

$\overline{w} = {}^{w}/_{w_r}$

H = pump head

s = pump speed

and

w = coolant flow rate

The r subscript refers to the rated value. The coefficients b_1 and b_2 are constant, b_3 and b_4 depend on the speed, flow rate and several empirical constants defined below:

$$b_3 = \begin{cases} b_{3m} & if\ \overline{s} > \in_m \overline{w} \\ b_{3t} & if\ \overline{s} \leq \in_m \overline{w}\ and\ \overline{w} \geq \overline{w}_t \\ b_{3l} & if\ \overline{s} \leq \in_m \overline{w}\ and\ \overline{w} < \overline{w}_t \end{cases}$$

$$b_4 = b_{4t}\ \ if\ \overline{s} > \in_m \overline{w}\ or\ \overline{w} \geq \overline{w}_t$$

$$b_4 = b_{4l} \;\; if \; \overline{s} \leq \in_m \overline{w} \; or \; \overline{w} < \; \overline{w}_t$$

These equations are based on the idea of using a stopped-rotor pressure drop if $\overline{s} < \in_m \overline{w}$. Furthermore, the stopped-rotor pressure drop is a laminar value if $\overline{w} < \; \overline{w}_t$, or a turbulent value if $\overline{w} \geq \; \overline{w}_t$. The default values for the coefficients are in Ref. [3].

This correlation could produce a discontinuity in pump head at the switch from spinning rotor to stopped rotor. With the default values, the pump head is continuous at the transition from turbulent to laminar flow.
Tab. 5 gives the pump parameters to be used for the EBR_II primary side simulation. While EBR-II has two "identical primary pumps, pump #2 has higher frictional torque losses and stops sooner during the coastdown.

The normalized measured fission power for the first twenty seconds of SHRT-17 is illustrated in Fig. 14. No measurements were taken to effectively collect either the total reactor power or the decay heat power during the transient. To estimate the total reactor power during this test, the decay heat power at the start of SHRT-17 was calculated based on the ANS decay standard. The light water reactor decay heat standard was used as there is not yet a fast reactor decay heat standard and also because it is not expected to make a significant difference. For this calculation, the pre-transient power history was assumed leading to a calculated initial decay heat power of 3.36 MW and scale fission power of 53.93 MW at the start of SHRT-17. It should be noted that the decay heat parameters for Run 129C are not available, therefore, kwon decay heat parameters from a later run with very similar core composition, assembly loading pattern and flux shape were used to calculate the initial SHRT-17 decay heat power.
The ANS decay heat standard was used once again to calculate the decay heat power during the transient as a function of the normalized measured fission power given in Fig. 14. The resulting decay heat power is plotted with the scaled fission power in Fig. 15 along with the sum of the two for the total reactor transient power.

The boundary conditions for the intermediate sodium loop for the SHRT-17 benchmark are the sodium flow rate and temperature at the inlet to the IHX. The IHX inlet sodium flow rate on the intermediate side during SHRT-17 is depicted in Fig. 17. This flow was driven by the coastdown of the intermediate side EM pump upon trip of the 2400-V breaker to the M-G set. The corresponding IHX inlet sodium temperature is shown in Fig. 17.

EBR-II had two types of control rod designs. The original design, which is designated in this report as the regular worth control rod design, did not include boron carbide poison but essentially consisted of a fuel element pin bundle for the reactivity control. In the High Worth Control Rod (HWCR) design version, the fuel element pin bundle was located below a boron carbide poison pin bundle section.
The poison section in the HWCR entered the core region when the fuel element pin bundle section was lowered out of the core. Conversely, when the fuel pin bundle section was raised, back into the core, this boron pin poison section was raised out of the core, this caused maximize maximization of the reactivity swing. For the SHRT-17 the control rods were fully inserted at the beginning of the test such that the bottom of the control rod fuel bundle was 14 inches below the bottom of the fuel bundle of the core driver subassemblies.
The safety rod subassemblies contained 61 fuel elements located in the approximate center of the rod subassembly. The safety rod was normally positioned in the reactor with the fuel elements either at the same elevation as the core region or 14 inches lower than the core region to position the

fuel element outside the core region. For SHRT-17 the safety rods were fully inserted at the beginning of the test such that the bottom of the safety rod fuel bundle was 14 inches below the bottom of the fuel bundle of the core driver subassemblies.

3.3 Description of SHRT-17

The SHRT-17 transient was initiated by a trip of the primary and intermediate pumps. The reactor was also instantaneously scrammed. The primary pump trip mode was a breaker trip in which the power to the motor-generator sets and the clutches was simultaneously lost. Each primary pump had its own controller and motor-generator (M-G set). The flow coastdown was governed by the kinetic energy stored in the inertia of M-G set. While the coastdown shapes for the SHRT-17 were designed to be identical for the two primary pumps, intrinsic differences between the two pump drive units caused a difference in stop times. The auxiliary electromagnetic pump in the primary loop was turned off and did not receive power from battery backups as would occur during a total station blackout. As the SHRT-17 test continued, the reactor decay power decreased due to fission product decay. After the start of the test, no automatic or operation action took place until the test had concluded.

Tab. 10, Tab. 11, Tab. 12 reports the facility configuration, the imposed sequence of main events and the resulting sequence of main events. The following relevant phases can be distinguished:

1. *Phase I – primary pump trip and SCRAM (0 – 50s).*
2. *Phase II – primary system energy increase and core temperatures rise (50 – 250s)*
3. *Phase III – buoyancy forces effective in removing energy from the core (250 – 500s).*
4. *Phase IV –long term cooling in natural circulation (500 – 900s)*

The test starts **(Phase I)** with the primary and intermediate pumps trip. From this time on, the loss of flow and loss of heat sink causes the unbalance of energy and the SCRAM signal (5s). The SCRAM causes the rapid decrease of temperature, mainly in the core and in the upper plenum. At 25s primary pump#2 change his trend (Fig. 18): for few seconds mass flow rate rises and then decreases. This is due to the intrinsic difference between the primary pumps: pump#1 is at rest before pump#2.

Phase II starts at about 50s, when primary pump #2 is at rest. In this phase forced flow decreases, the decay power heats channel sodium and causes the increase of temperature in the core: buoyancy forces begin to improve. The most important parameters that determine the peak fuel temperatures during a transition to natural circulation are: the heat generation rate (decay power), the abruptness with which the heat-removal rate changes (flow coastdown rate), heat transfer and flow redistributions within the reactor, and the natural heads and pressure drops at low-flow conditions. As the buoyancy forces improve, flow through subassemblies increases, and temperatures reaches the peak value.

Phase III: temperatures decrease because the buoyancy forces are effective in removing heat. After the temperature peak, a quasi-equilibrium is approached in which the gradually decreasing rate of heat generation in the core is almost matched by a gradually decreasing of heat removal by the coolant.

In the **Phase IV** primary system is in single phase natural circulation. The mass flow is driven from the balance between driving and resistant forces. Driving forces are the result of fluid density differences occurring between ascending (core side, inner zone) and descending sides (IHX side,

pool) of the main vessel. Mass flow rate and temperature are stable in the all system and in the subassemblies too.

The trends of the main parameters (sodium mass flow rate, coolant temperature and cladding temperature) are represented from Fig. 18 to Fig. 73.

Mass flow rate

Mass flow rate experimental data are available only for pump#2 and high and low-pressure coolant system #2 (see Fig. 18 and Fig. 19) and for instrumented assemblies, XX09 and XX10, (see Fig. 26 and Fig. 27).

In the first phase, sodium mass flow rate follows the pump coastdown, at 25s a mass flow rate inversion occurred. From 50s, when primary pump #2 is at rest, the buoyancy forces begin to prevails until natural circulation stabilizes and primary pump #2 mass flow rate stabilizes at 6 kg/s. The mass flow rate inversion is more evident in the high-pressure circuit with respect to low-pressure system, as shown in detail in Fig. 18, due to the velocity of coolant.

In the XX09 and XX10 mass flow rate decreases and reaches the minimum value after 50s, when pump#2 is at rest. When natural circulation prevails mass flow rate stabilizes in the XX09 subassembly at 0.05 kg/s (Fig. 26), while in the XX10 subassembly is 0.012 kg/s (Fig. 27).

Coolant Temperature

The inlet core sodium temperature, measured by thermocouples located in the high and low-pressure lower plenum, remains almost constant during the all transient, even if, from Phase III, low pressure inlet plenum temperature decrease of few degrees, this phenomena is due to the heat exchange with the pool (see Fig. 20 and Fig. 21).

In the upper plenum temperature decreases and the stratification phenomena occurred (see Fig. 22). In the top part of the upper plenum temperature decreases rapidly then in lower part: after the SCRAM, as the inertia forces prevail (pump#2 coastdown is not completed as show in Fig. 18 and Fig. 19), cold sodium from central subassemblies, where mass flow rate is greater, tends to go upward. Sodium from reflector and blanket subassemblies, that is hotter due to the decay heat of the stainless steel and blanket, remains in the lower part of the upper plenum. During Phase II temperature rise: in the top part of the upper plenum temperature is greater than in the lower part, as the buoyancy forces prevails and hot sodium tends to go upward in the stagnant zone. From 250s on temperature decreases and stratification phenomena characterized the last two Phase, espcecially in the top part of the upper plenum.

During the Phase I, IHX primary inlet temperature decreases while the IHX intermediate outlet temperature rises (Fig. 24): secondary flow coasts down faster than the primary flow so that the primary sodium in the IHX is temporarily undercooled. The IHX primary inlet temperature rises until 90 s then starts to decrease, the IHX intermediate outlet temperature decreases: natural head in the IHX starts to increase.

The IHX primary inlet and intermediate outlet temperature decrease parallel until 400 s then the IHX primary inlet temperature decreases more rapidly due to efficiency of buoyancy forces in heat removal.

The IHX primary inlet temperature stabilizes at 595 K: between primary side sodium inlet and sodium outlet ΔT is 112K. IHX coolant temperature drops below the pool temperature (625 K), that presents an unpredictable effect due to the top IHX structures. The IHX intermediate outlet temperature stabilizes at 645 K, the IHX primary side outlet temperature stabilizes at 630 K.

The steady increase of IHX head is caused by primary sodium stored in the Z-Pipe and the effectiveness of the secondary flow in removing heat in the IHX. The secondary flow is significantly larger than primary flow, and this difference tends to move the active heat-transfer region in the IHX to the upper tubesheet, decrease the average sodium density in the primary side of the IHX, and increase the overall primary-system natural convection driving head.
The IHX primary side outlet temperature (Fig. 25) is not uniform in the first 50s: it is caused by the convection flows in the IHX.

Coolant temperature in the core temperature is measured principally with the two instrumented assemblies: XX09 and XX10, representative respectively of a fuel assembly and a reflector assembly. Temperatures are measured by thermocouples located at different elevations. Measurements of coolant sodium temperature are made: at the assembly inlet and at the outlet of the assembly. At the XX09 inlet assembly coolant temperature change of few degrees: decreases in the first seconds, due to the SCRAM, then increases and reaches the peak (631 K): metallic structure of assembly lower adaptor heat coolant sodium (Fig. 28). From 400s on, temperatures are affected of smalls oscillations around 626 K. In the XX10 assembly, as the coolant sodium velocity is lower than XX09 assembly, the stratification phenomena occurred. At the inlet of the assembly, as shown in Fig. 34, during the all transient, lower flowmeter temperature is minor of upper flowmeter temperature. This phenomena is evidenced at the assembly exit (Fig. 38) and in the thimble annulus (Fig. 40).

Coolant sodium temperature is measured also by thermocouples in the top part of some other assemblies, data available are represented from Fig. 41 to Fig. 46. In Fig. 41 temperature of subassemblies in Row 1 and 2 (partial driver and driver fuel assemblies) are depicted. Temperature of assembly identified as 2E1, which is a driver assembly, differs from the others: during the pump coastdown temperature is lower, when the buoyancy forces begins to prevail temperature is major.
In Fig. 42 temperatures of subassemblies in Row 3 are represented: temperature of 3B1 assembly presents a minor peak of temperature.
The subassemblies of the external rows are affected by the different coastdown of primary pumps: Fig. 43 and Fig. 44 report temperature of subassembly in Row 4 and in Row 5 and 6, respectively, where differences in assembly temperature can be observed.
In Fig. 45 temperature of subassemblies in Row 7 are represented: 7A3 assembly temperature is almost constant, while 7D4 assembly temperature presents a minimum at 45s then increases of few degrees and from 450s on decreases slowly of few degrees.
Fig. 46 show temperature of reflectors and blanket assemblies of the external core region: after SCRAM temperature decrease than remain almost constant at 700 K.

Cladding Temperature
Measurements of cladding temperature are made with thermocouples located in the XX09 and XX10 assemblies at the reactor midplane, in a pattern across the bundle near the top of fueled section and near the exit of the assembly.

In the midplane of the assembly (Fig. 29) temperatures decrease after the SCRAM then rise and reach the peak. Temperature is affected by the proximity of fuel box as thermocouples of assemblies near the fuel box measure a temperature lower than central assemblies. This phenomena is present also in the top fuel (Fig. 30) and at the assembly exit section (Fig. 31). Coolant outlet temperature (Fig. 32) follow the trend of the other thermocouples: decreases of 100 K after the SCRAM then rises. Temperature measured by the thermocouples located in the top part of thimble annulus region, as shown in Fig. 33, present the same temperature as coolant outlet.

In the XX10 assembly midplane (Fig. 35) , in the top of core .(Fig. 36) and above the fuel region (Fig. 37) temperature decrease after SCRAM than rise and decrease again when pump#1 and #2 are at rest.

TEST DESCRIPTION	
Initial Power	57.3 [MW]
Initial Primary Coolant Flow Through Core (at 700 K)	456 [kg/s]
Initial Intermediate Coolant Flow (at 579 K)	311.43 [kg/s]
Initial Core Inlet Temperature	624.7 [K]
Primary and Intermediate Pump Coastdown Conditions	Power to motor-generator sets removed
Control Rods	Full insertion at test initiation
Auxiliary EM Pump Conditions	Power to Auxiliary EM Pump removed

Tab. 3 – EBR-II, SHRT-17 Test Description.

INITIAL CONDITIONS	
Core sodium mass flow rate (at 700 K)	456 [kg/s]
Average core inlet temperature	625 [K]
Pressure at discharge of primary sodium pump #1	295785 [Pa]
Pressure at discharge of primary sodium pump #2	288890 [Pa]
Upper plenum pressure	43850 [Pa]
Intermediate sodium mass flow rate (at 579 K)	311.43[kg/s]
EBR-II operated at full power for less than two hours prior to test Calculated initial decay heat Resulting initial fission power	 3.36 [MW] 53.93 [MW]

Tab. 4 – EBR-II, SHRT-17 Initial Conditions.

PARAMETER	RATED CONDITION
N_R (rated speed)	870 [rpm]
H_R (rated head)	43 [m]
Q_R (rated flow)	0.2946 [m^3/s]
NS (specific speed)	31.01/1602 [SI/gp]
I_P (inertia)	16.0 [kg m^2]
T_R (rated torque)	1300.0 [N m]
$T_{f,R}$ (friction torque)	0.0286 T_R (37.2) [N m]

Tab. 5 – EBR-II primary pump parameters.

TIME [s]	PUMP#1 [rpm]	PUMP#2 [rpm]
0	799.0	764.9
2	727.7	695.4
4	566.7	532.6
6.5	407.5	376.6
9	323.2	301.5
12.5	244.1	230.1
17.5	172.5	167.3
24.5	109.2	113.9
33	56.5	74.62
42	0.69	46.54
51	0.76	2.29
90	0.76	2.44
120	0.61	2.44
180	0.76	2.44
240	0.84	2.59
300	0.61	2.44
360	0.61	2.44
420	0.61	2.44
480	0.61	2.44
540	0.76	2.44
600	0.76	2.75
660	0.69	2.44
720	0.69	2.44
780	0.76	2.59
840	0.76	2.44
900	0.92	2.44

Tab. 6 – EBR-II, SHRT-17: Primary Pump Speeds.

TIME [s]	FISSION [MW]	DECAY HEAT [MW]	TOTAL POWER [MW]
0	53.93	3.36	57.29
1	8.24	3.12	11.36
2	6.86	2.95	9.81
3.5	5.61	2.77	8.38
5	4.76	2.63	7.39
7.5	3.82	2.46	6.29
10	3.23	2.33	5.56
15	2.47	2.15	4.62
22.5	1.85	1.95	3.8
30	1.46	1.82	3.28
40	1.1	1.7	2.79
50	0.84	1.6	2.44
60	0.66	1.52	2.19
90	0.38	1.35	1.73
120	0.25	1.24	1.49
180	0.13	1.09	1.22
240	0.1	1	1.1
300	0.1	0.93	1.02
360	0.08	0.88	0.96
420	0.08	0.83	0.92
480	0.08	0.8	0.88
540	0.08	0.77	0.84
600	0.08	0.74	0.82
660	0.08	0.71	0.79
720	0.07	0.69	0.76
780	0.08	0.67	0.75

Tab. 7 – EBR-II, SHRT-17: Total, Fission and Decay Heat Power.

TIME [s]	IHX MASS FLOW RATE [kg/s]
0	311.7
1	234.1
2.5	157.1
6	88.41
16.5	42.16
30	28.34
60	21.29
120	18.20
180	18.29
240	19.03
300	20.58
360	21.74
420	22.03
480	22.37
540	22.08
600	23.56
660	22.17
720	20.47
780	19.82
840	18.88
900	17.24

Tab. 8 – EBR-II, SHRT-17: Intermediate IHX Inlet Sodium Flow rate.

TIME [s]	IHX INLET TEMPERATURE [K]
0	574.3
60	574.2
120	574.0
180	574.1
240	573.9
300	573.5
360	573.2
420	572.9
480	572.6
540	572.5
600	572.1
660	571.3
720	570.0
780	568.5
840	566.7
900	565.3

Tab. 9 – EBR-II, SHRT-17: Intermediate IHX Inlet Sodium Temperature.

SYSTEMS	CHARACTERISTICS	STATUS
Primary and Intermediate Pump	Loop #1 Loop #2	Power to motor-generator sets removed
Control Rods	8 Rods	Full insertion at test initiation
Safety Rods	2 Rods	Full insertion at test initiation
Throttle Valve	Loop #1 Loop #2	Active
Auxiliary EM Pump Conditions	--	Power to Auxiliary EM Pump removed

Tab. 10 – EBR-II, SHRT-17: Facility configuration.

IMPOSED EVENT DESCRIPTION	SYSTEM	SIGNAL (TIME OR SET POINT)	REMARKS
Trip of the MCP and coastdown	MCP	0 s	Coast-down in Fig. 13
Scram	Control and Safety Rods	0 s	Total power in Fig. 15 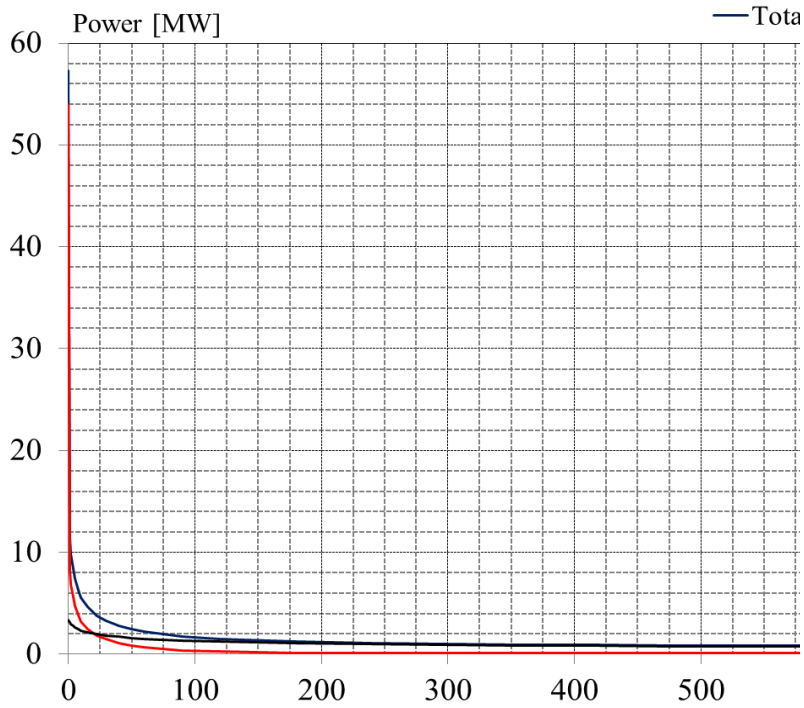
End of transient	--	900 s	--

Tab. 11 – EBR-II, SHRT-17: imposed sequence of main events.

Ph. W.	DESCRIPTION & PHENOMENA/PROCESSES	EVENT	TIME EXP[s]	NOTE
Phase I (0 – 50 s)	*Wall to fluid friction* *Pressure drops at discontinuities* *Heat transfer in covered core* *Heat transfer in IHX* *Heat transfer in passive structures and heat losses* *Global multidimensional coolant temperature and flow distributions* *Mixing and stratification*	Stop MCP	0	Imposed
		Initiating event: loss of IHX flow rate	0	Imposed
		SCRAM	0	Imposed

Phase II (50 – 250s)	*Wall to fluid friction* *Pressure drops at discontinuities* *Heat transfer in covered core* *Heat transfer in IHX* *Heat transfer in passive structures and heat losses* *Global multidimensional coolant temperature and flow distributions* *Mixing and stratification*	In core peak of temperature	100	--
Phase III (250 – 500s)	*1 Φ natural circulation* *Wall to fluid friction* *Pressure drops at discontinuities* *Heat transfer in covered core* *Heat transfer in IHX* *Heat transfer in passive structures and heat losses* *Global multidimensional coolant temperature and flow distributions* *Mixing and stratification*	Z-Pipe peak of temperature	210	--
Phase IV (500 – 900s)	*1 Φ natural circulation* *Wall to fluid friction* *Pressure drops at discontinuities* *Heat transfer in covered core* *Heat transfer in IHX* *Heat transfer in passive structures and heat losses* *Global multidimensional coolant temperature and flow distributions* *Mixing and stratification*	1 Φ natural circulation	--	--
		End of transient	900	Imposed

Tab. 12 – EBR-II, SHRT-17: resulting sequence of main events.

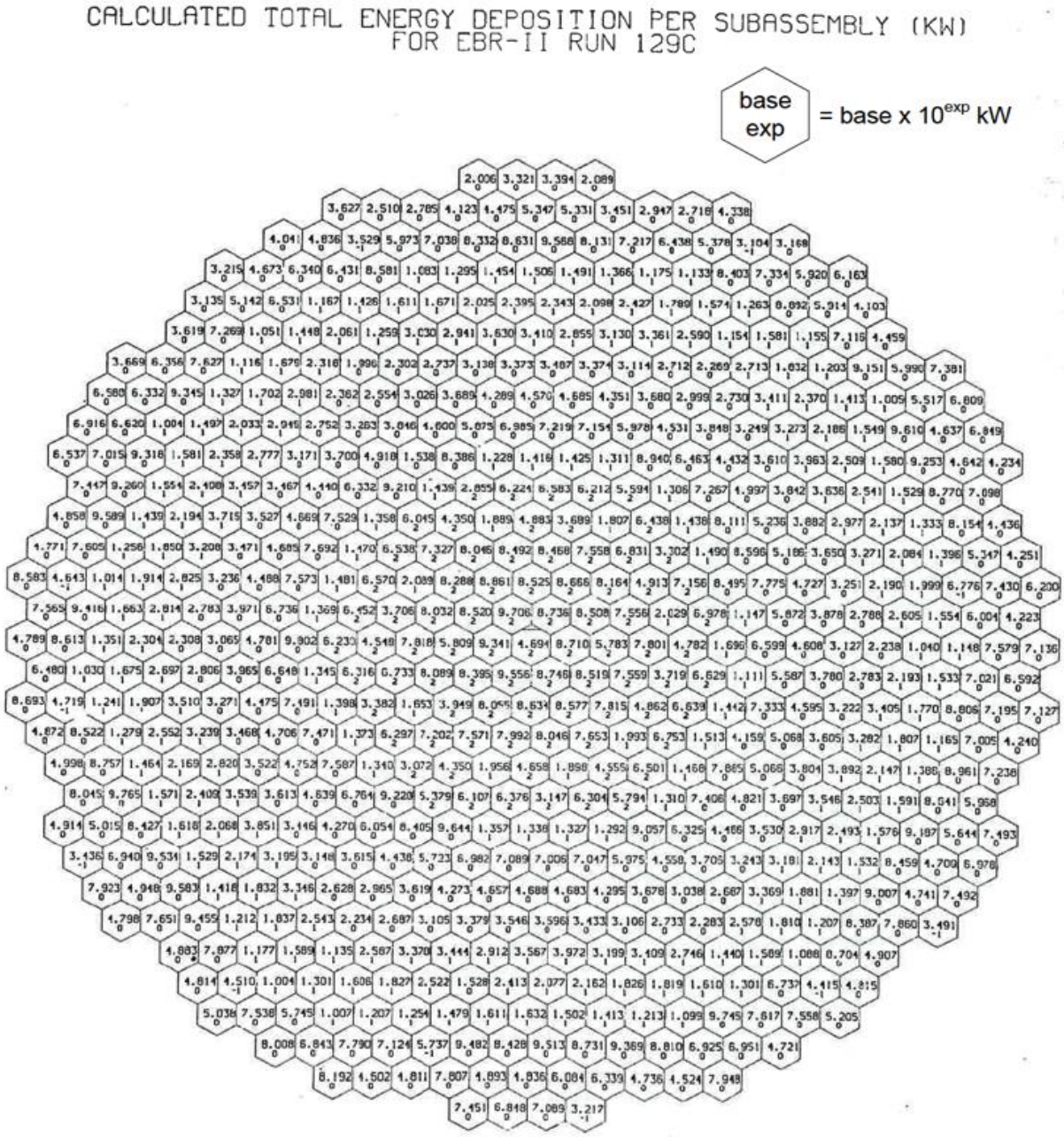

Fig. 11 – EBR-II, SHRT-17: Power per Subassembly.

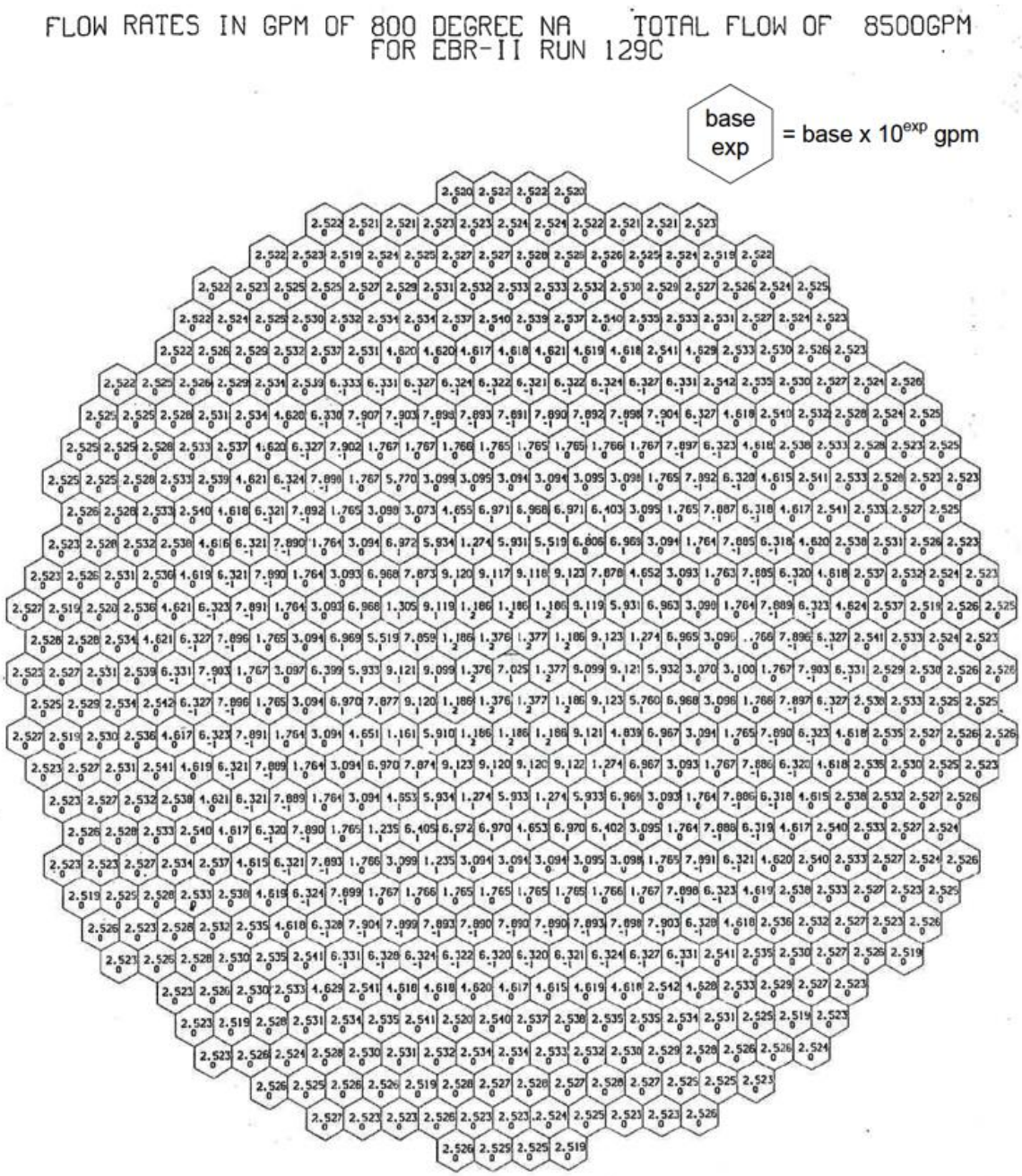

Fig. 12 – EBR-II, SHRT-17: Flow per Subassembly in gallons per minute.

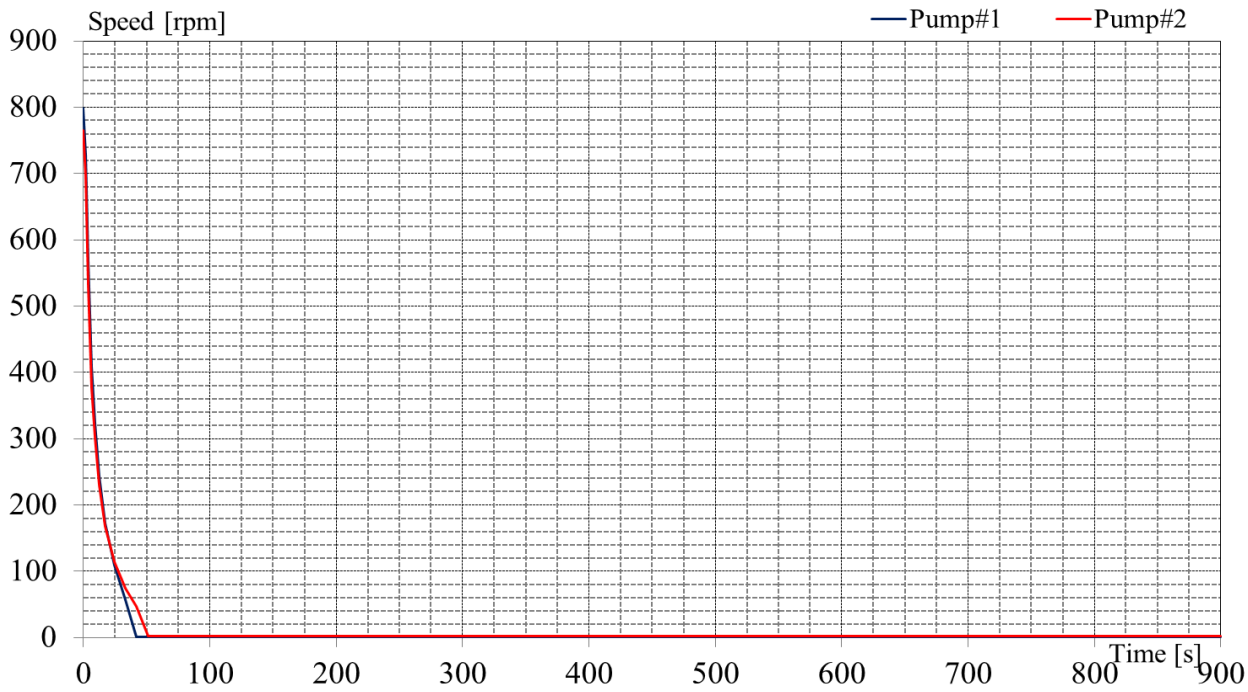

Fig. 13 – EBR-II, SHRT-17: Primary Pump Speeds.

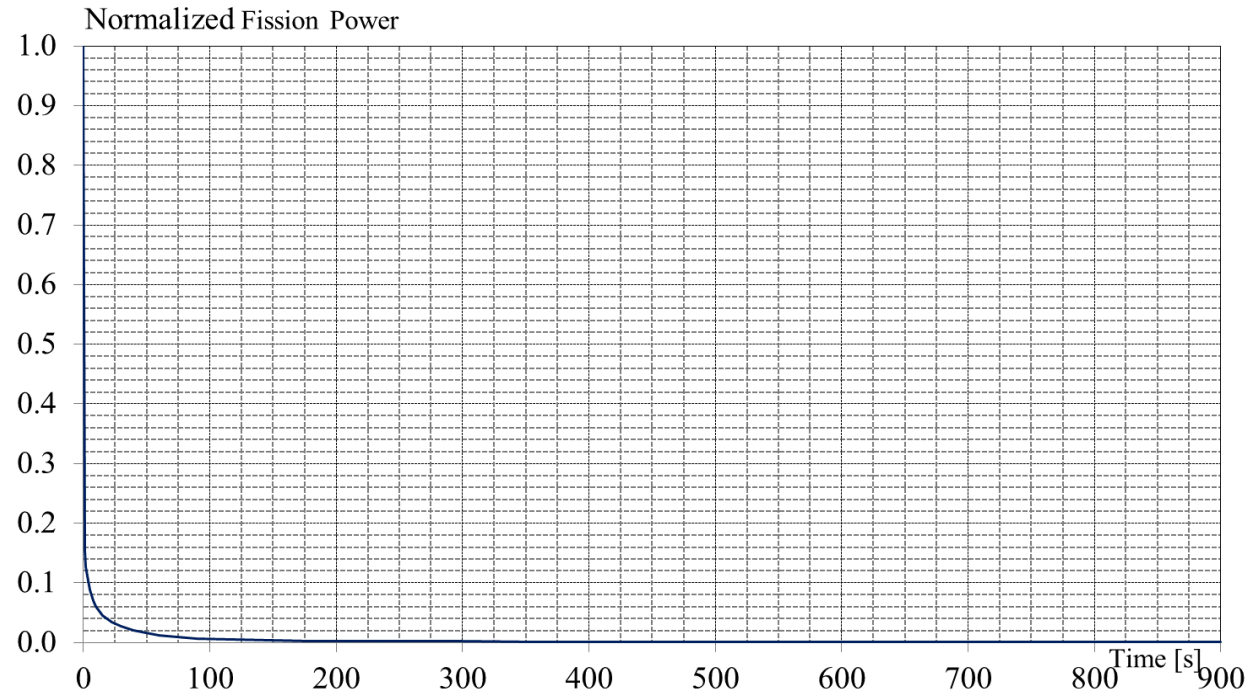

Fig. 14 – EBR-II, SHRT-17: Normalized Fission Power.

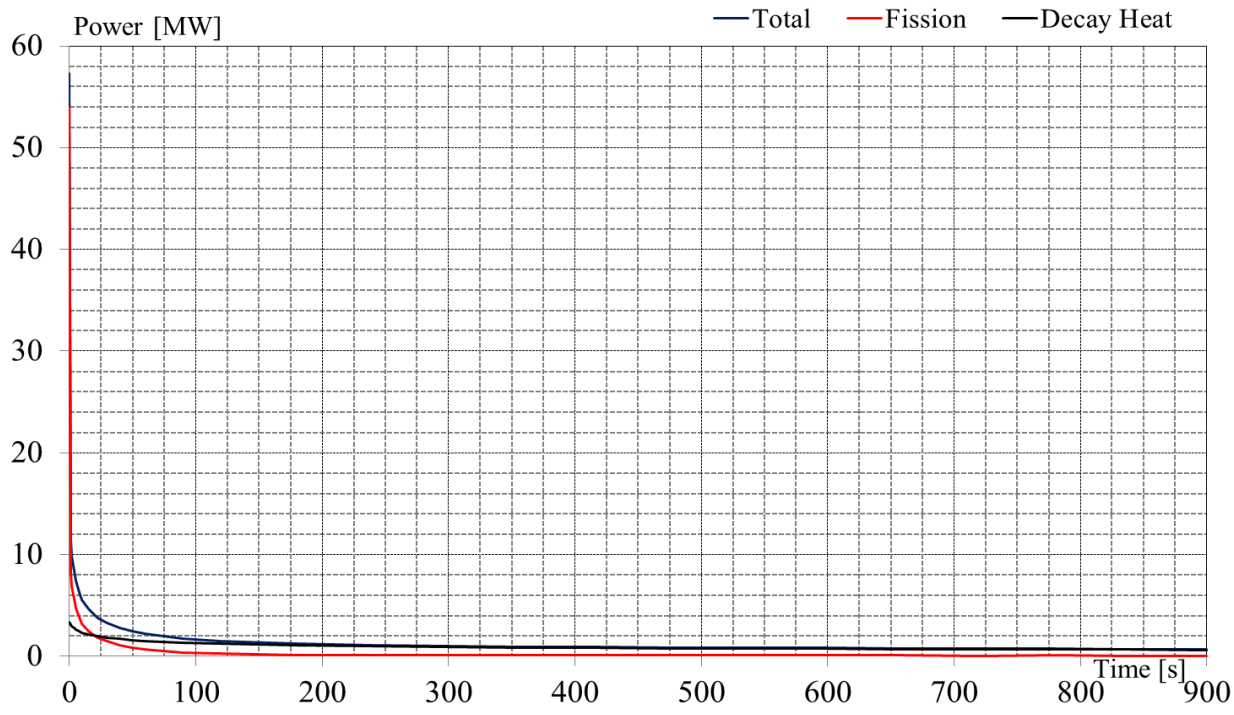

Fig. 15 – EBR-II, SHRT-17: Total, Fission and Decay Heat Power.

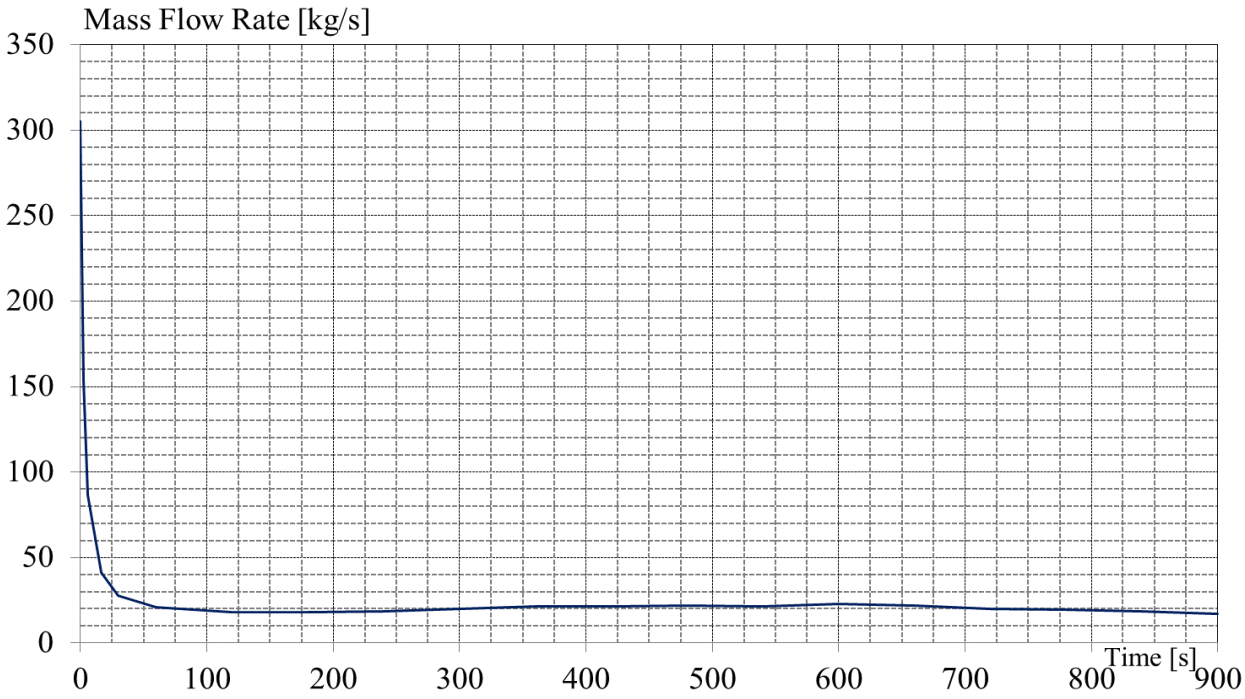

Fig. 16 – EBR-II, SHRT-17: IHX Intermediate Side Inlet Sodium Mass Flow Rate.

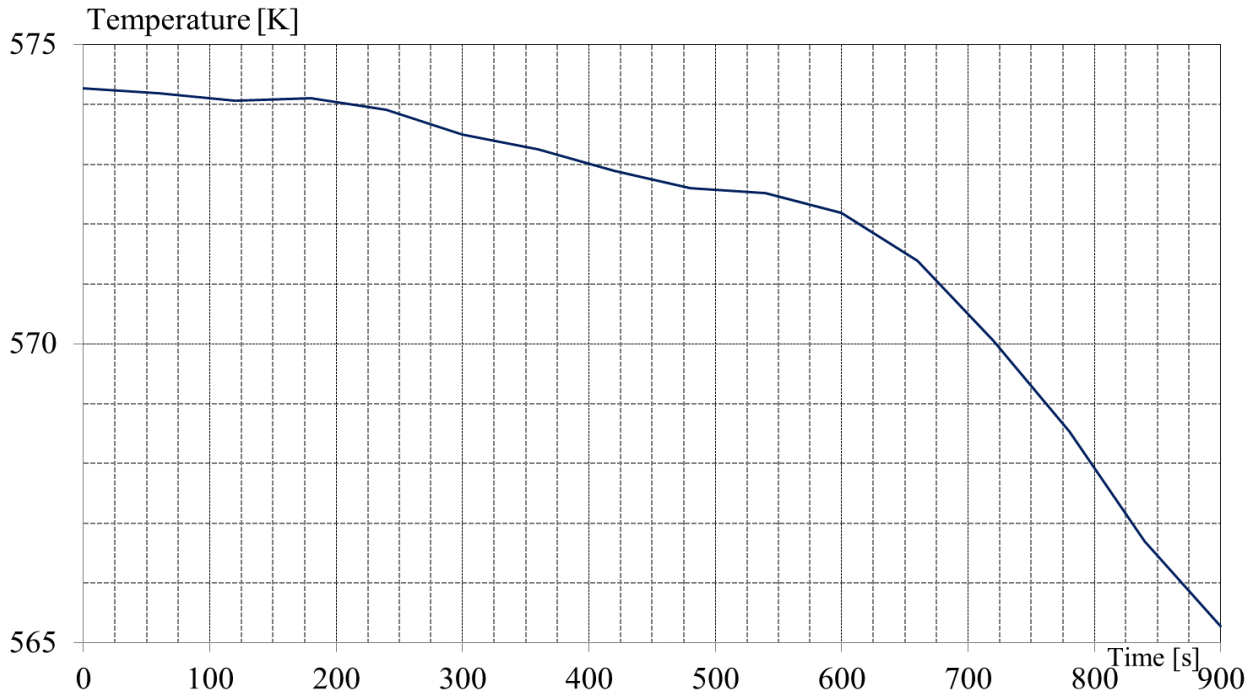

Fig. 17 – EBR-II, SHRT-17: IHX Intermediate Inlet Sodium Temperature.

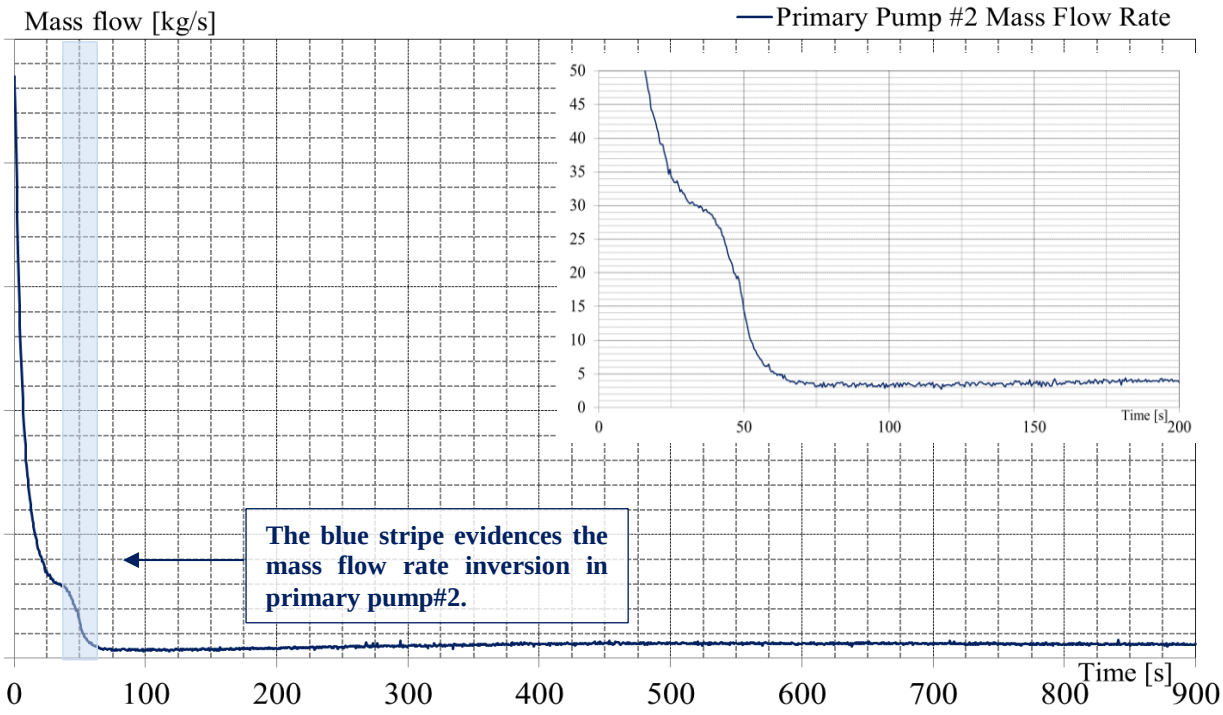

Fig. 18 – EBR-II, SHRT-17: Pump#2 Mass Flow Rate.

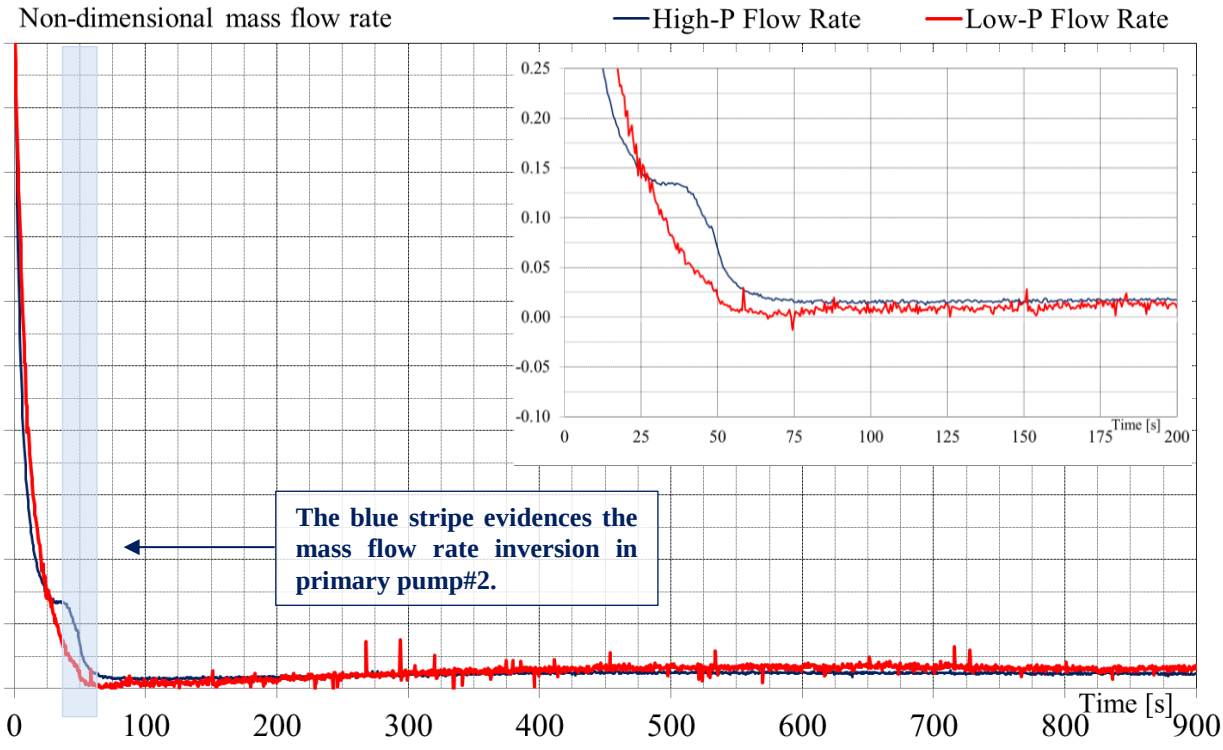

Fig. 19 – EBR-II, SHRT-17: High-and Low-Pressure Mass Flow Rate.

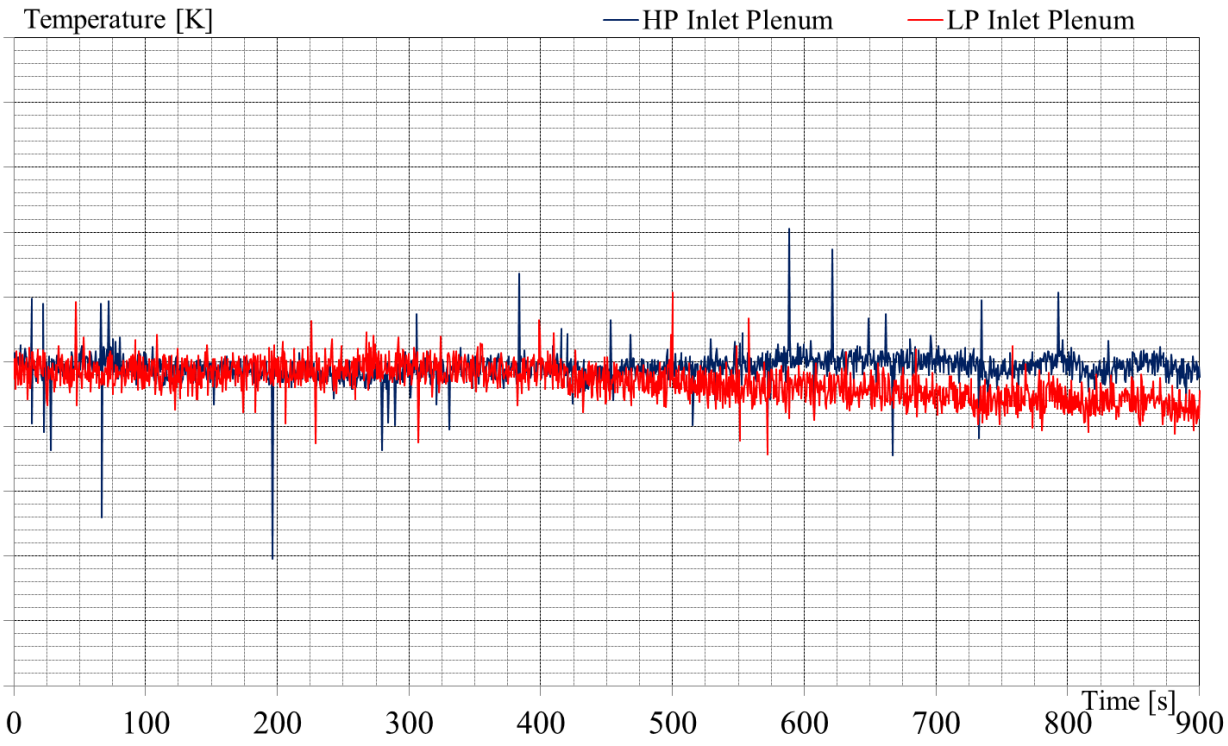

Fig. 20 – EBR-II, SHRT-17: Core Inlet Temperature.

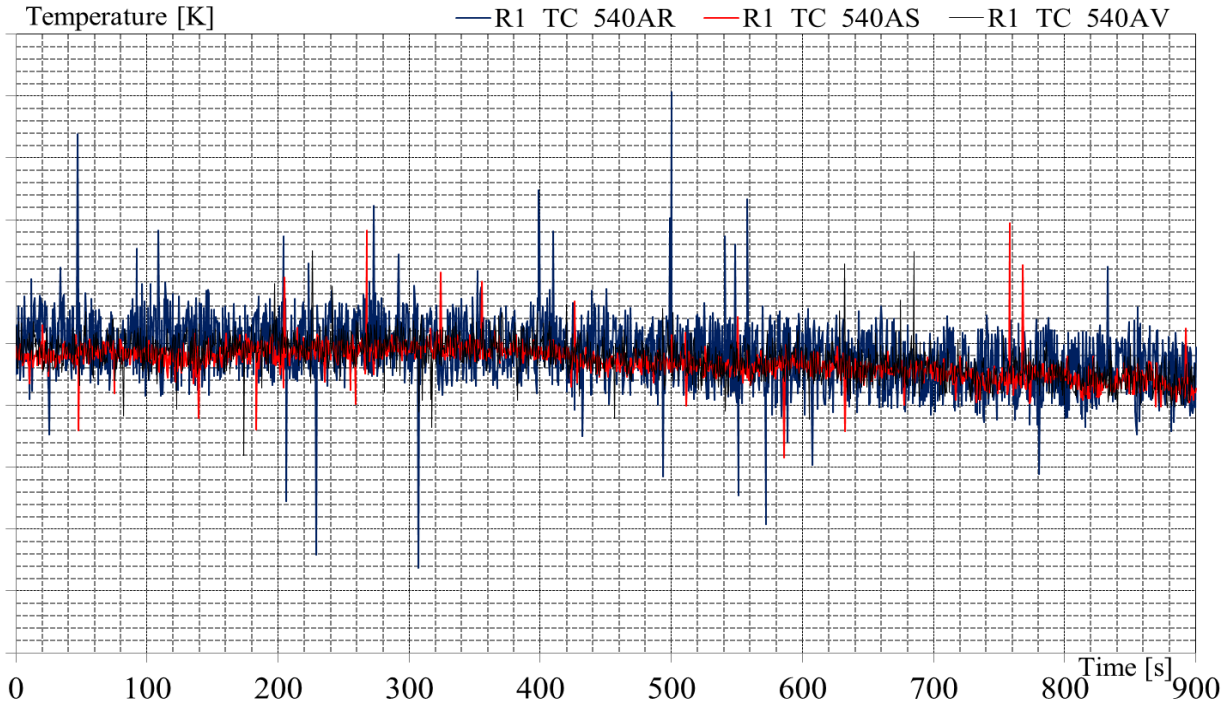

Fig. 21 – EBR-II, SHRT-17: Lower Plenum Temperature.

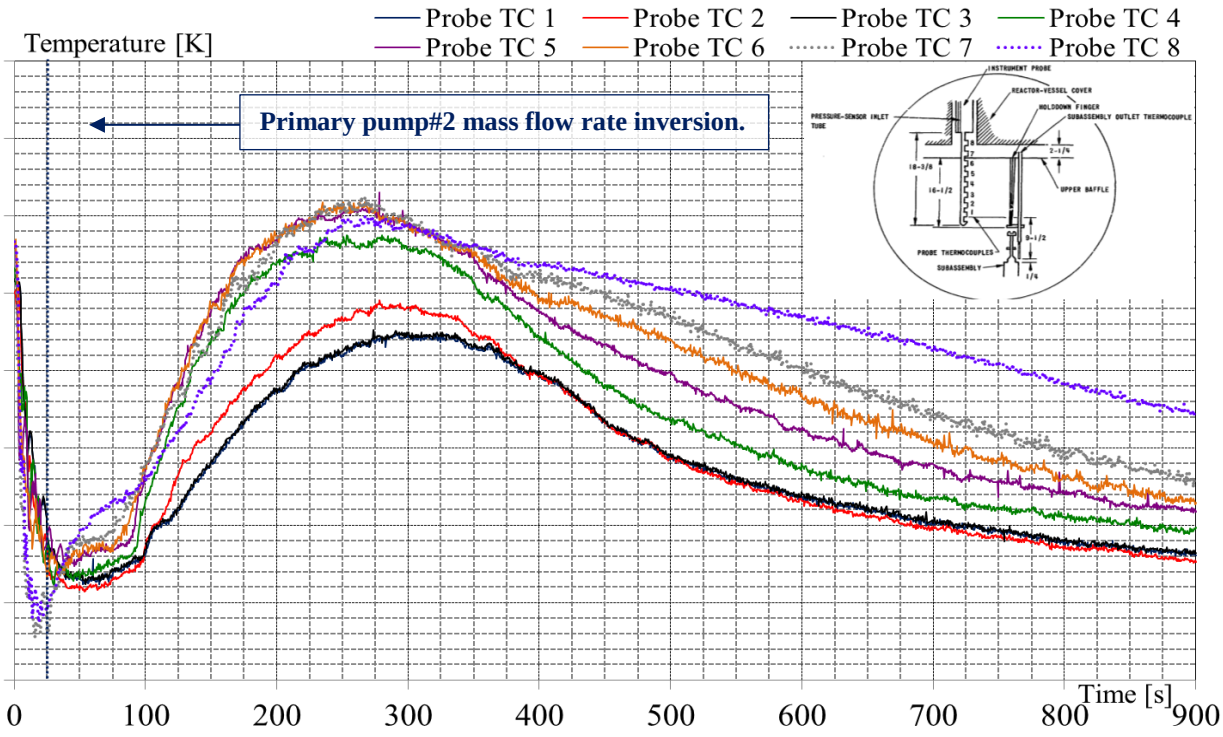

Fig. 22 – EBR-II, SHRT-17: Upper Plenum Temperature.

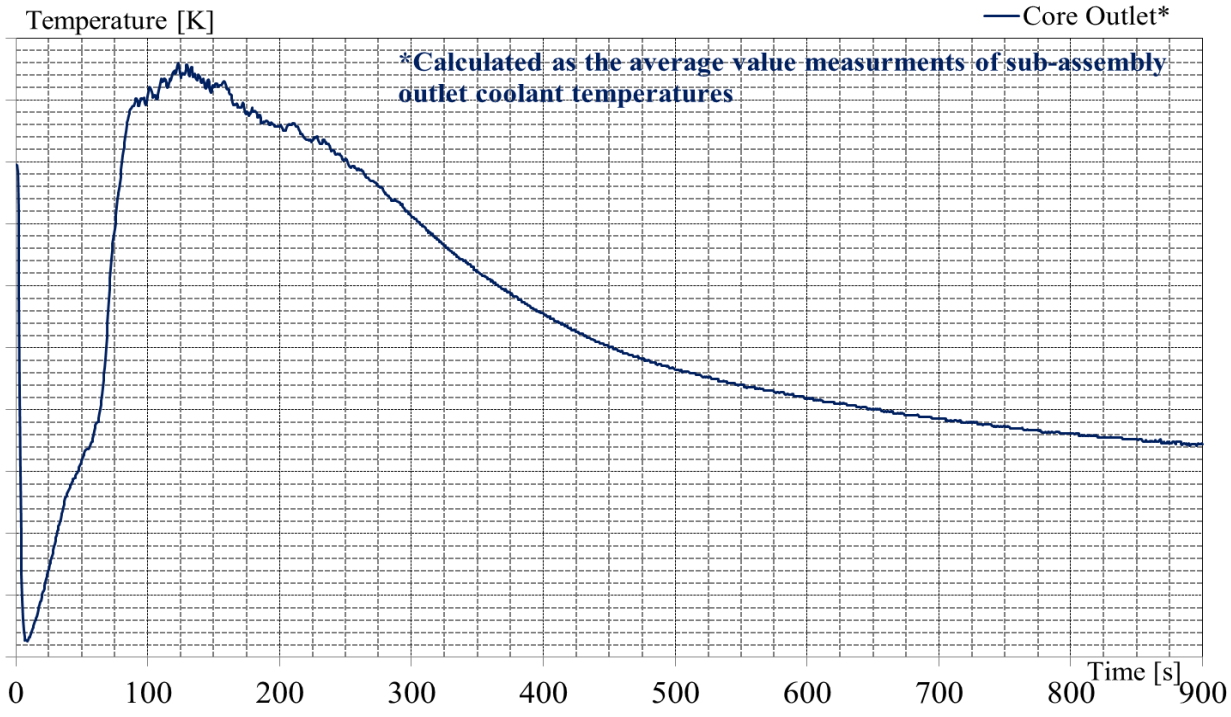

Fig. 23 – EBR-II, SHRT-17: Average Subassembly Outlet Temperatures.

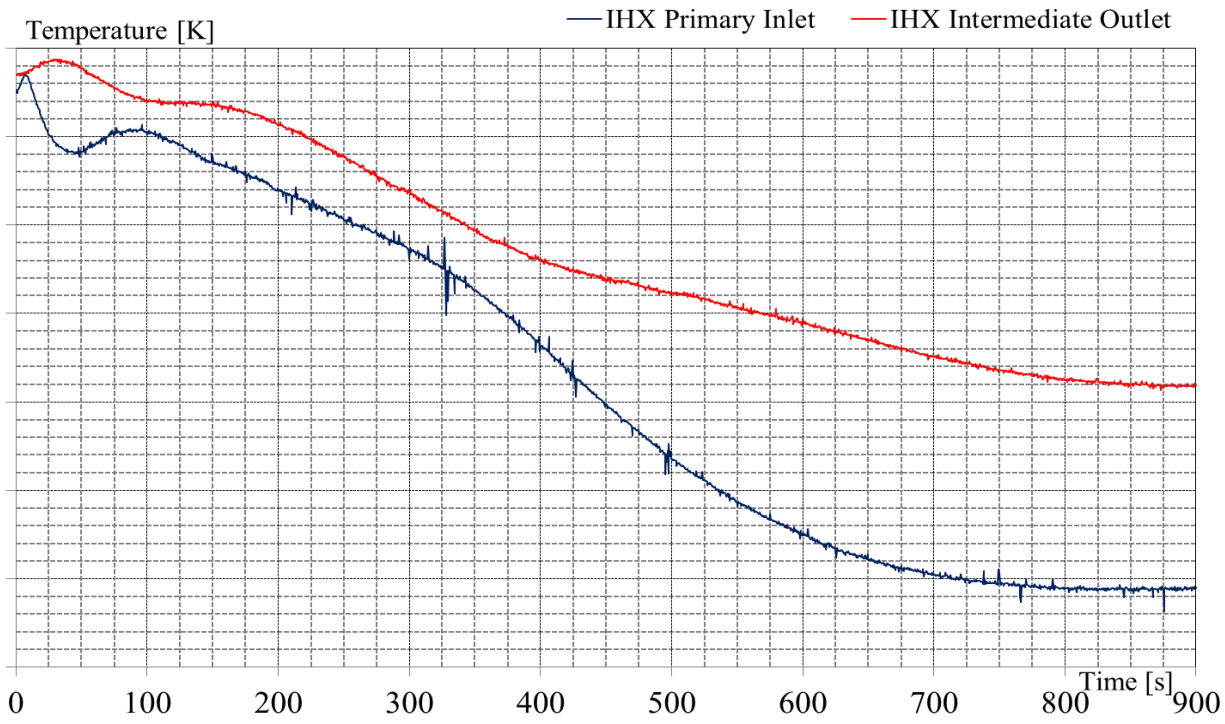

Fig. 24 – EBR-II, SHRT-17: IHX Primary Inlet and Intermediate Outlet Temperature.

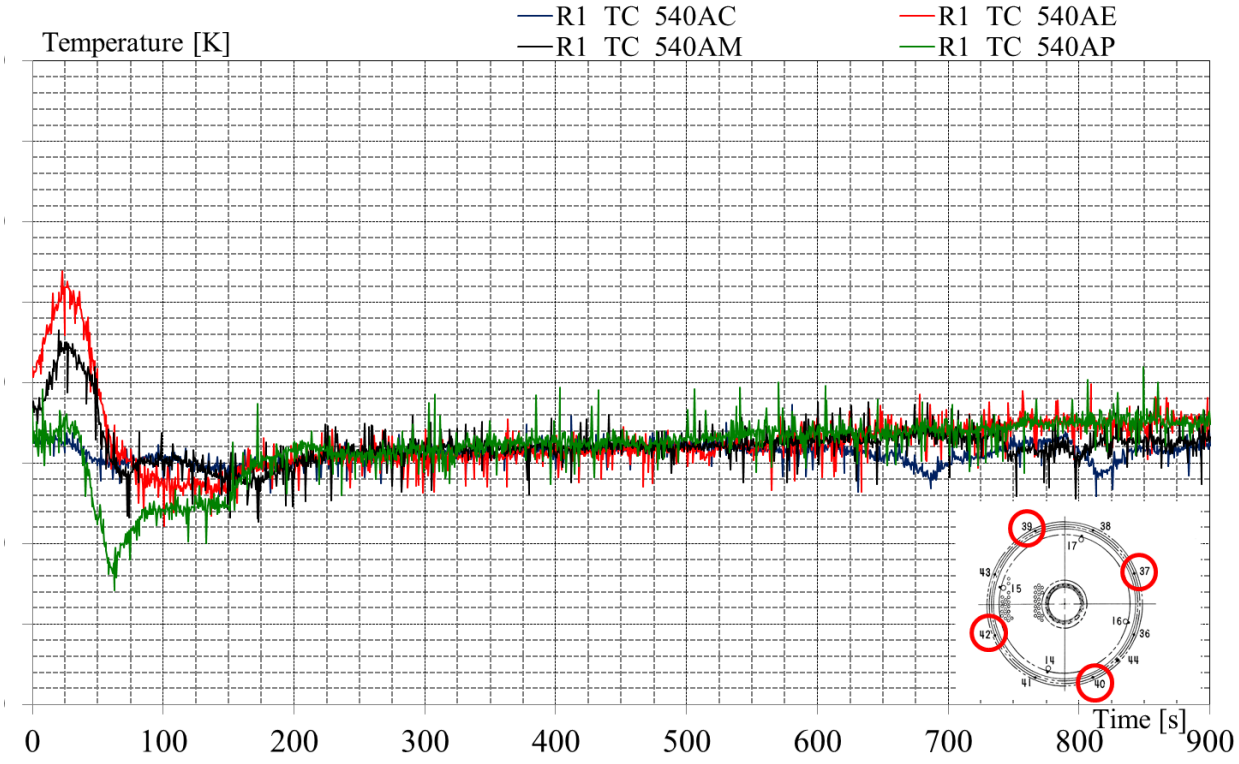

Fig. 25 – EBR-II, SHRT-17: IHX Primary Side Temperture.

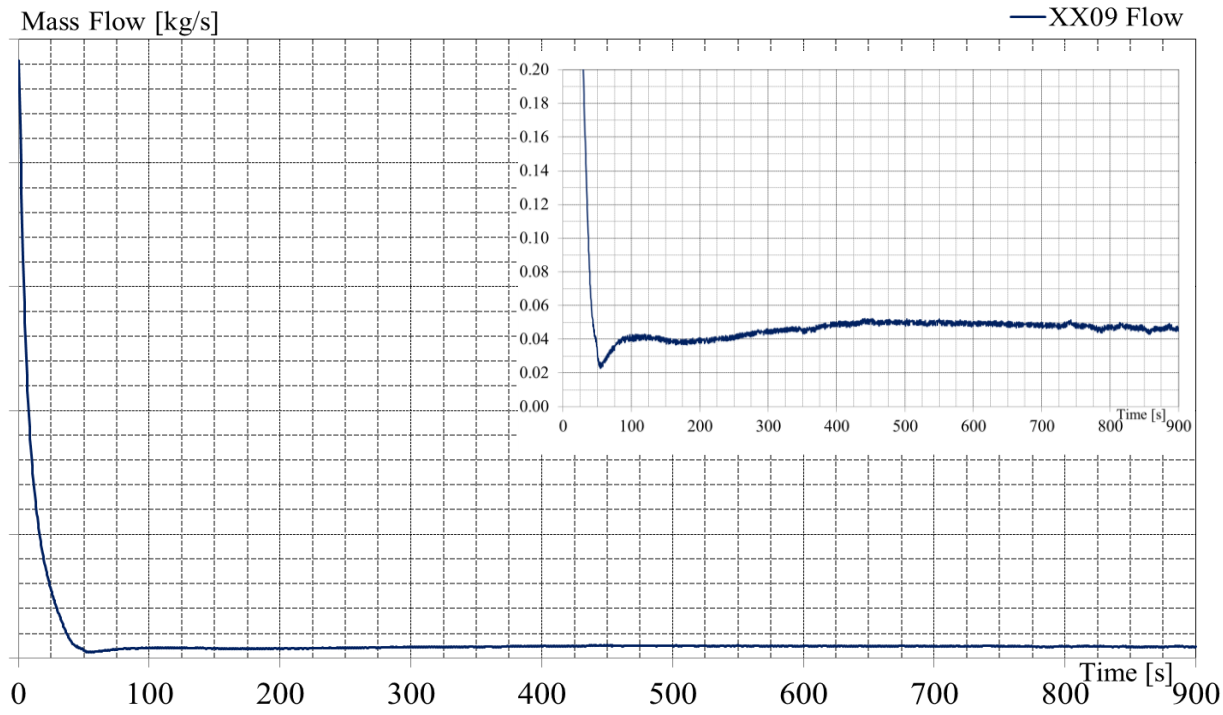

Fig. 26 – EBR-II, SHRT-17: XX09 Mass Flow Rate.

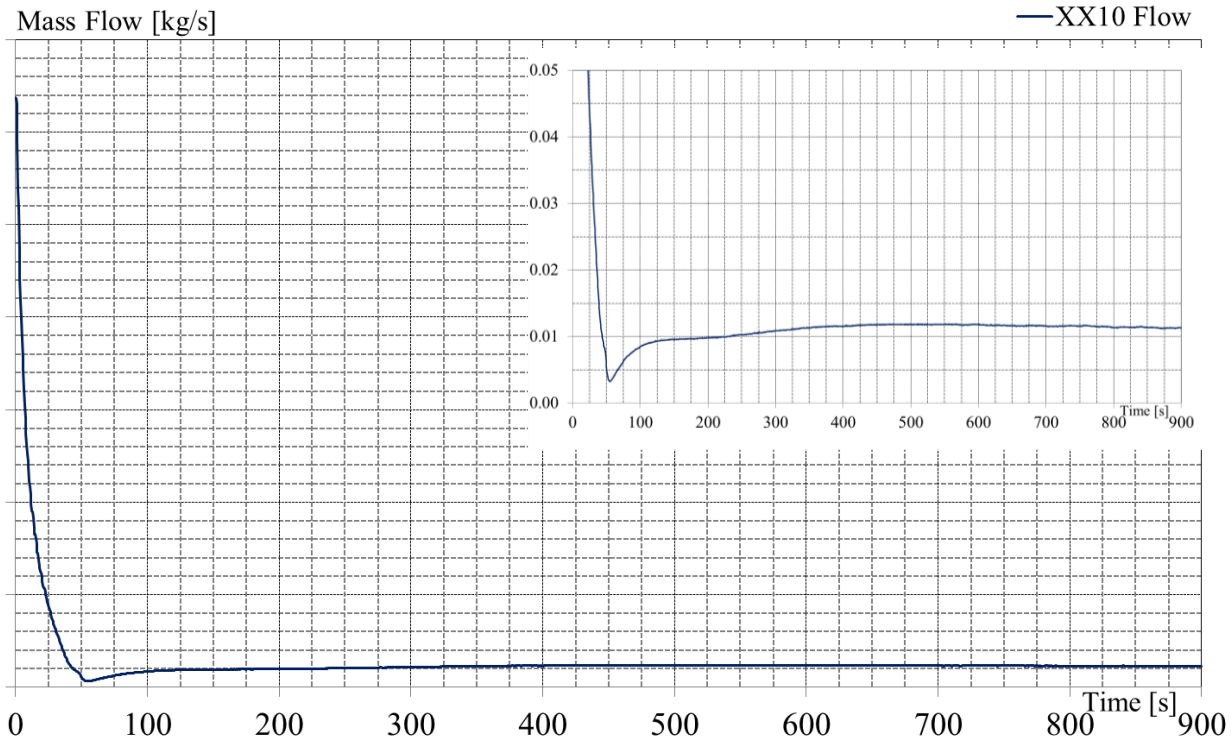

Fig. 27 – EBR-II, SHRT-17: XX10 Mass Flow Rate.

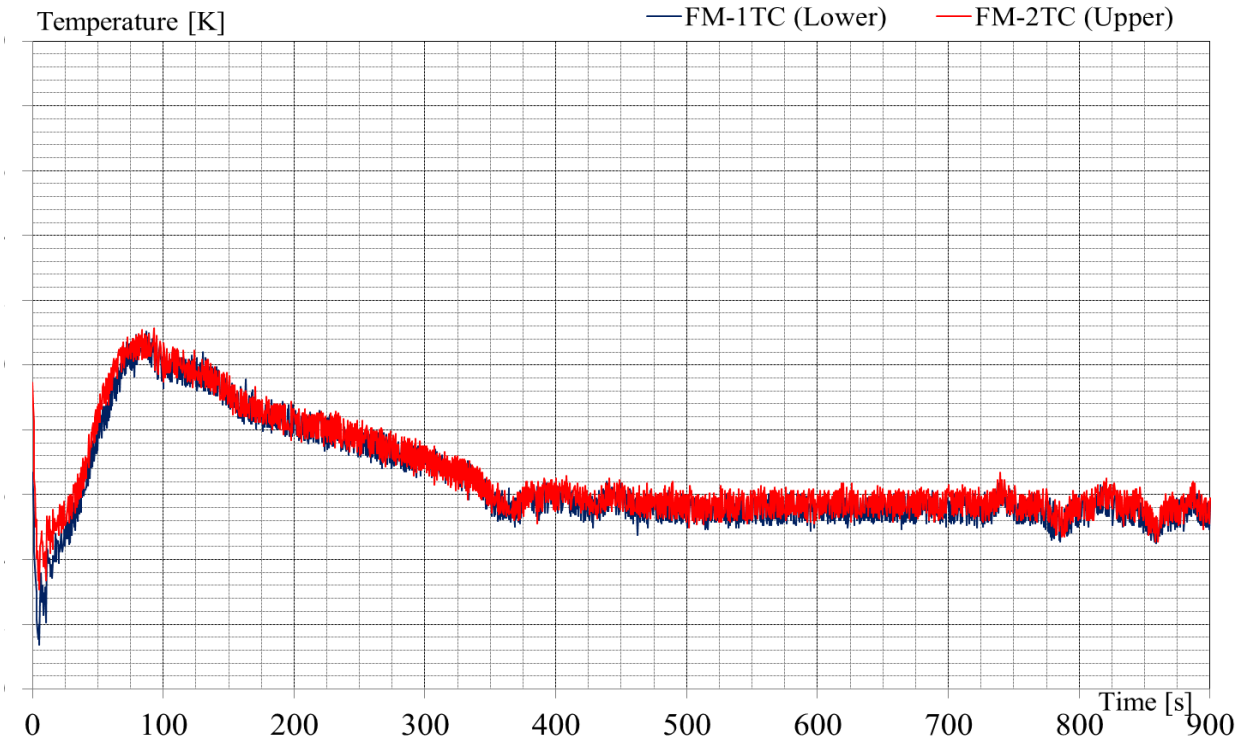

Fig. 28 – EBR-II, SHRT-17: XX09 Flowmeter Temperature.

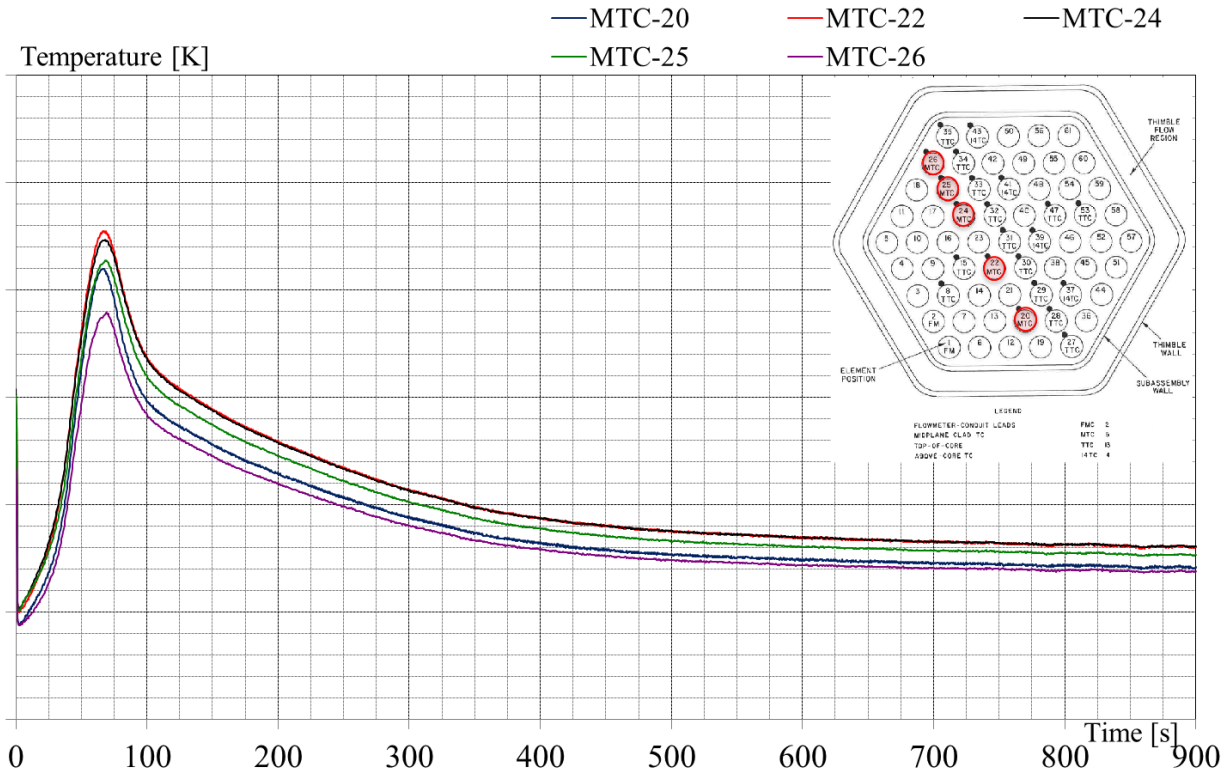

Fig. 29 – EBR-II, SHRT-17: XX09 Mid Core Temperature

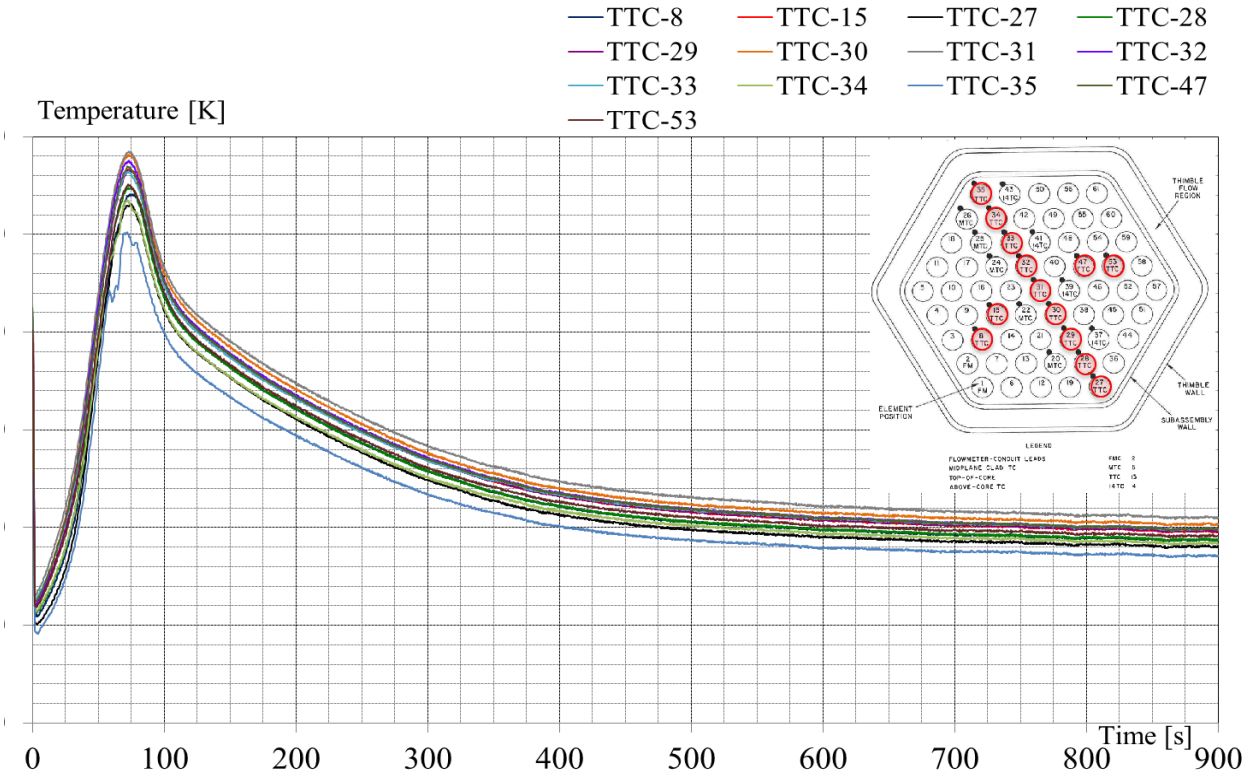

Fig. 30 – EBR-II, SHRT-17: XX09 Top of Core Temperature

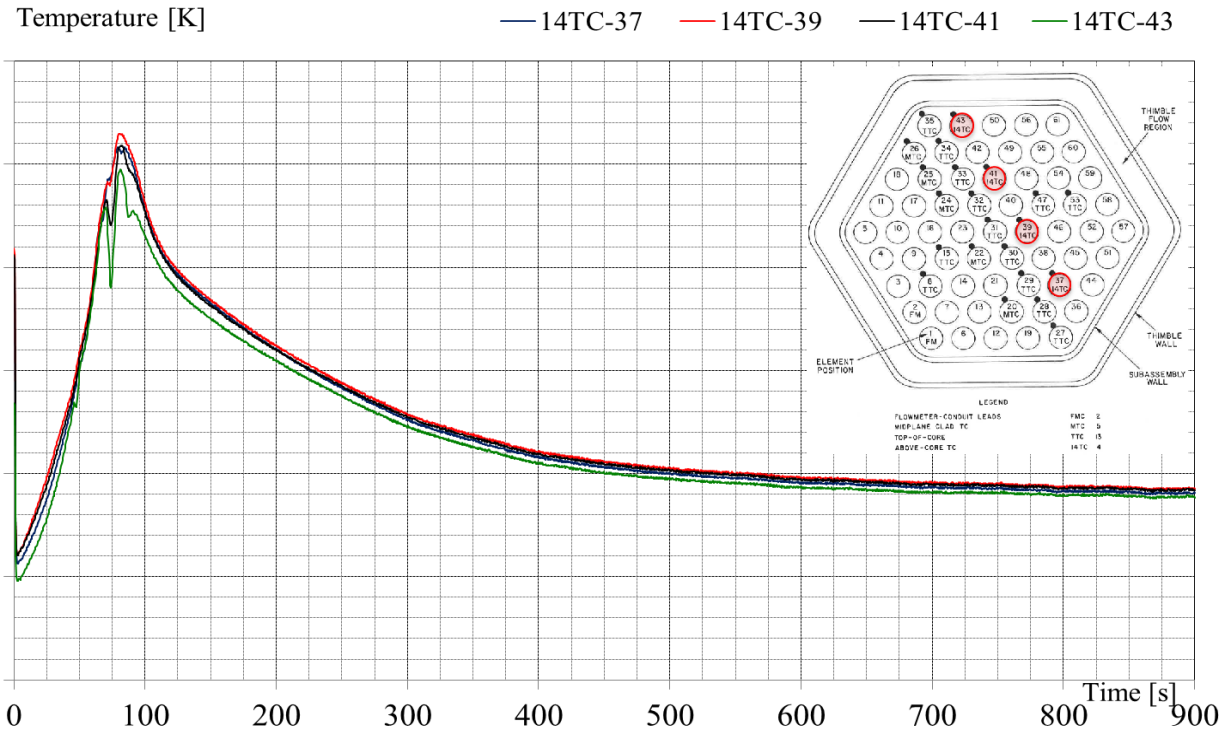

Fig. 31 – EBR-II, SHRT-17: XX09 Above Core Temperature.

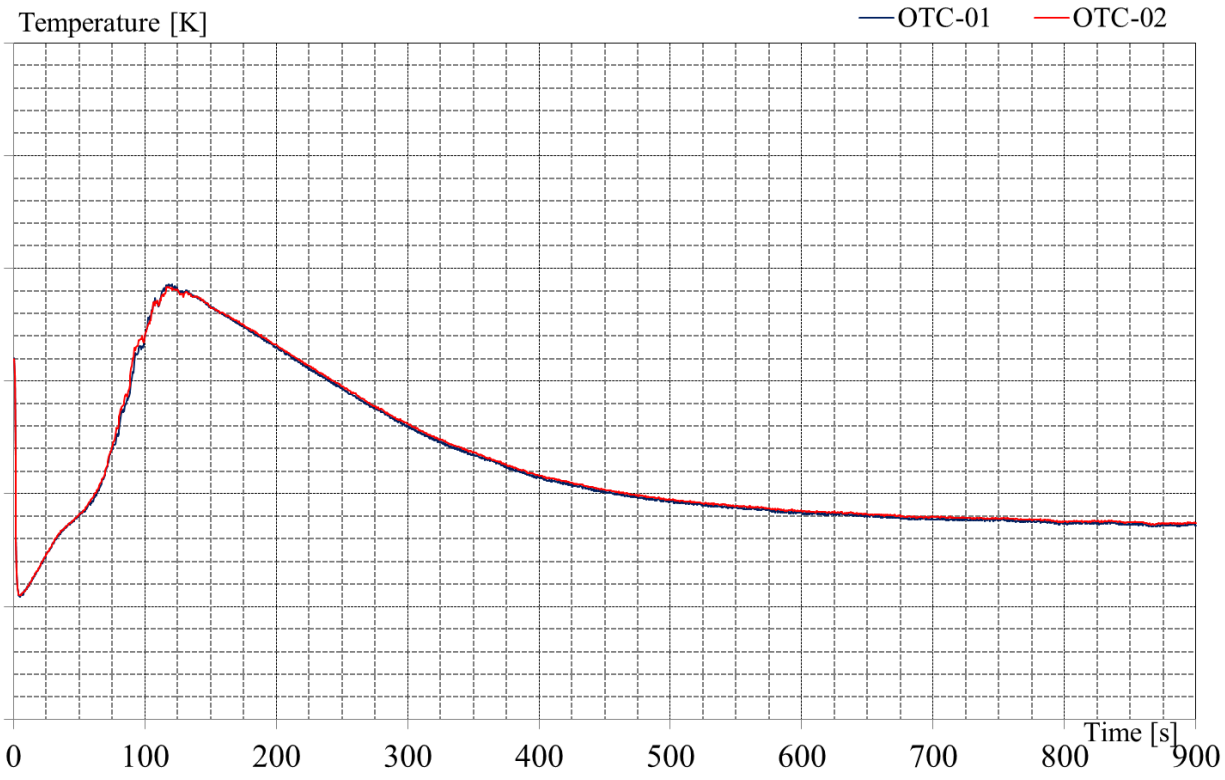

Fig. 32 – EBR-II, SHRT-17: XX09 Coolant Outlet Temperature.

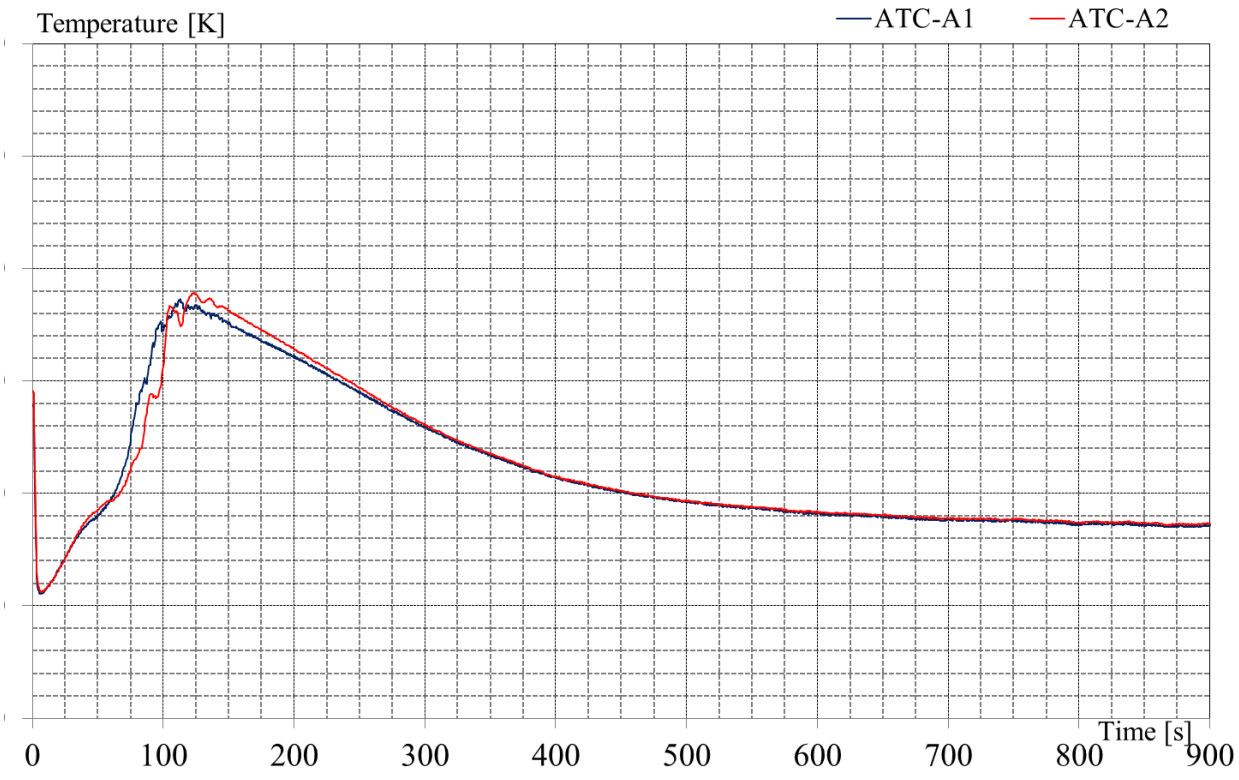

Fig. 33 – EBR-II, SHRT-17: XX09 Thimble Annulus Temperature.

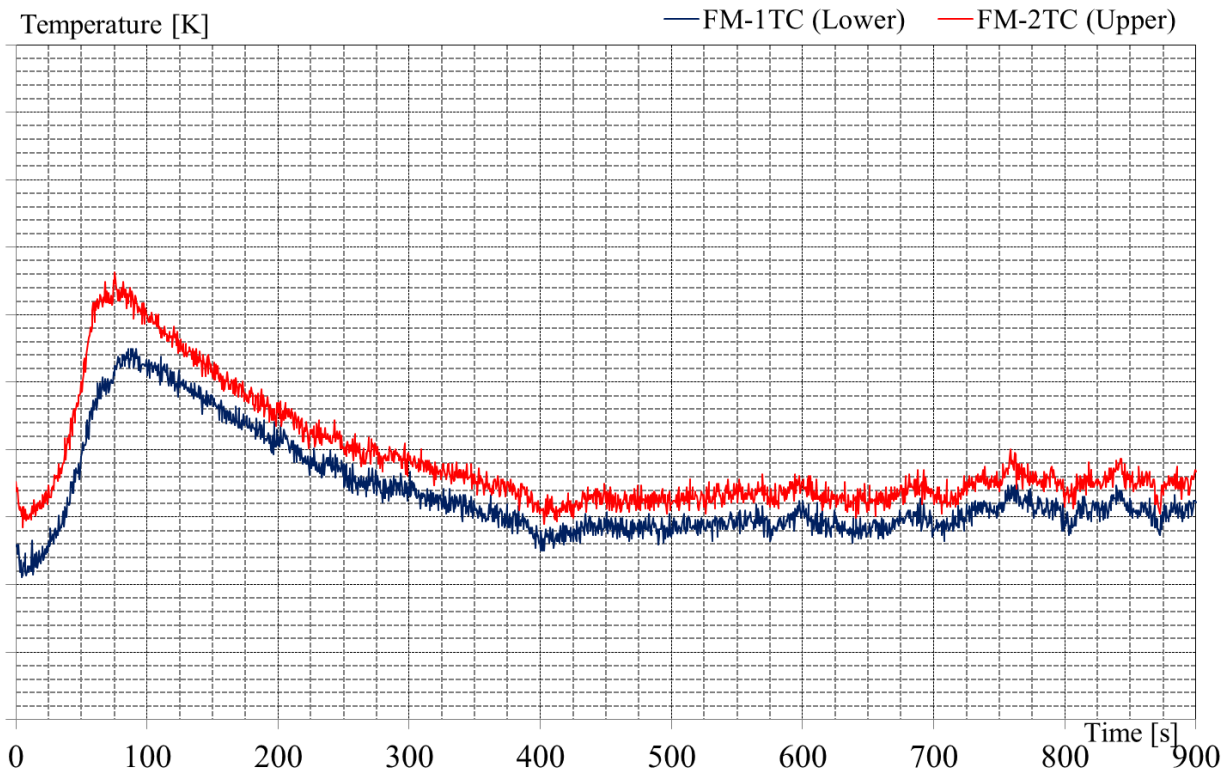

Fig. 34 – EBR-II, SHRT-17: XX10 Flowmeter Temperature.

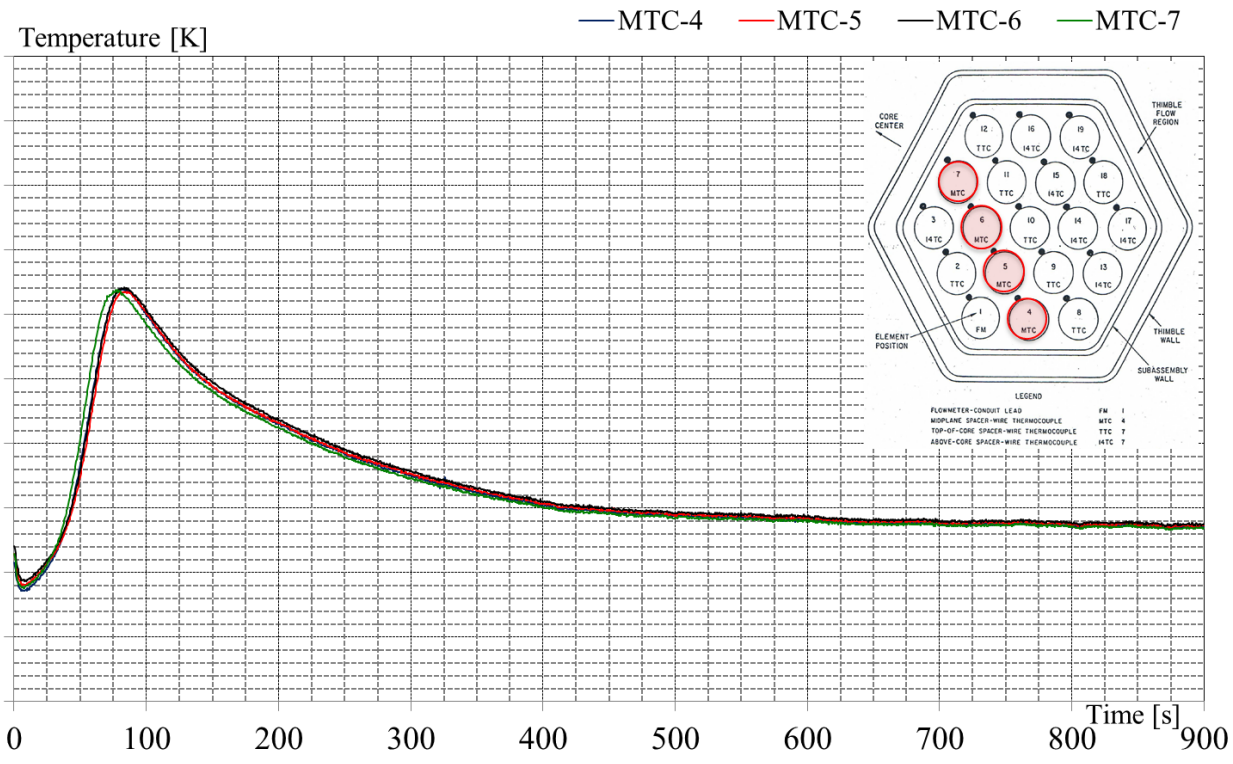

Fig. 35 – EBR-II, SHRT-17: XX10 Mid Core Temperature.

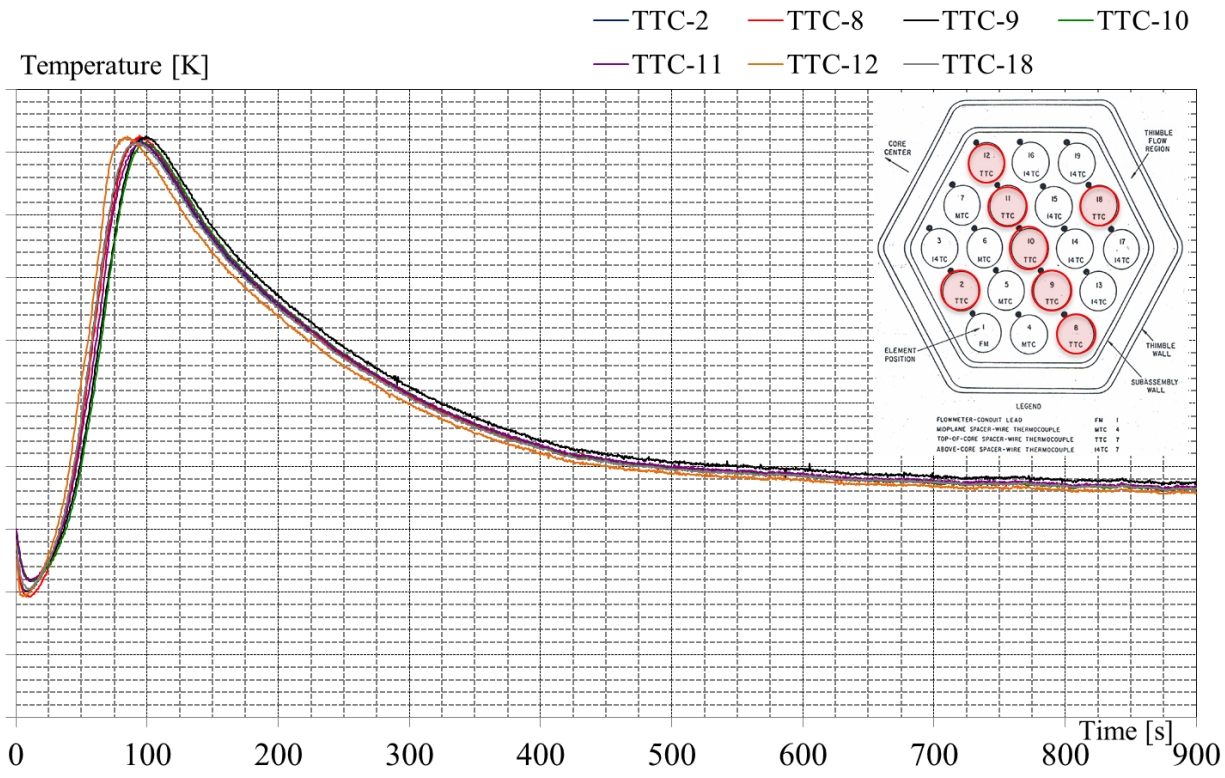

Fig. 36 – EBR-II, SHRT-17: XX10 Top of Core Temperature.

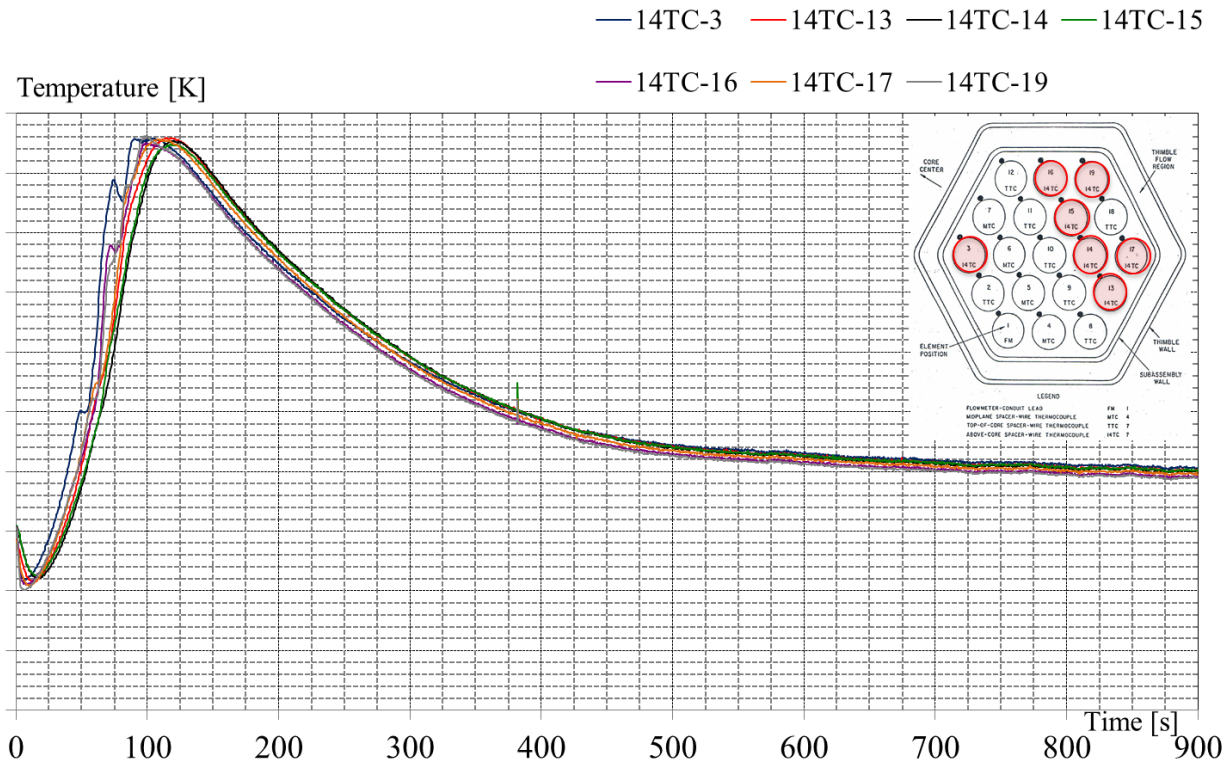

Fig. 37 – EBR-II, SHRT-17: XX10 Above Core Temperature.

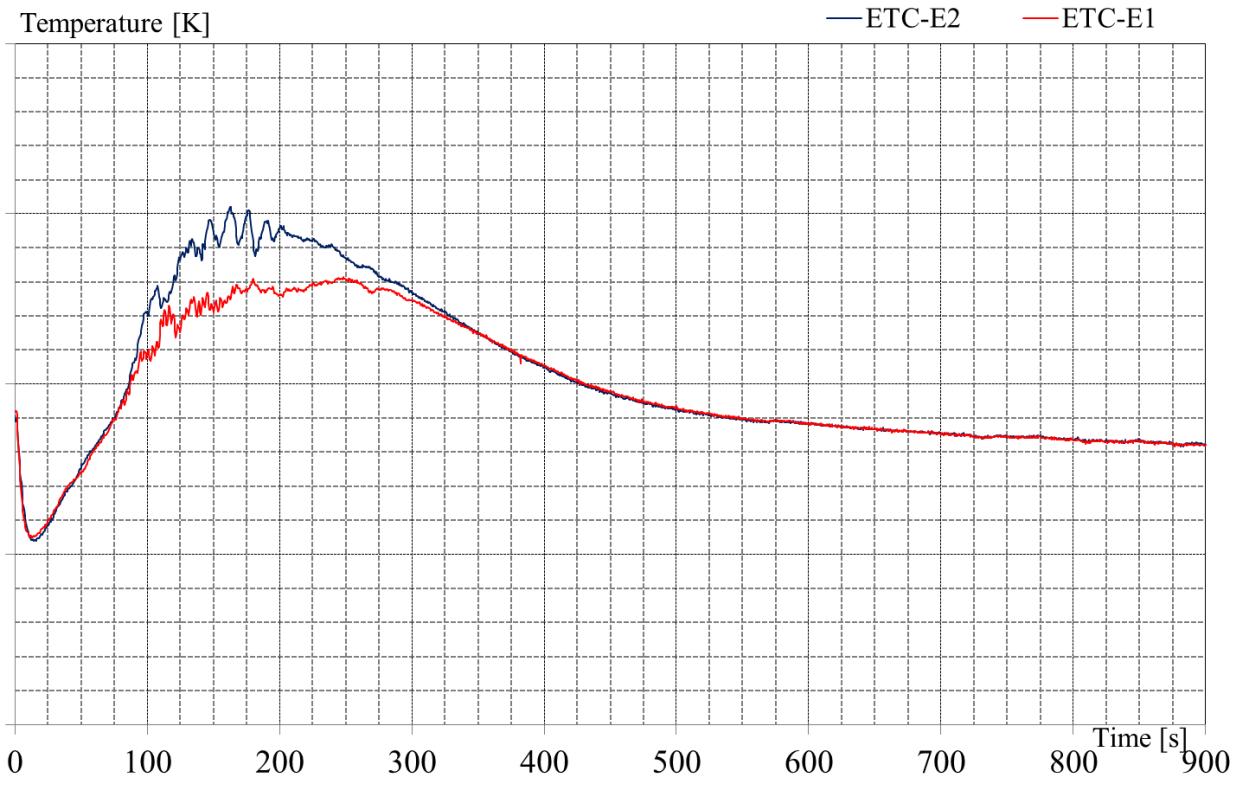

Fig. 38 – EBR-II, SHRT-17:XX10 Coolant Exit Temperature.

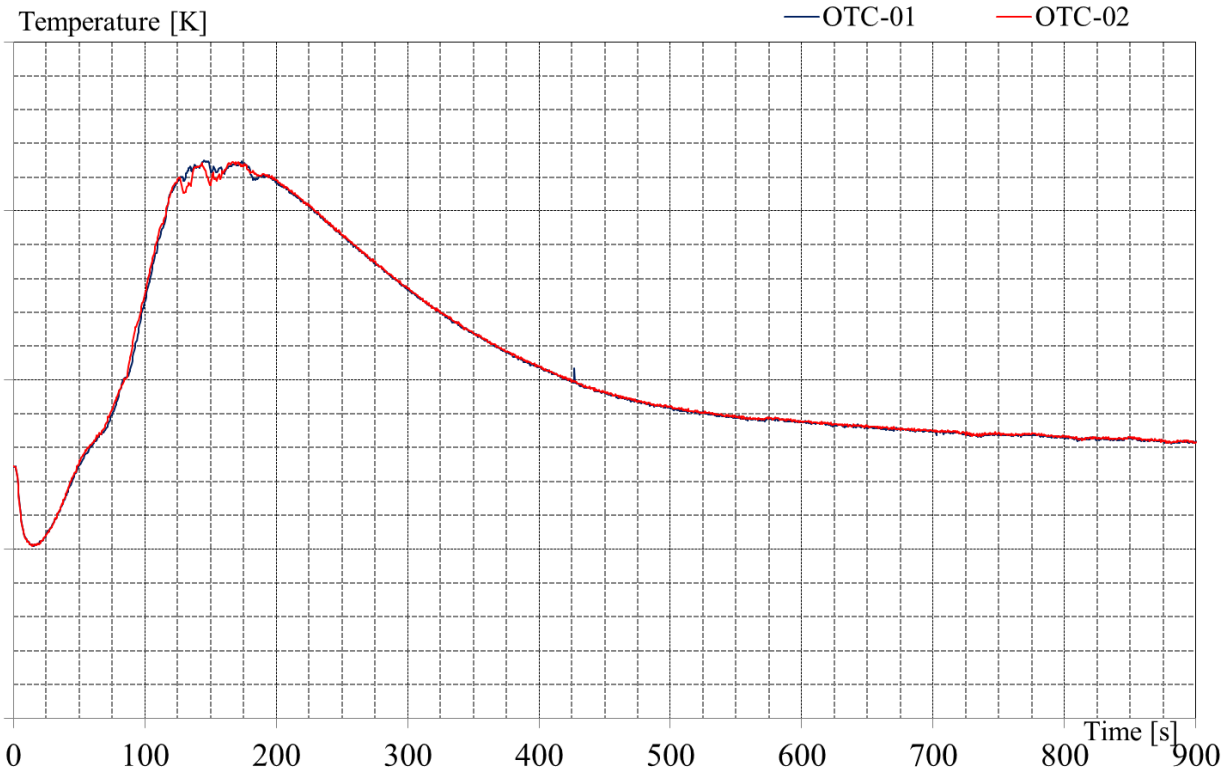

Fig. 39 – EBR-II, SHRT-17: XX10 Coolant Outlet Temperature.

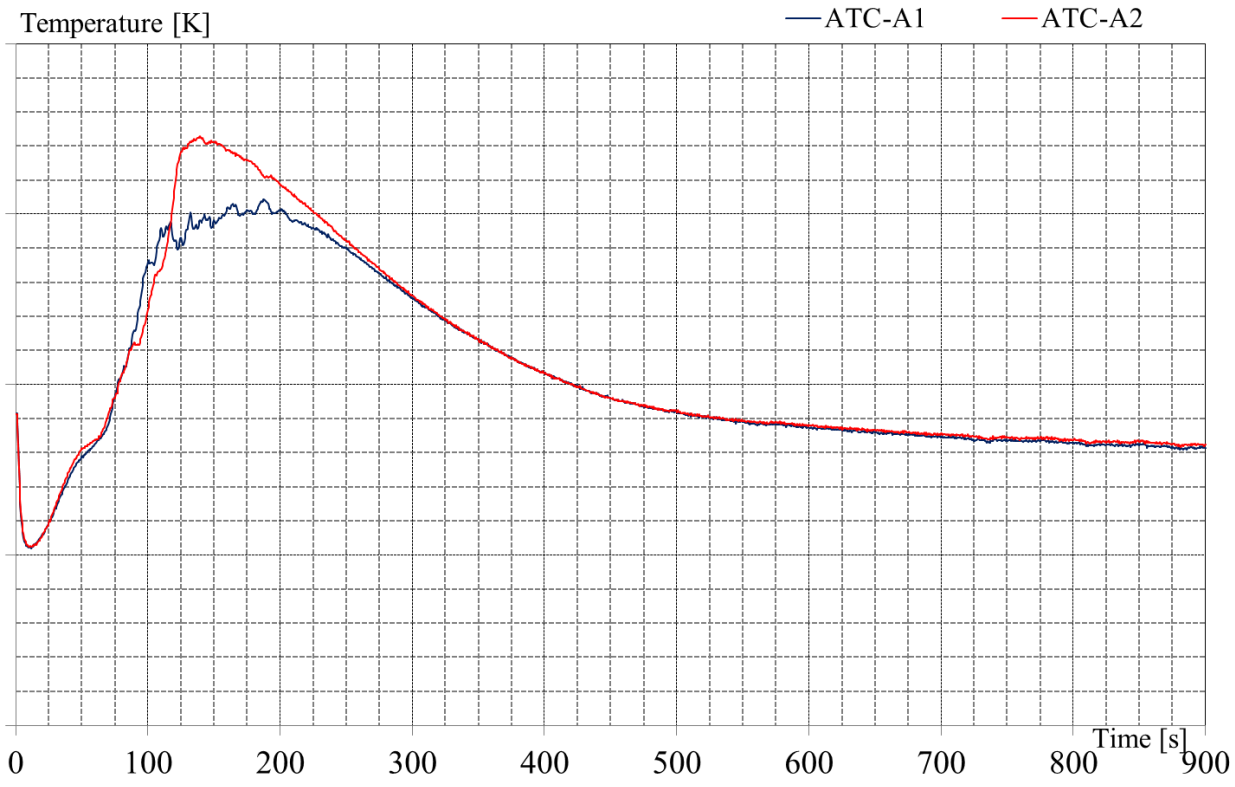

Fig. 40 – EBR-II, SHRT-17:XX10 Thimble Annulus Temperature.

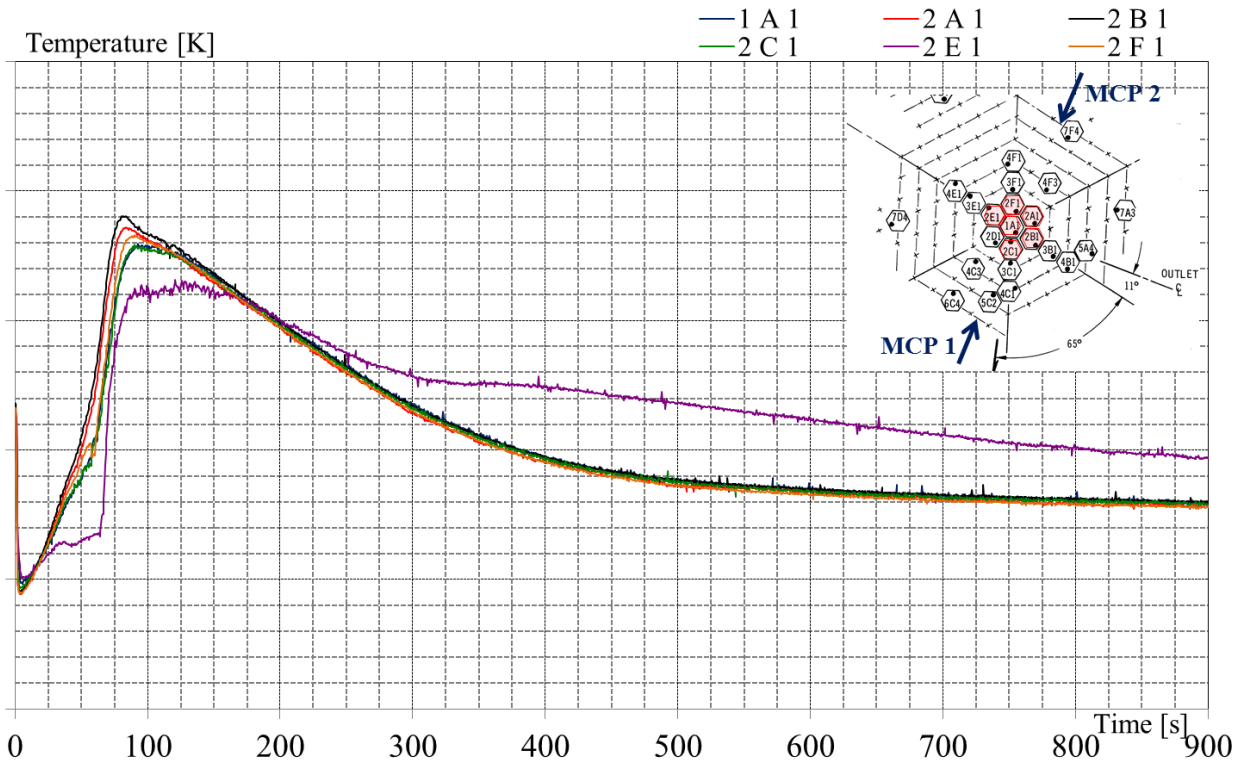

Fig. 41 – EBR-II, SHRT-17: Subassembly Outlet Temperature (Row 1 and 2).

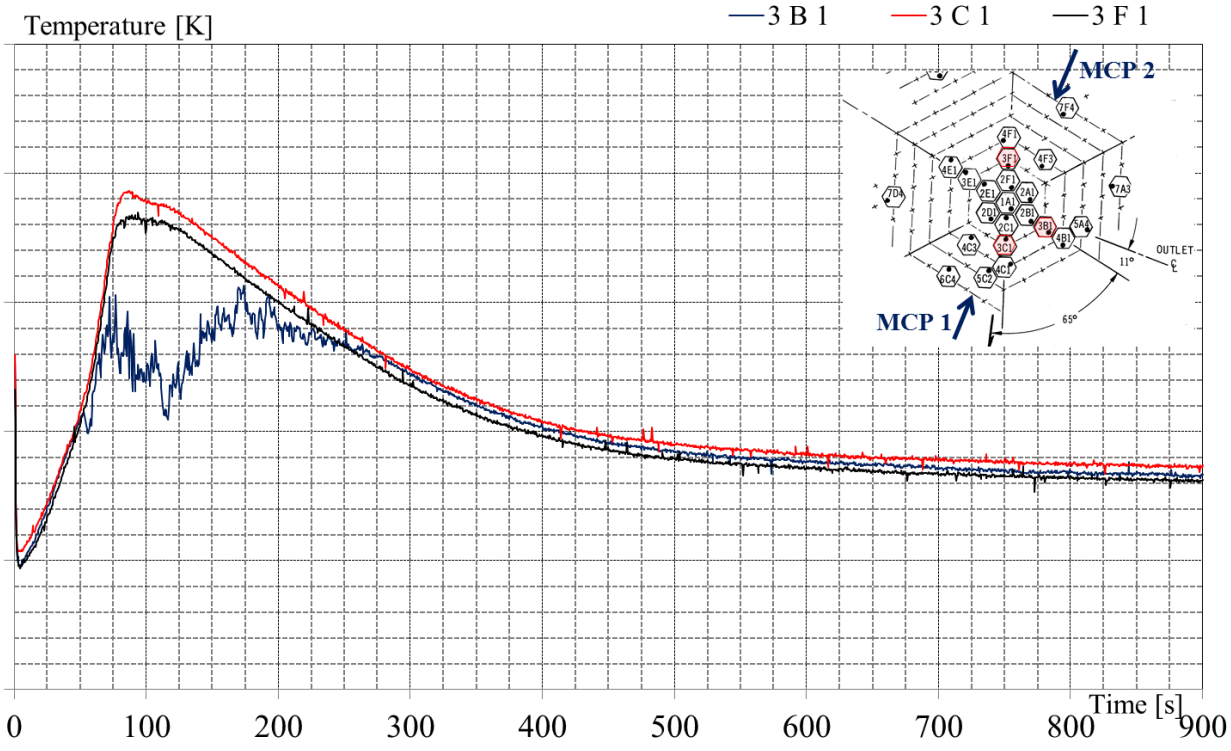

Fig. 42 – EBR-II, SHRT-17: Subassembly Outlet Temperature (Row 3).

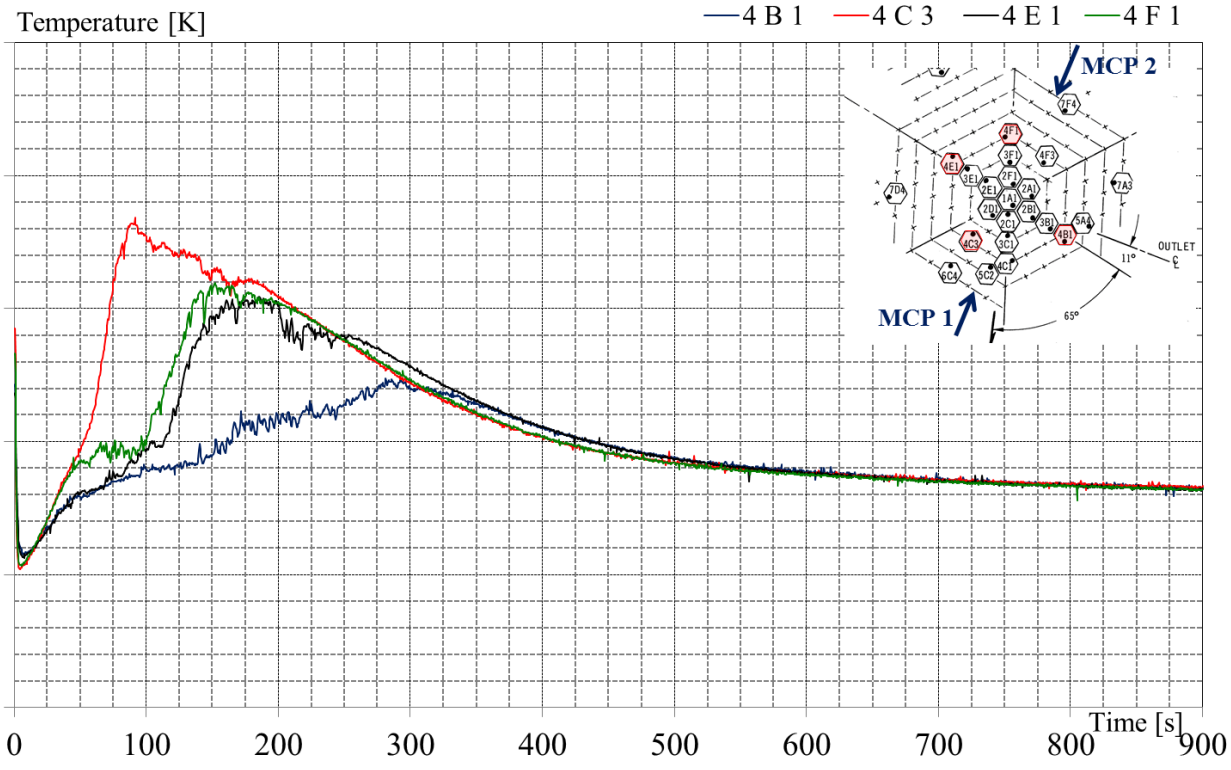

Fig. 43 – EBR-II, SHRT-17: Subassembly Outlet Temperature (Row 4).

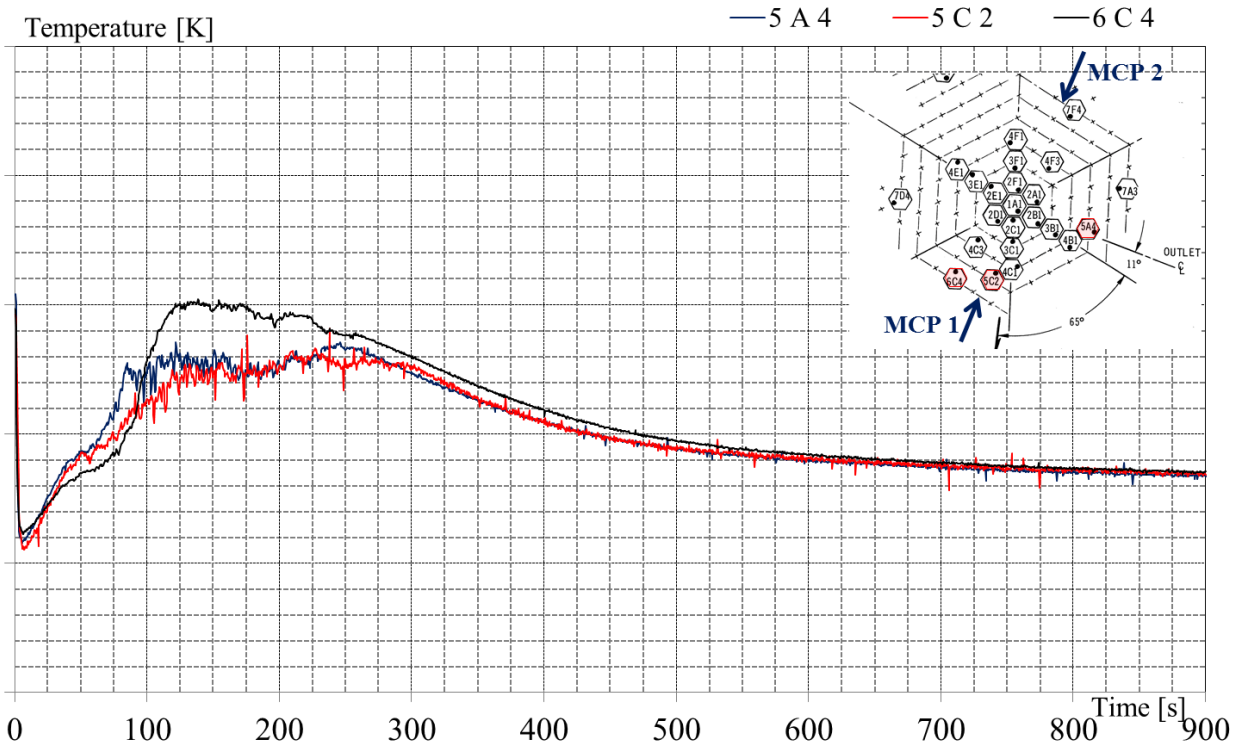

Fig. 44 – EBR-II, SHRT-17: Subassembly Outlet Temperature (Row 5 and 6).

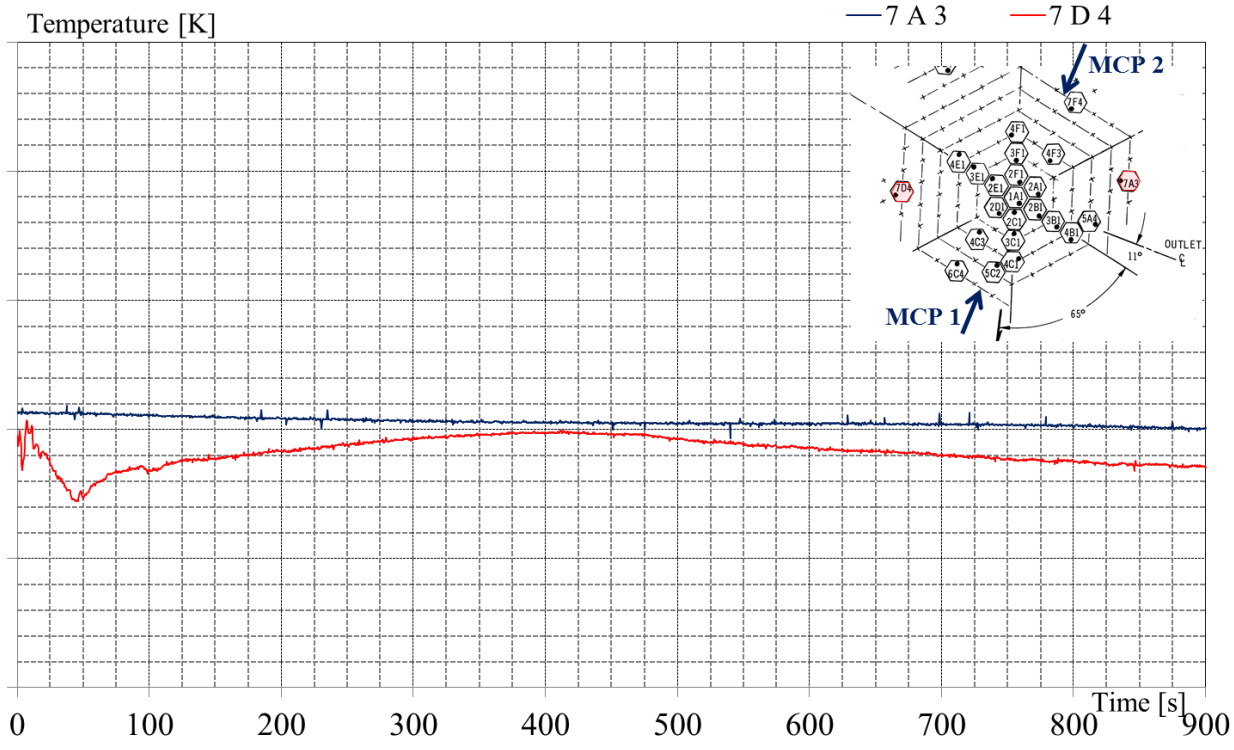

Fig. 45 – EBR-II, SHRT-17: Subassembly Outlet Temperature (Row 7).

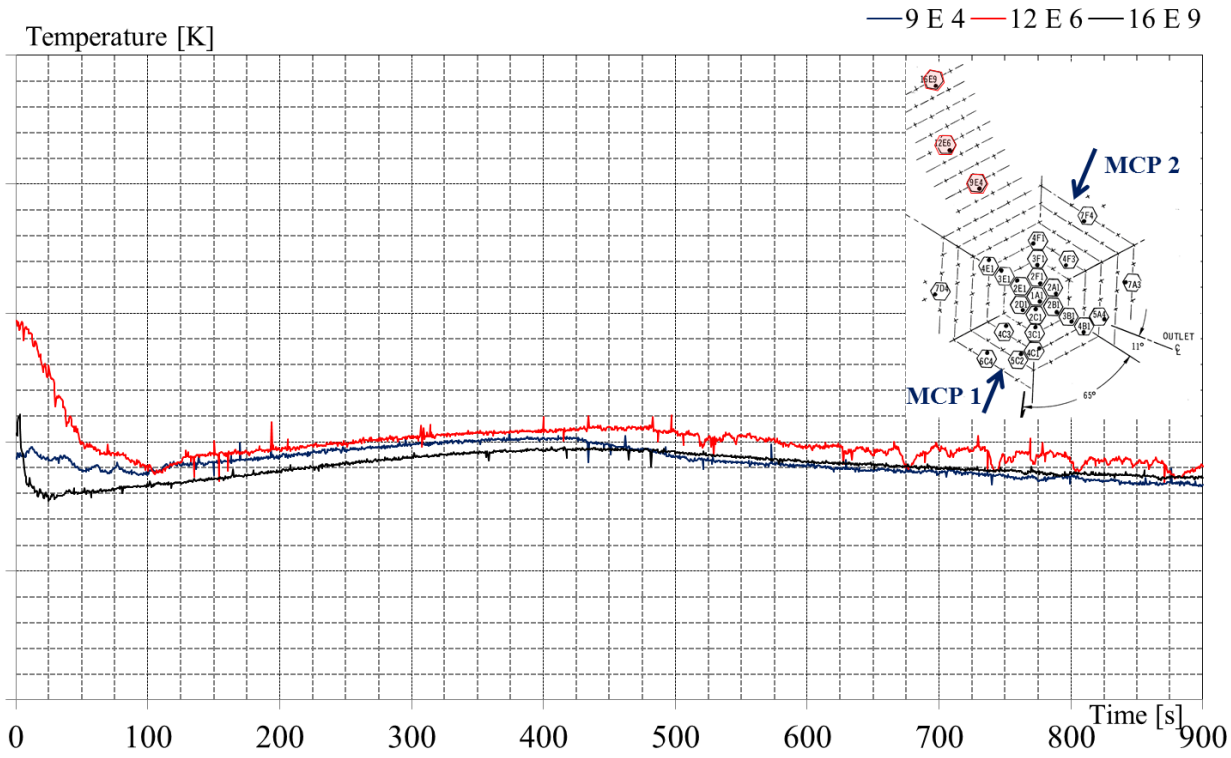

Fig. 46 – EBR-II, SHRT-17: Subassembly Outlet Temperature (Reflector and Blanket).

4 RELAP5-3D© NODALIZATION

4.1 RELAP5-3D©v4.0.3 code

The RELAP5 [19] series of code has been developed at the Idaho National Laboratory (INL) under sponsorship of the U.S. Department of Energy, the U.S. Nuclear Regulatory Commission, members of the International Code Assessment and Applications Program (ICAP), members of the Code Applications and Maintenance Program (CAMP), and members of the International RELAP5 Users Group (IRUG). Specific applications of the code have included simulations of transients in light water reactor (LWR) systems such as loss of coolant, anticipated transients without scram (ATWS), and operational transients such as loss of feedwater, loss of offsite power, station blackout, and turbine trip. RELAP5-3D© [20], the latest in the series of RELAP5 codes, is a highly generic code that, in addition to calculating the behavior of a reactor coolant system during a transient, can be used for simulation of a wide variety of hydraulic and thermal transients in both nuclear and nonnuclear systems involving mixtures of vapor, liquid, noncondensable gases, and nonvolatile solute [21][22][23].

The mission of the RELAP5-3D© development program was to develop a code version suitable for the analysis of all transients and postulated accidents in LWR systems, including large- and small-break loss-of-coolant accident (LOCAs) as well as the full range of operational and fusion reactor transient applications. Additional capabilities include space reactor simulations, gas cooled reactor applications, fast breeder reactor modeling, and cardiovascular blood flow simulations.

The RELAP5-3D© code is based on a nonhomogeneous and nonequilibrium model for the two-phase system that is solved by a fast, partially implicit numerical scheme to permit economical calculation of system transients. The RELAP5-3D© development effort from the outset was to produce a code that included important first-order effects necessary for accurate prediction of system transients but that was sufficiently simple and cost effective so that parametric or sensitivity studies were possible.

The code includes many generic component models from which general systems can be simulated. The component models include pumps, valves, pipes, heat releasing or absorbing structures, reactor kinetics, electric heaters, jet pumps, turbines, compressors, separators, annuli, pressurizers, feedwater heaters, ECC mixers, accumulators, and control system components. In addition, special process models are included for effects such as form loss, flow at an abrupt area change, branching, choked flow, boron tracking, and noncondensable gas transport.

The RELAP5-3D© version contains several important enhancements over previous versions of the code. The most prominent attribute that distinguishes the RELAP5-3D© code from the previous versions the fully integrated, multi-dimensional thermal hydraulic and kinetic modeling capability. This removes any restrictions on the applicability of the code to the full range of postulated reactor accidents. Enhancements include a new matrix solver for 3D problems, new thermodynamic properties for water, and improved time advancement for greater robustness. Enhancements also include all features and models previously available in the ATHENA configuration version of the code, which are as follows: addition of new working fluids (e.g. ammonia, blood, carbon dioxide, DowThermA, glycerol, helium, helium-xenon, hydrogen, lead-bismuth, lithium, lithium-lead, molten salts, nitrogen, potassium, R134a (SUVA®), sodium, sodium-potassium, and xenon) and a magneto-hydrodynamic model. The multi-dimensional component in RELAP5-3D© was developed to allow the user to more accurately model the multi-dimensional flow behavior that can be

exhibited in any component or region of a LWR system. Typically, this will be the lower plenum, core, upper plenum and downcomer regions of an LWR. However, the model is general, and is not restricted to use in the reactor vessel.[20]

4.2 EBR-II nodalization

A description of the RELAP5-3D© nodalization [22] is summarized below, distinguishing:

- The coolant system, that includes: the pool region, the lower and the top part of the pool; the major components in the primary sodium circuit: pumps, high and low pressure flow lines, throttle valve; the Z-Pipe and the intermediate heat exchanger, primary and secondary side.
- The reactor region, that includes the reactor vessel, including the lower plenum, the upper plenum and the core bypass; the core subassemblies, divided in the central core region (driver subassemblies) and outer blanket region (reflector and blanket subassemblies).

The EBR-II nodalization is shown from Fig. 47 to Fig. 51. The correspondence between the zones of the facility and the nodes of the code model are exposed from Tab. 14 to Tab. 29. These tables report the RELAP5-3D© hydraulic components numbers and types, according to the real EBR-II plant configuration. Relevant parameters characterizing the components are also indicated. The entire input deck consists of 3985 hydraulic volumes, 6428 hydraulic junctions and 5248 thermal structures. More details regarding the adopted code resources have been reported in Tab. 13.

Coolant system model
RELAP5-3D© nodalization of EBR-II coolant system represents the pool region, the reactor inlet piping, the reactor outlet piping and the IHX, primary and secondary side.

The pool region is modeled with a 3D component (i.e. MULTID). Fig. 47 a) shows a scheme of the nodalization. The 3D component has: 2 radial, 8 azimuthal and 19 axial subdivisions. The two radii correspond to the reactor vessel radius and to the tank radius, equal to 1.797 and 3.962, respectively. The number of azimuthal meshes have been chosen in order to represent with the least number of volumes the real position of the pumps, the inlet of the pipes and of the IHX. The axial meshes of the pool region have vertical lengths equal or multiple with respect to reactor region, pipes and IHX. It must been stressed that each component in the pool is positioned as in the real 3D geometry. Tab. 14 shows the correspondence between the real configuration of the pool and the nodes of the code model, the relevant parameters that characterize the multid component are also reported. The dead zone and the top part of the pool, that includes the layer of argon, have been modeled with two branch components. Tab. 15 report the main parameters of the two components.

The EBR-II primary system consist of two main pumps, connected to the reactor vessel with the inlet piping: the high and low pressure flow lines. The two loops are equals and symmetrical in the real configuration and in the nodalization, so the description of the RELAP5-3D© model that follows applies to both loops.

The pump has been modeled with a PUMP component. RELAP5-3D© [21][22] model parameter and rated parameter are compared in Tab. 17. The homologous curves (see Tab. 18) have been implemented using the characteristic curves provided for the pump, see Section 0, and varying the values of speed and flow rate. The speed range considered is from -80% of nominal speed to the nominal value; the flow rate is from -40% of nominal flow rate to +20% of nominal flow rate.

The high flow line has been modeled with a PIPE of 28 axial volumes and 27 junctions. A BRANCH represents the connection with the reactor vessel. The low pressure flow line has been modeled with two PIPE components: the ascending part, with 13 axial volumes and the 12 junctions, the descending and horizontal part, with 30 axial volumes and 29 junctions. The two pipes are connected with a valve (MOTOR VALVE) that models the throttle valve. The connection from the high pressure flow line to the low pressure flow line has been modeled with a BRANCH component, while a SINGLE JUNCTION models the connection from the low pressure flow line to the reactor vessel. The nodalization is represented in Fig. 49.

The reactor outlet pipe, or Z-Pipe, connects the reactor zone and the IHX, it has been modeled with a PIPE of axial 39 volumes and 38 junctions, the last 10 axial nodes represent the IHX primary side. The connections from the reactor vessel to the Z-Pipe and from the Z-Pipe to the pool have been modeled with single junctions.

The secondary side of the IHX is modeled with two TIME DEPENDENT VOLUME and one TIME DEPENDENT JUNCTION components for setting the boundary conditions according with reactor design (i.e. pressure at the outlet and coolant temperature and mass flow rate at the inlet). The secondary sodium temperature is imposed with the TIME DEPENDENT VOLUME component at the inlet, while the mass flow rate is regulated with a TIME DEPENDENT JUNCTION component. The system pressure is imposed with a TIME DEPENDENT VOLUME component at the outlet.
The central tube of the IHX, where the sodium flow downwards has been modeled with a pipe of 11 axial volumes and 10 junctions, the last axial node represents the lower plenum of the IHX connecting the central tube and the ascending tubes. The ascending tubes, have been modeled with an equivalent pipe of 11 axial volumes and 10 junctions; the hydraulic diameter is equivalent to the tube diameter (0.0134 m) with the exception of the last axial node that models the upper plenum, connecting the tube bundle and the secondary side outlet.
The heat exchange with the primary system is modeled with a thermal structure This RELAP5-3D© component exchange energy in concurrent direction (i.e. primary system and central tube) and counter-current direction (i.e. primary system and tube bundle).

In Fig. 48 a 2D scheme of the nodalization of the all system is reported, it includes the reactor vessel (in the center), with the exception of the core subassemblies.

In Tab. 15 the relevant parameters of the coolant systems, Z-Pipe and IHX model are shown with the correspondence between the element in the real configuration of the EBR-II and the RELAP5-3D© model.

The main heat structure modeling features of the coolant system are reported in Tab. 30. The table provides information related to the boundary conditions at which the heat structure is connected, the overall volumes of the structures (distinguish the insulation material), the surface areas of the structures and the models applied.

Reactor core model
The reactor vessel has been modeled with a 3D component that represents the lower plenum, the upper plenum and the core bypass. The 3D component has: 5 radial, 12 azimuthal and 17 axial subdivisions. Fig. 47 b) shows a scheme of the component. The radii have been chosen grouping the ring with respect to the three core regions: the first and second radius comprise the central core region, the third the expanded core region and the fourth the reflector and blanket region; while the last corresponds to the reactor shield (see Fig. 52). The azimuthal subdivision has been made in order to represent the real position of the inlet and outlet of the pipes and the hexagonal symmetry

of the core. The axial nodes have lengths equal or sub-multiple with respect of the meshes of the 3D component representing the pool region. In the core region the axial nodes are equals to the subassemblies meshes. Starting from the bottom, the first and the second layers model the low and high pressure coolant plena. From the layer 3 to the layer 15 there is the correspondence with core region. The last two layers represent the upper plenum.
The core bypass is connected with the high pressure coolant plenum in the bottom and the upper plenum on the top. It is thermally coupled with the FA, through the wrappers and the pool system through the neutronic shield.

The reactor core is divided into two main parts, according to the real configuration:

1. the central core and the expanded core region, that correspond to the first 7 rows, fed by the high flow plenum, which assemblies have been modeled one by one, according with the geometrical specification.

2. the outer blanket region, that includes the reflector and blanket assemblies, modeled as 24 equivalent pipe components, grouping separately according with azimuthal configuration.

A one-dimensional component has been used to represent the assembly; the model is rather detailed to represent all relevant geometric characteristics and positions: BAF, TAF and thermocouples. Fig. 51 shows an example of the model of the assembly, representing the MARK-IIAI driver assembly. The model used is a PIPE subdivided in 15 axial volumes, 5 of these are used to represent the active core. The meshes of this region are small and uniform, in order to center the position of the thermocouples and to obtain a more accurate temperature, and also to realize the coupling with a 3D neutronic code (i.e. PHYSICS). The choice of the mesh length has been made taking into account the difficulties of convergence by RELAP5-3D© code when the meshes are too small.

Maintaining the same axial subdivisions, each type of channel, as described in Ref.[3], have been modeled: i.e. reflector, blanket high flow driver, driver, partial driver, control, safety, steel, experimental, XX09, XX10 and XY-16. Tab. 19, Tab. 20, Tab. 21, Tab. 22, Tab. 23, Tab. 24, Tab. 25, Tab. 26, Tab. 27 and Tab. 28 summarize the relevant parameters of each type of channel modeled. The partial driver model has not been reported because it has same hydraulic model of the driver assembly. Tab. 29 presents the correspondence between the assemblies and the RELAP5-3D© model.
Some assemblies (Control Rod, Safety Rod, XX09 and XX10) have an external guide thimble, each of them has been modeled with a pipe component of 14 volumes and 13 junctions. The pipe is connected to the bottom and to the top of assembly with a single junction.

The RELAP5-3D© model does not represent the subassemblies exactly because of a lack of information about the power and flow distributions within the subassemblies and the geometry in the inlet and outlet regions. Fuel assembly orifices have been setup on the basis of mass flow rates data and overall dynamic pressure drops.
The assemblies have been connected to the 3D component with multiple junctions, according with the real position of each assembly with respect to the MULTID subdivision. The assembly to MULTID volume ratio is not equal to one, so the assemblies have been divided in the sectors uniformly and maintaining the symmetry. The Row 1 comprises only one assembly that has been connected with all 12 volumes; in Row 2 there are six assemblies, that have been connected to six of the sectors, alternately.

Tab. 30 summarizes the main features of the reactor vessel heat structures. The table includes information related to the boundary conditions at which the heat structure is connected, the overall volumes of the structures, the surface areas of the structures and the models applied.

4.3 Nodalization features

The main features of RELAP5-3D© input deck adopted are reported hereafter:

- A sliced approach is applied at all systems (i.e. coolant system, reactor core).
- The elevations of the different parts of the plant are maintained in the nodalization. More detailed nodalization has been implemented in regions where an higher accuracy of the prediction has been necessary (i.e. reactor core).
- The node to node ratio is kept uniform, as much as possible, with reference maximum ratio of 1.2 between adjacent sub-volumes.
- The roughness is set 3.2e-5 m with the exception of the core region, where is set 1.0e-6 m as consequence of the nodalization qualification as reported in 4.4.1.
- K-loss coefficient in junction have been evaluated or estimated on the basis of geometries.
- Recommended common rules involving characteristic dimensions, flow path area, elevations, heat structures and capacities have been taken into account from the EBR-II benchmark data.
  The friction correlations have been adequated to represent rod bundle with optionally form loss coefficient with a Reynolds dependence.

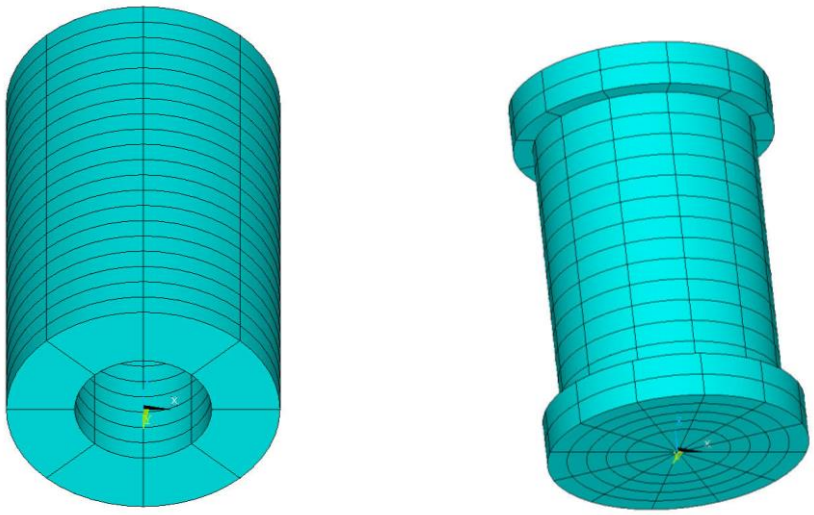

a) Scheme of the pool region *b) Scheme of the reactor vessel*

Fig. 47 – EBR-II SHRT-17, RELAP5-3D©: schematization of 3D components.

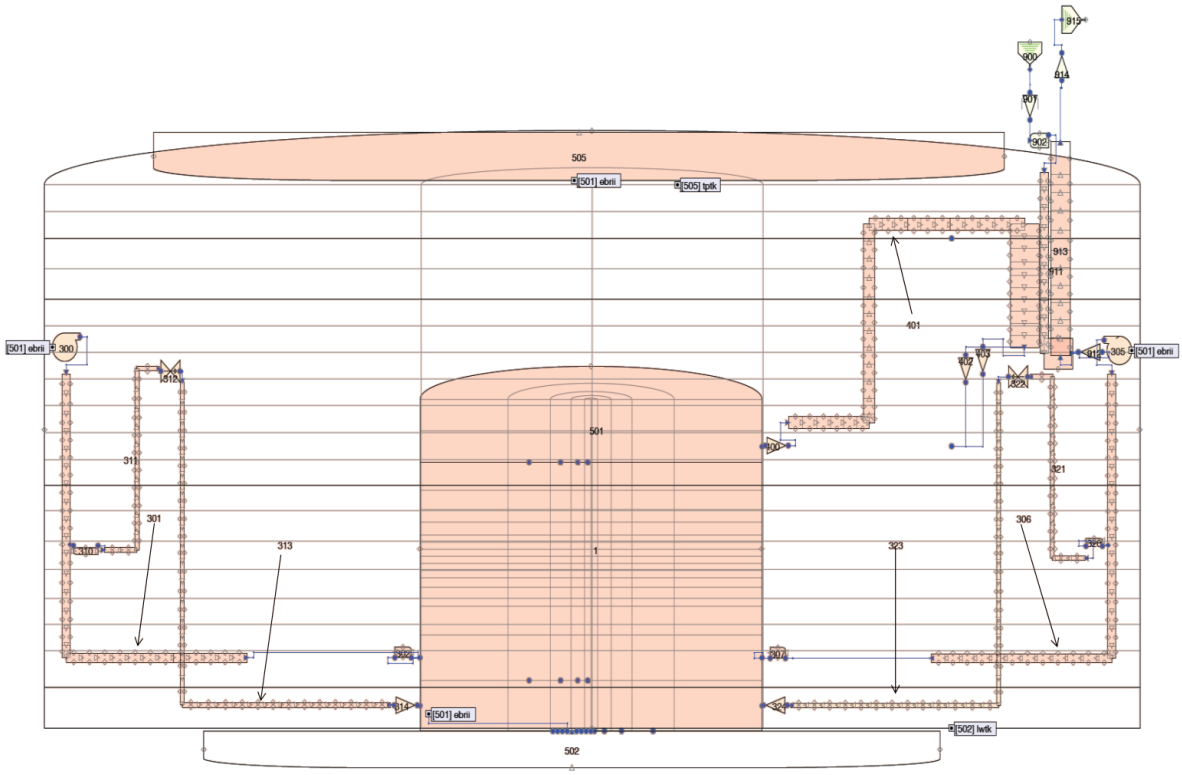

Fig. 48 – EBR-II SHRT-17, RELAP5-3D©: plant scheme.

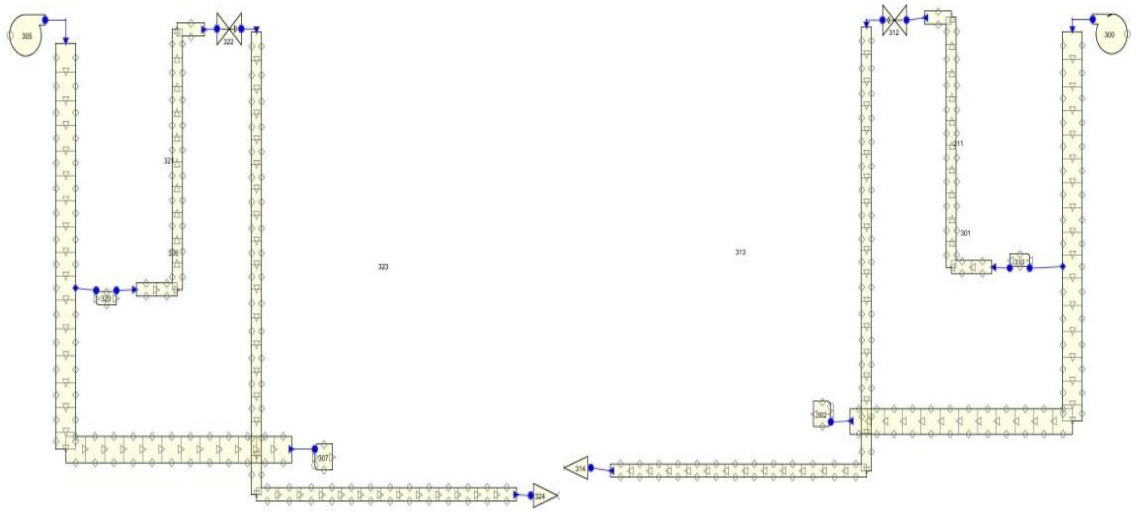

a) Pump#1, *b) Pump#2,*

[1] High and Low pressure flow lines#1

[2] High and Low pressure flow lines#2

Fig. 49 – EBR-II SHRT-17, RELAP5-3D©: scheme of pumps, high and low pressure flow lines.

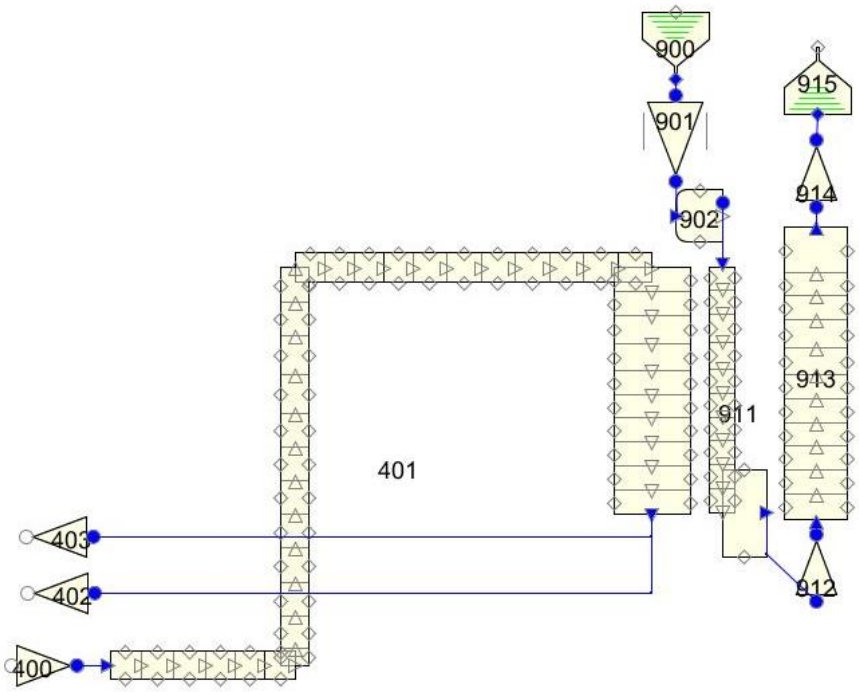

Fig. 50 – EBR-II SHRT-17, RELAP5-3D©: scheme of Z-PIPE, IHX primary and secondary side.

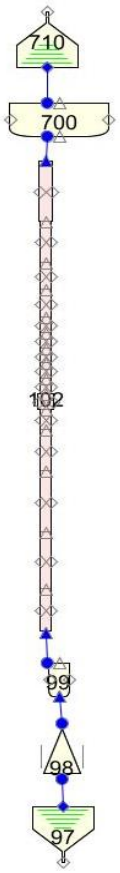

Fig. 51 – EBR-II SHRT-17, RELAP5-3D©: MARK-II AI fuel assembly

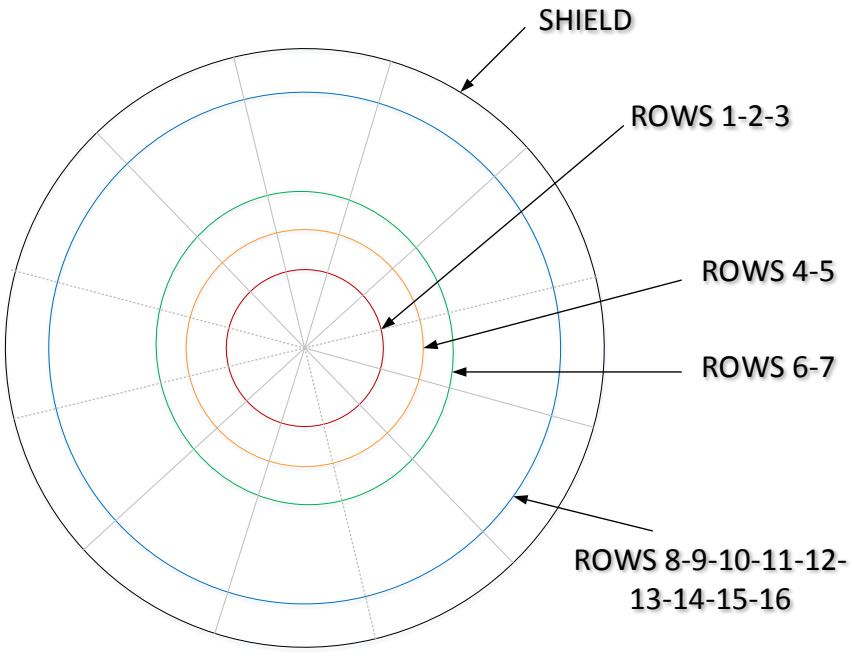

Fig. 52 – EBR-II SHRT-17, RELAP5-3D©: plane view of reactor core subdivision.

#	QUANTITY	Value
1	Tot. No. of HYDRAULIC volume	3985
2	Tot. No. of HYDRAULIC junction	6428
3	Tot. No. of HYDRAULIC volume in the core	2460
4	Tot. No. of heat structures	5248
5	Tot. No. of mesh points in the heat structures	31236
6	Tot. No. of core active structures (radial x axial)	8 x 5

Tab. 13 – EBR-II nodalization:adopted code resources

RELAP5-3D Component	RELAP5-3D Component Type	EBR-II Region	N° of r coordinates		N° of θ coordinates	N° of z coordinates
501	Multid	Pool	2		8	19
RELAP5-3D Component	**RELAP 5-3D Component Type**	**EBR-II Region**	**Radius (m)**		**(°)**	**Length (m)**
501-01	Multid	Low pressure flow inlet	1.797	3.962	45	0.48730
501-02		High pressure flow inlet	1.797	3.962	45	0.44030
501-03			1.797	3.962	45	0.31170
501-04			1.797	3.962	45	0.31170
501-05			1.797	3.962	45	0.34250
501-06			1.797	3.962	45	0.34080
501-07			1.797	3.962	45	0.36300
501-08			1.797	3.962	45	0.30380
501-09			1.797	3.962	45	0.30380
501-10		IHX outlet	1.797	3.962	45	0.32415
501-11			1.797	3.962	45	0.32415
501-12			1.797	3.962	45	0.31700
501-13			1.797	3.962	45	0.31700
501-14			1.797	3.962	45	0.31700
501-15			1.797	3.962	45	0.31700
501-16			1.797	3.962	45	0.36350
501-17		MCP inlet	1.797	3.962	45	0.36350
501-18			1.797	3.962	45	0.32100
501-19		IHX inlet	1.797	3.962	45	0.32100

Tab. 14 – EBR-II SHRT-17, RELAP5-3D©: pool region

RELAP5-3D Component	RELAP 5-3D Component Type	EBR-II Region	Length (m)	Area (m^2)	Vertical Angle (°)	Hydraulic Diameter (m)
HIGH AND LOW PRESSURE FLOW LINES						
296 (298)	Sngljun	Connection to Pool	--	--	--	--
297 (299)-01	Pipe	Pump Suction	0.3635	0.1418	90	0.2125
297 (299)-02		Pump Suction	0.3635	0.1418	90	0.2125
297 (299)-03		Pump Suction	0.321	0.1418	90	0.2125
300 (305)	Pump	Primary pump#1(#2)	0.642	0.37	--	--
301(306)-01	Pipe	High pressure flow line#1 (#2)	0.36350	0.0718	-90	0.30238
301(306)-02			0.36350	0.0718	-90	0.30238
301(306)-03			0.31700	0.0718	-90	0.30238
301(306)-03			0.31700	0.0718	-90	0.30238
301(306)-04			0.31700	0.0718	-90	0.30238
301(306)-05			0.31700	0.0718	-90	0.30238
301(306)-06			0.31700	0.0718	-90	0.30238
301(306)-07			0.32415	0.0718	-90	0.30238
301(306)-08			0.32415	0.0718	-90	0.30238
301(306)-09			0.30380	0.0718	-90	0.30238
301(306)-10			0.30380	0.0718	-90	0.30238

RELAP5-3D Component	RELAP 5-3D Component Type	EBR-II Region	Length (m)	Area (m^2)	Vertical Angle (°)	Hydraulic Diameter (m)
301(306)-11			0.36300	0.0718	-90	0.30238
301(306)-12			0.34080	0.0718	-90	0.30238
301(306)-13			0.34250	0.0718	-90	0.30238
301(306)-14			0.31170	0.0718	-90	0.30238
301(306)-15			0.31170	0.0718	-90	0.30238
301(306)-16			0.22015	0.0718	-90	0.30238
301(306)-17			0.32350	0.0718	0	0.30238
301(306)-18			0.32350	0.0718	0	0.30238
301(306)-19			0.31760	0.0718	0	0.30238
301(306)-20			0.31760	0.0718	0	0.30238
301(306)-21			0.31760	0.0718	0	0.30238
301(306)-22			0.31760	0.0718	0	0.30238
301(306)-23			0.31760	0.0718	0	0.30238
301(306)-24			0.31760	0.0718	0	0.30238
301(306)-25			0.31760	0.0718	0	0.30238
301(306)-26			0.29630	0.0718	0	0.30238
301(306)-27			0.29630	0.0718	0	0.30238
301(306)-28			0.29630	0.0718	0	0.30238
302 (307)	Branch	Connection to reactor vessel#1(#2)	0.2963	0.0718	0	--
310 (320)	Branch	Connection high and low flow lines#1 (#2)	0.341	0.0186	0	--
311(321)-01			0.34100	0.0186	90	0.15408
311(321)-02			0.34100	0.0186	90	0.15408
311(321)-03			0.34100	0.0186	90	0.15408
311(321)-03			0.30380	0.0186	90	0.15408
311(321)-04			0.30380	0.0186	90	0.15408
311(321)-05			0.32415	0.0186	90	0.15408
311(321)-06	Pipe	Low pressure flow line - Ascending part#1(#2)	0.32415	0.0186	90	0.15408
311(321)-07			0.31700	0.0186	90	0.15408
311(321)-08			0.31700	0.0186	90	0.15408
311(321)-09			0.31700	0.0186	90	0.15408
311(321)-10			0.31700	0.0186	90	0.15408
311(321)-11			0.36350	0.0186	90	0.15408
311(321)-12			0.36350	0.0186	90	0.15408
311(321)-13			0.45700	0.0186	90	0.15408
312 (322)	Valve	Throttle valve#1(#2)	--	--	--	--
313(323)-01			0.36350	0.0186	-90	0.15408
313(323)-02			0.36350	0.0186	-90	0.15408
313(323)-03			0.31700	0.0186	-90	0.15408
313(323)-03			0.31700	0.0186	-90	0.15408
313(323)-04			0.31700	0.0186	-90	0.15408
313(323)-05			0.31700	0.0186	-90	0.15408
313(323)-06		Low pressure flow line – Descending and horizontal part#1(#2)	0.31700	0.0186	-90	0.15408
313(323)-07	Pipe		0.32415	0.0186	-90	0.15408
313(323)-08			0.32415	0.0186	-90	0.15408
313(323)-09			0.30380	0.0186	-90	0.15408
313(323)-10			0.30380	0.0186	-90	0.15408
313(323)-11			0.36300	0.0186	-90	0.15408
313(323)-12			0.34080	0.0186	-90	0.15408
313(323)-13			0.34250	0.0186	-90	0.15408
313(323)-14			0.31170	0.0186	-90	0.15408
313(323)-15			0.31170	0.0186	-90	0.15408

RELAP5-3D Component	RELAP 5-3D Component Type	EBR-II Region	Length (m)	Area (m^2)	Vertical Angle (°)	Hydraulic Diameter (m)
313(323)-16			0.44030	0.0186	-90	0.15408
313(323)-17			0.48730	0.0186	-90	0.15408
313(323)-18			0.36375	0.0186	0	0.15408
313(323)-19			0.36375	0.0186	0	0.15408
313(323)-20			0.36375	0.0186	0	0.15408
313(323)-21			0.32343	0.0186	0	0.15408
313(323)-22			0.32343	0.0186	0	0.15408
313(323)-23			0.32343	0.0186	0	0.15408
313(323)-24			0.32343	0.0186	0	0.15408
313(323)-25			0.32343	0.0186	0	0.15408
313(323)-26			0.32343	0.0186	0	0.15408
313(323)-27			0.32343	0.0186	0	0.15408
313(323)-28			0.32300	0.0186	0	0.15408
313(323)-29			0.32300	0.0186	0	0.15408
313(323)-30			0.32300	0.0186	0	0.15408
314 (324)	Sngljun	Connection to RV	--	--	--	--
Z-PIPE						
400	Sngljun	Connection to RV	--	--	--	--
401-01			0.42773	0.0932	0	0.3429
401-02			0.42773	0.0932	0	0.3429
401-03			0.42773	0.0932	0	0.3429
401-04			0.39400	0.0932	0	0.3429
401-05			0.39400	0.0932	0	0.3429
401-06			0.39400	0.0932	0	0.3429
401-07			0.21482	0.0932	90	0.3429
401-08			0.42964	0.0932	90	0.3429
401-09			0.45842	0.0932	90	0.3429
401-10			0.45842	0.0932	90	0.3429
401-11			0.44831	0.0932	90	0.3429
401-12			0.44831	0.0932	90	0.3429
401-13			0.44831	0.0932	90	0.3429
401-14			0.44831	0.0932	90	0.3429
401-15			0.51407	0.0932	90	0.3429
401-16			0.51407	0.0932	90	0.3429
401-17			0.45396	0.0932	90	0.3429
401-18			0.45396	0.0932	90	0.3429
401-19			0.39300	0.0932	0	0.3429
401-20			0.39300	0.0932	0	0.3429
401-21			0.39300	0.0932	0	0.3429
401-22			0.39300	0.0932	0	0.3429
401-23			0.45587	0.0932	0	0.3429
401-24			0.45587	0.0932	0	0.3429
401-25			0.45587	0.0932	0	0.3429
401-26			0.45587	0.0932	0	0.3429
401-27			0.45587	0.0932	0	0.3429
401-28			0.45587	0.0932	0	0.3429
401-29			0.45587	0.0932	0	0.3429
401-30			0.32100	0.6362	-90	0.0163
401-31			0.32100	0.6362	-90	0.0163
401-32			0.36350	0.6362	-90	0.0163
401-33			0.36350	0.6362	-90	0.0163
401-34			0.31700	0.6362	-90	0.0163
401-35			0.31700	0.6362	-90	0.0163
401-36			0.31700	0.6362	-90	0.0163
401-37			0.31700	0.6362	-90	0.0163
401-38			0.32415	0.6362	-90	0.0163

Pipe

Z-PIPE

Z-PIPE IHX zone

RELAP5-3D Component	RELAP 5-3D Component Type	EBR-II Region	Length (m)	Area (m^2)	Vertical Angle (°)	Hydraulic Diameter (m)
401-39			0.32415	0.6362	-90	0.0163
402	Sngljun	Connection to pool	--	--	--	--
403	Sngljun	Connection to pool	--	--	--	--
INTERMEDIATE HEAT EXCHANGER						
900	Tmdpvol	Secondary side Na injection	0.5	1.0	-90	--
901	Tmdpjun	Secondary side pump	--	--	--	--
902	Branch	Secondary side inlet	0.32100	0.076	0	--
911-01	Pipe	IHX secondary side central tube	0.32100	0.076	-90	0.311
911-02			0.32100	0.076	-90	0.311
911-03			0.36350	0.076	-90	0.311
911-04			0.36350	0.076	-90	0.311
911-05			0.31700	0.076	-90	0.311
911-06			0.31700	0.076	-90	0.311
911-07			0.31700	0.076	-90	0.311
911-08			0.31700	0.076	-90	0.311
911-09			0.32415	0.076	-90	0.311
911-10			0.32415	0.076	-90	0.311
911-11			0.59000	--	0	--
912	Sngljun	IHX lower plenum	--	--	--	--
913-01	Pipe	IHX secondary ascending tubes	0.32415	0.4267	90	0.0134
913-02			0.32415	0.4267	90	0.0134
913-03			0.31700	0.4267	90	0.0134
913-04			0.31700	0.4267	90	0.0134
913-05			0.31700	0.4267	90	0.0134
913-06			0.31700	0.4267	90	0.0134
913-07			0.36350	0.4267	90	0.0134
913-08			0.36350	0.4267	90	0.0134
913-09			0.32100	0.4267	90	0.0134
913-10			0.32100	0.4267	90	0.0134
913-11			0.59000	0.4267	90	0.7370
914	Sngljun	IHX secondary side outlet	--	--	--	--
915	Tmdpvol	Secondary side Na injection	0.5	1.0	-90	--
BOTTOM AND TOP PART OF TANK						
502	Branch	Stagnant zone	0.61	36.98	90	--
505	Branch	Top part of EBR-II	0.888	49.31	90	--

Tab. 15 – EBR-II SHRT-17, RELAP5-3D©: coolant system.

RELAP5-3D Component	RELAP 5-3D Component Type	EBR-II Region	N° of r coordinates					N° of θ coordinates	N° of z coordinates
001	Multid	Reactor	5					12	17
RELAP5-3D Component	**RELAP Component Type**	**EBR-II Region**	**Radius (m)**					**(°)**	**Length (m)**
001-01	Multid	Lower Plenum	0.1348	0.2767	0.4242	0.8635	1.797	30	0.4873
001-02		Lower Plenum	0.1348	0.2767	0.4242	0.8635	1.797	30	0.4403
001-03			0.1348	0.2767	0.4242	0.8635	1.797	30	0.2772
001-04			0.1348	0.2767	0.4242	0.8635	1.797	30	0.1844
001-05		Lower Shield	0.1348	0.2767	0.4242	0.8635	1.797	30	0.0912
001-06		BAF	0.1348	0.2767	0.4242	0.8635	1.797	30	0.0706
001-07		Active Core	0.1348	0.2767	0.4242	0.8635	1.797	30	0.0685
001-08		Active Core	0.1348	0.2767	0.4242	0.8635	1.797	30	0.0685
001-09		Active Core	0.1348	0.2767	0.4242	0.8635	1.797	30	0.0685
001-10		Active Core	0.1348	0.2767	0.4242	0.8635	1.797	30	0.0685
001-11		Gas plenum	0.1348	0.2767	0.4242	0.8635	1.797	30	0.0685
001-12		Gas plenum	0.1348	0.2767	0.4242	0.8635	1.797	30	0.1244
001-13		FA region1	0.1348	0.2767	0.4242	0.8635	1.797	30	0.1244
001-14		FA region2	0.1348	0.2767	0.4242	0.8635	1.797	30	0.1840
001-15		FA region3	0.1348	0.2767	0.4242	0.8635	1.797	30	0.2710
001-16		Upper Plenum	0.1348	0.2767	0.4242	0.8635	1.797	30	0.3038
001-17		Top of UP	0.1348	0.2767	0.4242	0.8635	1.797	30	0.3038

Tab. 16 – EBR-II SHRT-17, RELAP5-3D©: reactor core

PARAMETER	UNIT	RATED CONDITION	RELAP5-3D
Speed	[rad/s]	91.10	91.10
Head	[kPa]	358.530	328.5
Flow	[kg/s]	250.2	251.40 / 251.34
Torque	[Nm]	1300.0	1204.1

Tab. 17 – EBR-II SHRT-17, RELAP5-3D©: pump parameter.

Octant	Indipendent Variable	Head	Torque
HAN	v/alpha	h/alpha^2	beta/alpha^2
1	0.000	1.174	0.000
	0.222	1.177	0.233
	0.444	1.155	0.458
	0.667	1.110	0.660
	0.778	1.079	0.748
	0.889	1.042	0.826
	1	1	0.891

Octant	Indipendent Variable	Head	Torque
HVN	alpha/v	h/v^2	beta/v^2
2	0.900	0.747	0.740
	0.600	0.205	0.305
	0.514	-0.254	-0.441
	0.450	-0.324	-0.643
	0.400	-0.371	-0.828
	0.345	-0.415	-1.071

Octant	Indipendent Variable	Head	Torque
HAD	v/alpha	h/alpha^2	beta/alpha^2
3	-0.694	1.248	-0.618
	-0.624	1.229	-0.684
	-0.416	1.189	-0.441
	-0.299	1.175	-0.251
	-0.124	1.168	-0.104

Octant	Indipendent Variable	Head	Torque
HVD	alpha/v	h/v^2	beta/v^2
4	-0.72	0.82099186	-0.508444
	-0.80064	0.96125188	-0.428279

Octant	Indipendent Variable	Head	Torque
HAT	v/alpha	h/alpha^2	beta/alpha^2
5	0.499	1.332	0.593
	8.519E-16	1.174	8.919E-16

Octant	Indipendent Variable	Head	Torque
HVT	alpha/v	h/v^2	beta/v^2
6	0.360	0.231	0.573
	0.400	0.315	0.702
	0.600	0.6130	0.911
	0.834	1.081	1.156

Octant	Indipendent Variable	Head	Torque
HAR	v/alpha	h/alpha^2	beta/alpha^2
7	-0.499	0.947	-0.421
	-0.799	0.653	-0.465

Octant	Indipendent Variable	Head	Torque
HVR	alpha/v	h/v^2	beta/v^2
8	-0.900	0.188	-0.187
	-0.450	-0.441	0.874
	-0.300	-0.535	1.592
	-0.257	-0.550	1.910
	-0.225	-0.558	2.212
	-0.200	-0.561	2.504
	-0.172	-0.562	2.905

Tab. 18 – EBR-II SHRT-17, RELAP5-3D©: pump model, single phase homologous curves

RELAP5-3D Component	RELAP5-3D Component Type	EBR-II Region	Length (m)	Area (m^2)	Vertical Angle (°)	Hydraulic Diameter (m)
101-01	Pipe	Lower adaptor	0.1888	0.0011160	90	0.037694
101-02			0.2515	0.0011160	90	0.037694
101-03		Lower shield	0.2772	0.0010235	90	0.036099
101-04			0.1844	0.0011771	90	0.014093
101-05			0.0912	0.0010241	90	0.036110
101-06		Bottom of pin	0.0706	0.0023253	90	0.056000
101-07		Active core	0.0685	0.0012286	90	0.002711
101-08			0.0685	0.0012286	90	0.002711
101-09			0.0685	0.0012286	90	0.002711
101-10			0.0685	0.0012286	90	0.002711
101-11			0.0685	0.0012286	90	0.002711
101-12		Top of pin	0.1244	0.0012286	90	0.002711
101-13			0.1244	0.0012286	90	0.002711
101-14		Upper shield	0.1840	0.0010235	90	0.036099
101-15			0.2710	0.0015790	90	0.024922

Tab. 19 – EBR-II SHRT-17, RELAP5-3D©: Driver assembly

RELAP5-3D Component	RELAP5-3D Component Type	EBR-II Region	Length (m)	Area (m^2)	Vertical Angle (°)	Hydraulic Diameter (m)
107-01	Pipe	Lower adaptor	0.1888	0.0017168	90	0.047625
107-02			0.2515	0.0004200	90	0.023125
107-03		Lower shield	0.2772	0.0010410	90	0.036407
107-04			0.1844	0.0004900	90	0.024978
107-05			0.0912	0.0010410	90	0.036407
107-06		Bottom of pin	0.0706	0.0010410	90	0.036407
107-07		Active core	0.0685	0.0008591	90	0.002759
107-08			0.0685	0.0008591	90	0.002759
107-09			0.0685	0.0008591	90	0.002759
107-10			0.0685	0.0008591	90	0.002759
107-11			0.0685	0.0008591	90	0.002759
107-12		Top of pin	0.1244	0.0008591	90	0.002759
107-13			0.1244	0.0008591	90	0.002759
107-14		Upper shield	0.1840	0.0010410	90	0.036407
107-15			0.2710	0.0008478	90	0.032855

Tab. 20 – EBR-II SHRT-17, RELAP5-3D©: Safety Rod assembly

RELAP5-3D Component	RELAP5-3D Component Type	EBR-II Region	Length (m)	Area (m^2)	Vertical Angle (°)	Hydraulic Diameter (m)
137-01	Pipe	Lower adaptor	0.1888	0.0016618	90	0.045510
137-02			0.2515	0.0005282	90	0.009900
137-03		Lower shield	0.2772	0.0003201	90	0.020188
137-04			0.1844	0.0008591	90	0.033073
137-05			0.0912	0.0008591	90	0.033073
137-06		Bottom of pin	0.0706	0.0008591	90	0.033073
137-07		Active Core	0.0685	0.0008591	90	0.033073
137-08			0.0685	0.0008591	90	0.033073
137-09			0.0685	0.0008591	90	0.033073
137-10			0.0685	0.0008591	90	0.033073
137-11			0.0685	0.0008591	90	0.002759
137-12		Top of pin	0.1244	0.0004757	90	0.003611
137-13			0.1244	0.0004757	90	0.003611
137-14		Poison pin	0.1840	0.0004757	90	0.003611
137-15			0.2710	0.0004757	90	0.003611

Tab. 21 – EBR-II SHRT-17, RELAP5-3D©: Control Rod assembly

RELAP5-3D Component	RELAP5-3D Component Type	EBR-II Region	Length (m)	Area (m^2)	Vertical Angle (°)	Hydraulic Diameter (m)
139-01	Pipe	Lower adaptor	0.1888	0.0011159	90	0.037694
139-02			0.2515	0.0011159	90	0.037694
139-03		SS Rod	0.2772	0.0019068	90	0.048986
139-04			0.1844	0.0018225	90	0.015493
139-05			0.0912	0.0018225	90	0.015493
139-06			0.0706	0.0018225	90	0.015493
139-07			0.0685	0.0018225	90	0.015493
139-08			0.0685	0.0018225	90	0.015493
139-09			0.0685	0.0018225	90	0.015493
139-10			0.0685	0.0018225	90	0.015493
139-11			0.0685	0.0018225	90	0.015493
139-12			0.1244	0.0018225	90	0.015493
139-13			0.1244	0.0018225	90	0.015493
139-14			0.1840	0.0018225	90	0.015493
139-15			0.2710	0.0018225	90	0.015493

Tab. 22 – EBR-II SHRT-17, RELAP5-3D©: Core Steel assembly

RELAP5-3D Component	RELAP5-3D Component Type	EBR-II Region	Length (m)	Area (m^2)	Vertical Angle (°)	Hydraulic Diameter (m)
145-01	Pipe	Lower adaptor	0.1888	0.0022840	90	0.053920
145-02			0.2515	0.0001979	90	0.015875
145-03		Lower shield	0.2772	0.0001979	90	0.015875
145-04			0.1844	0.0001740	90	0.002593
145-05			0.0912	0.0001740	90	0.002593
145-06		Bottom of pin	0.0706	0.0015941	90	0.014092
145-07		Active core	0.0685	0.0006845	90	0.002759
145-08			0.0685	0.0006845	90	0.002759
145-09			0.0685	0.0006845	90	0.002759
145-10			0.0685	0.0006845	90	0.002759
145-11			0.0685	0.0006845	90	0.002759
145-12		Top of pin	0.1244	0.0006845	90	0.002759
145-13			0.1244	0.0006845	90	0.002759
145-14		Upper shield	0.1840	0.0018645	90	0.046400
145-15			0.2710	0.0018645	90	0.046400

Tab. 23 – EBR-II SHRT-17, RELAP5-3D©: XX10 assembly

RELAP5-3D Component	RELAP5-3D Component Type	EBR-II Region	Length (m)	Area (m^2)	Vertical Angle (°)	Hydraulic Diameter (m)
151-01	Pipe	Lower adaptor	0.1888	0.0022840	90	0.053920
151-02			0.2515	0.0001979	90	0.026611
151-03		Lower shield	0.2772	0.0001979	90	0.030315
151-04			0.1844	0.0001740	90	0.014093
151-05			0.0912	0.0001740	90	0.014770
151-06		Bottom of pin	0.0706	0.0015941	90	0.002711
151-07		Active core	0.0685	0.0008591	90	0.002711
151-08			0.0685	0.0008591	90	0.002711
151-09			0.0685	0.0008591	90	0.002711
151-10			0.0685	0.0008591	90	0.002711
151-11			0.0685	0.0008591	90	0.002711
151-12		Top of pin	0.1244	0.0008591	90	0.002711
151-13			0.1244	0.0008591	90	0.002711
151-14		Upper shield	0.1840	0.0018645	90	0.030315
151-15			0.2710	0.0018645	90	0.014044

Tab. 24 – EBR-II SHRT-17, RELAP5-3D©: XX09 assembly

RELAP5-3D Component	RELAP5-3D Component Type	EBR-II Region	Length (m)	Area (m^2)	Vertical Angle (°)	Hydraulic Diameter (m)
162-01	Pipe	Lower adaptor	0.1888	0.0006370	90	0.028478
162-02			0.2515	0.0006370	90	0.028478
162-03		Lower shield	0.2772	0.0010235	90	0.036099
162-04			0.1844	0.0011771	90	0.014093
162-05			0.0912	0.0010241	90	0.036110
162-06		Bottom of pin	0.0706	0.0023253	90	0.056000
162-07		Active core	0.0685	0.0012286	90	0.002711
162-08			0.0685	0.0012286	90	0.002711
162-09			0.0685	0.0012286	90	0.002711
162-10			0.0685	0.0012286	90	0.002711
162-11			0.0685	0.0012286	90	0.002711
162-12		Top of pin	0.1244	0.0012286	90	0.002711
162-13			0.1244	0.0012286	90	0.002711
162-14		Upper shield	0.1840	0.0010235	90	0.036099
162-15			0.2710	0.0015790	90	0.024922

Tab. 25 – EBR-II SHRT-17, RELAP5-3D©: High Flow Driver assembly

RELAP5-3D Component	RELAP5-3D Component Type	EBR-II Region	Length (m)	Area (m^2)	Vertical Angle (°)	Hydraulic Diameter (m)
166-01	Pipe	Lower adaptor	0.1888	0.0006413	90	0.0285750
166-02			0.2515	0.0000273	90	0.0285750
166-03		Reflector Block	0.2772	0.0004663	90	0.0046296
166-04			0.1844	0.0004663	90	0.0046296
166-05			0.0912	0.0004663	90	0.0046296
166-06			0.0706	0.0004663	90	0.0046296
166-07			0.0685	0.0004663	90	0.0046296
166-08			0.0685	0.0004663	90	0.0046296
166-09			0.0685	0.0004663	90	0.0046296
166-10			0.0685	0.0004663	90	0.0046296
166-11			0.0685	0.0004663	90	0.0046296
166-12			0.1244	0.0004663	90	0.0046296
166-13			0.1244	0.0004663	90	0.0046296
166-14			0.1840	0.0004663	90	0.0046296
166-15			0.2710	0.0004663	90	0.0046296

Tab. 26 – EBR-II SHRT-17, RELAP5-3D©: Inner Reflector assembly

RELAP5-3D Component	RELAP5-3D Component Type	EBR-II Region	Length (m)	Area (m^2)	Vertical Angle (°)	Hydraulic Diameter (m)
228-01	Pipe	Lower adaptor	0.1888	0.0039143	90	0.0182280
228-02			0.2515	0.0039143	90	0.0209152
228-03		Reflector Block	0.2772	0.0069938	90	0.0053866
228-04			0.1844	0.0069938	90	0.0053866
228-05			0.0912	0.0069938	90	0.0053866
228-06			0.0706	0.0069938	90	0.0053866
228-07			0.0685	0.0069938	90	0.0053866
228-08			0.0685	0.0069938	90	0.0053866
228-09			0.0685	0.0069938	90	0.0053866
228-10			0.0685	0.0069938	90	0.0053866
228-11			0.0685	0.0069938	90	0.0053866
228-12			0.1244	0.0069938	90	0.0053866
228-13			0.1244	0.0069938	90	0.0053866
228-14			0.1840	0.0069938	90	0.0053866
228-15			0.2710	0.0069938	90	0.0053866

Tab. 27 – EBR-II SHRT-17, RELAP5-3D©: Outer Reflector assembly

RELAP5-3D Component	RELAP5-3D Component Type	EBR-II Region	Length (m)	Area (m^2)	Vertical Angle (°)	Hydraulic Diameter (m)
240-01	Pipe	Lower adaptor	0.1888	0.00717	90	0.0182280
240-02			0.2515	0.00717	90	0.0182280
240-03		Blanket	0.2772	0.07165	90	0.0110658
240-04			0.1844	0.07165	90	0.0110658
240-05			0.0912	0.07165	90	0.0110658
240-06			0.0706	0.07165	90	0.0110658
240-07			0.0685	0.07165	90	0.0110658
240-08			0.0685	0.07165	90	0.0110658
240-09			0.0685	0.07165	90	0.0110658
240-10			0.0685	0.07165	90	0.0110658
240-11			0.0685	0.07165	90	0.0110658
240-12			0.1244	0.07165	90	0.0110658
240-13			0.1244	0.07165	90	0.0110658
240-14			0.1840	0.07165	90	0.0110658
240-15			0.2710	0.07165	90	0.0110658

Tab. 28 – EBR-II SHRT-17, RELAP5-3D©: Blanket assembly

STRUCTURE	NAME	NUMBER	TYPE	VOLUME
SUBASSEMBLY RING-1				
PARTIAL DRIVER MARKII-AI - [1]	fu1	100	pipe	15
DRIVER MARK II AI - [2,A1]	fu2a1	101	pipe	15
X406 MARK II A - [2,B1]	fu2b1	102	pipe	15
DRIVER MARK II AI - [2,C1]	fu2c1	103	pipe	15
DRIVER MARK II AI - [2,D1]	fu2d1	104	pipe	15
DRIVER MARK II AI - [2,E1]	fu2e1	105	pipe	15
X407 MARK II A - [2,F1]	fu2f1	106	pipe	15
CS1	cs3a1	107	pipe	15
DRIVER MARK-II A1 - [3,A2]	fu3a2	108	pipe	15
DRIVER MARK II AI - [3,B1]	fu3b1	109	pipe	15
DRIVER MARK II AI - [3,B2]	fu3b2	110	pipe	15
DRIVER MARK II AI - [3,C1]	fu3c1	111	pipe	15
DRIVER MARK II AI - [3,C2]	fu3c2	112	pipe	15
CS2 - [3,D1]	cs3d1	113	pipe	15
DRIVER MARK II AI - [3,D2]	fu3d2	114	pipe	15
DRIVER MARK II AI - [3,E1]	fu3e1	115	pipe	15
DRIVER MARK II AI - [3,E2]	fu3e2	116	pipe	15
DRIVER MARK II AI - [3,F1]	fu3f1	117	pipe	15
DRIVER MARK II AI - [3,F2]	fu3e2	118	pipe	15
SUBASSEMBLY RING-2				
DRIVER MARK II AI - [4,A1]	fu4a1	119	pipe	15
X393 MARK II S - [4,A2]	fu4a2	120	pipe	15
DRIVER MARK II AI - [4,A3]	fu4a3	121	pipe	15
X408 MARK II A - [4,B1]	fu4b1	122	pipe	15
X390 MARK II AI - [4,B2]	fu4b2	123	pipe	15
DRIVER MARK II AI - [4,B3]	fu4b3	124	pipe	15
X409 MARK II A - [4,C1]	fu4c1	125	pipe	15
DRIVER MARK II AI - [4,C2]	fu4c2	126	pipe	15
DRIVER MARK II AI - [4,C3]	fu4c3	127	pipe	15
DRIVER MARK II AI - [4,D1]	fu4d1	128	pipe	15
DRIVER MARK II AI - [4,D2]	fu4d2	129	pipe	15
DRIVER MARK II AI - [4,D3]	fu4d3	130	pipe	15
DRIVER MARK II AI - [4,E1]	fu4e1	131	pipe	15
DRIVER MARK II AI - [4,E2]	fu4e2	132	pipe	15
DRIVER MARK II AI - [4,E3]	fu4e3	133	pipe	15

STRUCTURE	NAME	NUMBER	TYPE	VOLUME
DRIVER MARK II AI - [4,F1]	fu4f1	134	pipe	15
PARTIAL DRIVER MARKII-AI - [4,F2]	fu4f2	135	pipe	15
X400 MARK II A - [4,F3]	fu4f3	136	pipe	15
CR3 - [5,A1]	fu5a1	137	pipe	15
PARTIAL DRIVER MARKII-AI - [5,A2]	fu5a2	138	pipe	15
CORE STEEL - [5,A3]	fu5a3	139	pipe	15
X399 MARK II A - [5,A4]	fu5a4	140	pipe	15
CR1 - [5,B1]	fu5b1	141	pipe	15
CORE STEEL - [5,B2]	fu5b2	142	pipe	15
CR2 - [5,B3]	fu5b3	143	pipe	15
PARTIAL DRIVER MARKII-AI - [5,B4]	fu5b4	144	pipe	15
XX09 - [5,C1]	fu5c1	145	pipe	15
DRIVER MARK II AI - [5,C2]	fu5c2	146	pipe	15
CR4 - [5,C3]	fu5c3	147	pipe	15
CORE STEEL - [5,C4]	fu5c4	148	pipe	15
CR5 - [5,D1]	fu5d1	149	pipe	15
PARTIAL DRIVER MARKII-AI - [5,D2]	fu5d2	150	pipe	15
XX10 - [5,D3]	fu5d3	151	pipe	15
CORE STEEL - [5,D4]	fu5d4	152	pipe	15
CR6 - [5,E1]	fu5e1	153	pipe	15
CORE STEEL - [5,E2]	fu5e2	154	pipe	15
CR7 - [5,E3]	fu5e3	155	pipe	15
CORE STEEL - [5,E4]	fu5e4	156	pipe	15
CR8 - [5,F1]	fu5f1	157	pipe	15
DRIVER MARK II AI - [5,F2]	fu5f2	158	pipe	15
XY-16 [5,F3]	fu5f3	159	pipe	15
DRIVER MARK II AI - [5,F4]	fu5f4	160	pipe	15
SUBASSEMBLY RING-3				
X401 MARK II A - [6,A1]	fu6a1	161	pipe	15
HF DRIVER MARK II AI - [6,A2]	fu6a2	162	pipe	15
HF DRIVER MARK II AI - [6,A3]	fu6a3	163	pipe	15
HF DRIVER MARK II AI - [6,A4]	fu6a4	164	pipe	15
HF DRIVER MARK II AI - [6,A5]	fu6a5	165	pipe	15
INNER REFLECTOR - [6,B1]	fu6b1	166	pipe	15
PARTIAL DRIVER MARKII-AI - [6,B2]	fu6b2	167	pipe	15
HF DRIVER MARK II AI - [6,B3]	fu6b3	168	pipe	15
HF DRIVER MARK II AI - [6,B4]	fu6b4	169	pipe	15
HF DRIVER MARK II AI - [6,B5]	fu6b5	170	pipe	15
DRIVER MARK II AI - [6,C1]	fu6c1	171	pipe	15
HF DRIVER MARK II AI - [6,C2]	fu6c2	172	pipe	15
PARTIAL DRIVER MARKII-AI - [6,C3]	fu6c3	173	pipe	15
HF DRIVER MARK II AI - [6,C4]	fu6c4	174	pipe	15
HF DRIVER MARK II AI - [6,C5]	fu6c5	175	pipe	15
INNER REFLECTOR - [6,D1]	fu6d1	176	pipe	15
HF DRIVER MARK II AI - [6,D2]	fu6d2	177	pipe	15
HF DRIVER MARK II AI - [6,D3]	fu6d3	178	pipe	15
X402 MARK II A - [6,D4]	fu6d4	179	pipe	15
HF DRIVER MARK II AI - [6,D5]	fu6d5	180	pipe	15
DRIVER MARK II AI - [6,E1]	fu6e1	181	pipe	15
HF DRIVER MARK II AI - [6,E2]	fu6e2	182	pipe	15
PARTIAL DRIVER MARKII-AI - [6,E3]	fu6e3	183	pipe	15
HF DRIVER MARK II AI - [6,E4]	fu6e4	184	pipe	15
HF DRIVER MARK II AI - [6,E5]	fu6e5	185	pipe	15
DRIVER MARK II AI - [6,F1]	fu6f1	186	pipe	15
PARTIAL DRIVER MARKII-AI - [6,F2]	fu6f2	187	pipe	15
HF DRIVER MARK II AI - [6,F3]	fu6f3	188	pipe	15
PARTIAL DRIVER MARKII-AI - [6,F4]	fu6f4	189	pipe	15
HF DRIVER MARK II AI - [6,F5]	fu6f5	190	pipe	15

STRUCTURE	NAME	NUMBER	TYPE	VOLUME
INNER REFLECTOR - [7,A1]	fu7a1	191	pipe	15
INNER REFLECTOR - [7,A2]	fu7a2	192	pipe	15
INNER REFLECTOR - [7,A3]	fu7a3	193	pipe	15
INNER REFLECTOR - [7,A4]	fu7a4	194	pipe	15
INNER REFLECTOR - [7,A5]	fu7a5	195	pipe	15
INNER REFLECTOR - [7,A6]	fu7a6	196	pipe	15
X328 - [7,B1]	fu7b1	197	pipe	15
INNER REFLECTOR - [7,B2]	fu7b2	198	pipe	15
INNER REFLECTOR - [7,B3]	fu7b3	199	pipe	15
INNER REFLECTOR - [7,B4]	fu7b4	200	pipe	15
INNER REFLECTOR - [7,B5]	fu7b5	201	pipe	15
INNER REFLECTOR - [7,B6]	fu7b6	202	pipe	15
INNER REFLECTOR - [7,C1]	fu7c1	203	pipe	15
INNER REFLECTOR - [7,C2]	fu7c2	204	pipe	15
INNER REFLECTOR - [7,C3]	fu7c3	205	pipe	15
INNER REFLECTOR - [7,C4]	fu7c4	206	pipe	15
INNER REFLECTOR - [7,C5]	fu7c5	207	pipe	15
INNER REFLECTOR - [7,C6]	fu7c6	208	pipe	15
INNER REFLECTOR - [7,D1]	fu7d1	209	pipe	15
INNER REFLECTOR - [7,D2]	fu7d2	210	pipe	15
INNER REFLECTOR - [7,D3]	fu7d3	211	pipe	15
INNER REFLECTOR - [7,D4]	fu7d4	212	pipe	15
INNER REFLECTOR - [7,D5]	fu7d5	213	pipe	15
INNER REFLECTOR - [7,D6]	fu7d6	214	pipe	15
INNER REFLECTOR - [7,E1]	fu7e1	215	pipe	15
INNER REFLECTOR - [7,E2]	fu7e2	216	pipe	15
INNER REFLECTOR - [7,E3]	fu7e3	217	pipe	15
INNER REFLECTOR - [7,E4]	fu7e4	218	pipe	15
INNER REFLECTOR - [7,E5]	fu7e5	219	pipe	15
X320 UNKNOWN FA [7,E6]	fu7e6	220	pipe	15
INNER REFLECTOR - [7,F1]	fu7f1	221	pipe	15
X319 UNKNOWN FA [7,F2]	fu7f3	222	pipe	15
INNER REFLECTOR - [7,F3]	fu7f3	223	pipe	15
INNER REFLECTOR - [7,F4]	fu7f4	224	pipe	15
INNER REFLECTOR - [7,F5]	fu7f5	225	pipe	15
INNER REFLECTOR - [7,F6]	fu7f6	226	pipe	15
SUBASSEMBLY RING-4				
OUTER REFLECTOR	outref1	228	pipe	15
OUTER REFLECTOR	outref2	229	pipe	15
OUTER REFLECTOR	outref3	230	pipe	15
OUTER REFLECTOR	outref4	231	pipe	15
OUTER REFLECTOR	outref5	232	pipe	15
OUTER REFLECTOR	outref6	233	pipe	15
OUTER REFLECTOR	outref7	234	pipe	15
OUTER REFLECTOR	outref8	235	pipe	15
OUTER REFLECTOR	outref9	236	pipe	15
OUTER REFLECTOR	outref10	237	pipe	15
OUTER REFLECTOR	outref11	238	pipe	15
OUTER REFLECTOR	outref12	239	pipe	15
BLANKET	ublat1	240	pipe	15
BLANKET	ublat2	241	pipe	15
BLANKET	ublat3	242	pipe	15
BLANKET	ublat4	243	pipe	15
BLANKET	ublat5	244	pipe	15
BLANKET	ublat6	245	pipe	15
BLANKET	ublat7	246	pipe	15
BLANKET	ublat8	247	pipe	15
BLANKET	ublat9	248	pipe	15

STRUCTURE	NAME	NUMBER	TYPE	VOLUME
BLANKET	ublat10	249	pipe	15
BLANKET	ublat11	250	pipe	15
BLANKET	ublat12	251	pipe	15

Tab. 29 – EBR-II SHRT-17, RELAP5-3D©: correspondence between core assemblies and code nodalization

Component	Left boundary condition	Right boundary condition	Vol.	Vol. insulation	Inner surface area	Outer surface area	Inner convection boundary type	Outer convection boundary type
Reactor shielding	Reactor Vessel	Pool	56	--	4.68	20.3	Default	Default
Lower plate	Pool	Reactor Vessel	0.40	--	4.32	4.32	Default	Default
Lower grid plate	Reactor Vessel	Reactor Vessel	0.27	--	2.72	2.72	Default	Default
Upper grid plate	Reactor Vessel	Reactor Vessel	0.28	--	2.77	2.77	Default	Default
Coolant baffle plates (vertical)	Reactor Vessel	Reactor Vessel	0.02	--	0.1	0.1	Default	Default
High pressure flow line	High pressure flow line	Pool	0.19	--	0.14	0.16	Default	Default
Low pressure flow line	Low pressure flow line	Pool	0.67	--	0.04	0.05	Default	Default
Z-Pipe	Z-pipe	Pool	3.94	0.6	0.18	0.32	Default	Default
EBR-II main vessel	Pool	--	4.98	--	0.62	--	Default	--
MCP	Pool	Pool	0.74	--	0.61	0.74	Default	Default
IHX casing	Z-Pipe	Pool	7.0	0.62	2.6	2.8	Default	Default
IHX lower plenum	IHX secondary central tube	Pool	4.0	0.5	2.6	2.8	Default	Default
IHX ascending tubes	Z-Pipe	IHX secondary ascending tubes	0.001	--	2.8E-04	3.9E-04	Default	Default
IHX central tube	Z-Pipe	IHX secondary side central tube	0.47	--	0.15	0.16	Default	Default

Tab. 30 – EBR-II SHRT-17, RELAP5-3D©: main heat structures geometrical and modeling features.

4.4 Nodalization and code models verifications

The independent validation activities for non-aqueous working fluids are very limited, therefore, a preliminary evaluation has been carried out to determine the applicability of the code in predicting selected phenomena, which are relevant for the simulation. In view of this, the code performances have been checked and compared with models and correlations available in open literature. These tests are:

- The evaluation of the pressure drops in the wire wrapped fuel assembly as function of Reynolds number, calculated for the Mark-IIAI FA in the range of mass flow rates of interest.
- The verification of the heat transfer performance of the FA at different power levels (uniform linear power is imposed), considering the fuel assembly with the maximum mass flow rate.

4.4.1 Pressure Drops Analyses

The evaluation of the pressure drops in the wire-wrapped fuel bundle consisted in the comparison of the RELAP5-3D© results with correlations presents in literature: the Novendstern, Rehme and Cheng&Todreas correlations [9][10][11].

The Darcy-Weisbach friction factor is computed in RELAP5-3D© [23] from correlations for laminar and turbulent flows with interpolation in the transition regime. There are two turbulent flow friction factor models. The first model computes the turbulent friction factor using an engineering approximation to the Colebrook-White correlation [12][13], while the second model uses an exponential function with users' input coefficients.
The laminar friction factor model is based on the exact solution for fully developed flow and constant fluid properties

$$f_L = \frac{64}{Re\Phi} \quad for\ 0 \le Re \le 2200$$

Where Re is the Reynolds number and Φ is a shape factor that allows the user to account for geometries other than a circular tube.
The turbulent friction factor is calculated using the Zigrang-Sylvester approximation [14] to the Colebrook-White correlation [13].

$$\frac{1}{\sqrt{f_T}} = -2\log_{10}\left\{\frac{\varepsilon/D}{3.7} + \frac{2.51}{Re}\left[1.14 - 2\log_{10}\left(\frac{\varepsilon}{D} + \frac{21.25}{Re^{0.9}}\right)\right]\right\} \quad for\ 3000 < Re$$

Where ε is the surface roughness, and the *D* is the hydraulic diameter
The friction factor in the transition region between laminar and turbulent flow is computed by reciprocal interpolation as

$$f_{L,T} = \left(3.75 - \frac{8250}{Re}\right)\left(f_{T,3000} - f_{L,2200}\right) + f_{L,2200} \quad for\ 2200 < Re < 3000$$

Where $f_{L,2200}$ is the laminar factor at a Reynolds number of 2200, $f_{T,3000}$ is the turbulent friction factor at a Reynolds number of 3000.

The Zigrang-Sylvester equation has the advantage that is an explicit relation for the friction factor, while the Colebrook-White correlation is a transcendental function requiring iteration for the determination of the friction factor [6][8].

Novendstern [8][9] has developed a semi-empirical model that can accurately predict pressure losses in an hexagonal array of fuel pins utilizing a wire-wrap spacer system.
The range of applicability for the correlation is for bundle with rod pitch to diameter ratio from 1.06 to 1.42, wire pitch to diameter ratio from 8 to 96, number of rods from 19 to 217, rod diameter from 4.98 to 11.99 mm. The correlation is applicable for Reynolds number from 2600 to 200000.
The model developed to predict pressure loses in a wire-wrapped fuel assembly determines the flow distribution between the fuel pins theoretically, and multiplies the pressure drop for a smooth pipe, using equivalent diameter techniques, by an empirical correction factor. The empirical correction depends on fuel pin bundle dimensions and flow rate.

The velocity, V_1, in a central subchannel, formed by three rods in a triangular array, is determined from assembly dimensions and average fluid velocity, V_T , according to

$$V_1 = XV_T$$

The flow distribution factor, X, is calculated from central, side and corner subchannels, numbered 1 through 3

$$X = \frac{A_T}{N_1A_1 + N_2A_2\left(\frac{D_{e_2}}{D_{e_1}}\right)^{0.714} + N_3A_3\left(\frac{D_{e_3}}{D_{e_1}}\right)^{0.714}}$$

Flow areas, A, and equivalent diameters, D_e, are calculated including the wire wrap spacer geometry. The wire wrap is “smeard” uniformly in all subchannels.
Using the flow conditions for the central subchannel, the pressure drop is determined by:

$$\Delta P = Mf_{smooth}\frac{L}{D_{e_1}}\frac{\rho V_1^2}{2}$$

The multiplication factor , M, is used to take into account the geometry of the bundle and the wire:

$$M = \left[\frac{1.034}{(L/d)^{0.124}} + \frac{29.7(p/d)^{6.94}Re^{0.086}}{(h_w/d)^{2.239}}\right]^{0.885}$$

Where $h_w$is the wire pitch

The friction factor for flow in a smooth pipe, f_{smooth},

$$f_{smooth} = \left\{2\log_{10}\left[-\frac{5.028}{Re}\log_{10}\left(\frac{16.76}{Re}\right)\right]\right\}^2$$

The model is able to predict pressure drop to within ±14% over a wide range of geometries in the turbulent flow regime compared to experimental results with which it has been validated.

The Rehme [10][11] correlation has been developed to provide an accurate prediction of the pressure drops in wire-spaced bundle. The range of applicability for the correlation is for bundle with pitch to diameter ratio from 1.125 to 1.417, wire pitch to diameter ratio from 6 to 45, number of rods from 7 to 61. The correlation is applicable for Reynolds number from 1000 to 300000.
The friction factor is:

$$f = \left(\frac{64}{Re}F^{0.5} + \frac{0.0816}{Re^{0.133}}F^{0.9335}\right)\frac{\pi N(d + d_w)}{P_{wet}}$$

Where *F* is the corrective factor

$$F = \sqrt{\frac{p}{d}} + \left[7.6\frac{d + d_w}{h_w}\left(\frac{p}{d}\right)^2\right]^{2.16}$$

Where *N* is the rod number, *d* is the rod diameter, d_w is the wire diameter, h_w is the axial lead (height of one revolution) of the wire wrap, P_{wet} is the wetted perimeter and p is the rod pitch.
The values obtained with the Rehme correlation show an average error of 5% compared to the measured experimental data.

The RELAP5-3D© results of dynamic pressure drops for different roughness, as function of Reynolds number, are reported in Fig. 53a). The nominal parameters refer to the assembly with the minimum mass flow rate. The figure shows that the best estimate is for a roughness value of 1.0e-6 m, which is the value imposed in the core region, differently from the other components of the model.

Fig. 53b) and c) show the RELAP5-3D© dynamic pressure drops as function of mass flow rate and as function of Re, respectively, when roughness is 1.0e-6 m. In the range of interest, which is from the minimum mass flow rate to the maximum, the results obtained are comparable with the correlations. The Novendstern correlation approximates better the RELAP5-3D© results because the MARK-IIAI geometric characteristics are included in the range of applicability of this correlation (i.e. number of rod).

As the Novendstern and Rheme correlations are applicable only in the turbulent flow regime RELAP5-3D results has been compared also with the correlation proposed by Cheng and Todreas, developed to provide a prediction of frictional pressure drop of wire-wrapped bundles. The range of applicability for the correlation is for bundle with rod pitch to diameter ratio from 1.025 to 1.42, wire pitch to diameter ratio from 8 to 50. Empirical correlations were provided for the transitions between laminar and turbulent regimes that depended on the Reynolds number of the bundle and the pitch-to-diameter ratio of the rods. These empirical correlations are:

$Re < Re_L$ for the laminar regime where $Re_L = 10^{\left(1.7\frac{p}{d}+0.78\right)}$

$Re > Re_T$ for turbulent regime where $Re_T = 10^{\left(0.7\frac{p}{d}+3.3\right)}$

$Re_L < Re < Re_T$ for transition regime.

The correlations developed by Cheng and Todreas for the rod bundle are defined as

$$f_L = \frac{C_{fL}}{Re} \quad Re < Re_L$$

$$f_T = \frac{C_{fT}}{Re^{0.18}} \quad Re > Re_T$$

$$f = f_L(1-\varphi)^{\frac{1}{3}} + f_T\varphi^{\frac{1}{3}} \quad Re_L < Re < Re_T$$

where

$$C_{fL} = \left[-974.6 + 1612\frac{p}{d} - 598.5\left(\frac{p}{d}\right)^2\right]\left(\frac{h_w}{d+d_w}\right)^{0.06-0.085\frac{p}{d}}$$

$$C_{fT} = \left[0.8063 - 0.9022\log_{10}\left(\frac{h_w}{d+d_w}\right) + 0.3526\left[\log_{10}\left(\frac{h_w}{d+d_w}\right)\right]^2\right]\left(\frac{p}{d}\right)^{9.7}\left(\frac{h_w}{d+d_w}\right)^{1.78-2\frac{p}{d}}$$

$$\varphi = \frac{\log_{10} Re - 1.7\frac{p}{d} - 0.78}{2.2 - \frac{p}{d}}$$

Where d is the rod diameter, d_w is the wire diameter, h_w is the axial lead (height of one revolution) of the wire wrap.

Tab. 31 present the initial conditions.

4.4.2 Heat exchange test

The heat transfer analysis has been made evaluating the fuel center temperature, the cladding temperature and the coolant temperature, at different power levels (uniform linear power is imposed).

The fuel center temperature has been evaluated considering thermal expansion of the U-5 wt % Fs fuel pins during irradiation (see 0 for fuel properties). The analysis led to assume that, due to the thermal expansion of the pellet, the gap between the fuel pellet and the cladding is almost negligible.

The fuel temperature expected is less than 1283 K, that is the melting temperature of the U-5 wt % Fs fuel. It is difficult to raise the fuel temperature of metal alloy fuel because of the high thermal conductivity (30 W/mK at 800 K). Considering the small pin size (4.4 mm diameter and 34.3 cm length), a temperature rise through the reactor of ~360 K appeared achievable [5].
In Fig. 55a) the fuel centerline temperature is depicted for different gap size (nominal and 1.0e-6 m). The figure shows that, at nominal power and rated mass flow rate, the temperature is 850 K, so the temperatures raises of ~230 K.. Even in the worst case, mass flow rate decreased by 20% and power increased by 70% , the temperature raises of ~380 K. which confirms the assumptions.

As described before, the fuel elements of U-5Fs are sodium bonded. The sodium provides a very high thermal conductivity medium by which heat is easily transferred to the cladding and reactor coolant. The fuel slug is thermally bonded to the cladding using sodium [6].
Fig. 55b) and c) show the cladding temperature and the flow temperature, respectively, for different mass flow rate. The cladding temperature has been evaluated considering also different height of

the FA: at the Bottom of the Active Fuel (BAF), at the center of the active fuel and at the Top of Active Fuel (TAF).

Tab. 32 present the initial conditions.

The heat transfer from the surface of the fuel rod cladding to the liquid metal is governed by the one of the two heat transfer correlations used by RELAP5-3D© [23], depending on the geometry (non-bundle or bundle). For non-bundles the correlation [12][15][16][17] used is:

$$Nu = 5.0 + 0.025Pe^{0.8}$$

Where Pe is the Peclet number. This correlation is applicable for fully developed flow of a liquid metal in a tube with constant temperature.
For bundles, the Westinghouse correlation [12][18] used is:

$$Nu = 4.0 + 0.33\left(\frac{p}{D}\right)^{3.8}\left(\frac{Pe}{100}\right)^{0.86} + 0.16\left(\frac{p}{D}\right)^{5}$$

Where p is the rod pitch (distance between the centers of the adjacent rods) and D is the rod diameter. The correlation was developed for a range of pitch to diameter ratio from 1.1 to 1.4 and Pe from 10 to 5000. The correlation is validate for pitch to diameter ratio from 1.1 to 1.2 and under-predicts Nusselt numbers when the pitch to diameter ratio exceeded 1.2 [6][23].

INITIAL CONDITIONS	
Power	0 [MW]
Core inlet temperature	624.15 [K]
Upper plenum pressure	1.953e+05 [Pa]
Rated mass flow rate	3.6194 [kg/s]

Tab. 31 – EBR-II SHRT-17, RELAP5-3D©: Pressure drop test: initial conditions

INITIAL CONDITIONS	
Core Rated Power	57.3 [MW]
Fuel assembly rated power	892 [kW]
Core inlet temperature	624.15 [K]
Upper plenum pressure	4.658e+05 [Pa]
Rated Mass flow rate	7.70286 [kg/s]

Tab. 32 – EBR-II SHRT-17, RELAP5-3D©: Heat Exchange Test, initial conditions.

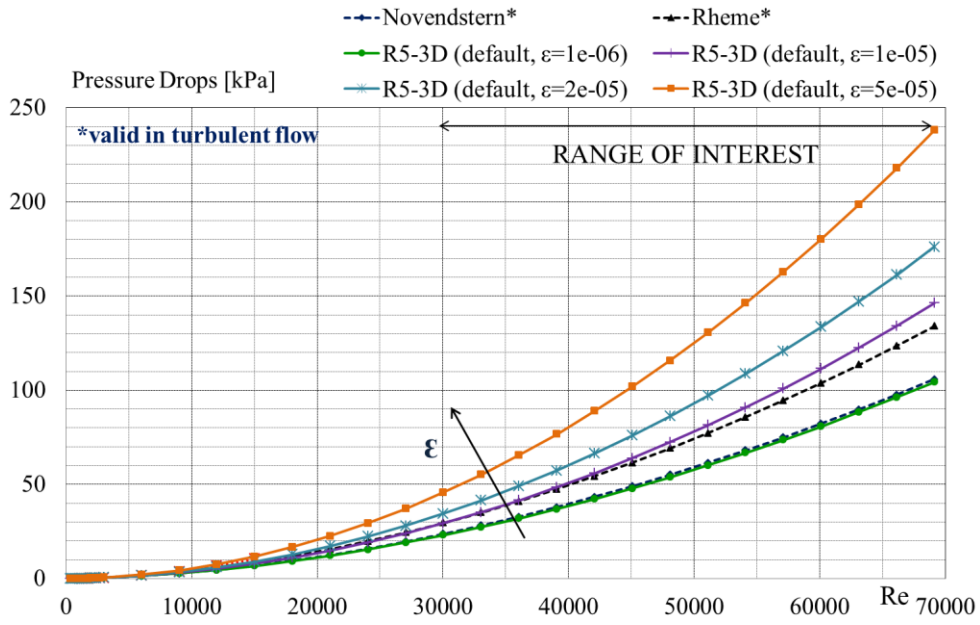

a) Dynamic pressure drops versus Re, for different roughness.

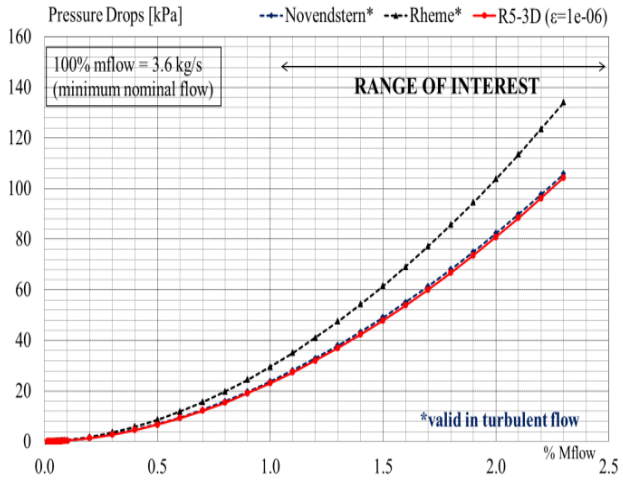

b) Dynamic pressure drops versus mass flow rate.

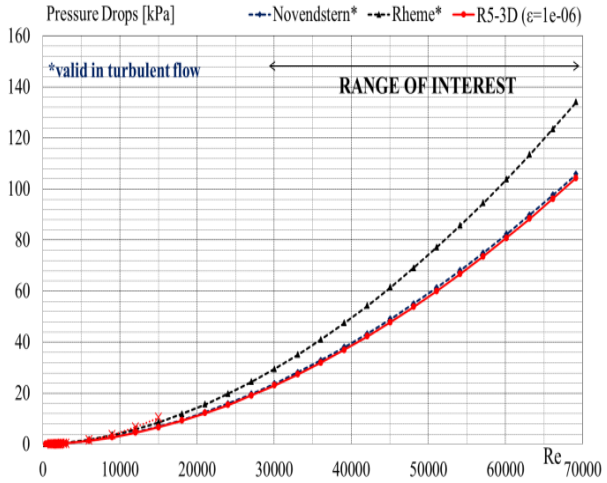

c) Dynamic pressure drops versus Re.

Fig. 53 – EBR-II SHRT-17, RELAP5-3D©: Pressure Drops Test.

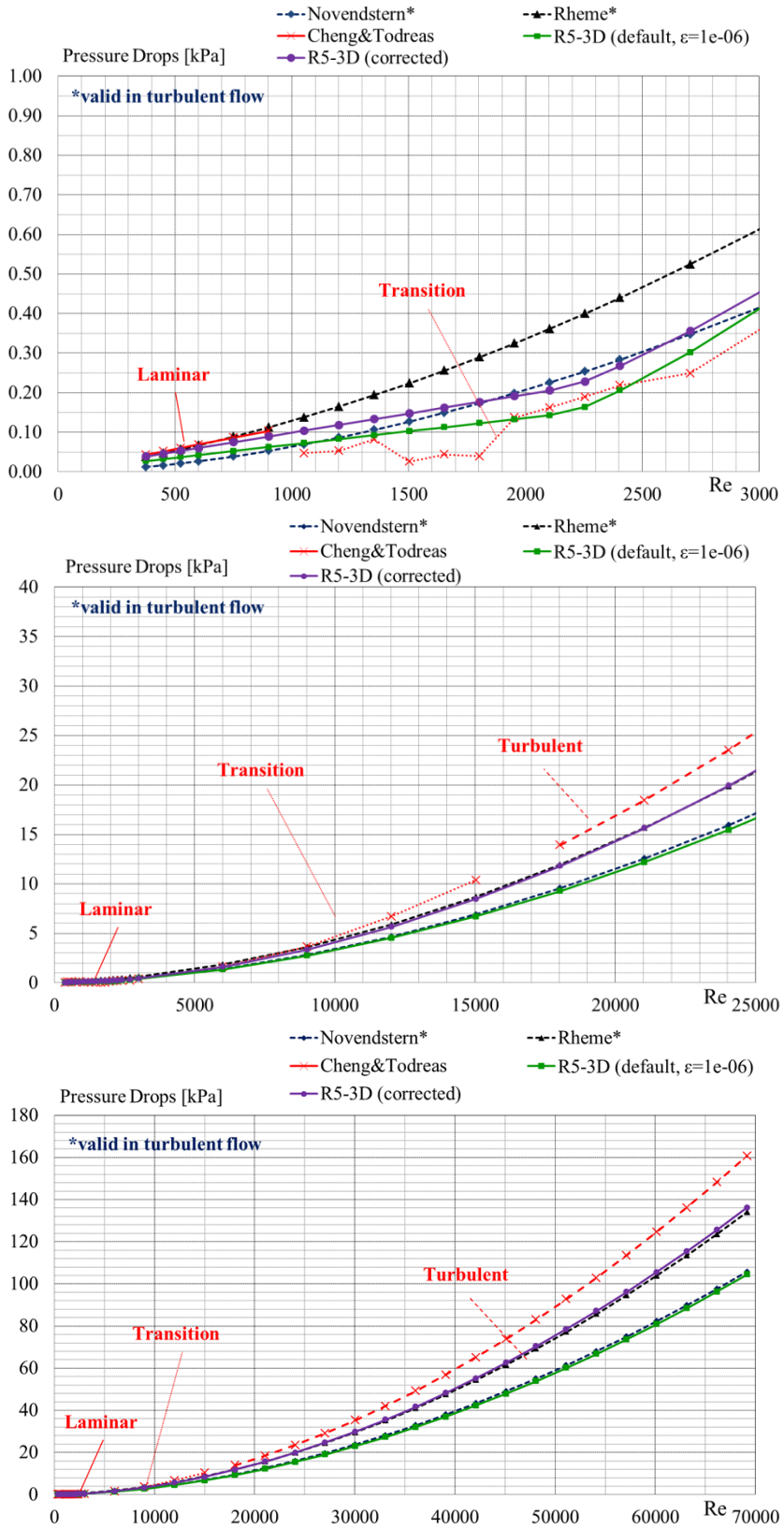

Fig. 54 – EBR-II SHRT-17, RELAP5-3D©: Pressure Drops Test.

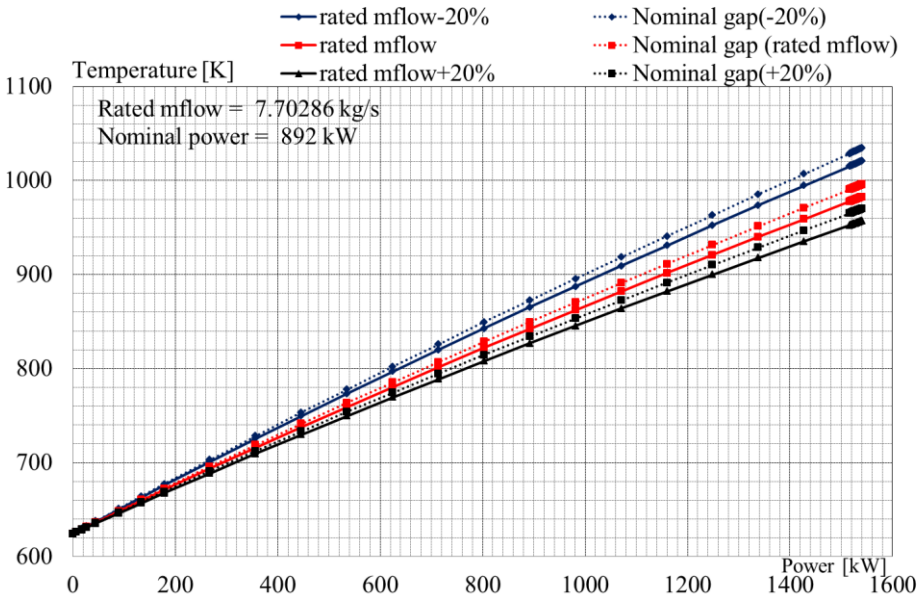

a) Fuel Centerline Temperature.

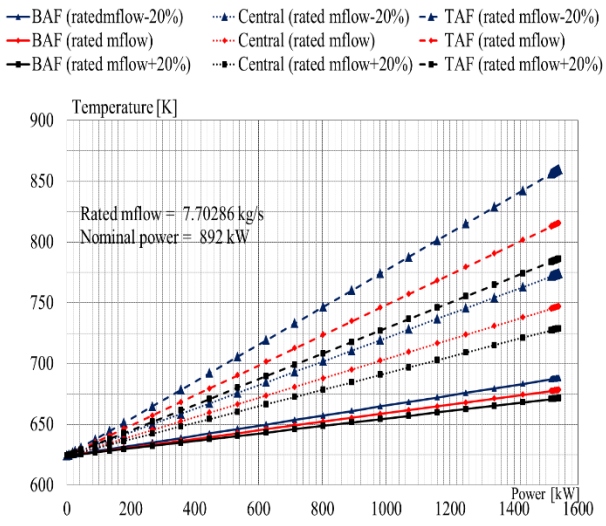

b) Cladding Temperature.

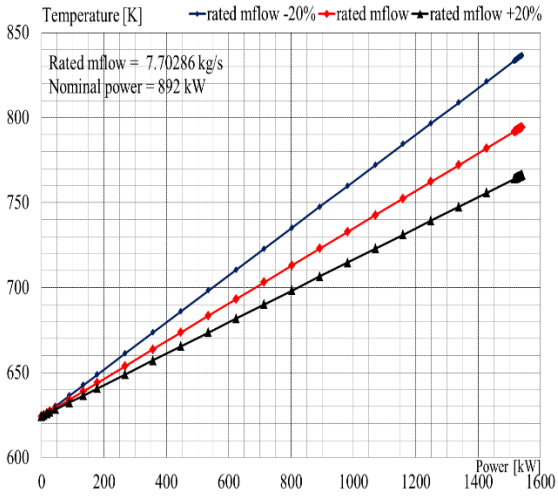

c) Fluid Temperature.

Fig. 55 – EBR-II SHRT-17, RELAP5-3D©: Heat Exchange Test.

5 BLIND SIMULATION OF SHRT-17

5.1 Steady state results

The stationary conditions are achieved after 1000s of "null transient" (steady state) calculation in order to stabilize the system. The initial conditions of the experiment are compared with the code results at the end of steady state in Tab. 33. This table includes the specification of the quantity considered, the measurement unit and the errors in the measures.

Steady state and initial conditions are achieved accordingly with the SHRT-17 test specifications, as given for the blind calculation. The calculated values are stable and acceptable. Minor differences are highlighted in the table and are hereafter discussed.

- Power and mass flow distributions are set up according with EBR-II RUN129c. Mass flow rate distribution in FA is satisfactory (see Tab. 34), even if there is an underestimation of the RING2 and RING3, connected with the overall pressure drop constraints.

- The pressure drop distribution along the primary system is reported in Fig. 56. The pressure drop between the primary coolant pump outlet and the upper plenum is comparable with experimental data [3]. Errors are observed between the pumps outlet and the upper plenum: the calculated value is underestimated in the code simulation with respect to the experimental value.

- Differences are observed in the MCP head, which is representative of the overall primary system pressure drop.

- Primary and Intermediate system mass flow rate distribution, including bypass flow rate, is satisfactory.

- Minor differences are observed in IHX, (i.e. mass flow rate) which can be connected to sodium properties used for the blind simulation. RELAP5-3D basic properties for sodium that are characterized by non-accurate value of the heat capacity. In the following calculations (not presented here) improved sodium properties table is used: stationary conditions in agreement with experimental data are achieved (reducing mass error). Non relevant differences are observed in the transient.

5.2 SHRT-17 transient results

The SHRT-17 is a protected loss of flow test [3] (see also Section 3). The results of the blind simulation, performed on the basis of the boundary conditions are presented hereafter. The trends of the main parameters are depicted from Fig. 57 to Fig. 73. Qualitative agreement between experimental data and calculated values has been obtained.

Mass Flow Rate

The mass flow rate results of primary pump#1 and #2, and of high and low-pressure system are reported in Fig. 57, Fig. 58 and Fig. 59. The experimental data are available only for primary pump#2 and for coolant system connected to primary pump#2. General trend of mass flow rate is in accordance with the experimental data, even if there is an overestimation of mass flow rate when primary pumps are at rest, that determines an increase of natural circulation. Sodium mass flow rate of primary pump#1 and #2 are represented in Fig. 57: in the firsts 50 seconds mass flow rate

decrease following the pump coastdown, when the buoyancy forces begins to prevail, natural circulation stabilizes. From 25s and 50s a mass flow inversion occurred due to the fact that pump#1 is at rest before primary pump#2 (Fig. 58). Mass flow inversion in primary pump#2 is not confirmed by experimental data, as they are not available.
High and low pressure flow rate is represented in Fig. 59: in the first seconds mass flow rate follows the pump coastdown, at 50s low-pressure flow rate reaches the minimum value then rises and from 150s on stabilizes.

Mass flow rate of XX09 and XX10 assemblies (see Fig. 65 and Fig. 66) present the same general trend of experimental data with some important differences. Mass flow rate of the XX09 assembly, which is the assembly representative of the fuel element, presents a mass flow rate greater than experimental values (85%), especially by the end of the pumps coastdown (see detail of Fig. 65). Mass flow rate of the XX10 assembly, which is representative of the reflector element, after the coastdown, is lower than the experimental data.
The flow rate through the subassembly is governed by the frictional characteristics [27] of the subassembly and the coastdown characteristics of the primary coolant pumps. The frictional characteristics of the subassembly are expected to be dominated by those of the inlet orifice and the wire-wrapped rod bundle. The orifices geometry has been selected on the basis of mass flow rate data available.

Coolant Temperature
The general trends of fluid temperature is well simulated in the blind test (see from Fig. 60 to Fig. 87), the most important differences are observed in the core, in the upper plenum and in the IHX.

Inlet temperature is qualitatively well predicted by the code simulation. After 400s lower plenum inlet temperature decrease of few degrees because of the heat exchange with the pool (see Fig. 61 and Fig. 60).
In the upper plenum differences are observed: calculated values are greater at the start of the transient until 100s, after are lower than experimental data (see Fig. 62). The stratification phenomena observed in the experimental data is not well predicted by the code, this can be connected to the RELAP5-3D© nodalization of the upper plenum.
In Fig. 63 Z-Pipe, IHX primary inlet and intermediate outlet temperature are represented. Differences between experimental and calculated values in IHX temperature can be due to unpredictable effect linked to the top of IHX structure and to minor local effect. Z-Pipe experimental data are not available for the evaluation.
In Fig. 86 the comparison between RELAP5-3D© Z-pipe temperature and the average value between calculated assembly coolant temperatures demonstrates that experimental data available represent the average value between available assembly coolant temperature.
General trend of pool temperature, at IHX primary side outlet, (Fig. 64) is in agreement with experimental data, but after 200s calculated values are lower than experimental data of few degrees.

Coolant temperature of instrumented assemblies (XX09 and XX10) is measured at the assembly inlet and outlet, and in the thimble annulus region. Regarding flowmeter temperature two main differences, comparing RELAP5-3D© results and experimental data, can be observed (see and Fig. 73). Temperature calculated by the code is almost constant and does not reproduce the peak of temperature after the pump coastdown. As the RELAP5-3D© model of the XX10 assembly is a 1d model the stratification phenomena is not simulated by the code.
The general trend of the coolant temperature at the outlet of the assemblies is in agreement with experimental data (see Fig. 71, Fig. 77 and Fig. 78). In the XX09 assembly calculated value

temperature differs from experimental after the pump#2 coastdown: from 50s 100s calculated value is greater than experimental than is lower. Fig. 77 show the comparison from experimental data and RELAP5-3D© results of XX10 coolant exit temperature. Fig. 72 and Fig. 79 presents thimble annulus coolant temperature of XX09 and XX10, respectively. As information about thermocouples position are not available and the code model is a 1D model, differences of temperature are not evidenced by code results.

Assemblies coolant temperature (from Fig. 80 to Fig. 85) is in agreement with experimental data. Regarding the assemblies in Row 1, 2 and 3 represented in Fig. 80 and Fig. 81, temperatures decrease with the same trend of experimental data but the peak of temperature is lower. After 74s, calculated value decrease, remaining lower than the experimental. Differences of temperature between assemblies are not evidenced in the blind simulation. In Row 4 (Fig. 82) differences between assemblies temperature can be observed: temperature of assembly identified with label 4B1, after 30 s, is lower than the other assemblies temperature: this can be due to position with respect to primary pumps and to Z-pipe inlet. Row 5 and 6 assemblies temperature are depicted in Fig. 83: as the calculated value present a peak of temperature in assemblies 5A4 and 5C2 greater than assembly 6C4, opposite in the experimental data the peak of temperature is in 5C2 assembly. This difference between experimental and calculated value can be linked to the core orientation with respect to primary pumps, as this information was not available, it is possible that in RELAP5-3D© model the primary pumps are inverted with respect to the real position. The blind simulation has been performed without experimental data of assemblies coolant temperature (with the exception of XX09 and XX10). In the post test analysis the corrected core orientation will be implemented in the model.
In Fig. 84 and Fig. 85 reflector assemblies temperatures are depicted: calculated value present a disagreement compared with experimental data. Row 7 assemblies calculated temperature (Fig. 84) has the same trend of assemblies in central core region. Calculated temperature of the external core region assemblies is almost constant. Temperature of 9E4 assembly, which is a reflector, is in agreement with experimental data; temperature of 12E6 and 16E9 assemblies, which are blanket assemblies, is not well simulated by the code in the first 100 s of the transient: peak of temperature is not revealed by the code.

Cladding Temperature
XX09 and XX10 cladding temperatures calculated by RELAP5-3D© code have a general trend that is in agreement with experimental data. Main difference is that, after the SCRAM, calculated value are lower than experimental, this can be connected to the greater mass flow rate in the XX09 assembly but, relatively to XX10 assembly an incoherence is observed as the mass flow rate is lower than the experimental.
XX09 midplane temperature, top fuel temperature and above core temperature are represented respectively in Fig. 68, Fig. 69 and Fig. 70. XX10 midplane temperature, top fuel temperature and above core temperature are represented in Fig. 74, Fig. 75 and Fig. 76. Peak fuel cladding and coolant temperature are shown in (Fig. 87).

The cladding temperature during a transient initiated by a loss of forced convection is primarily determined by the flow rate, the inlet fluid temperature, the heat transfer between the fuel rod and the fluid, and the reactor power.

The heat transfer from the fuel rod and coolant is governed by the heat conduction within the fuel rod and the convective heat transfer at the outer surface of the fuel rod to the coolant. The existing heat conduction models in RELAP5-3D© should adequately represent the heat conduction across

the fuel and the cladding. RELAP5-3D© has simple models to calculate gap conductance and geometrical changes in light water reactor. These models adequate for oxide fuel but they are not be applicable for metallic fuel with a sodium bond. A detailed fuel rod performance code is needed. The heat transfer from the surface of the fuel rod cladding to the coolant is governed by the heat transfer correlations used by RELAP5-3D© (see Section 4.4.2).

Because of the high thermal conductivity of sodium, axial conduction within the fluid and radial conduction between adjacent subchannels within a subassembly can be significant. RELAP5-3D© neglects axial and radial conduction in the working fluid because the thermal conductivity of water is relatively low. However the thermal conductivity of sodium is about 100 times greater than that of water, so axial and radial conduction can be important factors in liquid metal heat transfer [31]. The effects of axial and radial conductions could be significant during transients with reduced flow [26]. Thus, the capability to model axial conduction in the fluid might be necessary to RELAP5-3D©. Turbulent mixing effects could be necessary to added to RELAP5-3D© to accurately represent subchannel effects, that are usually calculated with subchannel or CFD codes rather than with a system code.

#	QUANTITY (*)	UNIT	DESIGN	RELAP5-3D	ER.
1	**PRIMARY CIRCUIT POWER BALANCE**				
1-1	Core thermal power - Driver/Blanket	MWth	57.3 52.28/5.02	57.01 51.7/4.95	0.51%
2	**PRESSURE**				
2-1	MCP out	kPa	441.2	452.5	-2.57%
2-2	Upper Plenum (UP)	kPa	213.9	217.1	-1.50%
3	**FLUID TEMPERATURE**				
3-1	Core inlet temperature	K	624.15	625.6	-0.23%
3-2	Core outlet temperature	K	--	749.8	--
3-3	IHX PS inlet coolant temperature	K	--	729.8	--
3-4	IHX PS outlet coolant temperature	K	--	624.8	--
3-5	IHX SS inlet coolant temperature	K	574.15	574.2	-0.02%
4	**PUMP VELOCITY**				
4-1	MCP#1 velocity	rpm	91.10	86.73	4.80%
4-2	MCP#2 velocity	rpm	91.10	86.73	4.80%
5	**PUMP HEAD**				
5-1	MCP#1 head	kPa	318.1	334.1	-5.03%
5-2	MCP#2 head	kPa	318.1	334.1	-5.03%
6	**LOCAL PRESSURE DROPS**				
6-1	Pressure drop [MCP_{OUT} – UP]	kPa	227.3	235.42	-3.57%
7	**FLOW RATES**				
7-1	MCP1/MCP2 mass flow rate	kg/s	466.7 233.5/233.2	462.1 231.2/230.9	0.99%
7-2	Lower plena inlet	kg/s	465.6	460.8	1.03%
7-3	Core mass flow rate - Driver - Blanket	kg/s	387.0/ 65.2	384.6 66.05	1% -1%
7-4	Reactor core outlet	kg/s	456.0	447.93	2%
7-5	IHX PS inlet	kg/s	452.7	446.82	1%
7-6	IHX PS outlet	kg/s	451.7	446.82	1%
7-7	IHX SS mass flow rate	kg/s	311.43	339.73	-9%
8	**BYPASS MASS FLOW RATES**				
8-1	Bypass MCP1	kg/s	0.156	0.176	-13.41%
8-2	Bypass MCP2	kg/s	0.156	0.177	-13.43%
8-3	Bypass vlv1	kg/s	0.392	0.417	-6.47%
8-4	Bypass vlv2	kg/s	0.392	0.417	-6.49%
8-5	Bypass RV Bot	kg/s	9.580	8.965	6.41%
8-6	Bypass core	kg/s	1.416	1.242	12.27%
8-7	Bypass RV Top	kg/s	3.298	3.883	-17.71%
8-8	Bypass IHX	kg/s	0.944	1.113	-17.87%

Tab. 33 – EBR-II SHRT-17, RELAP5-3D©: steady-state comparison.

RING	TYPE	N° FA	MASS FLOW	R5-3D	ERR
	Reflector	12	1.95	**1.95**	**0.00**
	Blanket	12	3.58	**3.56**	**-0.02**
Row 7	Reflector	33	0.17	**0.17**	**0.00**
	Experimental	3	0.68	**0.68**	**0.00**
Row 6	Experimental	2	3.88	**3.87**	**-0.03**
	High Flow Driver	18	3.88	**3.86**	**-0.03**
	Reflector	2	0.17	**0.17**	**0.00**
	Partial Driver	5	2.62	**2.62**	**-0.01**
	Driver	3	3.57	**3.56**	**-0.03**
Row 5	Control Rod	8	3.30	**3.62**	**0.01**
	Partial Driver	3	3.06	**3.06**	**0.00**
	SS FA	6	0.71	**0.69**	**-0.01**
	Experimental	1	4.38	**4.36**	**-0.02**
	XX10	1	0.33	**0.59**	**-0.01**
	Driver	3	4.38	**4.37**	**-0.01**
	XX09	1	2.69	**3.02**	**0.03**
	Dummy	1	0.64	**0.91**	**0.00**
Row 4	Driver	12	5.06	**5.03**	**-0.04**
	Experimental	5	5.07	**5.04**	**-0.03**
	Partial Driver	1	3.29	**3.28**	**-0.01**
Row 3	Safety	2	5.06	**5.14**	**-0.26**
	Driver	10	6.60	**6.55**	**-0.05**
Row 2	Driver	4	7.66	**7.30**	**-0.36**
	Experimental	2	7.65	**7.37**	**-0.29**
Row 1	Partial Driver	1	3.91	**3.78**	**-0.13**

Tab. 34 – EBR-II SHRT-17, RELAP5-3D©: mass flow rate distribution.

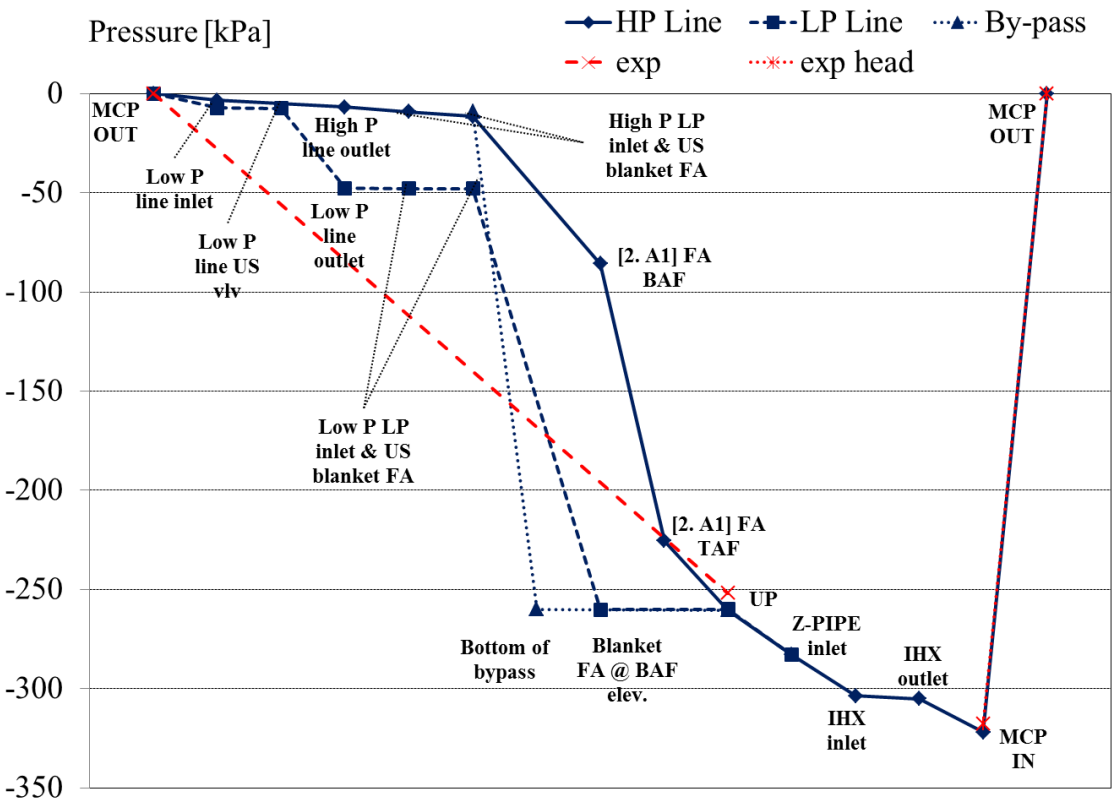

Fig. 56 – EBR-II SHRT-17, RELAP5-3D©: Pressure Drops Versus Length.

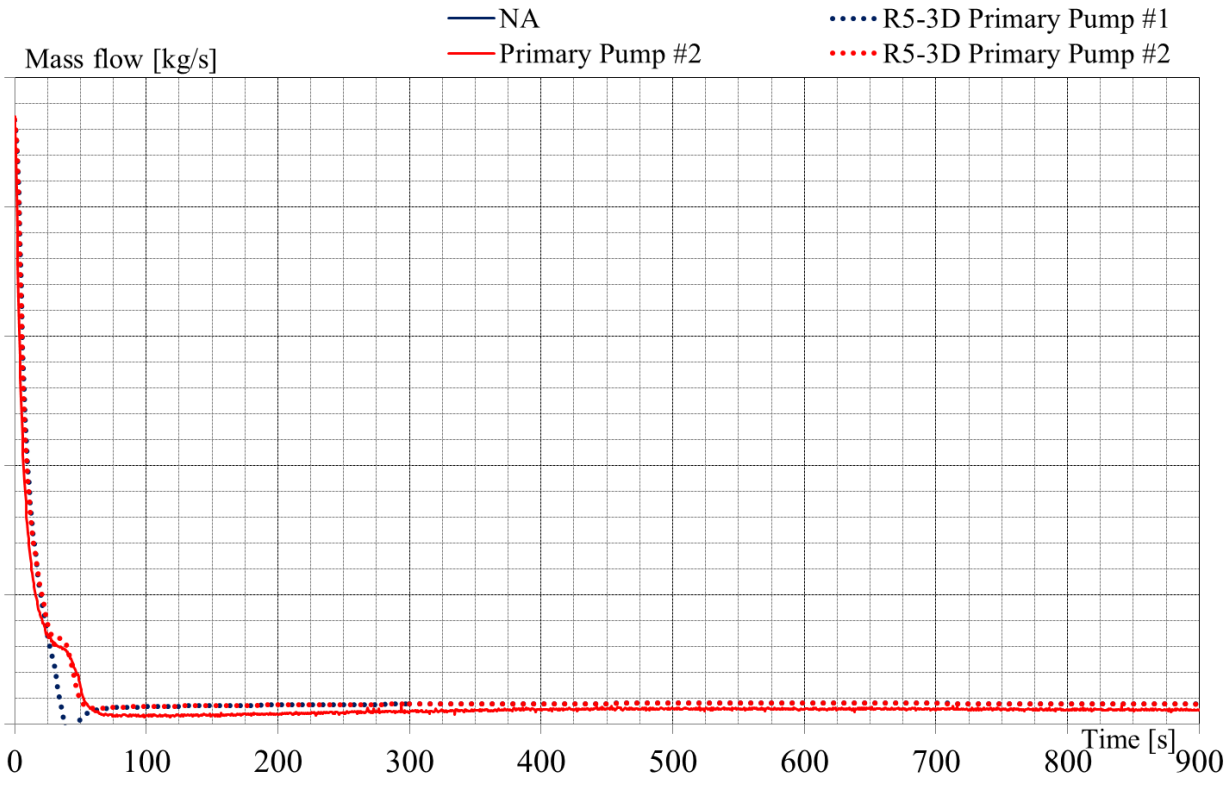

Fig. 57 – EBR-II SHRT-17, RELAP5-3D©: Primary Pump Sodium Mass Flow Rate.

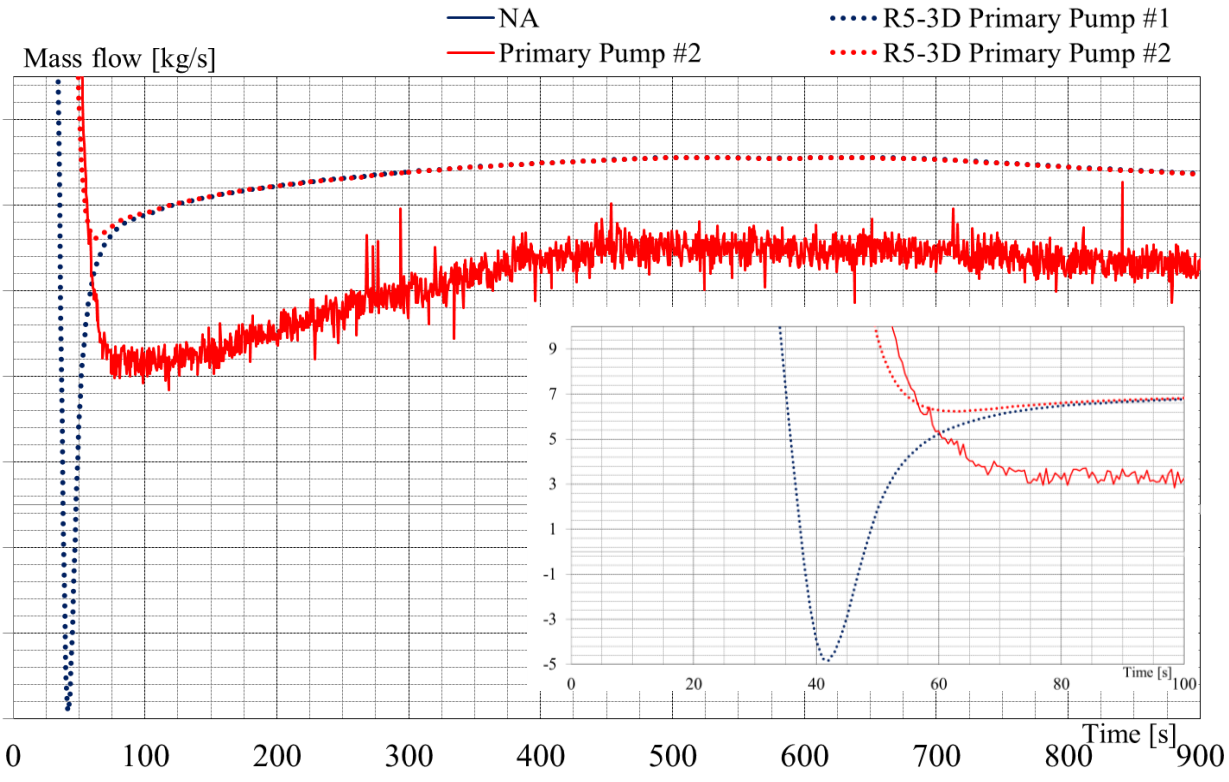

Fig. 58 – EBR-II SHRT-17, RELAP5-3D©: Primary Pump Sodium Mass Flow Rate (Detail).

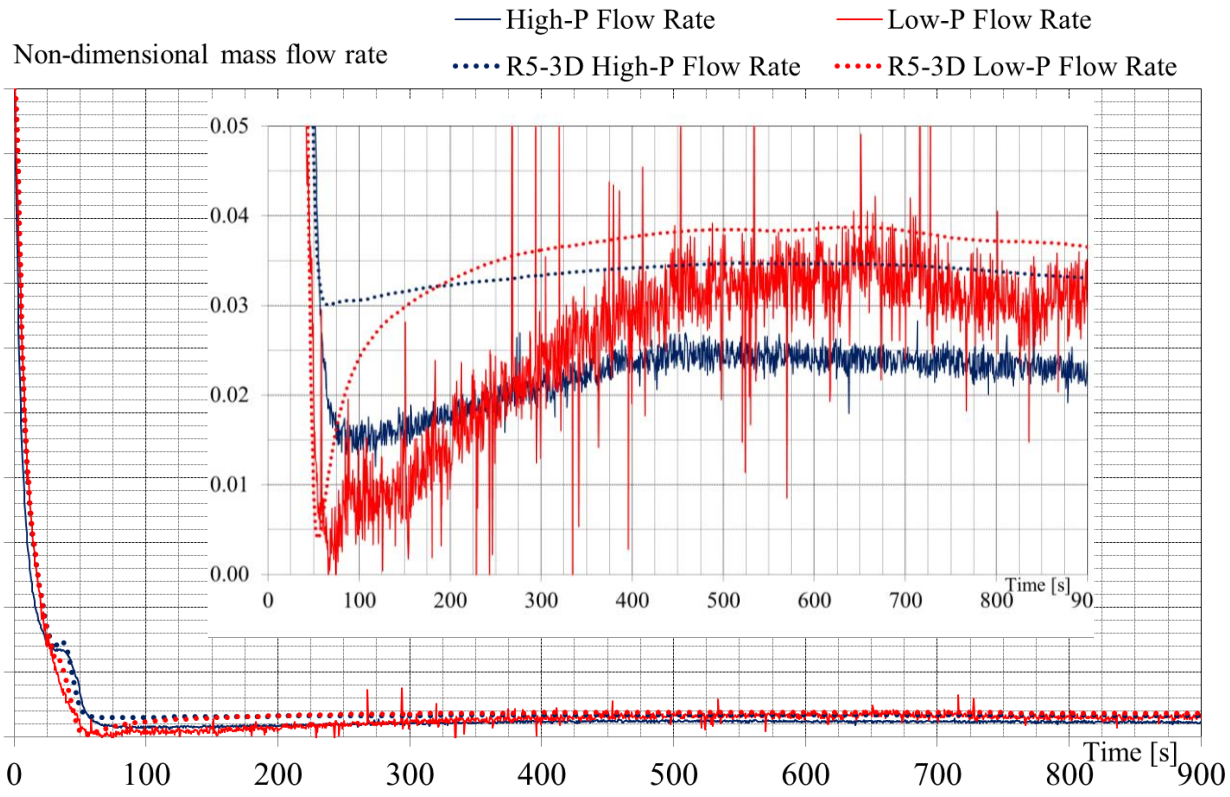

Fig. 59 – EBR-II SHRT-17, RELAP5-3D©: High and Low-Pressure Flow Rate (Non-dim.).

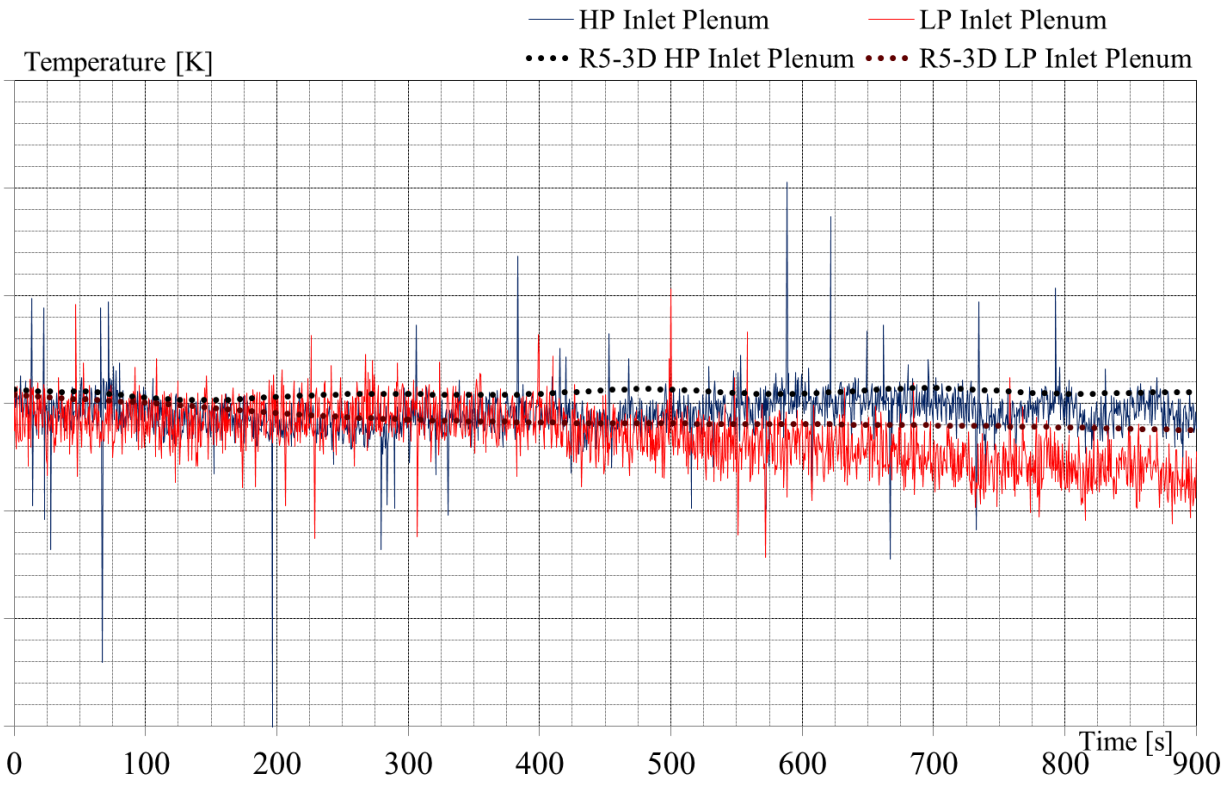

Fig. 60 – EBR-II SHRT-17, RELAP5-3D©: High and Low-Pressure Inlet Plenum Temperature.

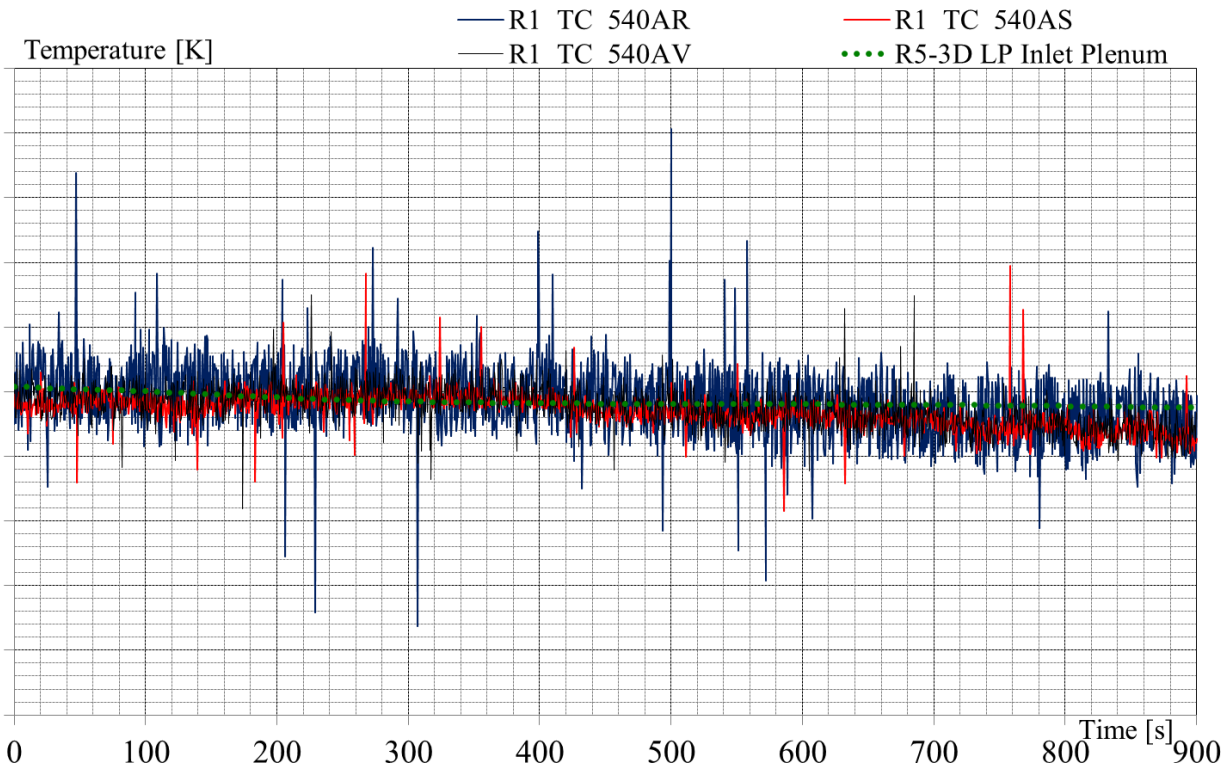

Fig. 61 – EBR-II SHRT-17, RELAP5-3D©: Lower Plenum Temperature.

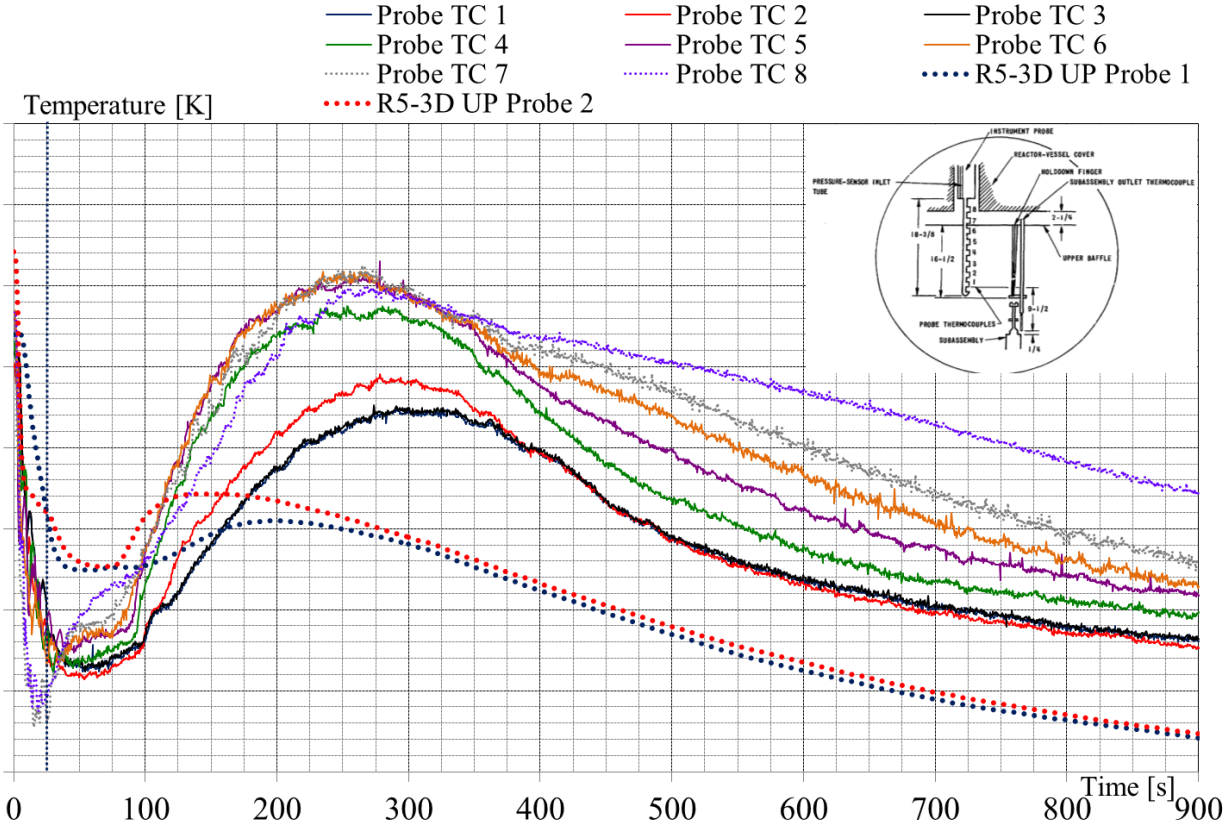

Fig. 62 – EBR-II SHRT-17, RELAP5-3D©: Upper Plenum Temperature.

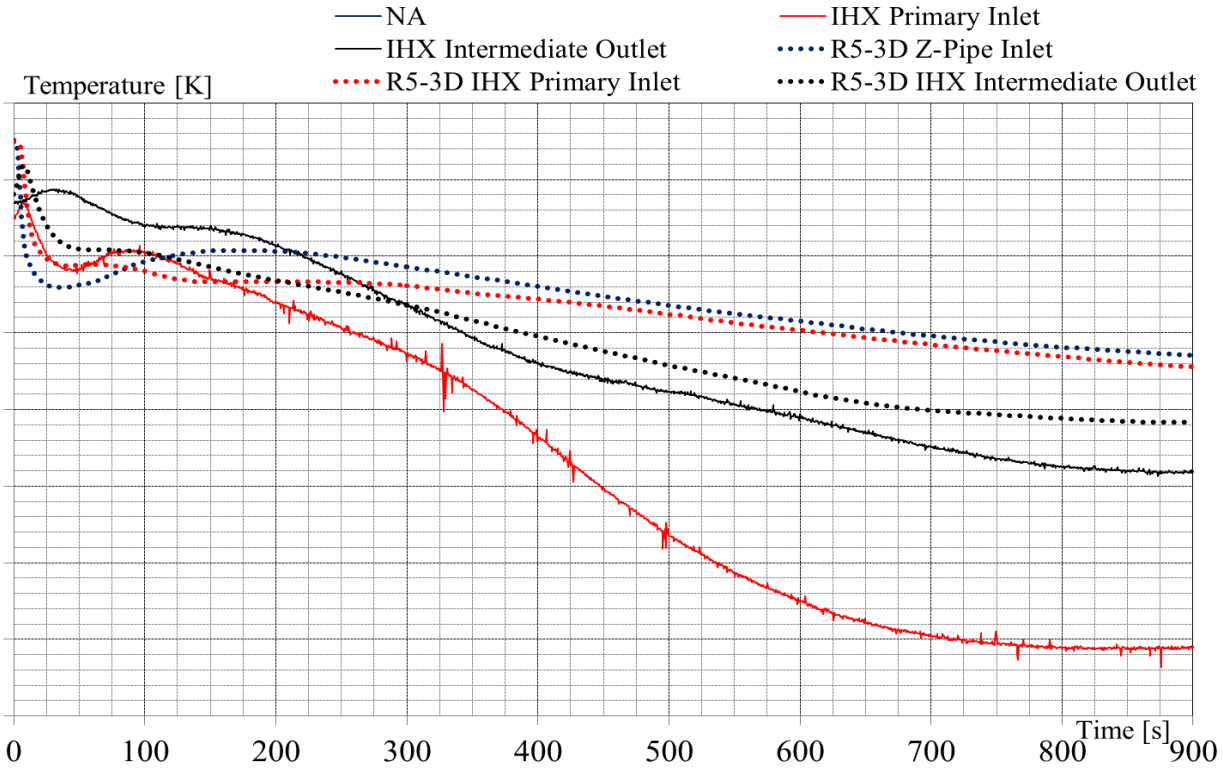

Fig. 63 – EBR-II SHRT-17, RELAP5-3D©: IHX Primary Inlet and Intermediate Outlet Temperature.

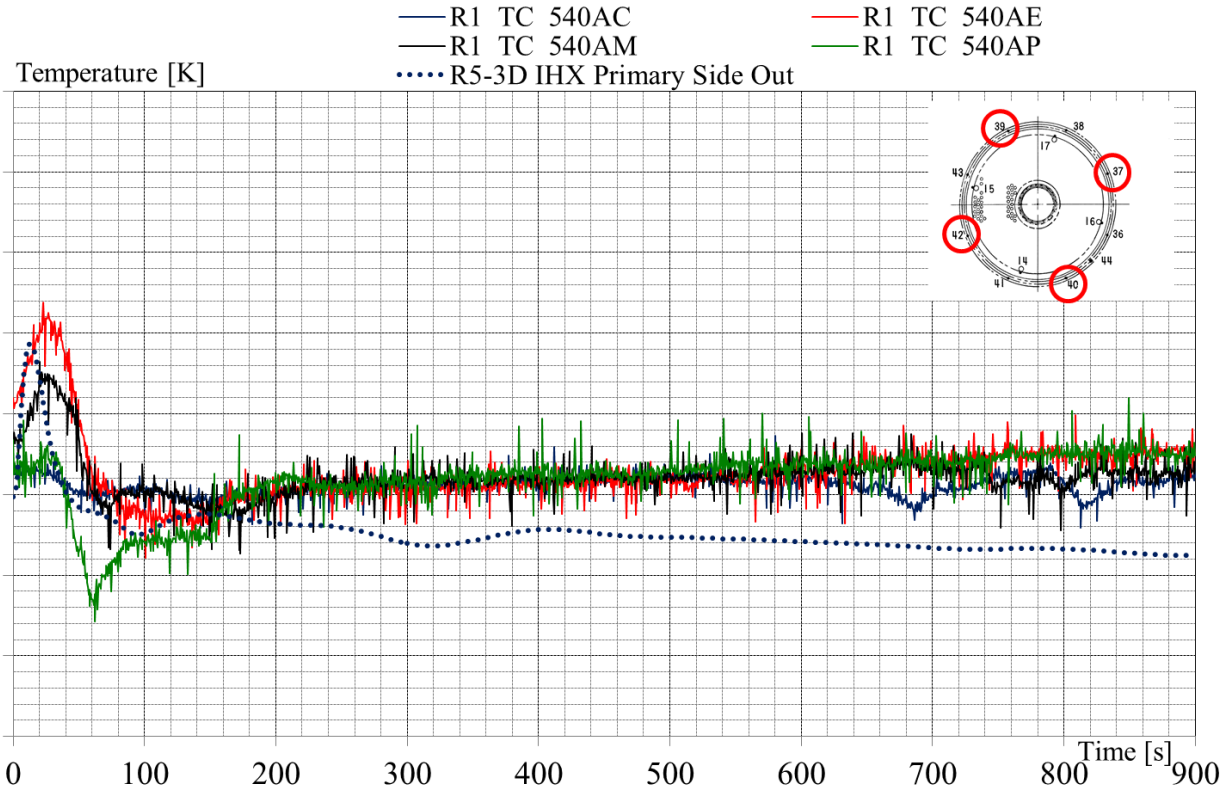

Fig. 64 – EBR-II SHRT-17, RELAP5-3D©: IHX Primary Side Outlet Temperature.

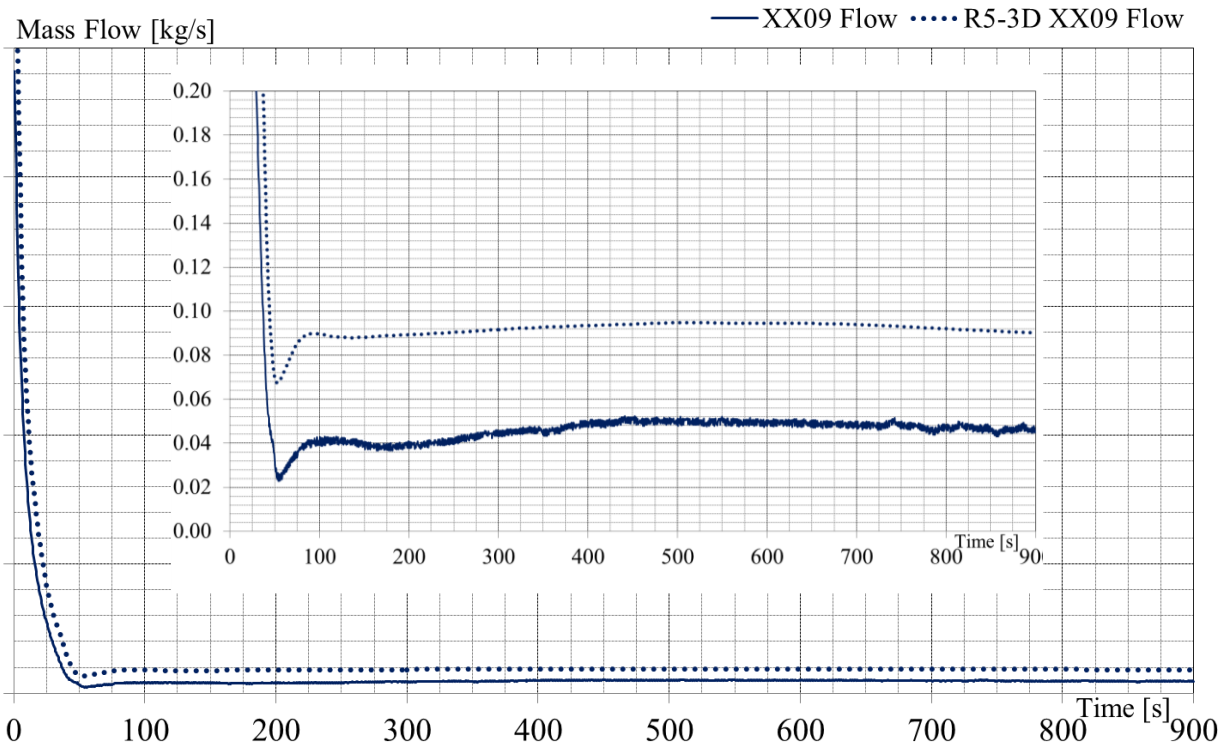

Fig. 65 – EBR-II SHRT-17, RELAP5-3D©: XX09 Mass Flow Rate.

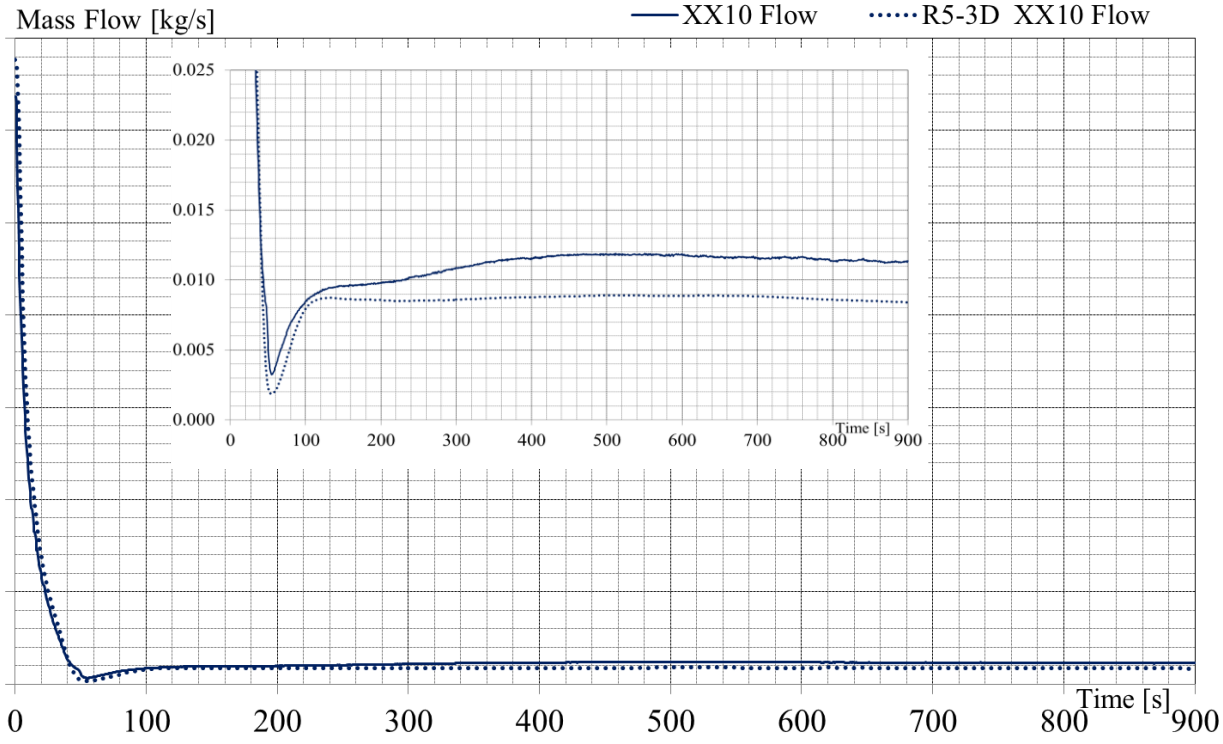

Fig. 66 – EBR-II SHRT-17, RELAP5-3D©: XX10 Mass Flow Rate.

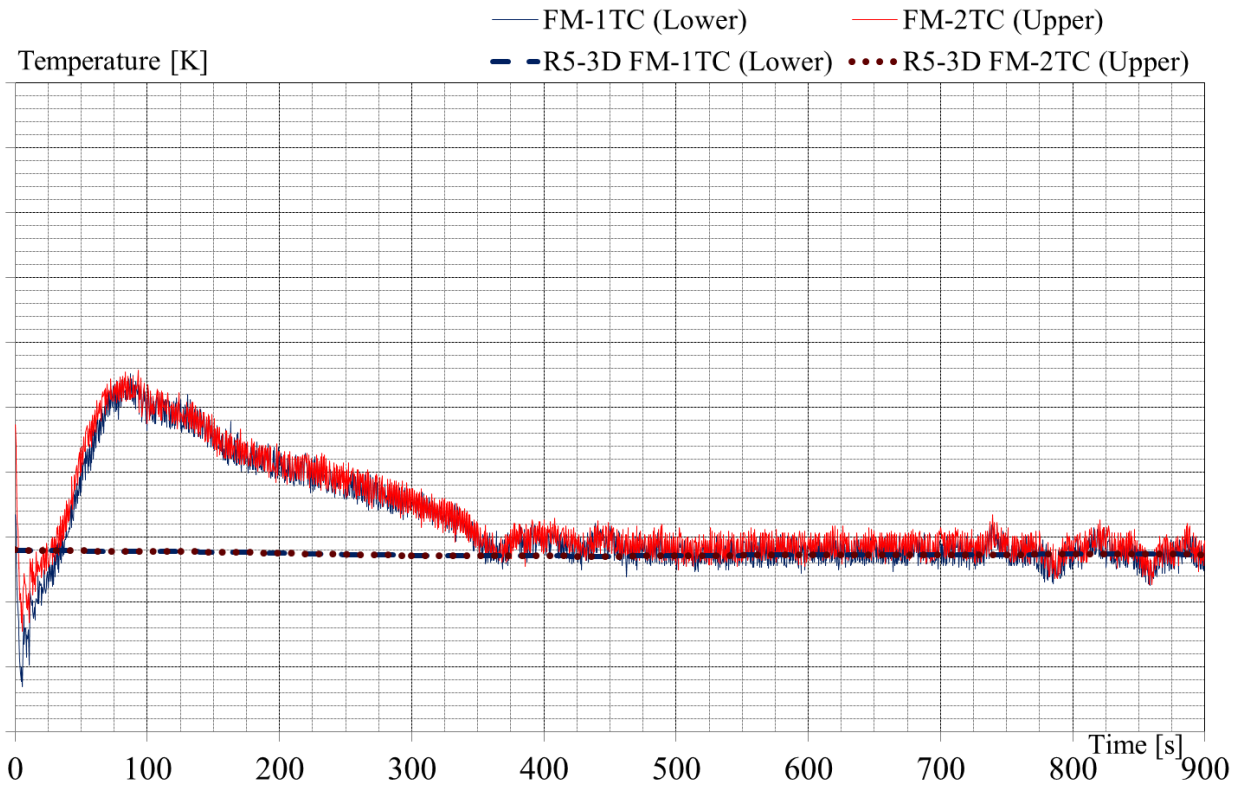

Fig. 67 – EBR-II SHRT-17, RELAP5-3D©: XX09 Flowmeter Temperatures.

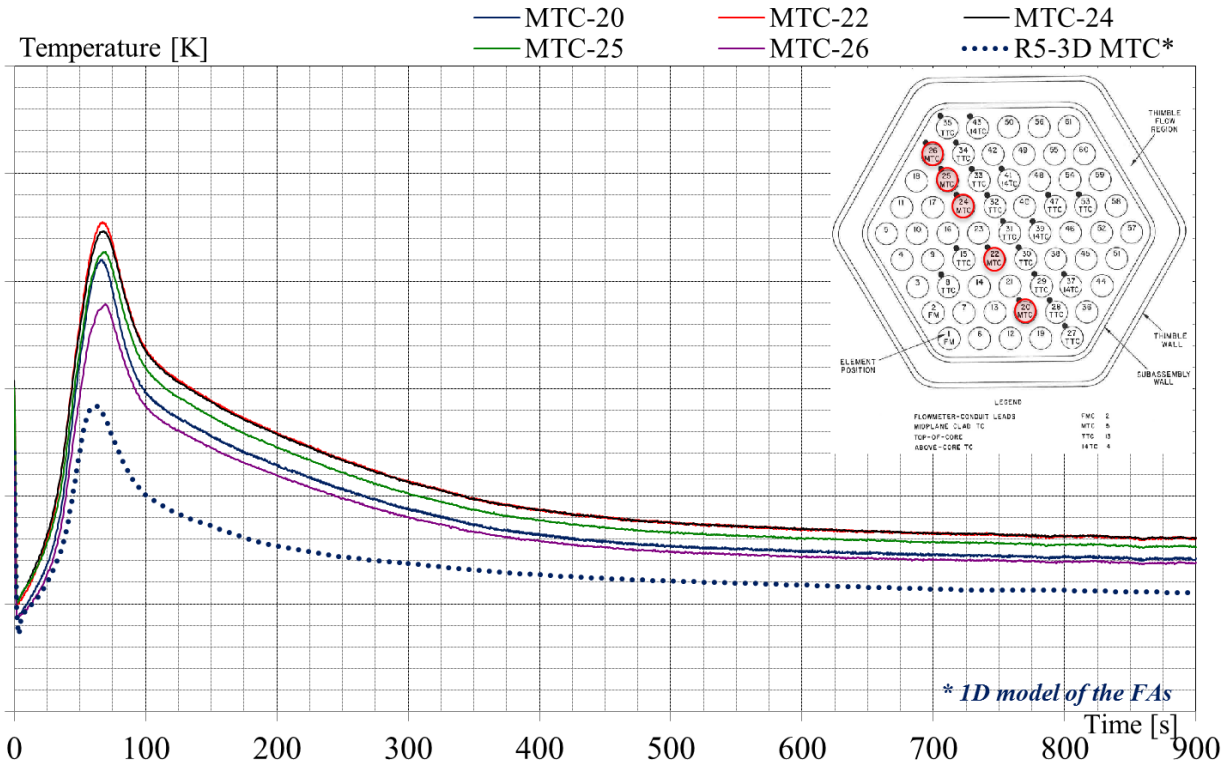

Fig. 68 – EBR-II SHRT-17, RELAP5-3D©: XX09 Mid Core Temperature.

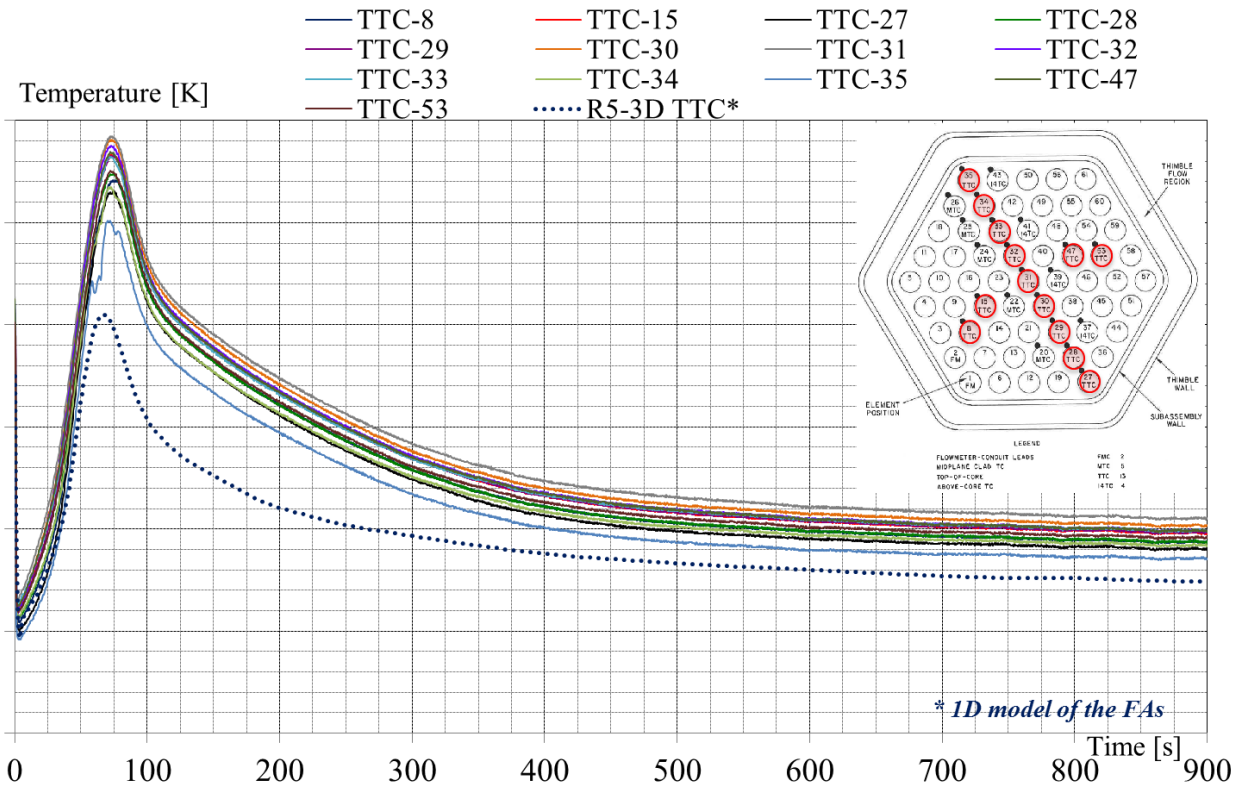

Fig. 69 – EBR-II SHRT-17, RELAP5-3D©: XX09 Top of Core Temperature.

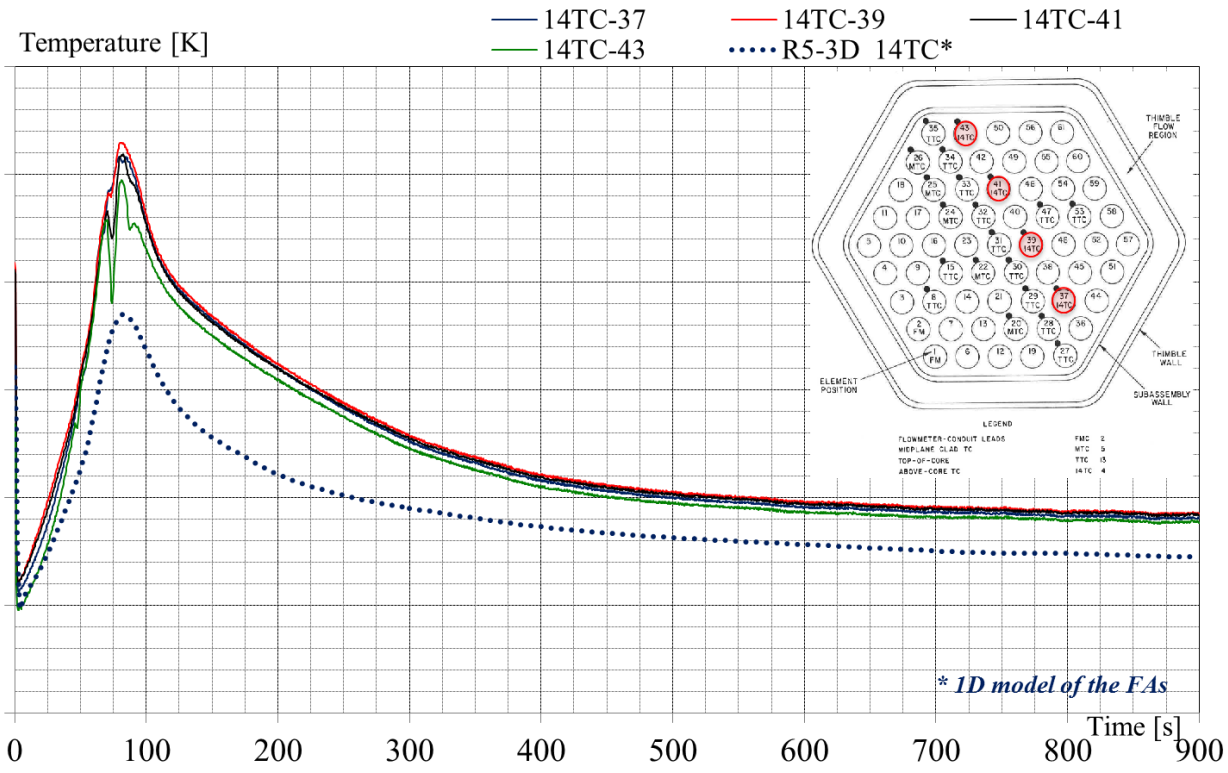

Fig. 70 – EBR-II SHRT-17, RELAP5-3D©: XX09 Above Core Temperature.

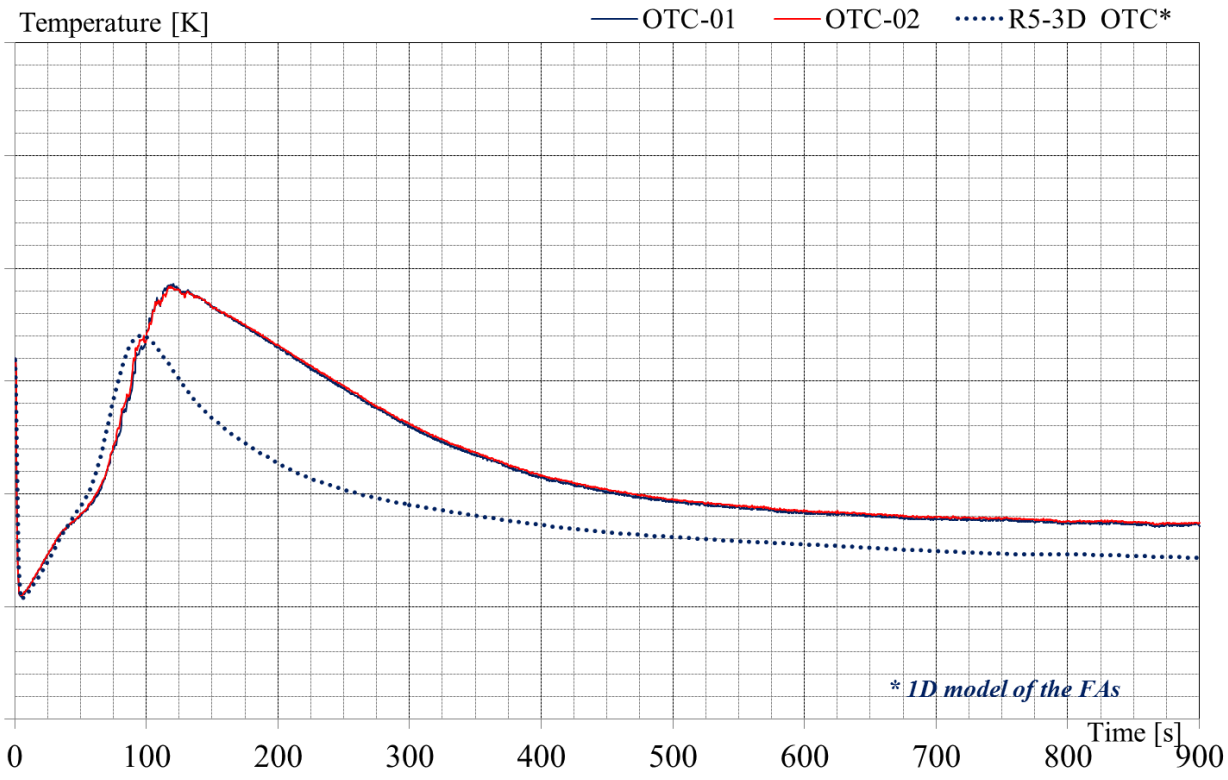

Fig. 71 – EBR-II SHRT-17, RELAP5-3D©: XX09 Coolant Outlet Temperature.

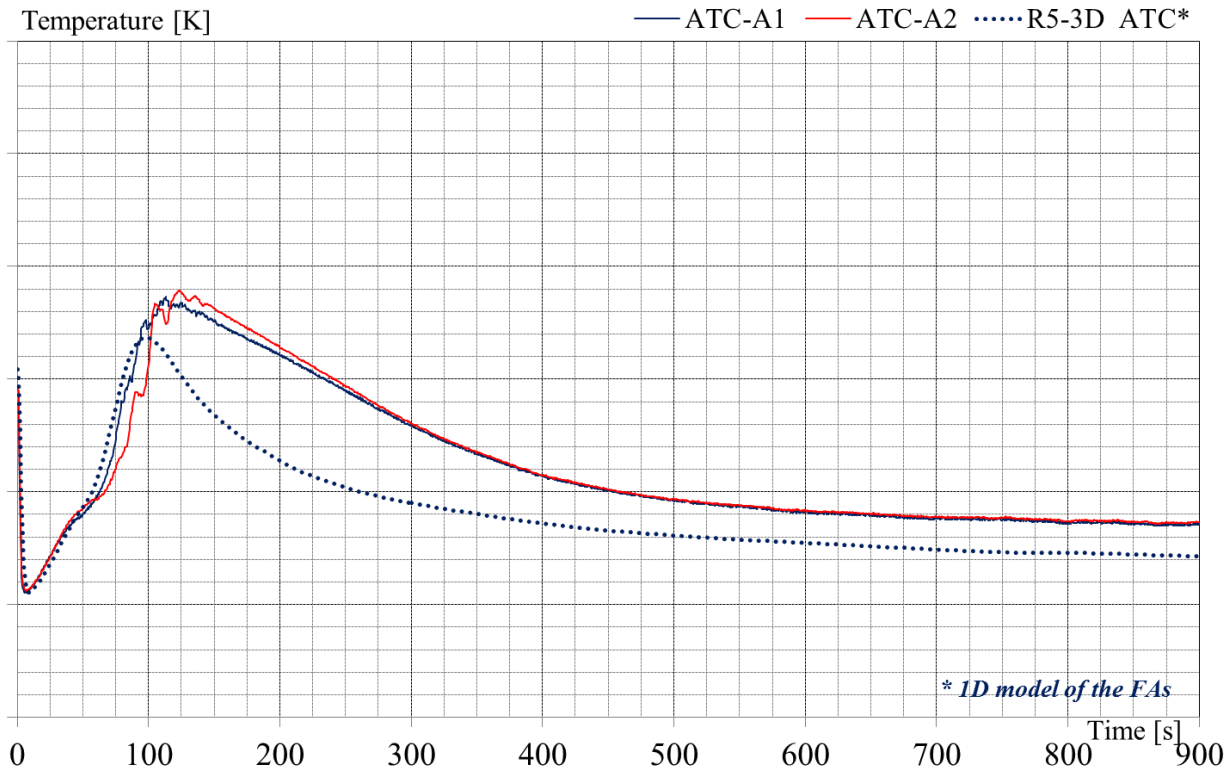

Fig. 72 – EBR-II SHRT-17, RELAP5-3D©: XX09 Thimble Annulus Temperature.

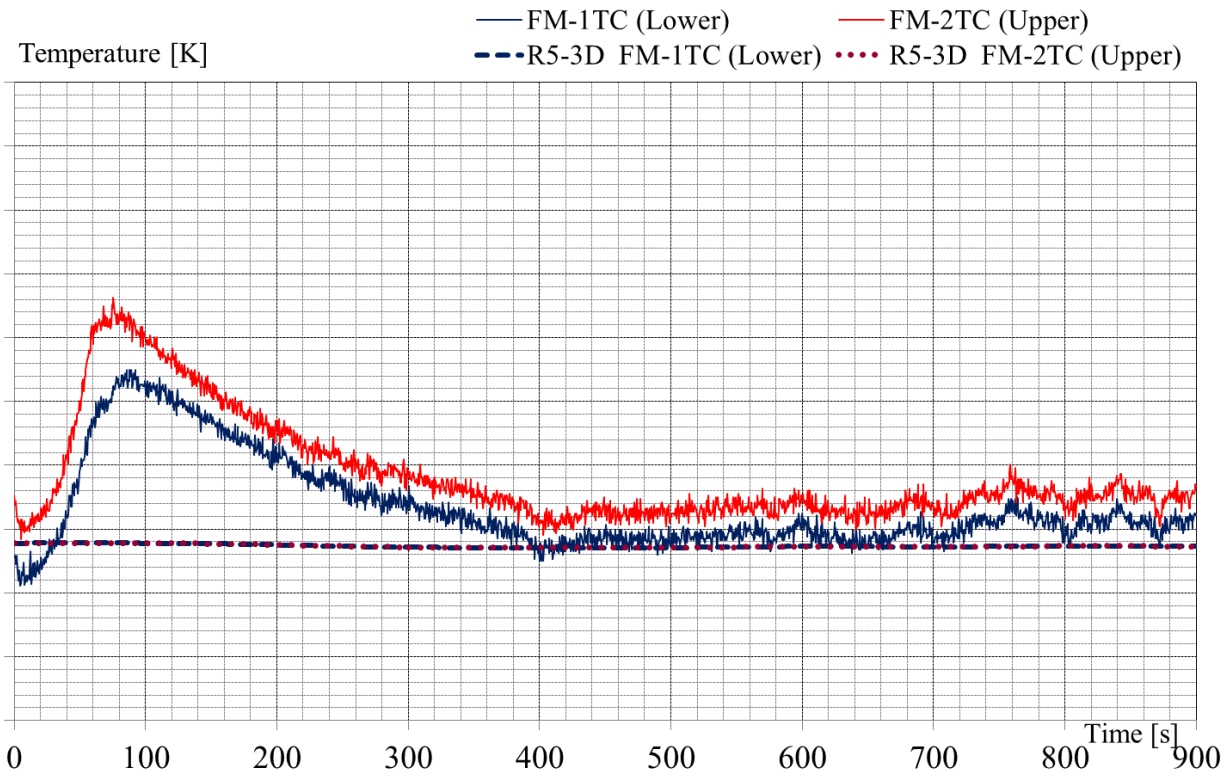

Fig. 73 – EBR-II SHRT-17, RELAP5-3D©: XX10 Flowmeter Temperature.

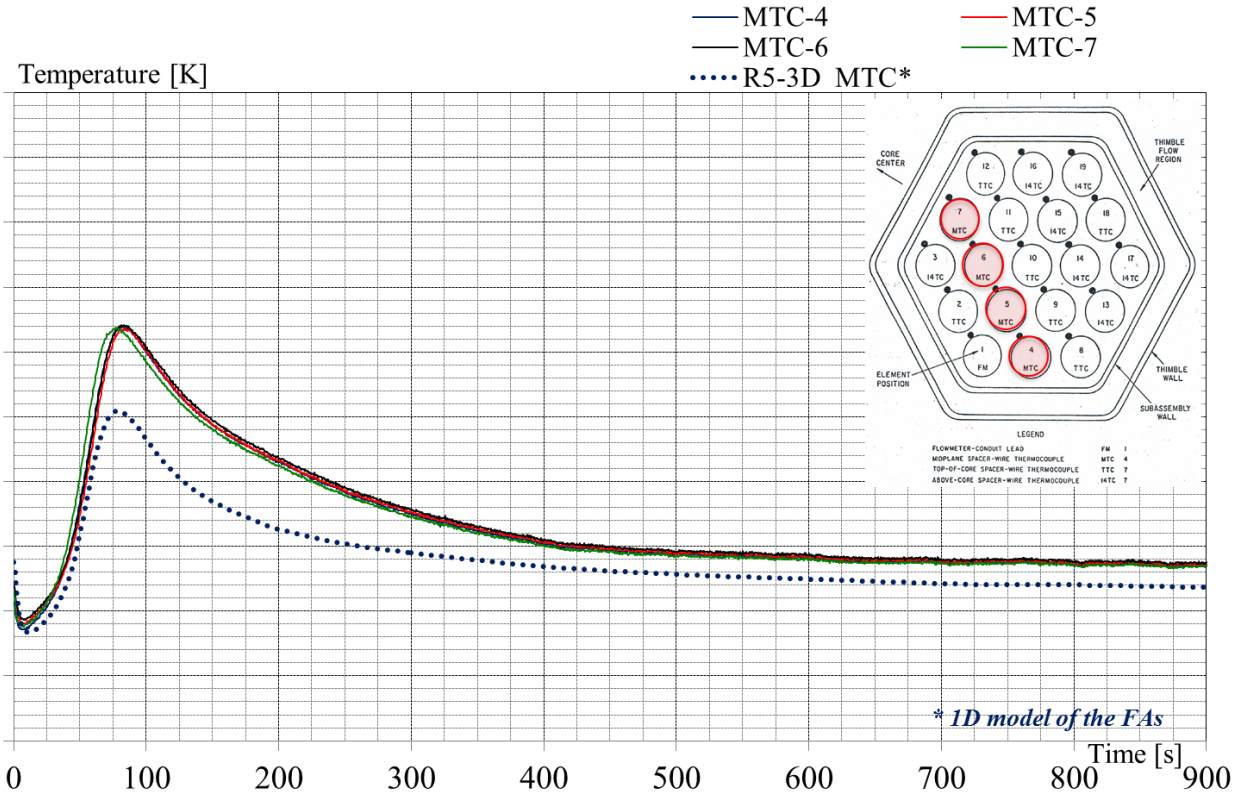

Fig. 74 – EBR-II SHRT-17, RELAP5-3D©: XX10 Mid Core Temperature.

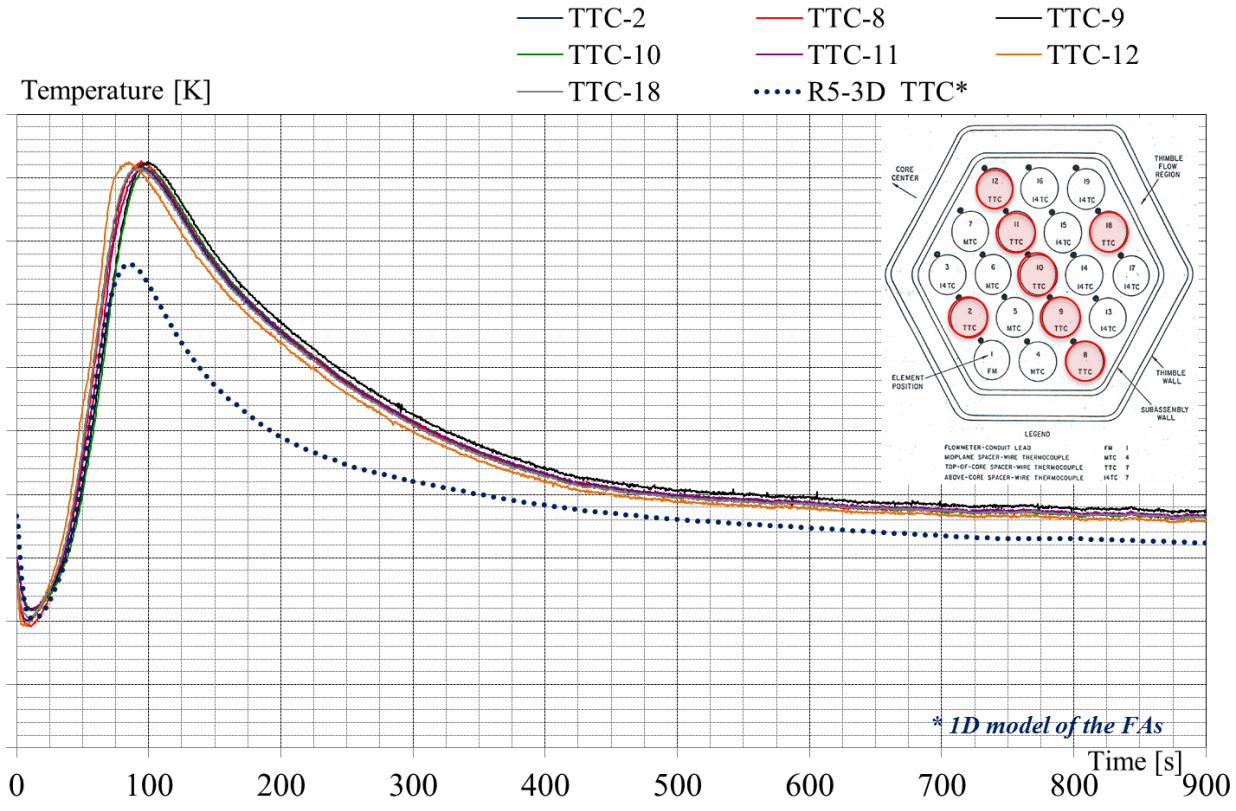

Fig. 75 – EBR-II SHRT-17, RELAP5-3D©: XX10 Top of Core Temperature.

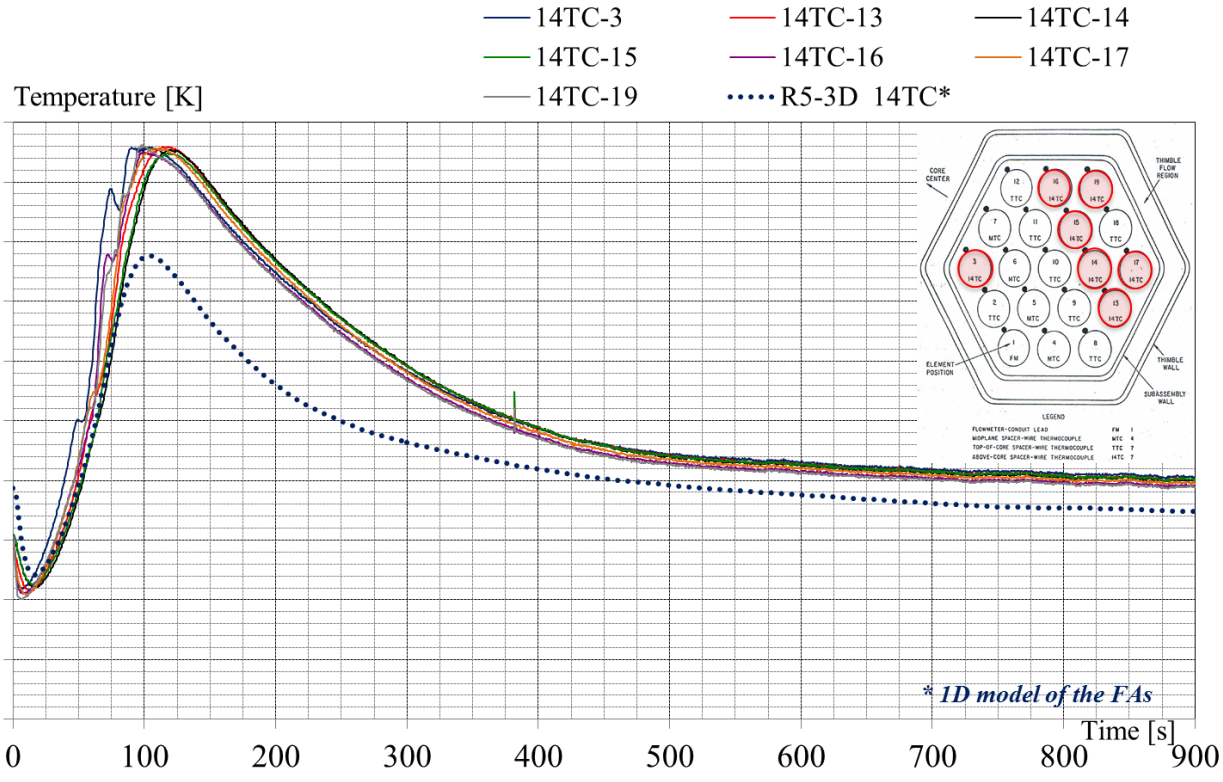

Fig. 76 – EBR-II SHRT-17, RELAP5-3D©: XX10 Above Core Temperature.

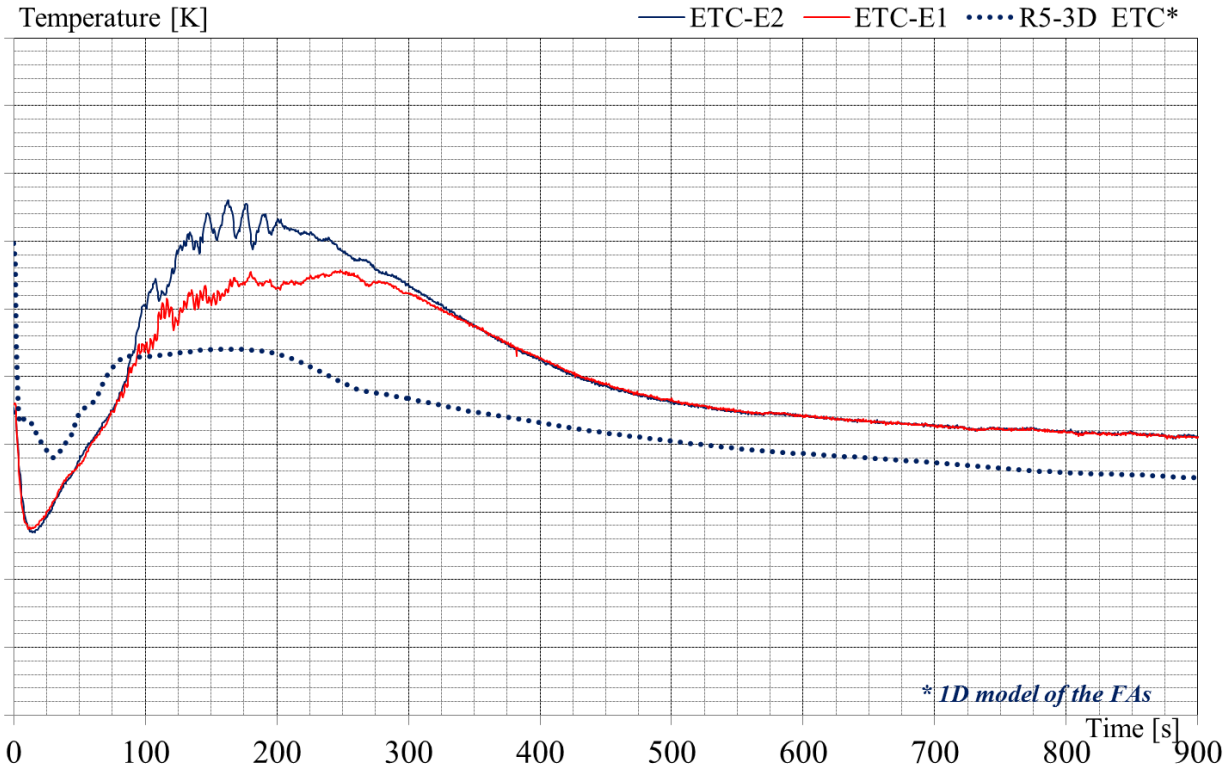

Fig. 77 – EBR-II SHRT-17, RELAP5-3D©: XX10 Coolant Exit Temperature.

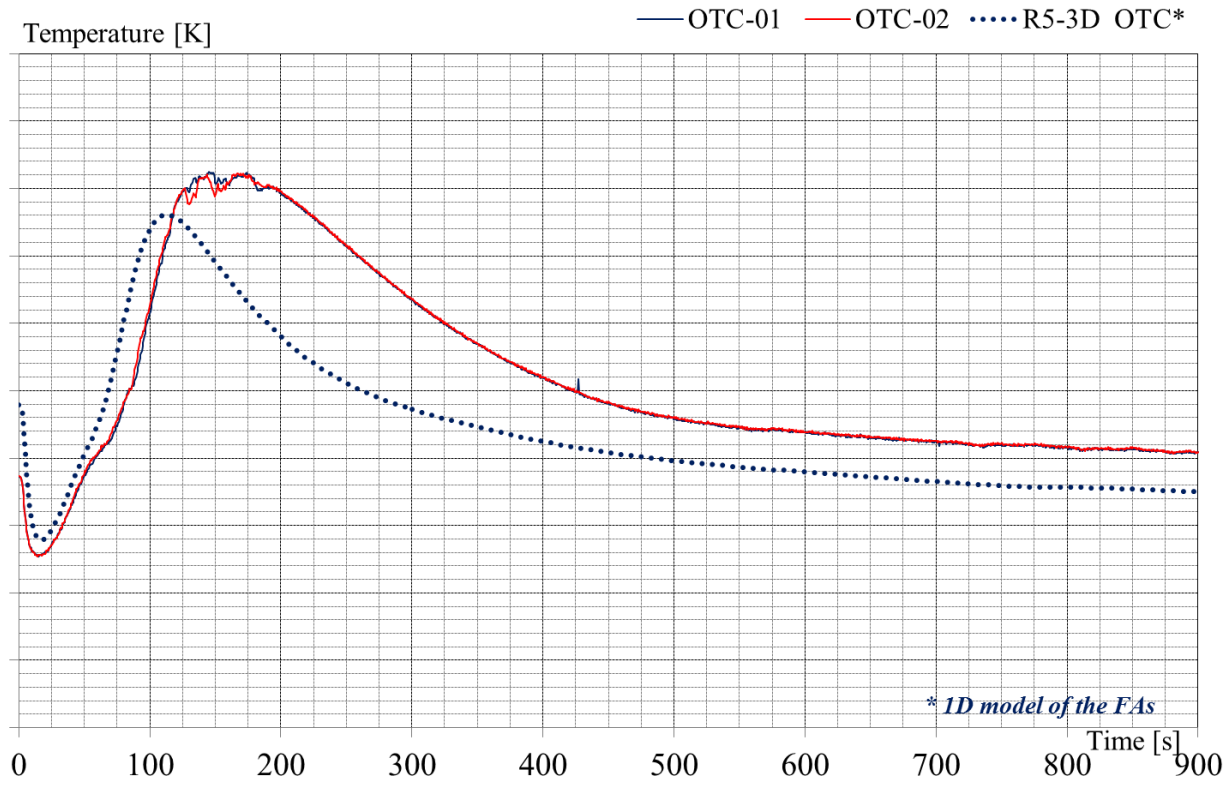

Fig. 78 – EBR-II SHRT-17, RELAP5-3D©: XX10 Coolant Outlet Temperature.

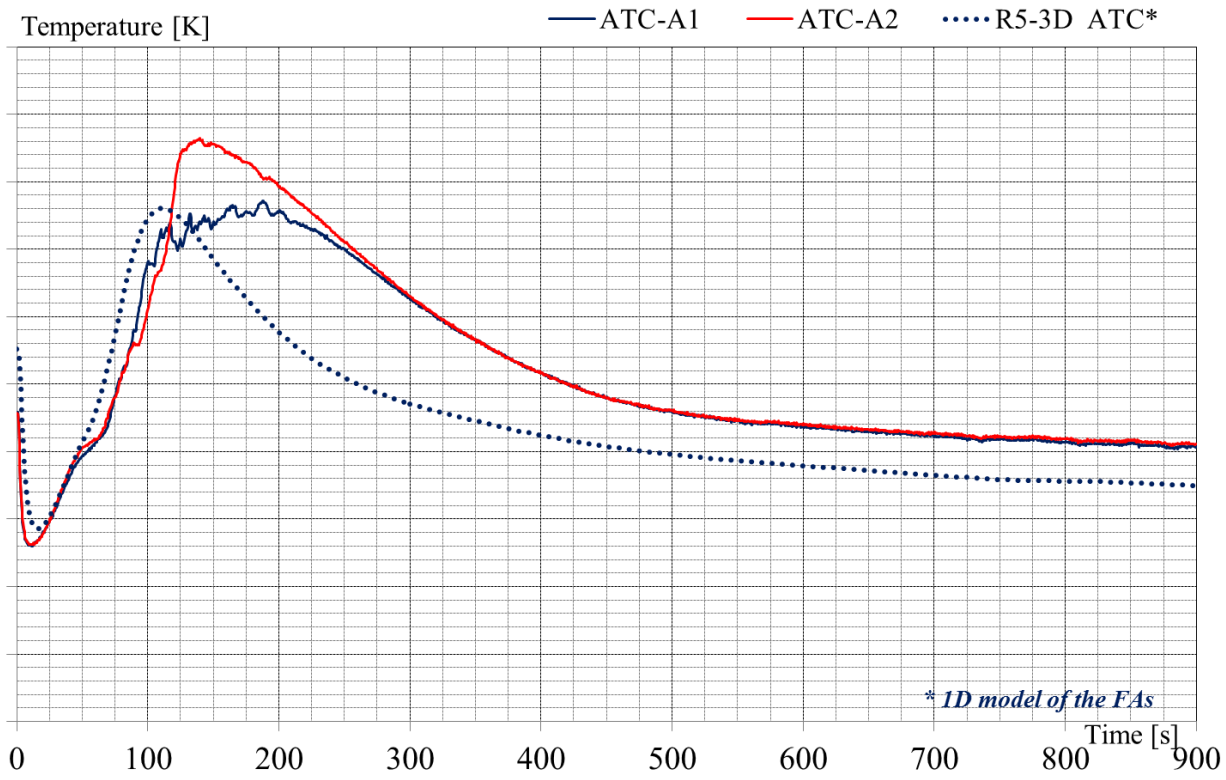

Fig. 79 – EBR-II SHRT-17, RELAP5-3D©: XX10 Thimble Annulus Temperature.

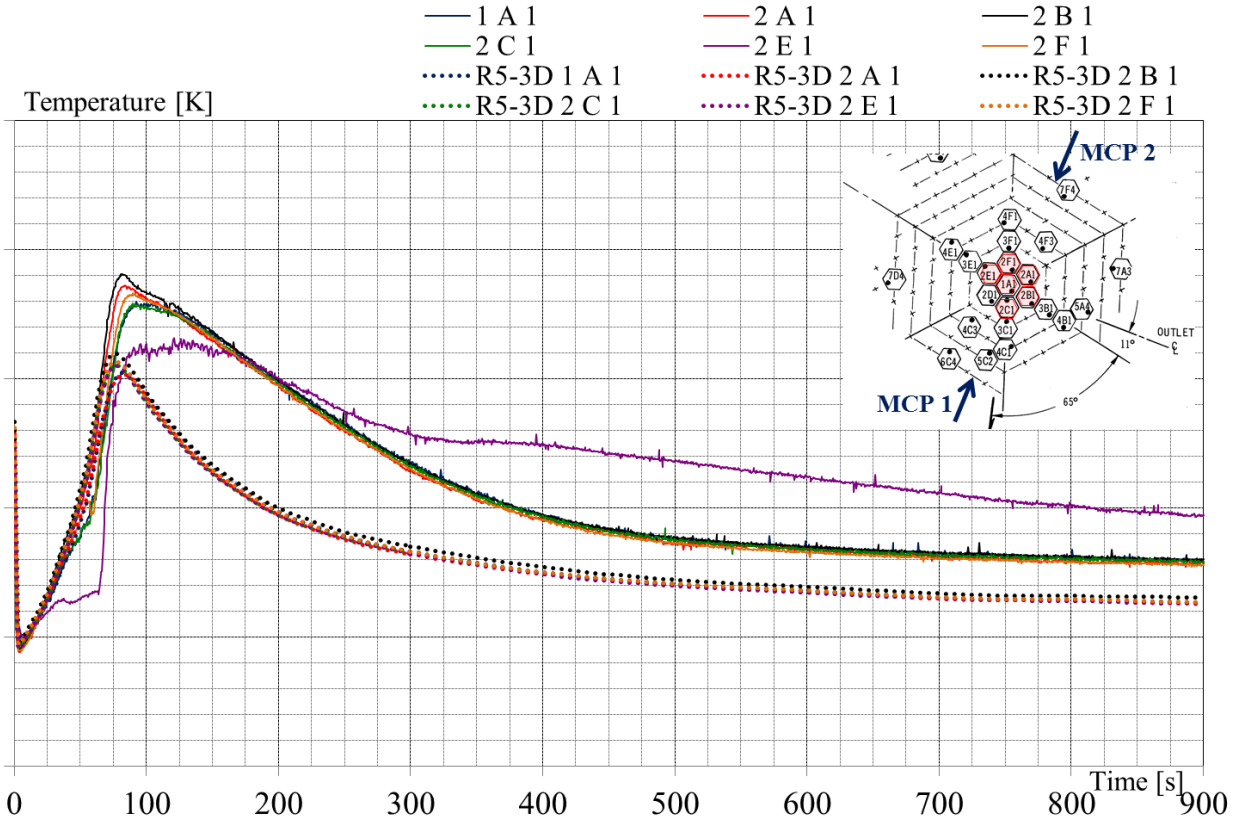

Fig. 80 – EBR-II SHRT-17, RELAP5-3D©: Subassembly Outlet Temperature (Row 1 and 2).

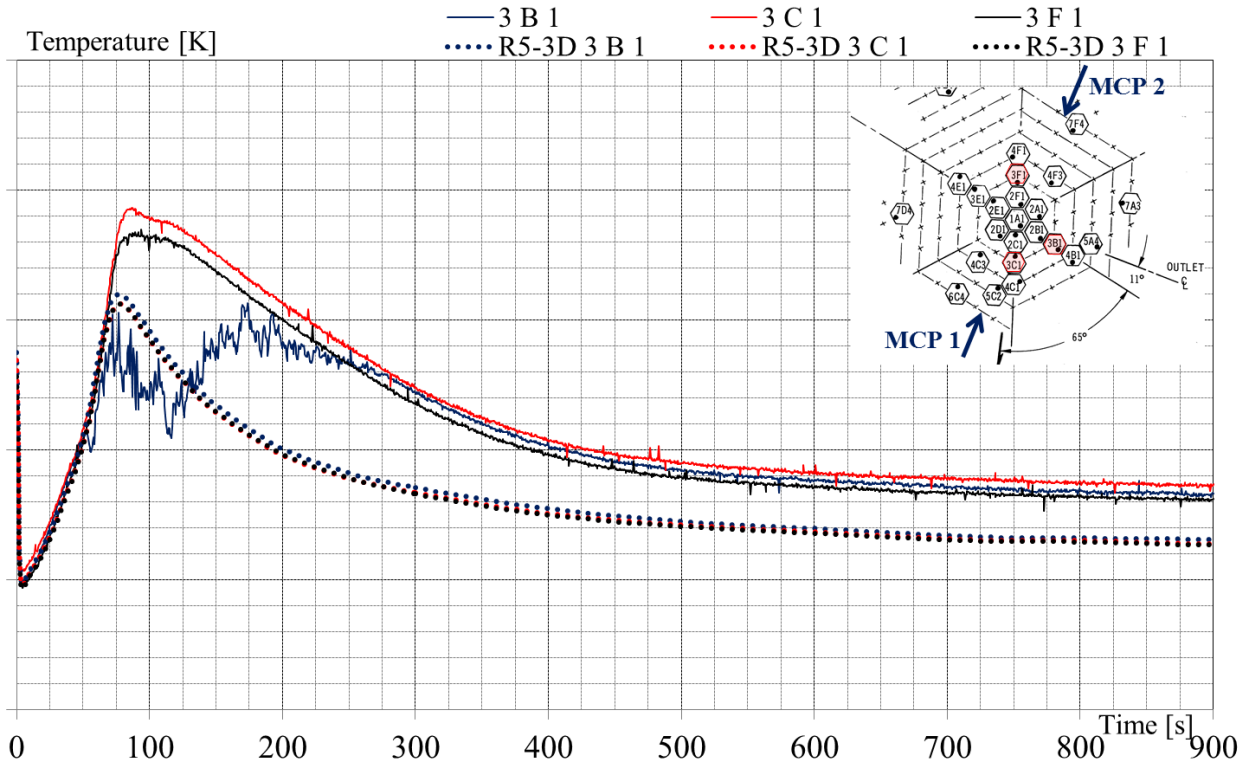

Fig. 81 – EBR-II SHRT-17, RELAP5-3D©: Subassembly Outlet Temperature (Row 3).

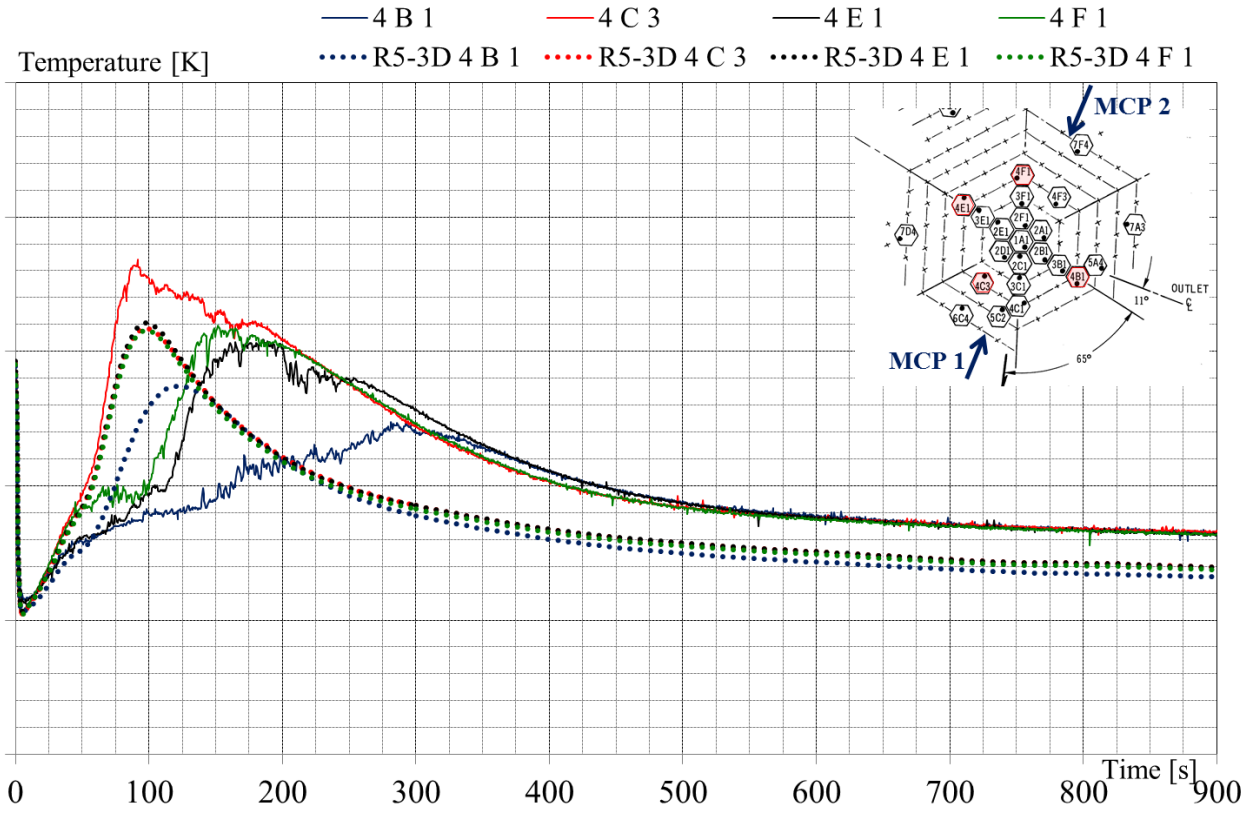

Fig. 82 – EBR-II SHRT-17, RELAP5-3D©: Subassembly Outlet Temperature (Row 4).

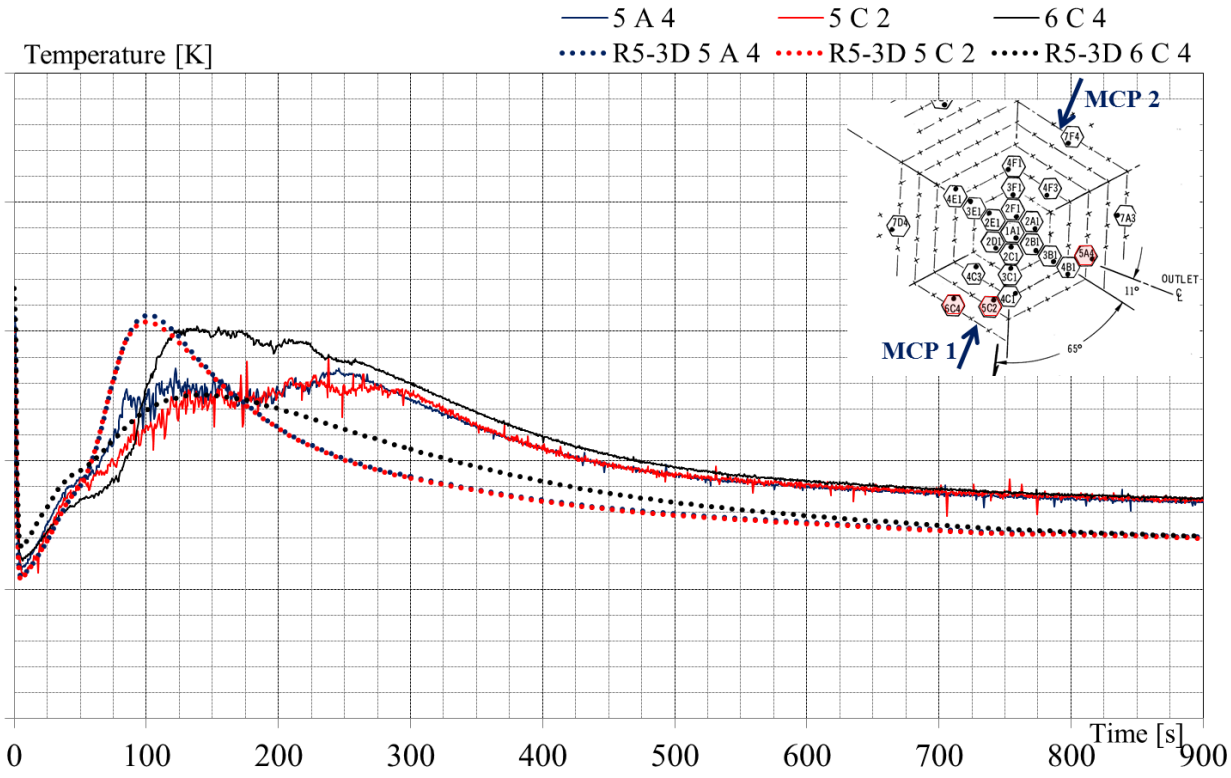

Fig. 83 – EBR-II SHRT-17, RELAP5-3D©: Subassembly Outlet Temperature (Row 5 and 6).

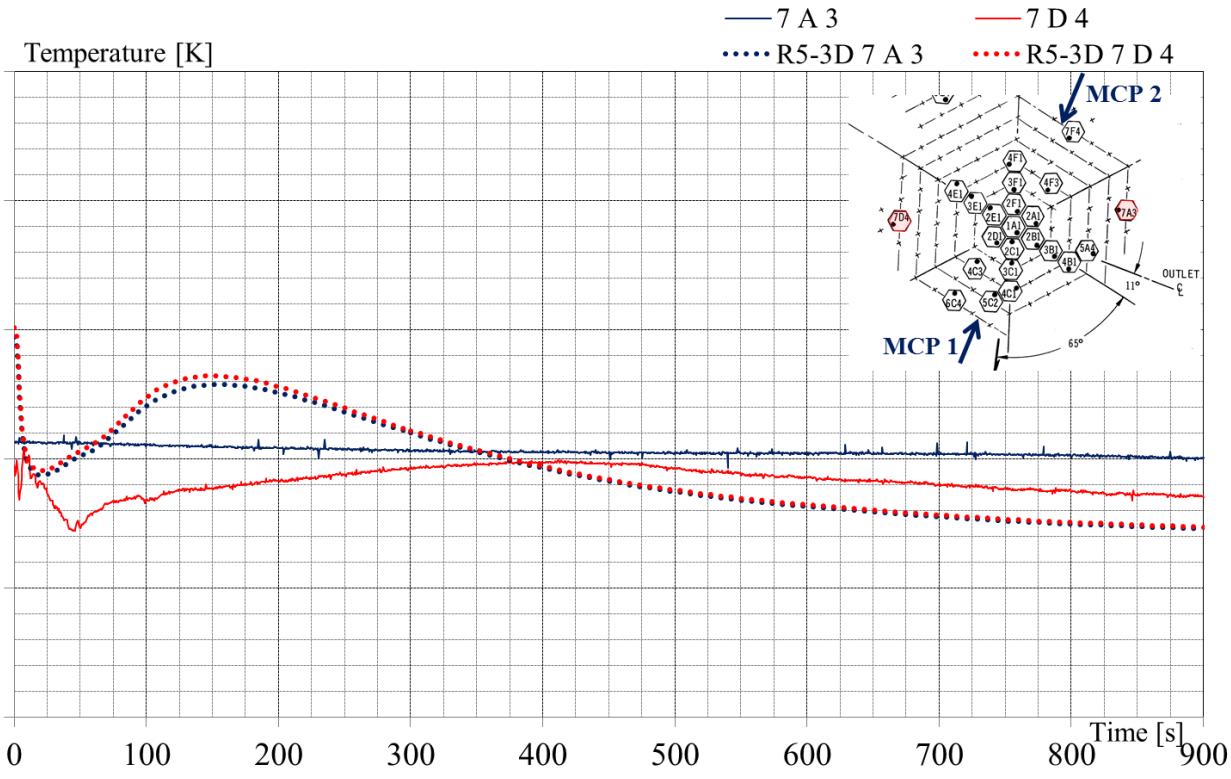

Fig. 84 – EBR-II SHRT-17, RELAP5-3D©: Subassembly Outlet Temperature (Row 7).

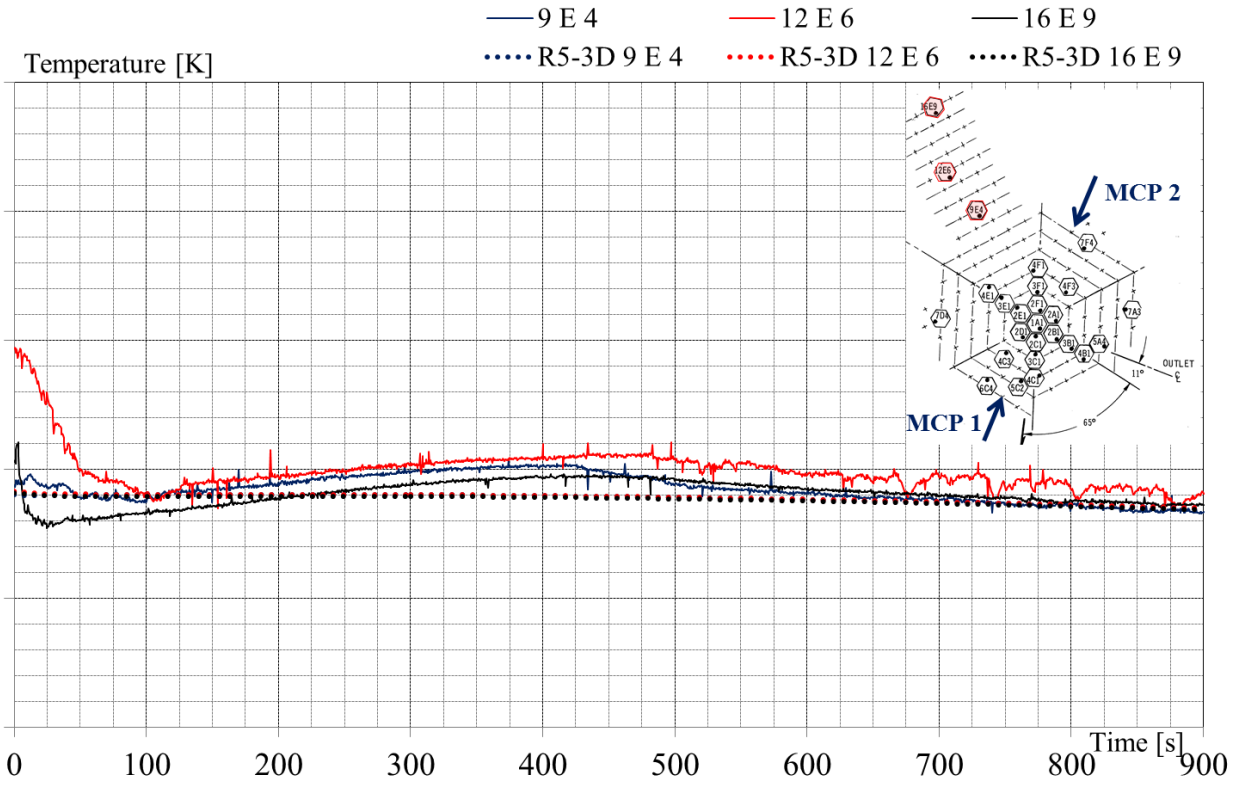

Fig. 85 – EBR-II SHRT-17, RELAP5-3D©: Subassembly Outlet Temperature (Row 9, 12 e 16).

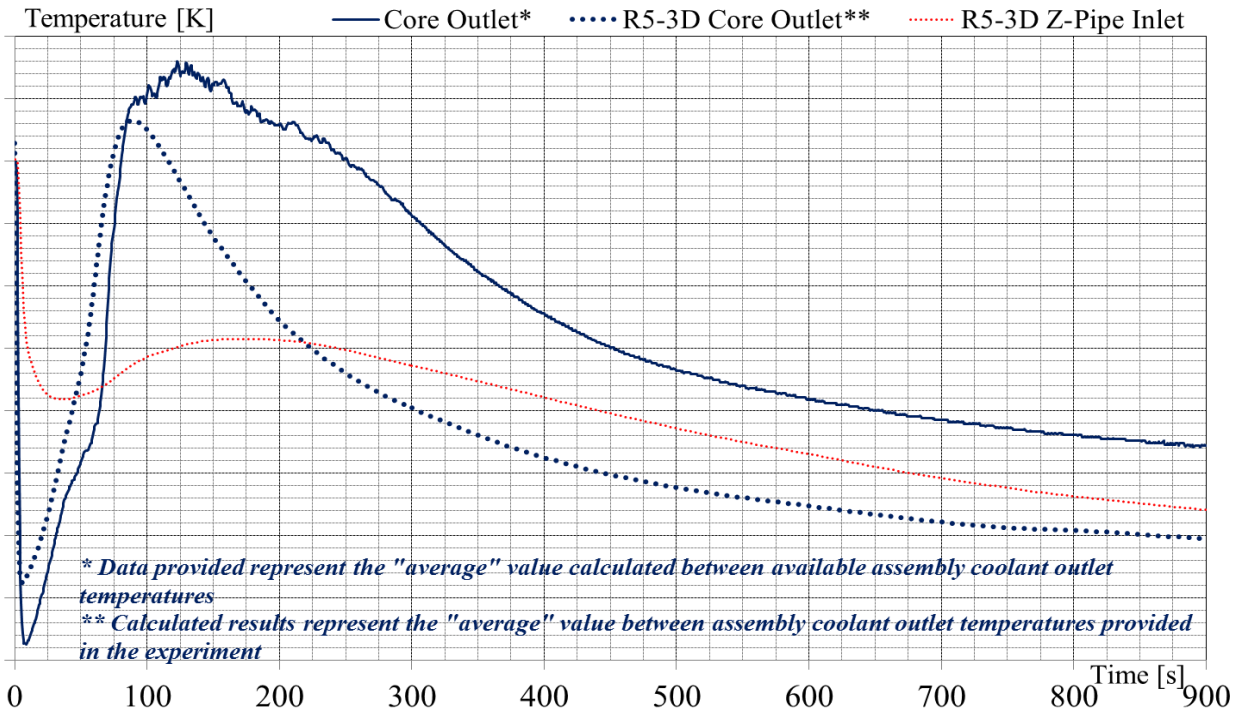

Fig. 86 – EBR-II SHRT-17, RELAP5-3D©: Core Outlet Temperature.

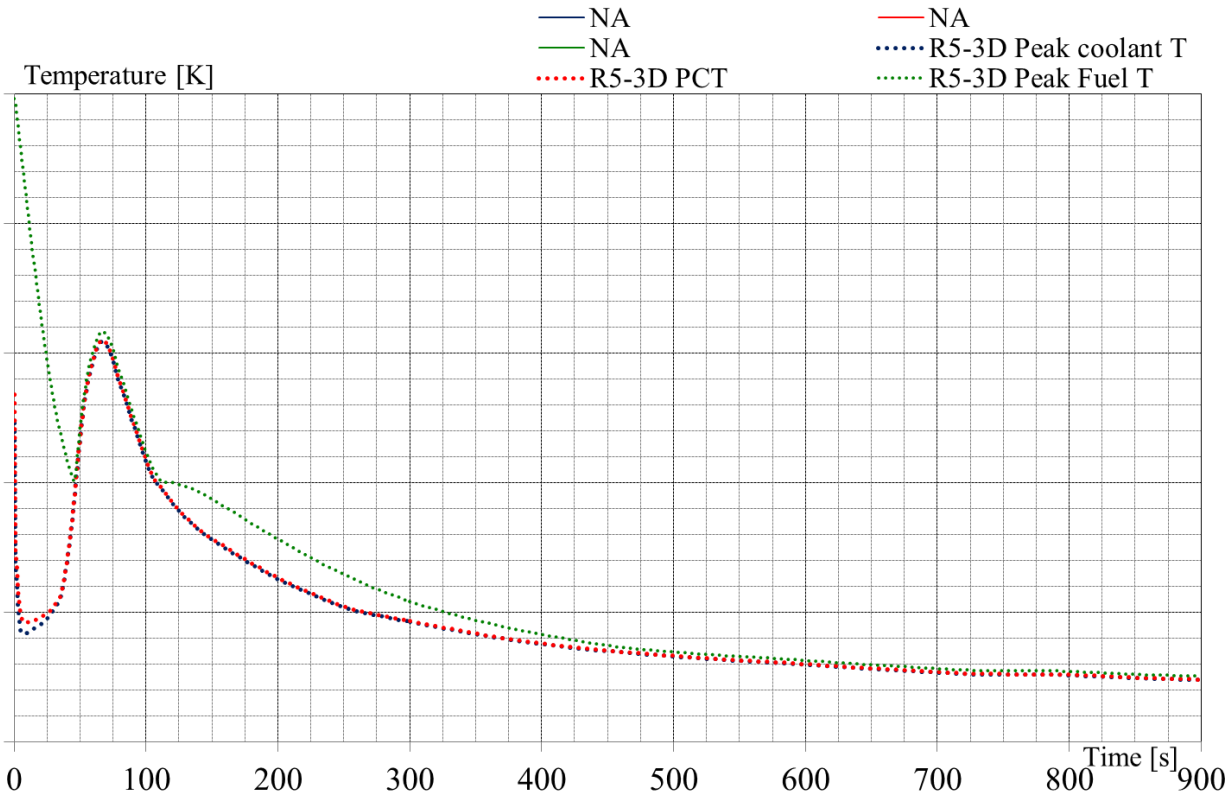

Fig. 87 – EBR-II SHRT-17, RELAP5-3D©: Peak Coolant Temperature.

6 CFD CODE PRELIMINARY ASSESSMENT FOR LM COOLED WIRE-SPACED FUEL ASSEMBLY

As a preparatory step to the CFD analysis of the XX09 EBR II Fuel Assembly, it is necessary to provide a preliminary validation of the ANSYS CFX code and the numerical approach for the wire-wrapped bundle geometry. The sodium cooled wire-wrap pin bundle designed and tested by M.H. Fontana et al. (1971) at ORNL was chosen as reference experimental data set. The working fluid is sodium and a large experimental campaign was carried out.

6.1 The experimental facility

The Fuel Failure Mockup (FFM) is a sodium test facility built specifically for testing simulated LMFBR core segments at Fast Test Reactor (FTR) design power and coolant flow conditions.

The FFM is a large, high-temperature sodium facility in which 19-pin bundles simulating LMFBR core segments were subjected to thermal-hydraulic testing at FTR conditions (see Fig. 88 for an overall layout). The core segments are simulated by electric cartridge heaters duplicating reactor fuel pin configuration and heat flux. Spirally wrapped wire-like spacers containing both grounded and ungrounded thermocouple junctions space the heaters in the assemblies.

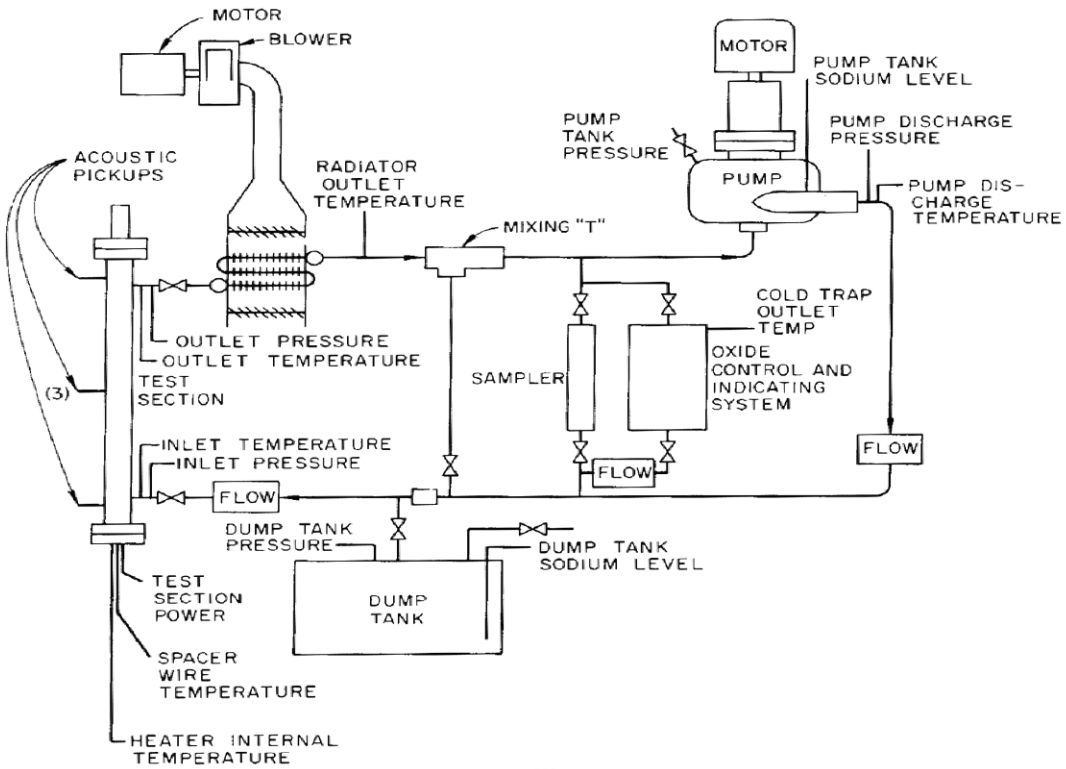

Fig. 88 – Fuel Failure Mockup test facility at ORNL.

These spacers have the same outside diameter and are installed at the same pitch as the spacers used in the FTR.
Sodium circulated in the FFM at temperatures as high as 650°C, and power levels in 19-rod test: bundles have been as high as 33.3 kW/m in the simulated fuel elements. In bundle 2A, the highest total power with all rods operating was 368 kW. The facility has logged 4310 hr of sodium circulation and approximately 500 hr with some power on the system. Flows as high as 12.2 kg/s

circulated through the test bundle, and tests were run in which the flow through the test section has been adjusted to less than 0.05 kg/s.
A number of heater bundles were scheduled to be tested in the FFM.
Bundles differ in number and power rating of the heaters, placement of instruments, configuration of the "can" which surrounds the bundle, and in mode of installation (i.e., from the top or bottom of the test section).

6.2 The test section and the rod bundle instrumentation

The test bundles are composed of 19 heaters assembled into a triangular pitch. A 1.42 mm diameter spacer wire, helically wrapped with a pitch of 305 mm is attached to each of the 19 heaters. The heaters are spaced so that the wire wraps on a given heater touch the adjacent heaters. The wire wraps for each of the heaters contain two thermocouples, which may be placed along the axial length of the heater to obtain temperature readings wherever desired. The wire wraps are supplied with either ungrounded- or grounded-junction couples. These grounded thermal elements provide two thermocouples that can measure the temperature on opposite sides of the wire wrap. By proper placement they can read temperatures in adjacent channels or at the wrap-heater interface and at the outside of the wire wrap.
Bundle 2A (simulated in this study), shown in Fig. 89, consisted of 19 pins with a rod diameter of 5.84 mm and a triangular pitch equal to 7.26 mm (pith to diameter ratio 1.24) with a wire pitch of 305 mm (12 in), contained in a hexagonal can, and was installed from the bottom of the test section. It consisted of a 305 mm-long (12 in.) unheated entrance section, a 533.75 mm (21 in.) heated section, and a 76.25 mm (3 in.) unheated exit section. A small clearance of 1.98 mm (0.078 in.) is present between the test section inner surface and the pin bundle simulator. The rod diameter (5.84 mm), the pitch to diameter ratio (1.24), the wire pitch (305 mm) and the length of the active region (533 mm) are shown in Tab. 35.

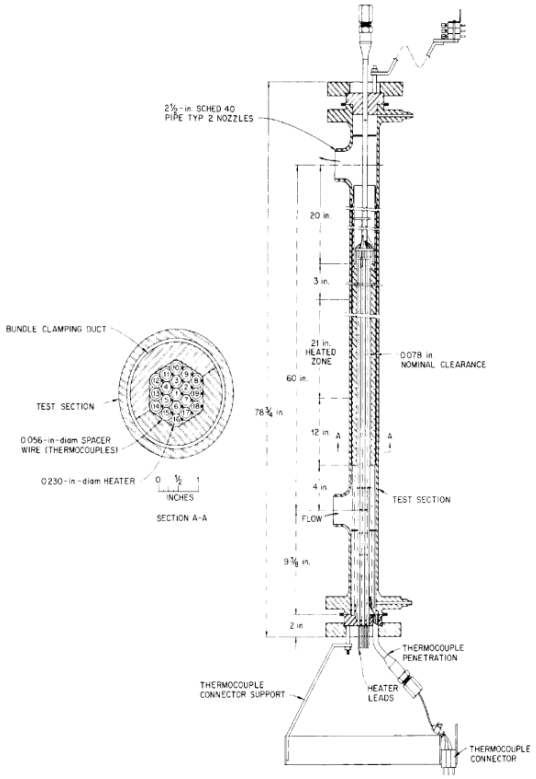

Fig. 89 – Bundle 2A test section of the FFM facility at ORNL.

	Fontana Bundle 2A
Rod diameter [mm]	5.84
Pitch to diameter ratio	1.24
Wire pitch [mm]	305
Length of the active region [mm]	533.75
Working Fluid	Sodium

Tab. 35 – Geometrical parameters of the Bundle 2A test section.

The purpose of the bundle 2A experiments was to provide data to be used for the design of the fuel elements for the Fast Flux Test Reactor (FTR) and to evaluate analytical models that were proposed to describe thermal-hydraulic behavior in the bundles.
Bundle 2A was designed to investigate local internal flow and heat transfer as affected by rod assembly spacers and to investigate the temperature profiles at and near the perimeter of a simulated FTR fuel pin bundle and wrapper. Fig. 90 and Fig. 91 show the configuration of bundle 2A and the temperature instrumentation installed. In these figures, the numbers in the large circles identify the heaters, and the numbers in the small circles indicate the axial position, in inches from the start of the heated zone at which thermocouple junctions exist. The position of the small circles relative to the large ones to which they are tangent indicates the azimuthal position of the wire-wrap spacer at the axial plane of the four internal thermocouple junctions. Fig. 91 shows how these spacers were arranged azimuthally. The crossed circles in Fig. 90 indicate the channels with exit thermocouples in the exit rake; the same figures also show the positions of thermocouples in the duct wall.

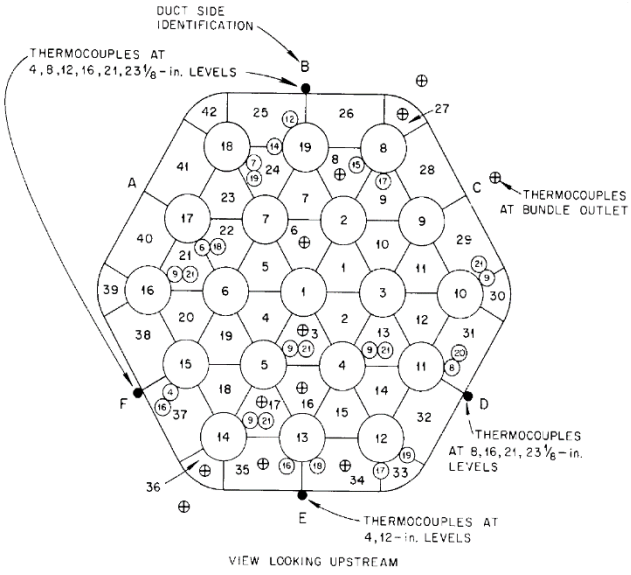

Fig. 90 – Locations of ungrounded-junctions in wire-wraps of bundle 2A.

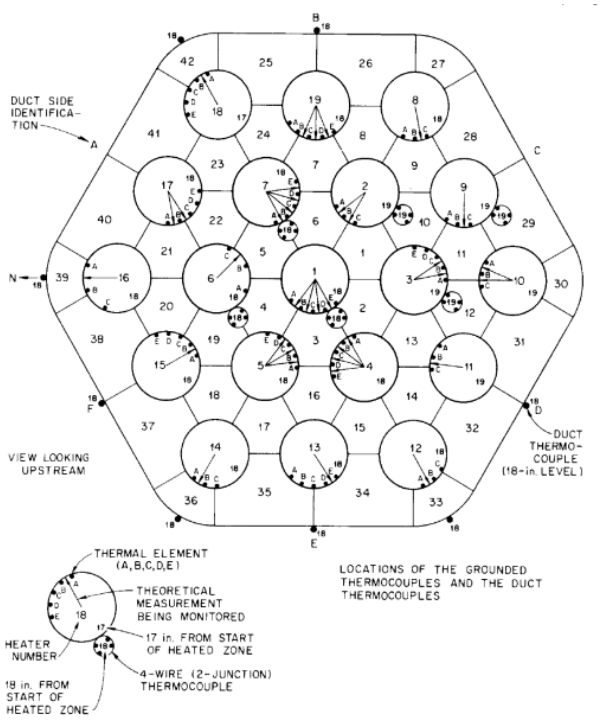

Fig. 91 – Locations of grounded-junctions in wire-wraps and heater internal thermocouples of bundle-2A.

6.3 The CFD model

The model developed includes the entire pin bundle length with the preceding and follower unheated regions and the heated one. The hexagonal duct is included into the model with the small annular fluid region between the test section housing and the pin bundle simulator for heat transfer reasons. The length of the hexagonal duct as the one of the annular region cover the heated region and the follower unheated one (because thermocouples are installed also there). A sketch of the model developed can be seen in Fig. 92.

The wire spacer is modeled with the interference solution widely adopted in the literature (see for example [37]). The annular region as well as the hexagonal duct are included to describe the conjugate heat transfer and to correctly describe the boundary conditions.

For the fluid into the pin bundle an unstructured tetrahedral mesh was adopted; the number of elements was increased near the solid structures achieving a y+ ~1 at the higher Reynolds number simulated. In the annular fluid region, a really fine structured mesh and an high resolution of the viscous sub-layer (y+ ~~1) was adopted. The hexagonal duct exploits a semi-structured mesh method.

The working fluid simulated is Sodium with constant properties fixed at 340 °C resumed in Tab. 36. Every buoyancy effect is neglected, being the Richardson number very small.

Sodium (340 °C)	
ρ [kg / m^3]	847
C_p [J / kg / K]	1300
μ [Pa s]	$2.3 \cdot 10^{-4}$
k [W / m / K]	70
Pr	$4.27 \cdot 10^{-3}$

Tab. 36 – Sodium properties implemented in the CFD model.

All the simulations are stationary RANS, the turbulence model generally adopted is the k-ω SST model [36], while the second order Omega Reynolds Stress model is used for a sensitivity study.

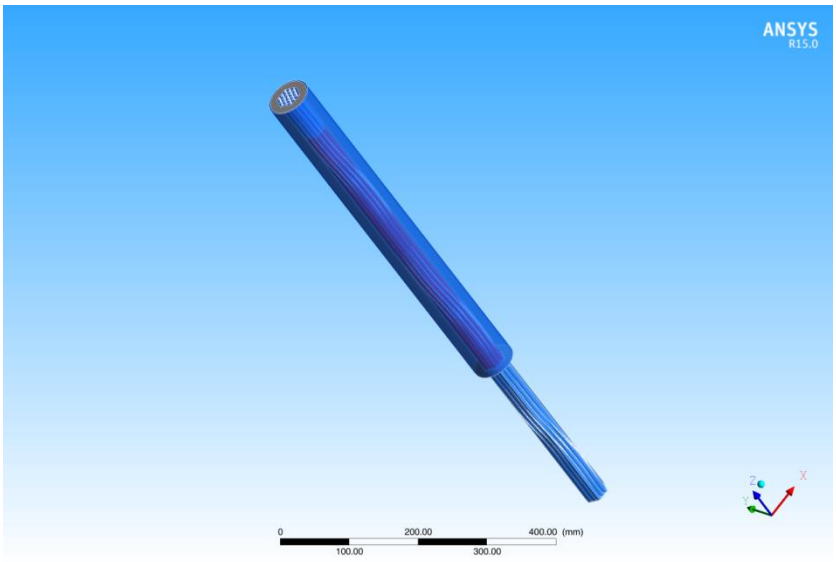

Fig. 92 – Layout of the CFD model developed for the bundle-2A.

The turbulent Prandtl number (Prt) imposed is 1.5 according to the literature [34].

The mass flow rate and the inlet temperature were imposed at the fluid inlet sections (both for bundle region and annular region). A constant zero pressure was kept on both outlet sections. A constant heat flux condition was imposed on the external surface of the annular region and on external hexagonal surfaces of the bundle inlet region (with not heated pins) because, during the tests, the outside heating cables were kept on; the total power imposed to simulate the heating cable power was derived from the declared data. A constant heat flux condition, specific for every pin, was imposed on pins' surfaces according to the test data.

Continuity of temperature and flux (interface conditions) were imposed on the interior and exterior surfaces of the hexagonal duct on the contact surfaces between fluid and solid.

For a better assessment of the ANSYS CFX code with wire wrapped geometry, the lower sub-channel Reynolds number cases were studied. The test series 4 experiments are particularly suitable because performed at low mass flow and low power.

6.4 Results for Bundle 2A

TEST SERIES 4, RUN 105 : The inlet mass flow rate (Gtotal) and the sub-channel Reynolds number are 0.27 kg / s and 8380 respectively. The inlet temperature is 587 K (596.84 °F). The total power given to the heated pins is 31.13 kW (Wpins), while the external power supplied by the heating cables and simulated equally distributed all over the model length is 5.95 kW (Wcables). The mass flow passing through the annular region is hypothesized as 5 % of the inlet one (Ganular), because it was not measured.

The CFD results are compared with temperatures measured near pins and walls by ungrounded thermocouples at different heights. As it can be observed from Fig. 93, the temperature difference between CFD results and experimental values could reach 13.6 K. More accurate predictions could be reached for the duct (internal wrap) wall temperatures shown in Fig. 94, where the maximum temperature difference is 9.9 K, while the mean difference is 3.4 K.
The different agreement shown in the two comparisons is justified by the absence of the solid structures of the pins in the CFX model and an inaccurate description by the authors of thermocouples position and the pin bundle geometry.

Further details and other test cases can be found in [38]. The CFD results have a good but not excellent agreement with the experimental data especially in the central region of the bundle. This not perfect agreement can be explained by the inaccurate description given by the authors of the pin bundle geometry, the considerable thermal gradient across the wire-wrap spacer and the unspecified exact position of the wire-wrap thermocouples.

On the overall, CFD code assessment and approach can be considered acceptable.

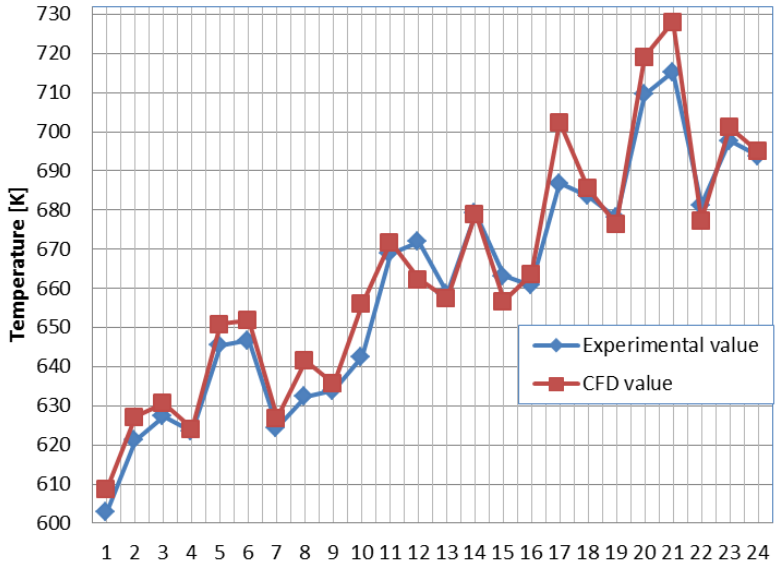

Fig. 93 – Comparison of pin temperature predictions at different heights with TEST SERIES 4-RUN105 experimental results.

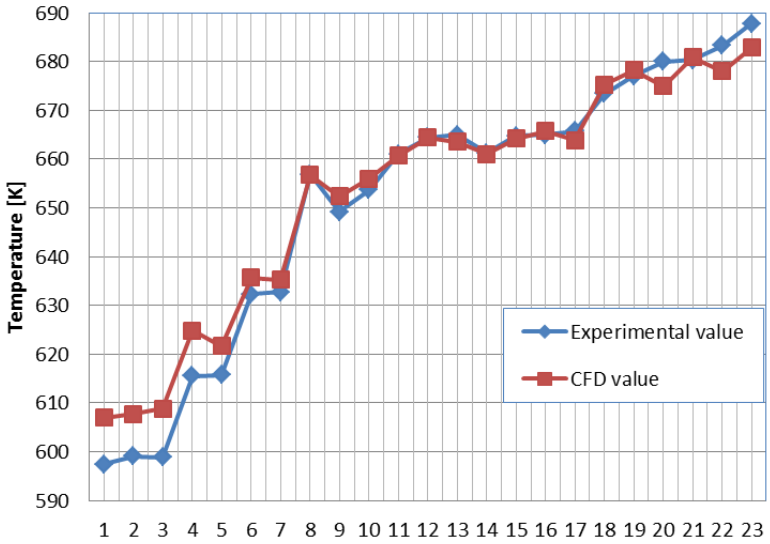

Fig. 94 – Comparison of duct (wrap internal) temperature predictions at different heights with TEST SERIES 4-RUN105 experimental results.

7 CFD MODEL OF THE XX09 INSTRUMENTED FA

7.1 Numerical Methods

The general purpose code ANSYS CFX 13 was used for all the numerical simulations presented in this paper. The code employs a coupled technique, which simultaneously solves all the transport equations in the whole domain through a false time-step algorithm. The linearized system of equations is preconditioned in order to reduce all the eigenvalues to the same order of magnitude. The multi-grid approach reduces the low frequency error, converting it to a high frequency error at

the finest grid level; this results in a great acceleration of convergence. Although, with this method, a single iteration is slower than a single iteration in the classical decoupled (segregated) SIMPLE approach, the number of iterations necessary for a full convergence to a steady state is generally of the order of 102, against typical values of 103 for decoupled algorithms.
The SST (Shear Stress Transport) k-ω model by [36] is used in this report. It is formulated to solve the viscous sub-layer explicitly, and requires several computational grid points inside this latter. The model applies the k-ω model close to the wall, and the k-ε model (in a k-ω formulation) in the core region, with a blending function in between. It was originally designed to provide accurate predictions of flow separation under adverse pressure gradients, but it was applied to a large variety of turbulent flows and is now the default and most commonly used model in CFX-13 and other CFD codes. This structural feature of the model to predict in a good way flow separation and recirculation gives a good confidence in applying the model to compute flow blockage in fuel subassemblies. The turbulent Prandtl number in the case of was fixed to 1.1, according to the suggestion of the literature [34].

7.2 The CFD model of the EBR2 XX09-XX10

The purpose of the CFD model is to provide information on the detailed temperature distribution of the generic FA. To achieve this goal and in order to validate the numerical method, the instrumented EBR II Fuel Assemblies XX09 and XX10 were chosen as reference. The exact geometry for the model was derived by the information in the Benchmark specification document for shutdown heat removal tests SHRT-17 and SHRT-45R. The XXX09/XX10 Fa consists of 61 pins with cladding O.D. 4.41 mm. The wire spacer has a diameter of 1.24 mm.

To better describe the heat transfer phenomena in the FA, the model was built including all the wire-wrapped regions and all the subchannels of the FA without any symmetry plane, see Fig. 95 for an overview.
In the mainstream flow direction, the model includes both the active region at the beginning, the non-active region downstream and the helicoidally wrapped wires. In this way, the fluid dynamic phenomena inside the FA can be well captured.
In the cross-section, the model includes the internal wrap, the thimble region, the external wrap and the Bypass region, see Fig. 96 for details. This kind of model allows to correctly keep into account the contribution of the radial heat transfer across the bundle by simulating the conduction in the wraps and convection in the thimble and in the bypass.
The conjugate heat transfer in the wire and in the clad will be introduced in the next year of activity.
The physical properties for Sodium were implemented coherently with the Database provided by Sobolev [40]. For the wraps, the AISI 304 SS properties were used according to the indications of the benchmark for XX09/XX10 FA.

The model was meshed in a semi-structural way in the wraps, in the bypass and in the thimble, while a non-structured approach was followed inside the FA. A zoom view of the computational model is shown in Fig. 97. A mesh independence study was carried out preliminary to assess the internal coherence of the study. The reference ‘H’ mesh was adopted for the calculations with about 3.3·107 nodes.

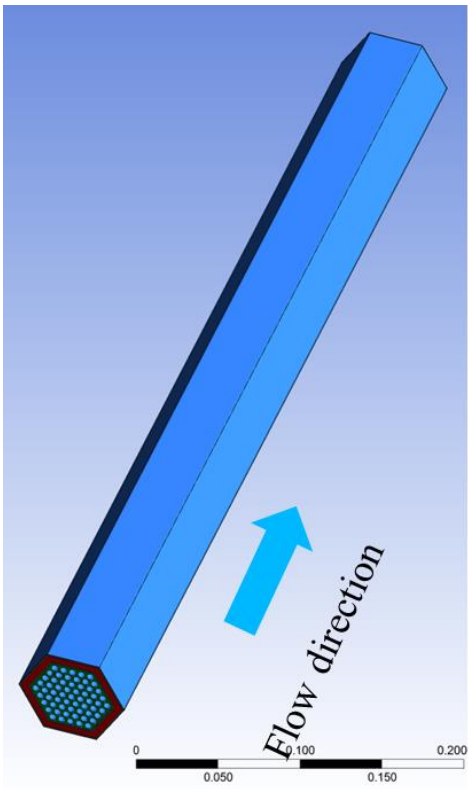

Fig. 95 – Overview of the CFD model for the XX09/XX10 FA of the EBR II reactor.

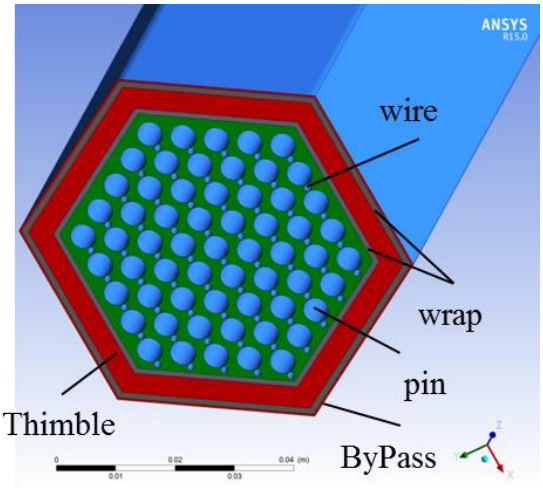

Fig. 96 – Cross section view of the CFD model for the XX09/XX10 FA of the EBR II reactor.

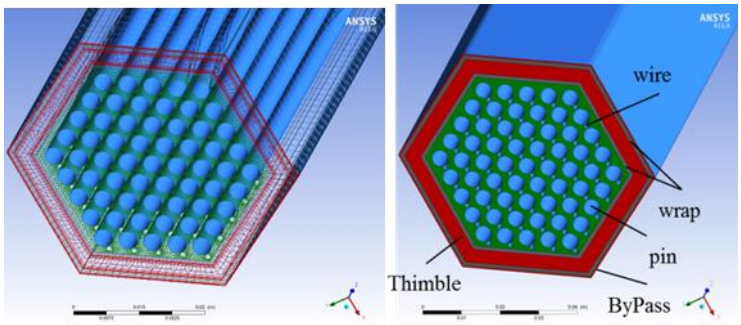

Fig. 97 – Zoom view of the computational mesh of the XX09/XX10.

The model is in principle time-dependent, but it can be run in stationary mode as well.
The goal of the first year of activity is to perform a one-way coupling with the RELAP model .RELAP will provide as Input information for the CFX model:

- The mass flow rate in the FA mFA;
- The mass flow rate in the Thimble mTHIMBLE;
- The mass flow rate in the Bypass mBYPASS;
- The inlet temperature Tinlet;
- The total power of the FA Wtot,FA;

The total power of the FA was imposed as heat flux qwall [W/m2] at the clad external wall. Mass flow and temperatures were imposed at the channel inlets, while a standard output pressure condition was imposed at the outlet.
The output of the CFD simulation are the detailed temperature distribution in the fluid and in the Thimble region.
At a first stage, and for the assessment of the method against experimental data, only stationary cases at full power were carried out. The 'Inertial Stationary' method will be adopted to simulate the details of the thermal and fluid dynamics field in the FA during the accident transient, see section 7.3 for details.

7.3 Results and future work

A stationary CFD simulation at full power in nominal conditions (CS03) was run according to the parameters reported in Tab. 37. The average velocity in the bundle is around 4 m/s with a fully turbulent flow.

m_{FA} *[kg/s]*	2.37
$m_{THIMBLE}$ *[kg/s]*	0.25
m_{BYPASS} *[kg/s]*	$6.076 \cdot 10^{-3}$
T_{inlet} *[K]*	626.1
Wtot,FA [kW]	464.7

Tab. 37 – Parameters used for a CFD simulation: stationary case CS03 at full power from RELAP input.

Three different measuring sections (MTC, TTC, 14TC) are present in the XX09 instrumented FA at the ANL, according to Tab. 38. Fig. 98 shows the XX09 Instrumented subassembly axial section with the indication of the measuring planes. The location of the thermocouples in the different measuring plane is then visible in Fig. 99. The total length of the active region is h=343 mm, therefore MTC is in the middle of the active region, TTC is at the top of the active region and 14TC is in the mixing region above the active region.

	Δh [mm]
MTC	172
TTC	322
14TC	480

Tab. 38 – Distance Δh of the measurement sections (MTC, TTC, 14TC) in the streamwise direction from the beginning of the active region.

A perspective view of the temperature contours in the rod bundle for CS03 is presented in Fig. 100. The behavior appears realistic with an overall temperature gradient along the streamwise direction and a radial temperature gradient with a hot region in the central pins. Moreover, the CFD model allows to study the mixing phenomena in the non-active region downstream. Pins 1 and 2 in Fig. 99 are not heated according to the benchmark description.

To make a meaningful comparison with the experimental data, in each measuring section (MTC, TTC, 14TC), thermocouples were ordered with a serial number from 1 to N. Values were then plotted for each section and compared with experimental data. In Tab. 39, a comparison between experimental data and temperatures values in the corresponding monitoring points of the CFD model is reported.
Fig. 101, Fig. 102 and Fig. 103 show the temperatures against the TC serial number for the ANL experimental data and CFD numerical simulation, for MTC section, TTC section and 14TC section respectively.

		ANL exp [K]	CFD CS03 [K]	err[K]
Lower Flowmeter Temperature (FM-1TC)		**626.7**	**626.1**	
Upper Flowmeter Temperature (FM-2TC)		**629.5**	**626.1**	
Flow		**2.377**	**2.377**	
TC Number				
1	Mid Core (MTC-20)	**727.4**	**726.4**	**-1.0**
2	Mid Core (MTC-22)	**750.3**	**725.3**	**-25.0**
3	Mid Core (MTC-24)	**753.9**	**719.5**	**-34.4**
4	Mid Core (MTC-25)	**750.5**	**708.9**	**-41.6**
5	Mid Core (MTC-26)	**716.5**	**672.5**	**-43.9**
1	Core Top (TTC-8)	**778.9**	**786.0**	**7.1**
2	Core Top (TTC-15)	**807.5**	**805.1**	**-2.4**
3	Core Top (TTC-27)	**761.2**	**779.4**	**18.1**
4	Core Top (TTC-28)	**792.7**	**809.2**	**16.5**
5	Core Top (TTC-29)	**800.3**	**815.4**	**15.1**
6	Core Top (TTC-30)	**805.9**	**813.9**	**8.0**
7	Core Top (TTC-31)	**814.0**	**812.1**	**-1.8**
8	Core Top (TTC-32)	**810.7**	**807.0**	**-3.7**
9	Core Top (TTC-33)	**811.7**	**795.3**	**-16.4**
10	Core Top (TTC-34)	**785.0**	**763.1**	**-21.9**
11	Core Top (TTC-35)	**728.3**	**717.7**	**-10.5**
12	Core Top (TTC-47)	**812.4**	**809.9**	**-2.5**
13	Core Top (TTC-53)	**801.3**	**802.5**	**1.3**
1	Above Core (14TC-37)	**791.9**	**815.6**	**23.7**
2	Above Core (14TC-39)	**809.1**	**822.9**	**13.8**
3	Above Core (14TC-41)	**805.9**	**803.3**	**-2.6**
4	Above Core (14TC-43)	**734.4**	**742.9**	**8.5**
Coolant Outlet (OTC-01)		**758.7**		
Coolant Outlet (OTC-02)		**759.6**		
Thimble Annulus (ATC-A1)		**739.4**		
Thimble Annulus (ATC-A2)		**745.9**		

Tab. 39 – Comparison between experimental and numerical CFD results for CS03 (XX09).

XX09

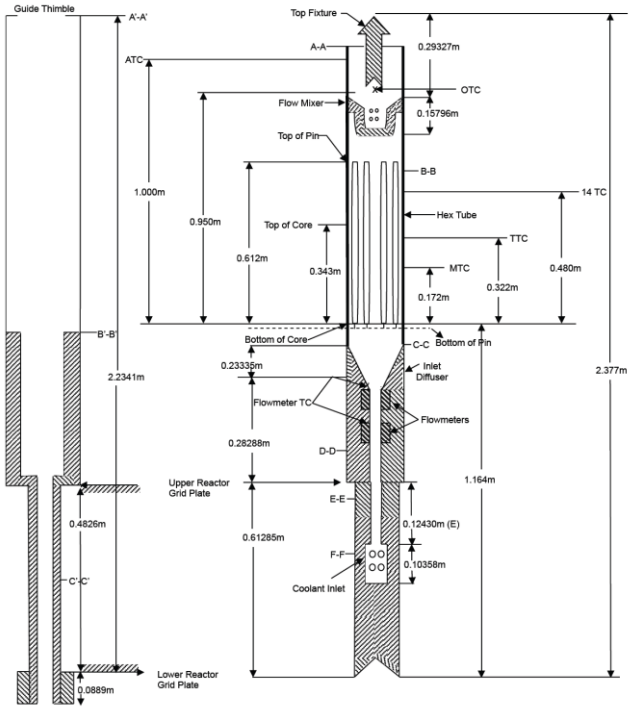

Fig. 98 XX09 Instrumented subassembly axial section.

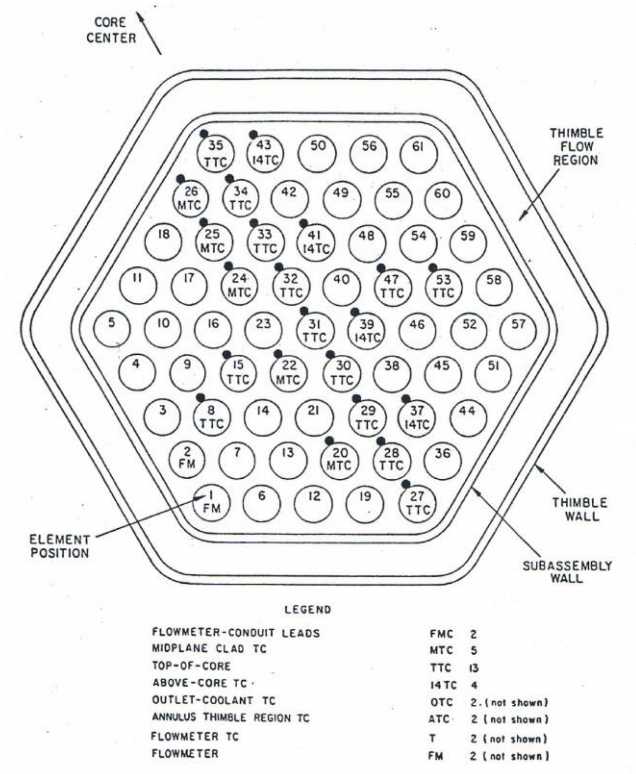

Fig. 99 XX09 Instrumented subassembly instrument loading.

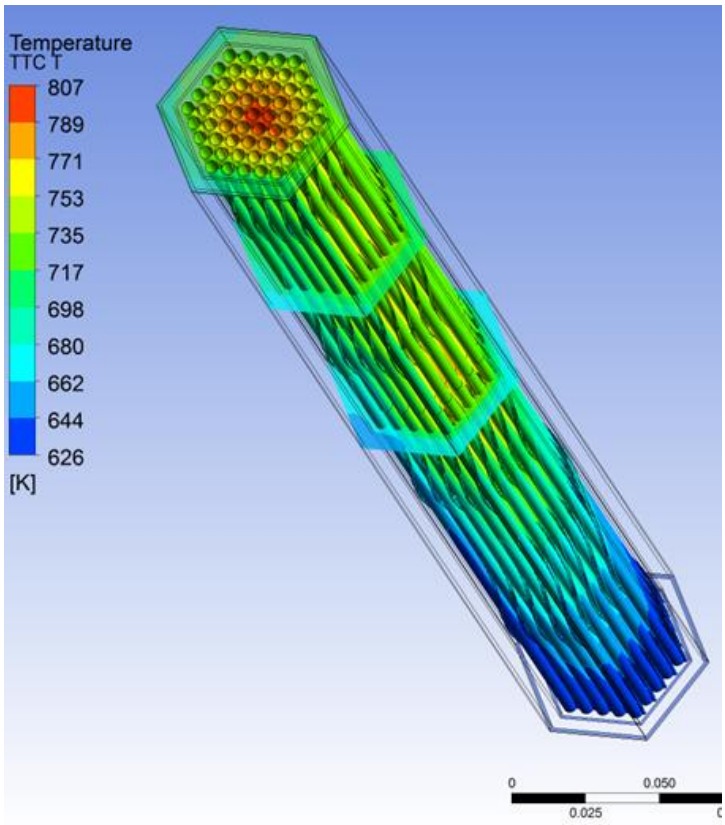

Fig. 100 – Perspective view of the temperature field in the rod bundle XX09 by CFD simulation, CS03.

In the MTC measuring section in the middle of the active region, Fig. 101, a large under-estimation is present, with a maximum difference of 44 °C for TC 5 (MTC-26), i.e. in the peripheral subchannels. This large error is probably due to the developing region for the thermal boundary layer. It should be remembered that it is well known from the literature that the developing length for temperature is very high for liquid metal cooled wire-wrapped fuel assembly [39]. To improve the results, probably the mesh must be refined in the developing region to correctly compute conduction losses. Nevertheless, apart from this latter known limitations, at least part of the error is due to the missing geometry information on the wire position. Practically the exact geometry is not precisely known and the detail of the detachment angle of the wire at the inlet of the active region was not specified with the benchmark and not released by ANL.
In the TTC measuring section at the end of the active region, Fig. 102, the overall behavior is well captured and the error is low. The main conclusion is that the model has a good local refinement and the conduction losses as well as the convective heat transfer are both well captured in the middle-top of the active region of the FA.
In the 14TC measuring section in the non-active region, Fig. 103, the overall behavior is well captured; the error is low in TC-41 and in TC-43 and higher in TC-37 and TC-39.

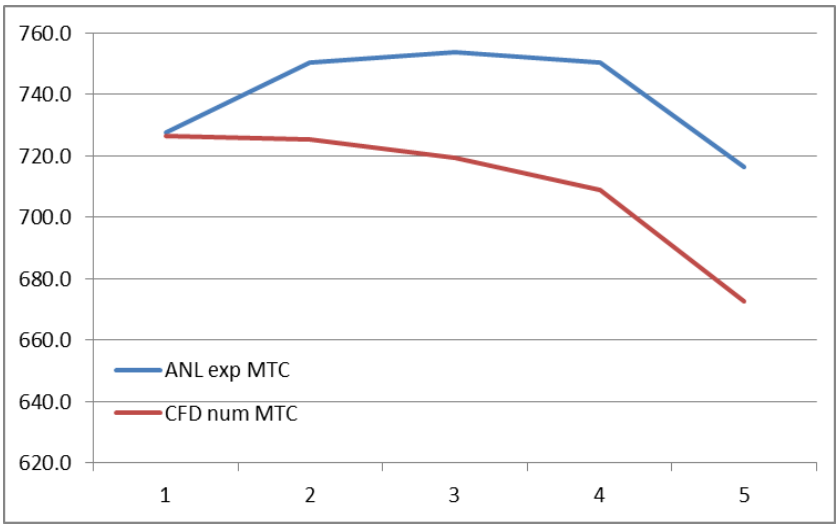

Fig. 101 – Temperature in K against the thermocouple number for section MTC, CS03: comparison between experimental data and numerical results.

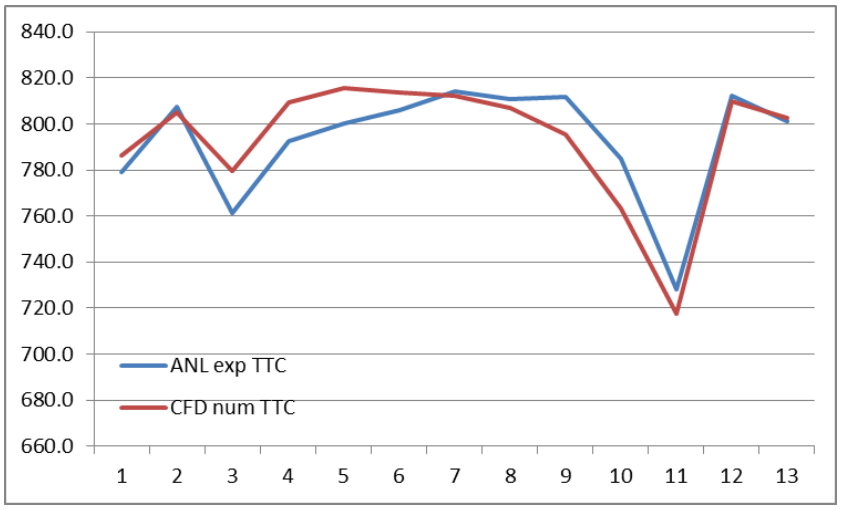

Fig. 102 – Temperature in K against the thermocouple number for section TTC, CS03: comparison between experimental data and numerical results

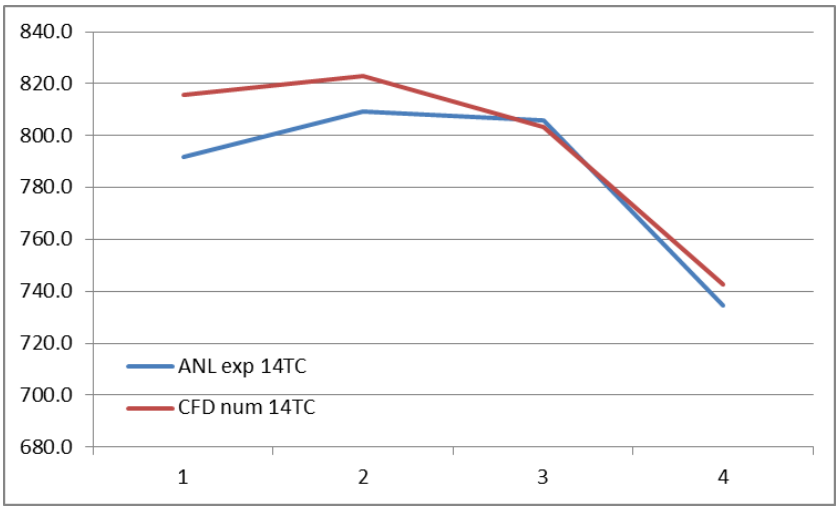

Fig. 103 – Temperature in K against the thermocouple number for section 14TC, CS03: comparison between experimental data and numerical results.

Results show that the model is globally well balanced, the resolution is enough, and the physics inside is sufficient to capture the basic features. At the beginning of the active region the error in the prediction is high but this is probably due to the lack of geometric information.
The same CFD approach was validated in a similar geometry for the Sodium cooled Fuel Failure Mockup (FFM) of the Oak Rigde National Laboratory [35], see section 6. Results showed that the agreement between experimental data and numerical CFD data is very good in the peripherals subchannels and the role of the conjugate heat transfer is very important. In the central subchannels the agreement is sufficient and globally the CFD model provides good results.

Fig. 104 shows the temperature distribution in the measuring cross-sections according to the CFD model. The temperature scale is the same for the three sections and the cold spot in the bottom left corner is due to the fact that pins 1 and 2 are not active. The asymmetry in the temperature distribution in the core (sections MTC and TTC) is due to the wire orientation that induces a strong cross flow in the bundle. In the non-active region above the active region, the symmetry is recovered because of the overall mixing. It should also be noticed that it is necessary to model the thimble and the bypass in order to get realistic boundary conditions for the FA. In fact the role of radial and conjugate heat transfer through the structures is relevant.

The cross-flow in the FA is visible in Fig. 105, where the secondary vector plots are colored by the vector magnitude. As it was expected, strong flows in the peripherals subchannels take place; the magnitude of this secondary flow is of the order of 10% of the mainstream flow (0.5 m/s against 4 m/s).

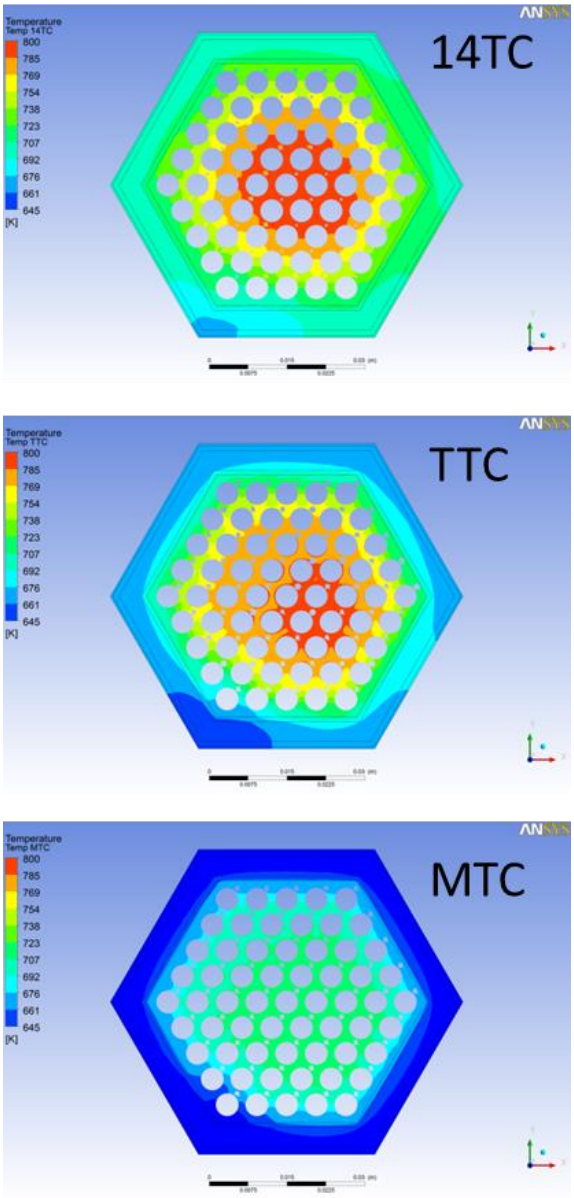

Fig. 104 – Temperature contours in the XX09 FA , CS03, in the measuring planes, according to the CFD simulation.

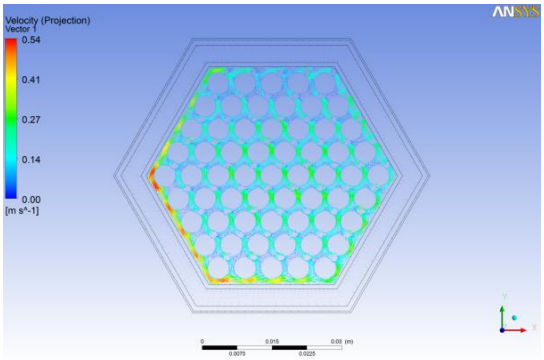

Fig. 105 – Secondary velocity vector plot in the MTC cross-section. The color scale is the module of the vector.

Regarding the future work, it is virtually impossible to follow the entire 900 s transient for SHRT-17 by CFD. This is because the computational cost would be too large.

For comparison with transient experimental results, some 'CFD picture' will be taken in the most relevant instants of the transient. A simple CFD simulation with boundary condition taken from RELAP would imply a large error due to the missing inertia contributions. For this reason, a method called 'Inertial Stationary'(IS) must be implemented. To take into account of the relevant inertia of the fuel, at the generic time t0, a corrected wall heat flux will be imposed:

$$q_{wall}(t_0) = \frac{\mathrm{Re}lapPower(t_0)}{S_{active}} - M_{fuel} c_{p,\,fuel} \left.\frac{dT_{fuel}}{dt}\right|_{t_0} \cdot \frac{1}{S_{act}} \qquad (1)$$

This corrected wall heat keeps into account that part of the power is actually used to change the Fuel temperature via the specific heat c_p. From the available data, it was estimated that the correction with respect to the 'simple' wall heat flux can be of the order of 25 % and it is maximum when the fuel temperature derivative is maximum.
The method provides 'CFD stationary picture' at a given instant coherent with the physics of heat transfer.
Another improvement could be the introduction of the Fuel and the clad into the model. This improvement is not strictly mandatory for the IS method because the correction (1) is already implemented. On the other side, the conjugate heat transfer in the clad and in the wire could be relevant and it should be included into the model.
Tab. 40 shows the test matrix to be run in the next numerical campaign in 2014-2015.
The mesh H4 adopted for the stationary nominal case CS03 is by far sufficient to capture flow features at lower Reynolds numbers during the transient.

CASE	ASSEMBLY	MESH	TYPE	t0[s]	Qtot [W]	mFA0[kg/s]	mTHIMBLE0[kg/s]	mBpass0[kg/s]	Tinlet0[K]	PHYSPROP	Scheme	Inertia CORR	IC	Run state
CS03(G)	XX09	G	STAT	0	464417	2.37	0.249	5.00E-03	626.1	CONST	UPW	NO	-	X
CS03(H5)	XX09	H5	STAT	0	464417	2.37	0.249	5.00E-03	626.1	CONST	UPW	NO	-	X
CS03(H4)	XX09	H4	STAT	0	464417	2.37	0.249	5.00E-03	626.1	CONST	UPW	NO	-	X
CS04	XX09	H4	STAT	0	464417	2.37	0.249	5.00E-03	626.1	VAR	HighOrd	NO	-	X
CS05	XX09	H4	IS	48	20343	0.0756	0.0079	1.59E-04	626.1	VAR	HighOrd	YES	-	X
CS06	XX09	H4	IS	54	Relap	Relap	Relap	Relap	Relap	VAR	HighOrd	YES	-	
CS07	XX09	H4	IS	60	Relap	Relap	Relap	Relap	Relap	VAR	HighOrd	YES	-	
CS08	XX09	H4	IS	66	Relap	Relap	Relap	Relap	Relap	VAR	HighOrd	YES	-	
CS09	XX09	H4	IS	72	Relap	Relap	Relap	Relap	Relap	VAR	HighOrd	YES	-	
CS10	XX09	H4	IS	78	Relap	Relap	Relap	Relap	Relap	VAR	HighOrd	YES	-	
CS11	XX09	H4	IS	84	Relap	Relap	Relap	Relap	Relap	VAR	HighOrd	YES	-	
CS12	XX09	H4	IS	90	Relap	Relap	Relap	Relap	Relap	VAR	HighOrd	YES	-	
CT01	XX09	H4	TRANS	48	464417	Relap	Relap	Relap	Relap	VAR	HighOrd	YES	C05	

Tab. 40 – EBR-II SHRT-17: Test matrix for the CFD IS method to be performed in 2014-2015.

8 ERANOS CORE MODEL

EBR-II core model considered within the framework of the present study is implemented in ERANOS 2.1 neutronic deterministic code, according to details provided in benchmark guidelines (see Section 2.3).

All assemblies are modeled through ECCO cell code obtaining related spectra and cross-sections, then all cell parameters are associated to geometry regions during reactor core calculation phase – according to core pattern (see Fig. 3 and Fig. 4).
Central core standard driver fuel assembly composition is reported as an example – see Fig. 106. Active zone parts require detailed cross-section evaluations. By contrast, subcritical media are treated accounting for single composition as a whole. For instance, composition for Mark-II AI according to axial sections in Fig. 106 are reported in Tab. 41. Each cell data is stored for reactor calculation either in heterogeneous form or in the homogeneous one.

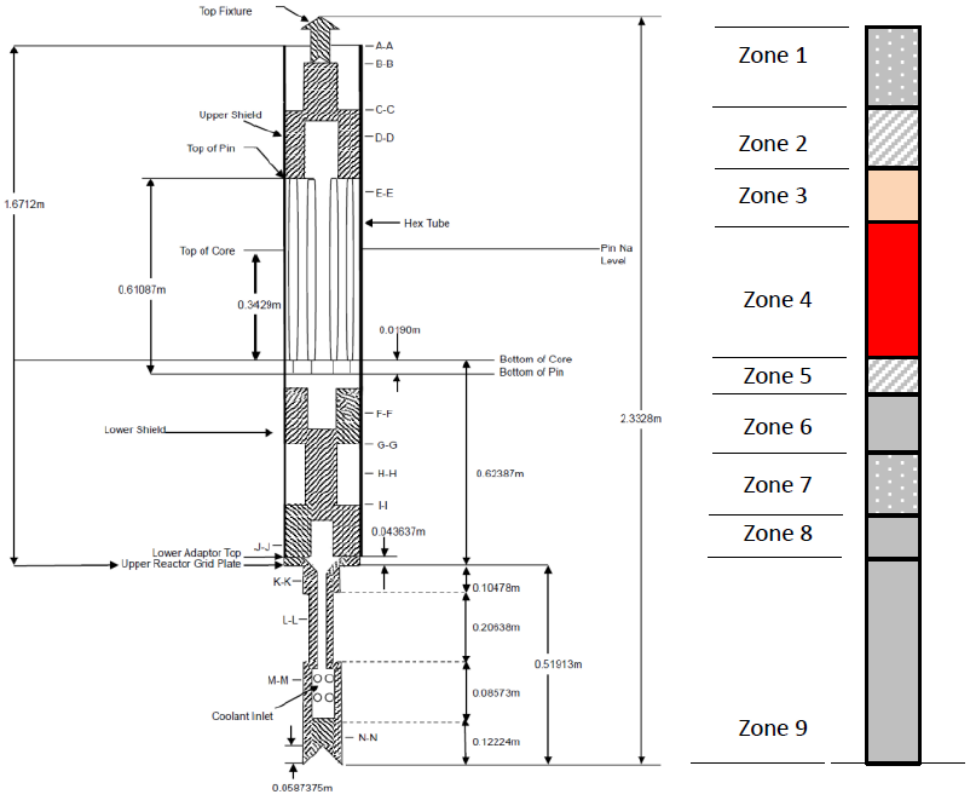

Fig. 106 – EBR-II: Axial breakdown of driver fuel subassembly Mark-II AI.

Deterministic calculations are carried out starting from cell code ECCO which is a part of ERANOS 2.1 package. A cell is intended as a reactor region in which a particular neutron spectrum is present – dedicated neutronic calculations are performed.
Cell description is either homogeneous or heterogeneous depending on impact of Doppler self-shielding and resonances in spectrum definition – regarding macroscopic cross-sections of the system. Nuclear data are processed by means of cell code ECCO.
Pin geometry – or particular frames - are implemented and lattice structure is considered. Nuclear data cross section calculations are carried out according to JEFF 3.1.1 nuclear data. Domain is treated at homogeneous level at 72 energy groups, P1 approximation thorough iterations

approaching criticality – namely buckling imposed and self-shielding is evaluated. A second iteration is performed with 172 energy groups and heterogeneous domain. In addition, collision probability is used here accounting for an exact geometry. Energy structure is then extended to 1968 groups and all elements are treated for resonances. Energy structure is then condensed to 33 groups and finally homogeneous P1 data are stored for next reactor simulations. Reactor core domain is then prepared. Hexagonal standard geometry is described through several annulus – size is coherent with RELAP3D simulation. ERANOS standard nodal solver VARIANT is replaced with AVNM solver - which is similar to standards DSA methods for diffusion acceleration techniques of transport theory. Direct calculations are performed and core normal configuration is simulated – control rod positions defined in order to characterize initial state for shutdown simulation.

	AISI 316	AISI 304	Sodium	Gas /Fuel	Cell geometry
Zone 1a	6,86%	--	93,14%	--	Homogeneous
Zone 1b	6,86%	52,96%	40,17%	--	Homogeneous
Zone 2a	6,86%	56,52%	36,61%	--	Homogeneous
Zone 2b	6,86%	60,44%	32,70%	--	Heterogeneous
Zone 3	23,20%	--	41,95%	34,85% (gas)	Heterogeneous
Zone 4	23,20%	--	41,95%	34,85% (fuel)	Heterogeneous
Zone 5a	43,48%	--	56,52%	--	Heterogeneous
Zone 5b	6,86%	--	93,14%	--	Heterogeneous
Zone 6a	6,86%	60,44%	32,70%	--	Heterogeneous
Zone 6b	6,86%	56,52%	36,61%	--	Homogeneous
Zone 7	6,86%	32,70%	60,44%	--	Homogeneous
Zone 8	6,86%	56,52%	36,61%	--	Homogeneous
Zone 9a	6,86%	60,44%	32,70%	--	Homogeneous
Zone 9b	--	26,73%	73,27%	--	Homogeneous

Tab. 41 – EBR-II: Geometry and composition for central core subassembly Mark-II AI in ECCO cell code.

9 EBR-II MCNP NEUTRONIC MODELLING

Static neutronic modelling of EBR-II core was achieved performing Monte Carlo simulations. The reference tool chosen for such analysis is the Monte Carlo neutron transport code MCNP6 [41], developed by Los Alamos National Laboratory (USA). ENEA acquired the code license and installed it on CRESCO high performance computing (HPC) machine [42] during 2014. The code allows to perform neutron transport calculations with detailed geometry modelling (up to the pin level), including fuel depletion calculations. Capabilities of MCNP6 on SFR simulation were tested in the framework of the PELGRIMM EU FP7 Project [43] (see Fig. 107).

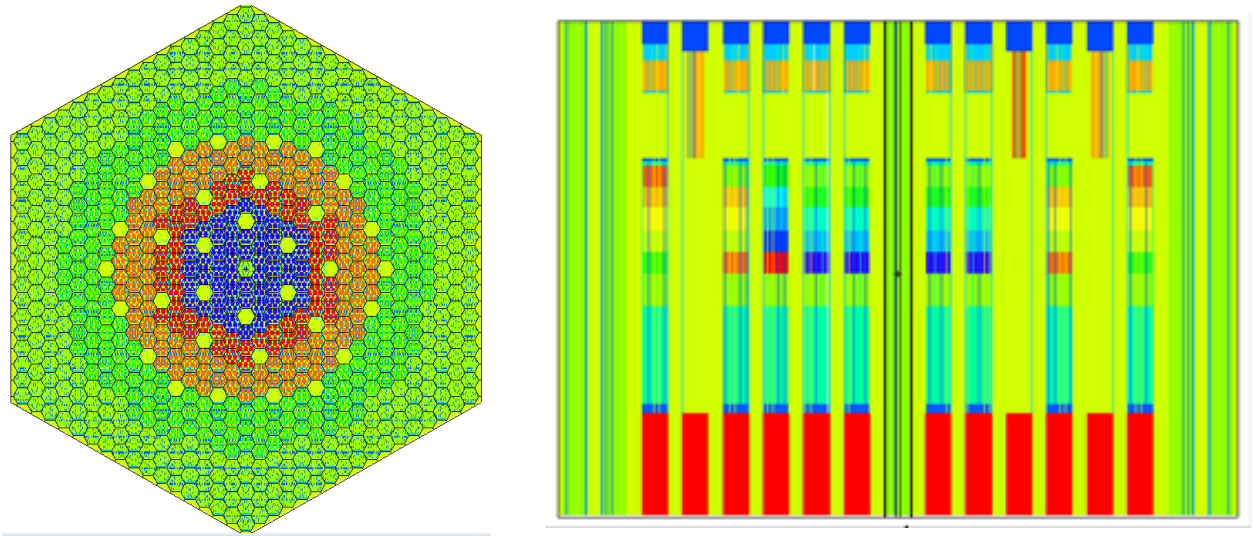

Fig. 107 – MCNP SFR Core Neutronic Modelling.

EBR-II core is a quite heterogeneous system, requiring simulation of the different hexagonal sub-assemblies (S/A) composing the core (61 S/A), the inner blanket (66 S/A) and the outer blanket (510 S/A), the Control and Safety S/A, etc. The core configuration that was modeled is shown in Fig. 108.

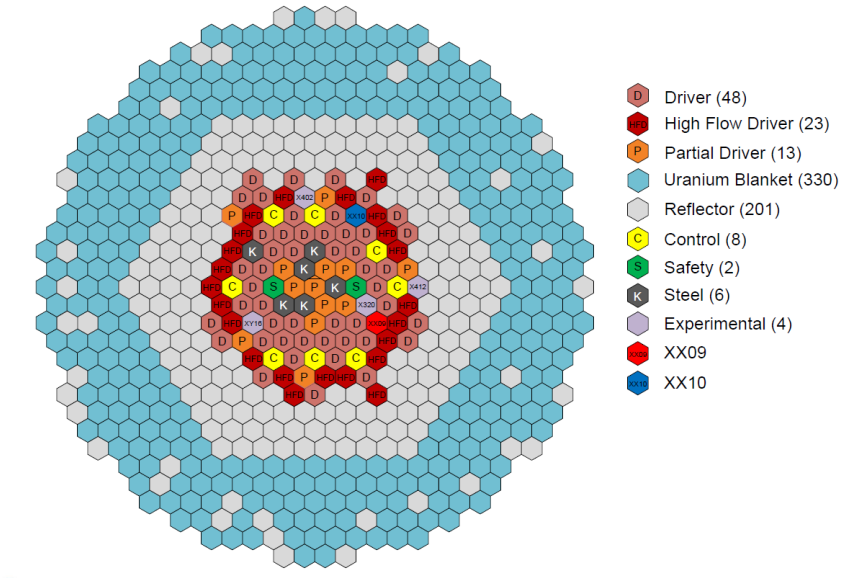

Fig. 108 – Core Neutronic Modelling.

Lower and upper part of the core was also modeled in order to take into account axial neutron leakages effects.
Fuel studied in the benchmark exercise, including driver and blanket assemblies, was partially depleted. Therefore, dedicated material compositions were assigned to the materials cards of the MCNP6 model, including fission products too. The EBR-II benchmark developers lumped several fission products according to the original fissioned nucleus for easing such task.
In order to achieve a good and fast fission source and keff convergences, preliminary calculations with few neutron histories (NH) were run. This was done for getting a good initial source distribution. Then, production calculations were performed by using at least 50 Million of NH (MNH), performing 25000 NH simulations per 2000 cycles.
ENDF/B-VII.1 [44] continuous-energy cross sections libraries, included in the MCNP6 release, were used. The temperature effects on the cross sections were simulated using the MAKXSF [45] code. MNCP6 tally features and the use of at least 100 MNH allowed to calculate the power distribution in each S/A. Reactivity coefficients were also calculated by performing several criticality calculations (KCODE option). Final results are being prepared and released by the next IAEA “EBR-II” meeting, scheduled for March 2015 at ENEA Brasimone Research Center.

10 CONCLUSIVE REMARKS AND FOLLOW UP

The objective of the report is to document:

- The information related to the boundary and initial condition of the transient;
- The experimental data trends, provided by the Benchmark;
- The results of the blind simulation and the analysis, comparing with experimental data;
- The information needed for the post-test analysis;
- The ANSYS CFX model, for the CFD analysis;
- The preliminary assessment of neutronic model that will be implemented.

The blind simulation of EBR-II SHRT-17 has been successfully executed. The comparisons executed bring to the conclusion that RELAP5-3D code has the capability to deal with the relevant thermal-hydraulic phenomena involved in SHRT-17. The following conclusive remarks can be point-out:

- RELAP5-3D© nodalization of EBR-II with the configuration of SHRT-17 is available. Steady state conditions are achieved and transient behavior is satisfactory.

- SHRT-17 blind simulation is completed and results have been submitted for the participation in the IEA CRP on EBR-II.

- CFD model with of the XX09 assembly is developed and preliminary assessment of ANSYS CFX code are implemented.

The follow up of the activity will be performed with following logic:

- Post-test analysis will be improved on the basis of experimental data, relevant to understanding thermohydraulic processes that occur during the transient.

- RELAP5-3D© SHRT-45 model will be implemented. RELAP5-3D© model will be completed with the implementation with the neutron point kinetic and qualified in steady state condition. Next, the model will be applied to the simulation of the transient of SHRT-45, and then qualified comparing with experimental data.

- The geometric model and the EBR-II reactor core structural composition with a neutronic code, possibly comparing a dual modelling approach. A deterministic analysis with ERANOS 2.1 code, the European reference code for fast reactor, will be supported by a comparison with methods of a Monte Carlo code. The multiplication factor, the delayed neutron fractions, the power distribution and the reactivity coefficients will be calculated, with deterministic and Monte Carlo code, for the EBR-II reactor configurations. Results will be compared in face of the available data (code to data and code to code benchmark).

- RELAP5-3D© thermalhydraulic model will be coupled with 3D neutron kinetic code (i.e. PHISICS). Results of the coupling will be compared with those obtained with 0D kinetic and with experimental data available.

- On the basis of RELAP5-3D© system code results will be implemented the CFD calculation of instrumented assemblies, with ANSYS CFX code.

LIST OF REFERENCES

[1] *L. Briggs, C. Choin, W. Hub, L. Maas, W. Maschek, B. Merk, K. Mikityuk, H., Mochizuki, S. Monti, K. Morita, A. Del Nevo, H. Ohira, A. Petruzzi, U. Partha Sarathy, A. Shin, I. Shvetsov, M. Stempniewicz, D. Sui, B. Truong, Benchmark analyses of the Shutdown Heat Removal Tests Performed in the EBR-II Reactor.*

[2] *IAEA. Status of Fast Reactor Research and Technology Development. IAEA-TECDOC-1691, Vienna, 2012.*

[3] *T. Sumner and T.Y.C. Wei, Benchmark Specifications and data Requirements for EBR-II Shutdown Heat Removal tests SHRT-17 and SHRT-45R, ANL-ARC-226 (rev 1), May 31, 2012.*

[4] *H.P. Planchon, R.M. Singer, D. Mohr, E.E. Feldman, L.K- Chang and P.R. Betten, The Experimental Breeder Reactor II inherent Shutdown Heat Removal Tests – Results and Analysis, Nuclear Engineering and Design 91(1986) 287-296, 1985.*

[5] *L.J. Koch, Experimental Breeder Reactor II (EBR-II) – An Integrated Experimental Fast Reactor Nuclear Power Station, Authorized by Argonne National Laboratory.*

[6] *W.J. Carmack, D.L. Porter, Y.I. Chang, S.L. Hayes, M.K. Meyer, D.E. Burkes, C.B. Lee, T. Mizuno, F. Delage, J. Somers, Metallic fuels for advanced reactors, ScienceDirect, Journal of Nuclear Materials 392(2009) 139-150.*

[7] *A. Del Nevo, C. Venturi, E. Martelli, D. Rozzia, Qualifica di codici di calcolo dedicati alle analisi di sistema avanzati quando applicati nella simulazione di impianti a metallo liquido, ENEA, ADPFISS-LP2-039, 24 Settembre 2013.*

[8] *I. Di Piazza, M. Scarpa, Rassegna di letteratura sulla termoidraulica dei bundle refrigerati a metallo liquido pesante fluente, ENEA, LM-F-R 001,*

[9] *E.H. Novendstern, Turbulent Flow pressure drop model for fuel rod assemblies utilizing a helical wire-wrap spacer system, Nucl. Eng. Des., 22, pp. 19-27, 1972.*

[10] *K. Rheme, Pressure drop performance of rod bundles in hexagonal arrangement, Int. J. Heat Mass Transfer, 15, pp2499-2517, 1972.*

[11] *K. Rehme, Pressure drop correlations for fuel element spacers, Nuclear Technology, 17, pp. 15-23, 1973.*

[12] *N.E. Todreas, M.S. Kazimi, Nuclear Systems I: Thermal Hydraulic Foundamentals, Washington DC: Hemisphere, 1990.*

[13] *C.F. Colebrook, "Turbulent Flow in Pipes with Particular reference to the Transition Region Between Smooth and Rough Pipe Laws", Journal of Institute of Civil Engineers, 11, pp. 133-156, 1939.*

[14] *D.J. Zigrang, N.D. Sylvester, "A Review of Explicit Friction Factor Equations" Transactions of ASME, Journal of Energy Resources Technology, 107, pp.280-283, 1985.*

[15] *R.B. Bird, W.E. Stewart, E.N. Lightfoot, Transport properties, New York: Wiley, 1960.*

[16] *R.A. Seban, T.T. Shimazaki, "Heat transfer to a Fluid Flowing Turbulently in a Smooth pipe with Walls at Constant Temperature", ASME Paper 50-A-128, 1950.*

[17] *R.A. Seban, T.T. Shimazaki, "Heat transfer to a Fluid Flowing Turbulently in a Smooth pipe with Walls at Constant Temperature", Transactions of the ASME, 73, 1951, pp. 803-809.*

[18] *M.S. Kazimi, M.D. Carelli, Clinch River Breeder Reactor Plant Heat Transfer Correlation for analysis of CRBRP Assemblies, CRBRP-ARD-0034, Westinghouse, 1976.*

[19] *ISL Inc, RELAP5/MOD3.3 Code Manual Volume I: Code Structure, System Models, and Solution Methods, Nuclear Safety Analysis Division, July 2003.*

[20] *INL, RELAP5-3D© Code Manual Volume I: Code Structure, System Models and Solution Methods, INEEL-EXT-98-00834, Revision 4.0, June 2012.*

[21] *INL, RELAP5-3D© Code Manual Volume II: User's Guide and Input Requirements, INEEL-EXT-98-00834, Revision 4.0, June 2012.*

[22] *INL, RELAP5-3D© Code Manual Volume II: Appendix A Input Requirements, INEEL-EXT-98-00834, Revision 4.0, June 2012.*

[23] *INL, RELAP5-3D© Code Manual Volume IV: Models and Correlations, INEEL-EXT-98-00834, Revision 4.0, June 2012.*

[24] *R.R. Shultz, RELAP5-3D© Code Manual Volume V: User's Guidelines, INEEL-EXT-98-00834, Revision 4.0, June 2012.*

[25] *SCDAP/RELAP5 Development Team, SCDAP/RELAP5/mod3.2 Code Manual Volume IV: MATPRO – A Library of Materials Properties For Light-Water-Reactor Accident Analysis, NUREG/CR-6150, INEL-96/0422 Revision 1 Volume IV.*

[26] *C.B. Davis, Evaluation of the Use of Existing RELAP5-3D Models to Represent the Actinide Burner Test Reactor, INL/EXT-07-12228, February 2007.*

[27] *C.B. Davis, Applicability of RELAP5-3D for Thermal-Hydraulic Analyses of a Sodium-Cooled Actinide Burner Test Reactor, INL/EXT-06-11518, July 2006.*

[28] *N. AKSAN, F. D'AURIA, H. GLAESER, R. POCHARD, C. RICHARDS, AND A. SJOBERG, Separate effects test matrix for thermal-hydraulic code validation Vol.I: phenomena characterization and selection of facilities and tests, OECD/GD(94)82, Paris, France, July 1994*

[29] *N. AKSAN, F. D'AURIA, H. GLAESER, R. POCHARD, C. RICHARDS, AND A. SJOBERG, Separate effects test matrix for thermal-hydraulic code validation Vol.II: phenomena characterization and selection of facilities and tests, OECD/GD(94)83, Paris, France, July 1994*

[30] *D. Mohr, L.K. Chang, E.E. Feldman, P.R. Betten, H.P. Planchon, "Loss-of-Primary-Flow Without-Scram Tests: Pretest Predictions and Preliminary Results" , Nuclear Engineering and Design, 101, pp. 45-56, 1987.*

[31] *W.M. Kays, M.E. Crowford, Convective Heat and Mass Transfer, Second Edition, McGraw Hill Book Company, New York, 1980.*

[32] *ANSYS CFX Release 13 User Manual, 2011.*

[33] *M.H. Fontana, L.F. Parsly, J.L. Wantland, 1971, Analytical Studies, ORNL*

[34] *Cheng, X., Tak, N.I., 2006. CFD analysis of thermal-hydraulic behavior of heavy liquid metals in sub-channels, Nuclear Engineering and Design 236, pp.1874-1885.*

[35] *Han, J.T., Fontana, M.H., 1977. Blockages in LMFBR Fuel Assemblies – A Review. Proc. Winter Annual ASME meeting.*

[36] *Menter, F.R., 1994. Two-equation eddy-viscosity turbulence models for engineering applications, AIAA J, 32, pp.269-289.*

[37] *Natesan, K., Sundararajan, T., Narasimhan, A., Velusamy, K., 2010. Turbulent flow simulation in a wire-wrap rod bundle of an LMFBR, Nuclear Engineering and Design 240 (5), pp. 1063–1072.*

[38] *Ranieri, M., 2014. Pre-test CFD analysis of the rod bundle experiment in the Heavy Liquid Metal facility NACIE-UP, Master Thesis University of Pisa.*

[39] *Rasu, N.G., Velusamy, K., Sundararajan, T., Chellapandi, P., 2014. Simultaneous development of flow and temperature fields in wire-wrapped fuel pin bundles of sodium cooled fast reactor, Nuclear Engineering and Design 267, pp. 44-60.*

[40] *Sobolev, V., 2011. Database of thermophysical properties of liquid metal coolants for GEN-IV. SCK CEN-BLG-1069.*

[41] *T. Goorley et al., "Initial MCNP6 Release Overview," LA-UR-11-05198, Los Alamos National Laboratory, USA*

[42] *CRESCO, "Centro Computazionale di Ricerca sui Sistemi Complessi", http://www.cresco.enea.it/*

[43] *FP7, PELGRIMM—PELlets versus GRanulates: Irradiation, Manufacturing & Modelling. Grant Agreement Annex I - "Description of Work". Collaborative project No. 295664. FP7-Fission-2011.*

[44] *J. L. Conlin et al., "Continuous Energy Neutron Cross Section Data Tables Based upon ENDF/B-VII.1", LA-UR-13-20137, Los Alamos National Laboratory, USA*

[45] *F. B. Brown, "The MAKXSF Code with Doppler Broadening", LA-UR-06-7002, Los Alamos National Laboratory, USA*